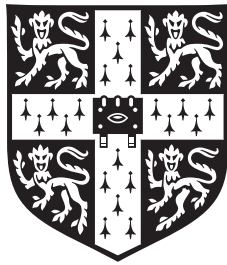


Spin transport in few-layer graphene



Wenjing Yan
Jesus College
University of Cambridge

This dissertation is submitted for the degree of
Doctor of Philosophy
February 2014

Summary

Spin transport in multilayer graphene Wenjing Yan

Graphene spintronics refers to spin injection, spin transport and spin detection, using magnetic electrodes and single/multilayer graphene. Although it has been very actively researched since 2006, there is still disagreement regarding the spin diffusion length (l_{sf}). This is partially because insufficient attention has been paid to the micromagnetics of the electrodes, particularly regarding the interpretation of local magnetoresistance (MR), where the spin-valve signal can be confused with tunnelling anisotropic magnetoresistance (TAMR) at the contacts.

The magnetisation-reversal in unpatterned films of $\text{La}_{0.67}\text{Sr}_{0.33}\text{MnO}_3$ (LSMO) on substrates of NdGaO_3 (001), NdGaO_3 (100) and SrTiO_3 (110) were studied. And the study found nucleation-propagation along the easy axes at room temperature and 150 K. For LSMO on NdGaO_3 (001) at 150 K, there was strong pinning to domain propagation. For LSMO on NdGaO_3 (100) or SrTiO_3 (110), there was sharp switching, with the switching field roughly equal to the nucleation field.

The 150 K magnetic domain structures of patterned LSMO electrodes on NdGaO_3 (001), NdGaO_3 (100) and SrTiO_3 (110) were imaged at remanence using photoemission electron microscopy with X-ray magnetic circular dichroism contrast (XMCD-PEEM). For the electrodes on NdGaO_3 (001), intermediate magnetic fields yielded domains with opposing magnetisations that formed along the length of each electrode, and domain propagation was likely pinned due to defects introduced by patterning along the electrode edges. For the electrodes on NdGaO_3 (100) or SrTiO_3 (110), there were sharp switching at different fields. A magneto-optic Kerr effect microscopy (MOKE) study of the electrodes on NdGaO_3 (100) and SrTiO_3 (110), performed at room temperature and low temperature, showed that the electrodes have easy axes across their lengths, and sharp, well-defined switching, as desired for investigating spin transport through graphene, rather than TAMR. Electrical transport measurements were carried out on 15 devices, out of which only one device showed a low-field MR of 5.5%. This result was analysed using the drift-diffusion model, which implied a 70 μm spin diffusion length and provided evidence for graphene to be used a channel for long distance spin transport.

Acknowledgements

It has been a challenging three-and-half years working on this project in many aspects. Of course the project itself was not easy, but surprisingly, the most challenging task was to stay clam, overcome the disappointment and carry on with a positive attitude, when seemingly exciting results turned out to be boring noises. During this process, I have received very generous help from my supervisor, collaborators and colleagues, without which this work could not have been accomplished.

First and for most, I thank my supervisor Neil Mathur who has been a wonderful supervisor and a very considerate mentor. I thank him for giving me the opportunity to work on this challenging and very exciting project. If not for the excitement of the project, considering the difficulties and scientific disappointments, I would not have proceed this far. I also appreciate very much the time and effort he spent thoroughly reading my dissertation, going through tedious English checks and having inspirational discussions.

I would like thank Lee Phillips, for all the hard work he has done that provided the foundation of this work, and for his generosity and kindness teaching me the necessary laboratory skills and sharing of scientific thought. I would also like especially thank my wonderful collaborators, Antonio Lombardo and Matteo Barbone who helped to transfer graphene, and Sampo Hämäläinen who performed the magneto-optic Kerr effect measurements. I thank Massimo Ghidini for the fruitful discussion and experimental suggestions for the study of magnetisation reversal, and Zili Zhang for carrying out the SEM measurements. I thank Sam Crossley for sharing his knowledge on electrical measurement and his help maintaining the pulse laser deposition system in the best working condition, Xavier Moya for his help with vibrating sample spectrometry, X-ray diffraction, pulsed laser deposition and much

more.

I particularly thank Lee Phillips, Massmio Ghidini and Xavier Moya for offering me the opportunities to work on exciting synchrotron experiments in the Diamond Light Source. I thank Luis Hueso for giving me the opportunity to present my work to his group and discussions. Aside from this, I also thank Lee Phillips, Robert Hoye, Matteo Barbone and Prasanta Muduli for proof read chapters of my thesis, Mary Vickers for her assistance with XRD, Nadia Stelmashenko for general help in the Device materials group (DMG), Lara San Emeterio-Alvarez and Robert Hoye for evaporation, Oon Jew Lee for X-ray diffraction, and all my kind DMG colleagues who have made my time here enjoyable.

I thank all my friends, who are scattered in many places of the world, for their caring and support. My sincere thanks and regards to my dearest parents, brother and sister for their love, support and understanding all these years.

Declaration

This dissertation is submitted for the degree of Doctor of Philosophy in the University of Cambridge. This dissertation is the result of my own work and has been carried out since October 2010 in the Department of Materials Science and Metallurgy. This dissertation includes nothing which is the outcome of work done in collaboration except where indicated in the text. No part of this work has been or is being submitted for any other qualification at this or any other university.

This dissertation does not exceed 60,000 words.

Contents

1 Spintronics	5
1.1 Background	5
1.2 Spin injection and detection	8
1.2.1 Ferromagnetic metal/Ferromagnetic metal interface	11
1.2.2 Ferromagnetic metal/Nonmagnetic metal interface	14
1.2.3 The resistance model and multiple interfaces	16
1.2.4 Non-local MR	19
1.3 Spin relaxation	20
2 Carbon Spintronics	23
2.1 Introduction	23
2.2 Carbon Spintronics	23
3 Manganites	37
3.1 Introduction	37
3.1.1 Crystallographic and electronic structure	39
3.1.1.1 Double exchange and superexchange	40
3.1.1.2 Jahn-Teller distortion	42
3.1.2 Magnetic and electronic phases	44
3.2 The magnetic properties of half-metallic $\text{La}_{1-x}\text{Sr}_x\text{MnO}_3$ ($x \sim 0.3$)	47
3.2.1 The effect of strain on epitaxial $\text{La}_{1-x}\text{Sr}_x\text{MnO}_3$ ($x \sim 0.3$)	49
3.2.2 Magnetic anisotropy	53
4 Experimental methods	59
4.1 Pulsed laser deposition (PLD)	59
4.2 Atomic force microscopy (AFM)	63
4.3 X-ray diffraction (XRD)	65

CONTENTS

4.4	Magnetic characterisation	68
4.4.1	Vibrating sample magnetometry (VSM)	68
4.4.2	Photoemission electron microscopy with X-ray magnetic circular dichroism contrast (XMCD-PEEM)	70
4.4.3	Magneto-optic Kerr effect microscopy (MOKE)	74
4.5	Electrical transport measurement	76
5	Macroscopic magnetic properties of $\text{La}_{0.67}\text{Sr}_{0.33}\text{MnO}_3$ films	79
5.1	LSMO (001) _{pc} on NGO (001)	79
5.1.1	Structural characterisations	80
5.1.2	Magnetic properties	81
5.2	LSMO (110) _{pc} on NGO (100)	85
5.2.1	Structural characterisations	85
5.2.2	Magnetic properties	90
5.3	LSMO (110) _{pc} on STO (110)	97
5.3.1	Structural characterisations	97
5.3.2	Magnetic properties	100
5.4	The effect of Au capping layer on the magnetic property of epitaxial LSMO film	105
5.5	Conclusions	107
6	Characterisation and Magneto-transport measurements of Graphene Spin-Valve Devices	109
6.1	Device fabrication	110
6.1.1	Photolithography	110
6.1.2	Graphene transfer	114
6.2	Device characterisations	116
6.2.1	Raman spectrometry	116
6.2.2	Atomic force microscopy	117
6.3	Magnetic properties of the LSMO electrodes	123
6.3.1	XMCD-PEEM images	123
6.3.2	MOKE measurements	127
6.4	Magneto-transport measurements	133
6.4.1	Devices with tunnel barriers	133
6.4.2	Devices with no tunnel barriers	136
7	Conclusions	145

CONTENTS

A The drift-diffusion model	149
A.1 General Expression	149
A.2 FMM/FMM Interface	152
A.3 FMM/NMM Interface	154
A.4 Analysis of graphene spin-valves using the drift-diffusion model	154
B Other graphene spin-valves results	157
B.1 Negligible or no tunnelling $I - V$ characteristic	157
B.2 Asymmetrical $I - V$ characteristic	158
C List of samples	161
References	171

CONTENTS

List of Abbreviations and symbols

Roman Symbols

H_c coercive field

T_C paramagnetic-ferromagnetic transition temperature (Curie temperature)

T_{MI} metal-insulator transition temperature

AFM Atomic force microscopy

AMR anisotropic magnetoresistance

BLG Bilayer graphene

BTO BaTiO_3

CMR colossal magnetoresistance

CNT carbon nanotube

DP The D'yakonov-Perel mechanism

EY Elliott-Yafet mechanism

FM ferromagnetic

FMM ferromagnetic metal

HMF half-magnetic metal

LAO LaAlO_3

LAST $(\text{LaAlO}_3)_{0.3} \cdot (\text{SrAl}_{0.5}\text{Ta}_{0.5}\text{O}_3)_{0.7}$

LMO LaMnO_3

CONTENTS

LSMO $\text{La}_{0.67}\text{Sr}_{0.33}\text{MnO}_3$

lwPMMA low molecular weight poly(methyl methacrylate)

MCD magnetic circular dichroism

MLG multilayer graphene

MOKE Magneto-optic Kerr effect microscopy

MR magnetoresistance

MWCNT multiwall carbon nanotube

NGO NdGaO_3

NMM non-magnetic metal

PEEM Photoemission electron microscopy

PMMA poly(methyl methacrylate)

SC semiconductor

SLG single layer graphene

SPES spin-resolved photoemission spectroscopy

SQUID superconducting quantum interference device

STO SrTiO_3

TAMR tunnelling anisotropic magnetoresistance

VSM vibrating sample magnetometer

XMCD X-ray magnetic circular dichroism

Greek Symbols

β bulk spin asymmetry coefficient

$\Delta\mu$ spin accumulation

γ interfacial spin asymmetry coefficient

μ electrochemical potential

CONTENTS

ρ resistivity

$\rho_{F(N)}$ resistivity of the FMM (NMM)

$\rho_{\pm}^{F(N)}$ resistivity of the spin up + and spin down - channel in FMM(NMM)

f tolerance factor

H_K anisotropy field

J current density

K_u uniaxial anisotropy constant

l_{sf} spin diffusion length

$l_{sf}^{F(N)}$ spin diffusion length in FMM(NMM)

$r_{F,N,b}$ the resistance area product in the FMM, NMM or interface

$R^{P,AP}$ resistance in the parallel and antiparallel magnetisation configuration of the electrodes

r_b^* interfacial resistance

t_{ij} hopping parameter

V volume

$(hkl)_{pc}$ lattice plane (hkl) using the pseudocubic lattice

$[hkl]_{pc}$ crystal axis $[hkl]$ using the pseudocubic lattice

CONTENTS

Chapter 1

Spintronics

1.1 Background

Electrons are negatively charged particles with an intrinsic spin angular momentum that gives rise to spin quantum numbers $+\frac{1}{2}$ and $-\frac{1}{2}$. The charge and spin properties of the electron were treated separately. Traditionally, information was stored in the macroscopic collection of spins, represented by magnetic domains, and manipulated using optical excitation or magnetic field. In spintronics, or spin electronics, the use of electron spin itself as the information carrier allows one to manipulate the property of spin electronically. The foundation of this field lies in the introduction and the application of the two-current model developed by Mott, Fert and Campbell in the 1960s [1]. The two-current model states that the spin-up and spin-down electrons flow in two parallel channels independently. Figure 1.1 shows how the degree of scattering of spins, and therefore the resistance of the device, depends on the relative orientation of the transported spin and the direction of magnetisation in the multilayer. This is the Giant Magnetoresistance effect (GMR), a direct application of the two-current model, which led to revolutionary changes in the magnetic hard-disk read heads and won the 2007 Nobel prize in physics [2].

An important experiment performed by Johnson and Silsbee *et al.* [3] demonstrated that spins flow in the two channels can redistribute themselves once in contact with a non-magnetic metal. When the spin-polarised charge current passes through a ferromagnetic metal (permalloy) to a paramagnetic metal (Al), it induces magnetisation in the Al. The induced magnetism can then be electrically measured as a closed-circuit current or an open-circuit voltage (Figure 1.2a). This experiment therefore demonstrated spin-charge

1. SPINTRONICS

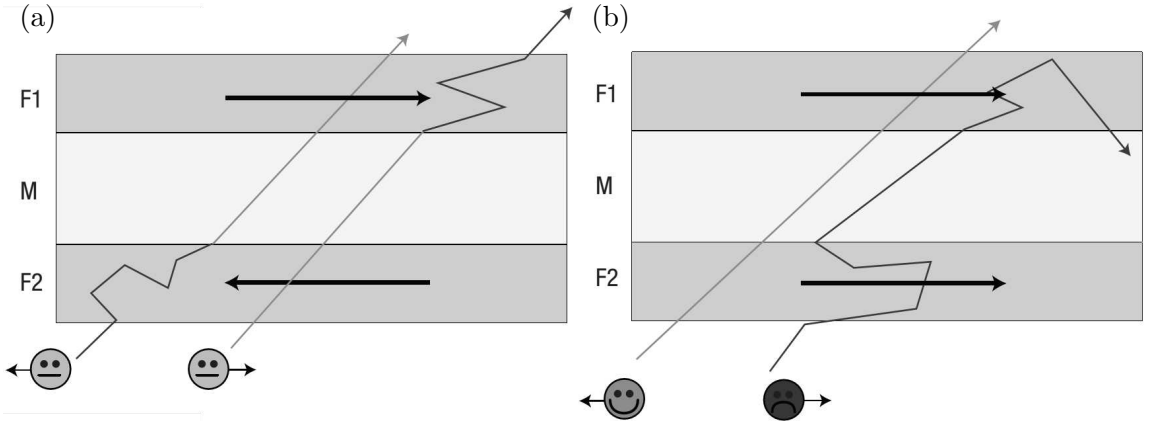


Figure 1.1: Schematic shows the mechanism of GMR. (a) When the two magnetic layers are anti-parallel, spins from both channels experience strong scattering, therefore the resistance of the device is large. (b) When the two layers are parallel, spins from one channel experience strong scattering, but the other spin direction can go through easily and the resistance is small [2].

coupling. Subsequently, van Son et al. calculated the chemical potential profile across a ferromagnetic metal (FMM)/non-magnetic metal (NMM) interface [4] and found a discontinuity in the chemical potential at the interface, which is the spin accumulation. Spin accumulation is the driving force for the spin redistribution between the spin-up and down channels (Figure 1.2b). The ability to convert a charge current to a magnetic imbalance and then measure this electrically is very exciting. This property allows one to manipulate spin transport by both magnetic field using the H  nle effect and electrical field through spin-orbit coupling, therefore realising the Datta-Das spin field effect transistor (Figure 1.2c) [5].

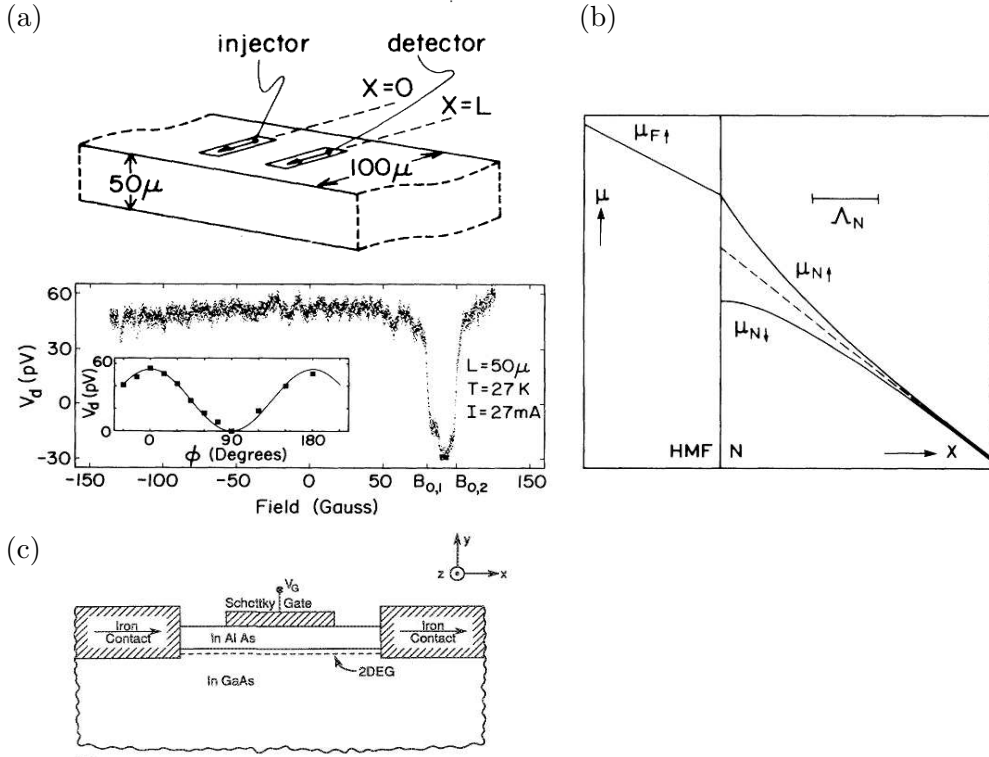


Figure 1.2: (a) Spin injection experiment used by Johnson *et al.* Spin current is injected into the Al channel from the Permalloy electrode. A separate Permalloy electrode is placed 50 μm away from the injector. By sweeping the magnetic field in plane along the length of the electrodes, low (high) voltage was measured with the injector and detector parallel (anti-parallel) to each other [3]. (b) Electrochemical potential profile for the spin-up (\uparrow) and spin-down (\downarrow) electrons near the interface of a half-metallic ferromagnet (HMF) and a non-magnetic metal (NMM) [4]. (c) Schematic of the spin transistor model where spin is injected into a semiconductor channel and manipulated by gate voltage via spin-orbit coupling [5].

1. SPINTRONICS

1.2 Spin injection and detection

Spin transport properties in the Datta-Das spin transistor can be best described using the ‘drift-diffusion’ model, which was initially introduced by Valet and Fert for ferromagnetic metal (FMM)/non-magnetic metal (NMM) multilayers with either transparent or opaque interfaces [6]. Derivation of the drift-diffusion model and simulations for realistic materials system are reproduced in this chapter following the work published in the references [6–8].

In order to discuss the drift-diffusion model, the definition of key physical terms and how to calculate them from measurable material parameters are given below.

In the ferromagnetic metal (FMM):

l_{sf}^F is the spin diffusion length in FMM

β is the bulk spin asymmetry coefficient

$\rho_{\pm}^F = 2[1 \mp \beta]\rho_F^*$, ρ_{\pm}^F is the resistivity of spin up (+) and spin down (−) channel respectively in the FMM.

$\rho_F = \rho_F^*(1 - \beta_F^2)$, ρ_F is the bulk resistivity of FMM

$r_F = \rho_F^* l_{sf}^F$, r_F is the resistance-area product in FMM.¹

In the non-magnetic metal (NMM)

$\rho_{\pm}^N = 2\rho_N^*$, ρ_{\pm}^N is the resistivity in the + and – channel respectively in the NMM.

$\rho_N = \rho_N^*$, ρ_N is the bulk resistivity of NMM.

$r_N = \rho_N^* l_{sf}^N$, r_N is the resistance-area product in NMM.

For the interface:

γ is the interfacial spin asymmetry coefficient

$r_{\pm} = 2r_b^*[1 \pm \gamma]$, r_{\pm} is the spin dependent boundary resistance-area product.

$\rho_b = r_b^*(1 - \gamma^2)$, ρ_b is the resistance-area product of the interface.

r_b^* is the spin averaged resistance.

Consider the following case (Figure 1.3), where spin polarised current is injected from layer A (FMM) into layer B (NMM), in which it diffuses across the interface similar to the way a particle diffuses.

¹In the literature, $r_{F,N,b}$ is often used than resistivity, because it directly reflect the spin-dependent resistance property of the layers considered.

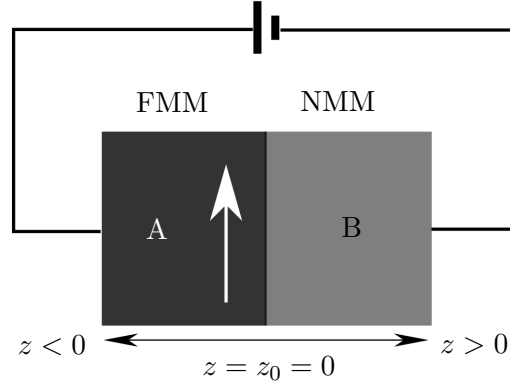


Figure 1.3: Schematic showing spin injection and detection. The white arrow indicates the direction of magnetisation. At the interface between A and B $z = z_0 = 0$

The injected spins undergo a random walk and obey the 1D diffusion law for particles (Equation 1.1) and the Ohm's law for charge transport (Equation 1.2).

$$\frac{\partial^2 \Delta\mu}{\partial z^2} = \frac{\Delta\mu}{l_{sf}^2} \quad (\mu_{\pm} = \bar{\mu} \pm \Delta\mu), \quad (1.1)$$

$$J_{\pm} = \frac{\sigma_{\pm}}{e} \frac{\partial \mu_{\pm}}{\partial z}. \quad (1.2)$$

At the interface of layer A and B, where $z = z_0$, the spin current (J_{\pm}) and chemical potential (μ_{\pm}) must be continuous, such that:

$$J_{\pm}(z = z_0^+) = J_{\pm}(z = z_0^-) \quad , \quad (1.3)$$

$$\mu_{\pm}(z = z_0^+) - \mu_{\pm}(z = z_0^-) = er_{\pm} J_{\pm}(z = z_0). \quad (1.4)$$

1. SPINTRONICS

Solving Equation 1.1 and 1.2 using the boundary as shown in Appendix A, the general solution is as follows [6]:

$$\mu_+(z) = (1 - \beta_n^2)e\rho_n^*Jz + K_1^n + (1 + \beta_n)[K_2^n \exp(\frac{z}{l_{sf}^n}) + K_3^n \exp(-\frac{z}{l_{sf}^n})], \quad (1.5)$$

$$\mu_-(z) = (1 - \beta_n^2)e\rho_n^*Jz + K_1^n - (1 - \beta_n)[K_2^n \exp(\frac{z}{l_{sf}^n}) + K_3^n \exp(-\frac{z}{l_{sf}^n})], \quad (1.6)$$

$$\Delta\mu(z) = K_2^n \exp(\frac{z}{l_{sf}^n}) + K_3^n \exp(-\frac{z}{l_{sf}^n}), \quad (1.7)$$

$$F(z) = (1 - \beta_n^2)\rho_n^*J + \frac{\beta_n}{el_{sf}^n}[K_2^n \exp(\frac{z}{l_{sf}^n}) - K_3^n \exp(-\frac{z}{l_{sf}^n})], \quad (1.8)$$

$$J_+(z) = (1 - \beta_n)\frac{J}{2} + \frac{1}{2er_n}[K_2^n \exp(\frac{z}{l_{sf}^n}) - K_3^n \exp(-\frac{z}{l_{sf}^n})], \quad (1.9)$$

$$J_-(z) = (1 + \beta_n)\frac{J}{2} - \frac{1}{2er_n}[K_2^n \exp(\frac{z}{l_{sf}^n}) - K_3^n \exp(-\frac{z}{l_{sf}^n})]. \quad (1.10)$$

where the subscript or superscript n when replaced by A(B) stands for the relevant physical quantity in A(B) and,

$$K_1^A = K_3^A = K_2^B = 0, \quad (1.11)$$

$$K_2^A = J[(\beta_A - \beta_B) + (\beta_A - \gamma)\frac{r_b^*}{r_B}] \frac{er_A r_B}{r_B + r_A + r_b^*}, \quad (1.12)$$

$$K_1^B = (1 + \beta_A)K_2^A - (1 + \beta_B)K_3^B + r_b^*(1 + \gamma)e[J(1 - \beta_A) + \frac{K_2^A}{er_A}], \quad (1.13)$$

$$K_3^B = J[(\beta_A - \beta_B)r_A + r_b^*(\gamma - \beta_B)] \frac{er_B}{r_B + r_A + r_b^*}. \quad (1.14)$$

The spin accumulation, $\Delta\mu$, as expressed in Equation 1.7, clearly follows an exponential decay away from the interface with the characteristic length l_{sf} . The above solution is a general solution that can be used for both FMM/NMM and FMM/FMM interfaces. By substituting for the material parameters, simulation of the following systems were reproduced from reference [6, 7] to demonstrate the idea of spin accumulation and the conductivity mismatch problem.

1.2.1 Ferromagnetic metal/Ferromagnetic metal interface

For two identical FMM electrodes in parallel (Appendix A.2), when ignoring interfacial scattering, it is effectively a single ferromagnetic metal¹. The chemical potential far away from the interface in the FMM on the left is taken as zero, and the linear increase of μ upon z is a result of the applied voltage bias (Figure 1.4a). At the interface the chemical potential of the spin-up and spin-down electrons is the same for both sides and there is no spin accumulation (Figure 1.4b), although there is spin-polarised current through the interface as shown in Figure 1.4c,d. If instead there is spin dependent scattering at the interface, which means the interface has a spin-dependent interfacial resistance r_{\pm} , then spin accumulation as stated in Equation 1.15 will arise at the interface. The magnitude of the spin accumulation is only affected by r_b^* and γ . Therefore, interfacial resistance can break the continuity of the chemical potential and introduce spin accumulation.

$$\Delta\mu^A = \Delta\mu^B = [r_b^*(\beta - \gamma)] \frac{eJr_A}{r_B + r_A + r_b^*}. \quad (1.15)$$

In the case of anti-parallel electrode magnetisation, the magnitude of the spin polarisation far away from the interface is β . But at the interface, the spin-up and down electrons redistribute between the two current channels under the driving force of spin accumulation (Figure 1.5a,b). Therefore, the spin current (Figure 1.5c) and the current spin polarisation (Figure 1.5d) decay exponentially away from the interface. Figure 1.6 compares the electric field F^2 across the interface between the parallel and anti-parallel case. The area under the curve in the anti-parallel case is associated with the induced interfacial resistance $2\beta^2r_F$.

¹This situation does not represent any physical system in reality, it is derived here purely to introduce the model.

² $F(z) = \frac{1}{e} \frac{\partial \bar{\mu}}{\partial z}$

1. SPINTRONICS

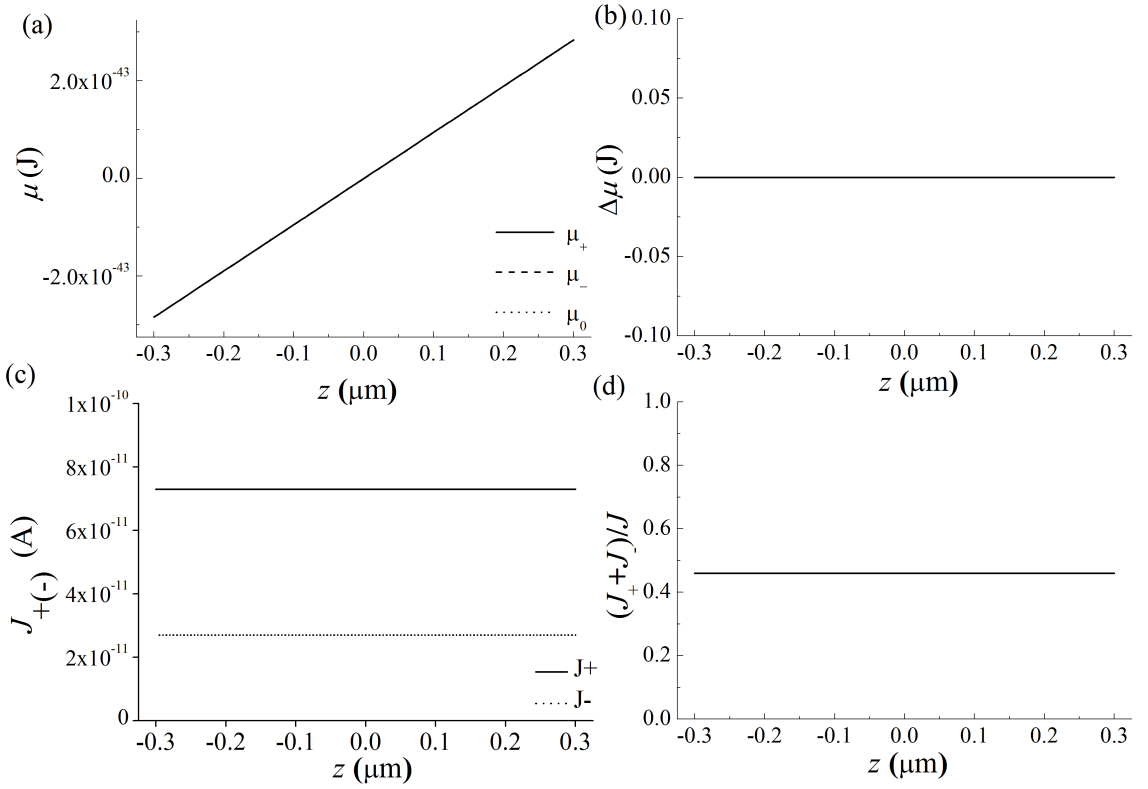


Figure 1.4: (a) The electrochemical potential μ as a function of z is a result of the applied voltage. And simulation of (b) $\Delta\mu$, (c) J_{\pm} , (d) current spin polarisation, as a function of z for Co/Co interface with parallel magnetisation assuming no interface scattering. The simulation uses $r_{\text{Co}} = 4.5 \times 10^{-15} \Omega\text{m}^2$, $l_{\text{sf}}^{\text{Co}} = 60 \text{ nm}$, $\rho_{\text{Co}}^* = 7.5 \times 10^{-8} \Omega\text{m}$, $\beta = 0.46$.

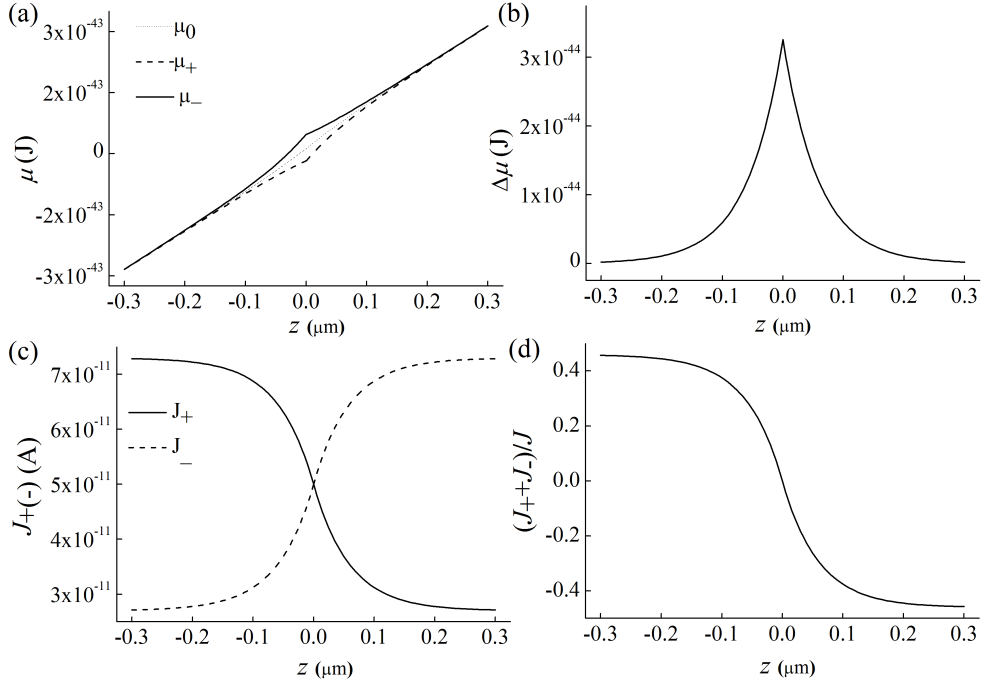


Figure 1.5: Simulation of (a) μ , (b) $\Delta\mu$, (c) J_{\pm} , (d) current spin polarisation, as a function of z for a Co/Co interface with anti-parallel magnetisation assuming no interfacial scattering. The simulation uses $r_{\text{Co}} = 4.5 \times 10^{-15} \Omega\text{m}^2$, $l_{\text{sf}}^{\text{Co}} = 60 \text{ nm}$, $\rho_{\text{Co}}^* = 7.5 \times 10^{-8} \Omega\text{m}$, $\beta = 0.46$. Results are similar to those in [6].

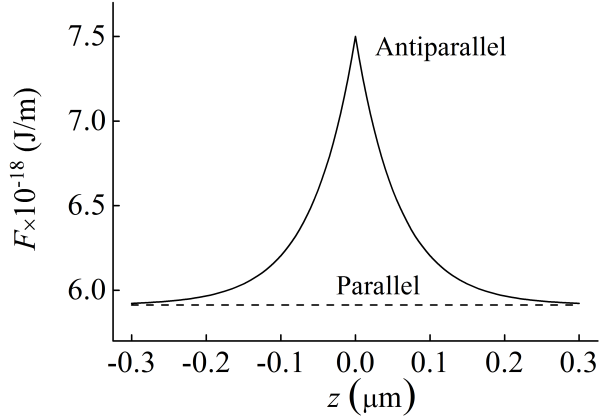


Figure 1.6: Simulation of electric field F as a function of z near a Co/Co interface with anti-parallel (solid line) and parallel magnetisation (dashed line), assuming no interfacial scattering. The simulation uses $r_{\text{Co}} = 4.5 \times 10^{-15} \Omega\text{m}^2$, $l_{\text{sf}}^{\text{Co}} = 60 \text{ nm}$, $\rho_{\text{Co}}^* = 7.5 \times 10^{-8} \Omega\text{m}$, $\beta = 0.46$. Results are similar to those in [6].

1. SPINTRONICS

1.2.2 Ferromagnetic metal/Nonmagnetic metal interface

In the case of a transparent interface between a FMM and NMM, the spin accumulation either side of the interface decays exponentially and is affected by $\rho_{F(N)}^* l_{sf}^{F(N)}$ according to Equation 1.7, 1.12 and 1.14. The key factors that affect spin injection are: (1) the relative spin diffusion length l_{sf} and (2) the relative resistivity of the FMM and NMM.

The effect of the spin diffusion length on the spin accumulation and current spin polarisation are plotted in Figure 1.7. The longer the spin diffusion length of the NMM, the higher the spin accumulation in the NMM near the interface, and therefore the larger the current spin polarisation near the interface. This suggests using semiconductors (SC) instead of a normal metal can enhance spin injection due to its long spin diffusion length.

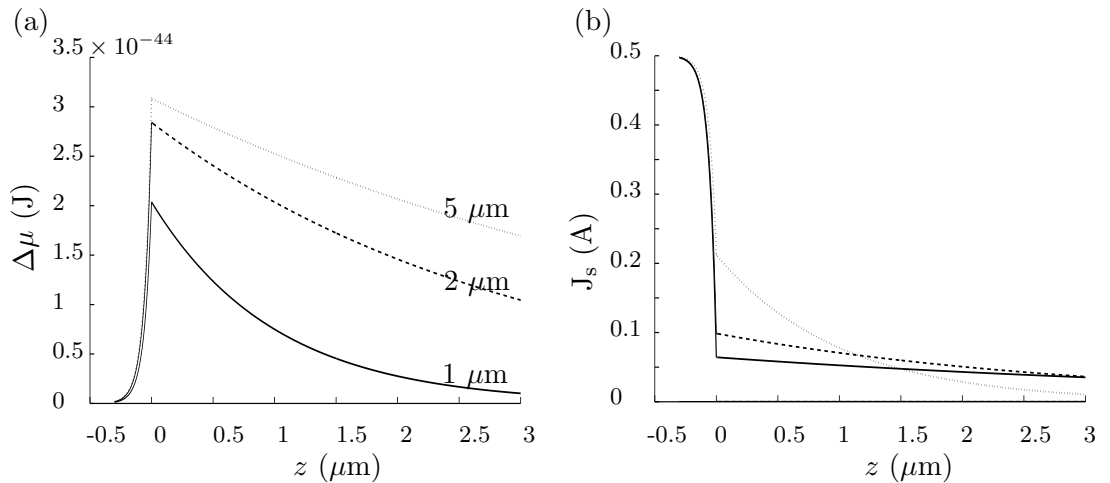


Figure 1.7: Spin accumulation (a), current spin polarisation (b) near the Co/NMM interface plotted for different spin diffusion length in the NMM. For the FMM, $\beta_{\text{Co}} = 0.46$, $\rho_{\text{Co}}^* = 7.5 \times 10^{-8} \Omega\text{m}$, $r_{\text{Co}} = 4.5 \times 10^{-15} \Omega\text{m}^2$, For NMM=Cu, $\beta_{\text{N}} = 0$, $\rho_{\text{Cu}}^* = 6 \times 10^{-9} \Omega\text{m}$, $l_{sf}^{\text{Co}} = 60 \text{ nm}$, $l_{sf}^{\text{N}} = 1, 3$ and $5 \mu\text{m}$. For the interface, $\gamma = 0$. Results are similar to those in [7].

However, this advantage is diminished when considering the relative values of $\rho_N l_{sf}^N$ and $\rho_F l_{sf}^F$. Here we see although there is large $\Delta\mu$, there is nearly no spin-polarised current in the SC due to the conductivity mismatch problem (Figure 1.8a).

This conductivity mismatch problem was first addressed by Schmidt *et al.* [9]. It is because although one can have significant spin accumulation at the interface (Figure 1.8a), due to the low density of states in the SC, the majority of the spins reside in the FMM side¹ and there is significant relaxation. Therefore there is nearly zero spin polarisation in the SC (Figure 1.8b). One possible solution is to replace the FMM with a ferromagnetic semiconductor, however, high- T_C semiconducting ferromagnets are rare. Rashba, and Fert *et al.*, proposed introducing a spin-dependent interfacial resistance, for example, a tunnel barrier, to solve the conductivity mismatch problem [7, 10]. The interfacial resistance produces a discontinuity in the chemical potential as seen in the calculation for the parallel magnetisation configuration in the FMM/FMM geometry (Equation 1.15). The larger the interfacial resistance, the higher the spin accumulation in the SC, and therefore the higher the spin polarisation in the SC region (Figure 1.9b, solid lines). Compared to Rashba's work, Fert *et al.* put an upper limit on r_b^* because the interface has to be sufficiently transparent, otherwise spin spends too much time dwelling in the channel. The optimum value of r_b^* for magnetoresistance (MR) is $r_N(t_N/l_{sf}^N) < r_b^* < r_N(l_{sf}^N/t_N)$.

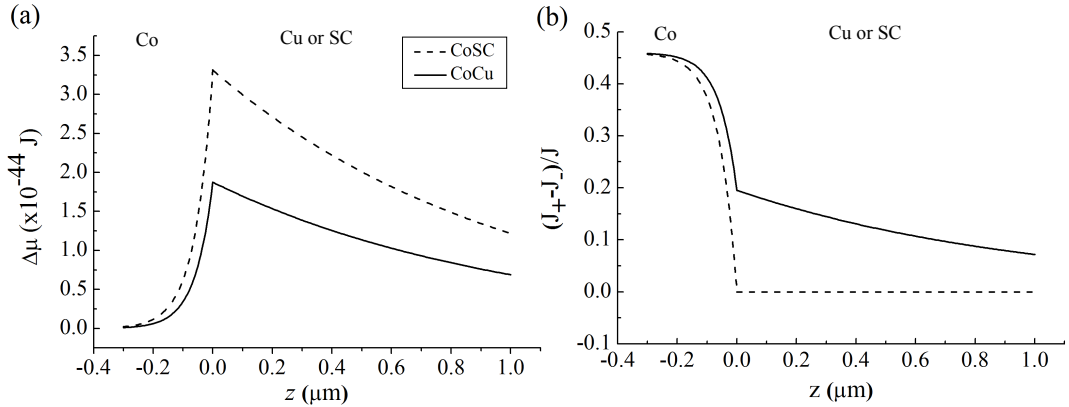


Figure 1.8: Spin accumulation (a), current spin polarisation (b) near Co/Cu and Co/Semiconductor interfaces. The simulation uses $\gamma = 0$, $r_b^* = 0$, $J_0 = 1 \times 10^{-10}$ A, $\beta_{Co} = 0.46$, $\beta_{Cu} = 0$, $\beta_{SC} = 0$, $\rho_{Co}^* = 7.5 \times 10^{-8}$ Ωm , $r_{Co} = 4.5 \times 10^{-15}$ Ωm^2 , $l_{sf}^{Co} = 60$ nm, $\rho_{SC}^* = 1 \times 10^{-3}$ Ωm , $l_{sf}^{SC} = 1 \times 10^{-6}$ m, $r_{SC} = 1 \times 10^{-9}$ Ωm^2 , $r_{Cu} = 6 \times 10^{-15}$ Ωm^2 , $l_{sf}^{Cu} = 1 \times 10^{-6}$ m. Results are similar to those in [7].

¹The number of electrons per unit volume at energy E is $N = \Delta\mu n(E)$, where $n(E)$ is the density of states at energy E. For SC $n(E)$ is small, hence holds small number of electrons.

1. SPINTRONICS

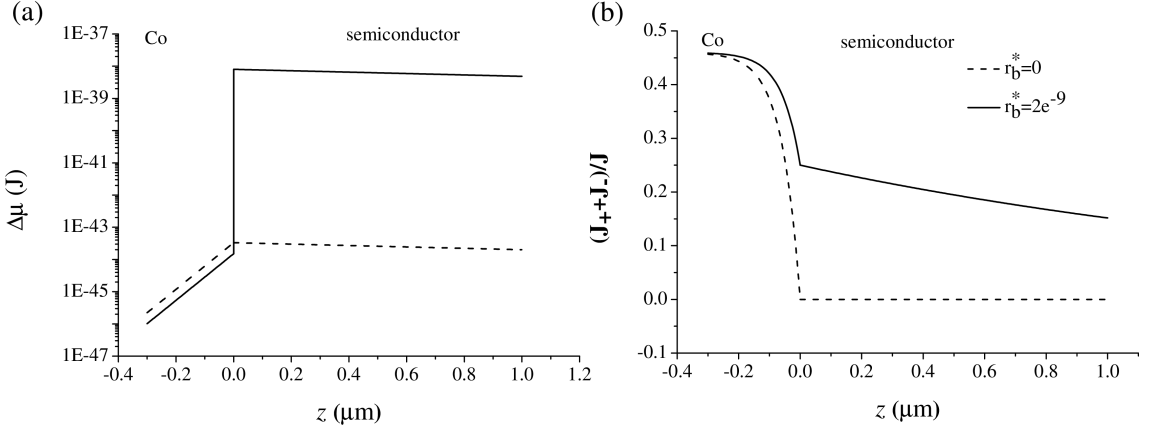


Figure 1.9: Spin accumulation (a), and current spin polarisation (b) near the Co/semiconductor interface plotted for $r_b^* = 0, 2 \times 10^{-9} \Omega\text{m}$. Materials parameters used: $\gamma = 0.5$, $\beta_{\text{Co}} = 0.46$, $\beta_{\text{SC}} = 0$, $\rho_{\text{Co}}^* = 7.5 \times 10^{-8} \Omega\text{m}$, $r_{\text{Co}} = 4.5 \times 10^{-15} \Omega\text{m}^2$, $l_{\text{sf}}^{\text{Co}} = 60 \times 10^{-9} \text{ m}$, $l_{\text{sf}}^{\text{SC}} = 2 \times 10^{-6} \text{ m}$, $\rho_{\text{SC}}^* = 1 \times 10^{-3} \Omega\text{m}$, $r_{\text{SC}} = 2 \times 10^{-9} \Omega\text{m}^2$. Results are similar to those in [7].

1.2.3 The resistance model and multiple interfaces

Fert *et al.* extended the analysis by imposing boundary conditions at each interface and derived a simple resistance model for multilayer structures as shown in Figure 1.10 [7]. Following the resistance model, the total device resistance R in the parallel and anti-parallel state $R^{\text{P,AP}}$ is:

$$R^{\text{P,AP}} = M(r_0 + 2r_{\text{SI}}^{\text{P,AP}}), \quad (1.16)$$

where $r_0 = (1 - \beta^2)\rho_{\text{F}}^*t_{\text{F}} + \rho_{\text{N}}^*t_{\text{N}} + 2(1 - \gamma^2)r_b^*$ and r_{SI}^{P} , $r_{\text{SI}}^{\text{AP}}$ are given in Equation 41 and 42 in ref [6], ΔR and R_{P} are then expressed as

$$\Delta R = \frac{2(\beta r_{\text{F}} + \gamma r_b^*)^2}{(r_b^* + r_{\text{F}}) \cosh\left(\frac{t_{\text{N}}}{l_{\text{sf}}^{\text{N}}}\right) + \frac{r_{\text{N}}}{2}[1 + (\frac{r_b^*}{r_{\text{N}}})^2] \sinh\left(\frac{t_{\text{N}}}{l_{\text{sf}}^{\text{N}}}\right)}, \quad (1.17)$$

$$R^{\text{P}} = 2(1 - \beta^2)r_{\text{F}} + r_{\text{N}} \frac{t_{\text{N}}}{l_{\text{sf}}^{\text{N}}} + 2(1 - \gamma^2)r_b^*, \quad (1.18)$$

$$+ 2 \frac{(\beta - \gamma)^2 r_{\text{F}} r_b^* + r_{\text{N}}(\beta^2 r_{\text{F}} + \gamma^2 r_b^*) \tanh\left(\frac{t_{\text{N}}}{2l_{\text{sf}}^{\text{N}}}\right)}{(r_{\text{F}} + r_b^*) + r_{\text{N}} \tanh\left(\frac{t_{\text{N}}}{2l_{\text{sf}}^{\text{N}}}\right)}. \quad (1.19)$$

Assuming the thickness of the FMM layer $t_{\text{F}} \gg l_{\text{sf}}^{\text{F}}$ and thickness of the NMM layer $t_{\text{N}} \ll l_{\text{sf}}^{\text{N}}$, $R_{\text{P}} \simeq 2r_{\text{F}}(1 - \beta^2)$ when $r_b^* = 0$ and $R_{\text{P}} \simeq 2r_b^*(1 - \gamma^2)$ when $r_b^* \neq 0$.

The MR is then calculated as:

$$MR = \Delta R / R_P. \quad (1.20)$$

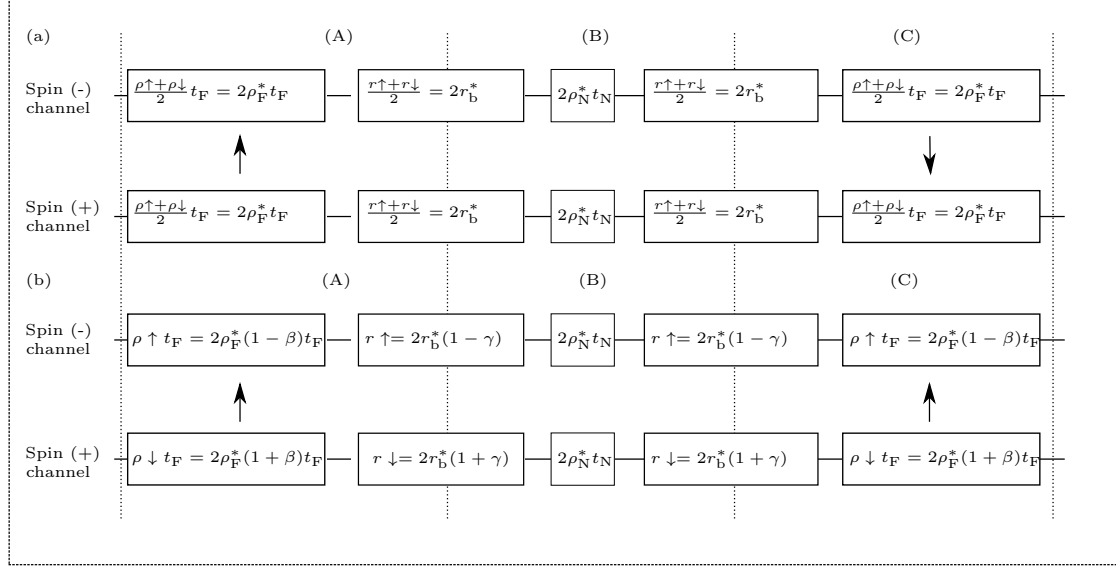


Figure 1.10: The resistance model developed for multi-layer structures when the magnetic layers are (a) anti-parallel and (b) parallel [6].

For a ultra-thin conduction channel like graphene, r_F and r_N can be normalised with respect to the cross-sectional area of the conduction path following Equation 1.21 and 1.22:

$$R_F = r_F / A1 = \frac{\rho_F^* l_{sf}^F}{A1} = \frac{1}{1 - \beta_F^2} \frac{\rho_F^* l_{sf}^F}{A1}, \quad \text{where } A1 = wl \quad (1.21)$$

$$R_{ch} = r_N / A2 = \frac{\rho_N^* l_{sf}^N}{A2} = \frac{\rho_N^* l_{sf}^N}{t_N w} = \frac{\rho_{sq}^N l_{sf}^N}{w}, \quad \text{where } A2 = wt_N \quad (1.22)$$

where w and t_N are the width and thickness of graphene, l is the width of the electrode, as shown in the cartoon (Figure 1.2.3), ρ_{sq}^N is the sheet (square) resistance of graphene.

Figure 1.12 is calculated for a graphene spin-valve with Co electrodes as discussed in Chapter 2. It shows that as the interfacial resistance r_b^* increases, ΔR increases until it saturates due to the increased spin accumulation (Figure 1.12a, solid line). However, the value of R_P keeps increasing with r_b^* , thus, defining a window of optimum interfacial

1. SPINTRONICS

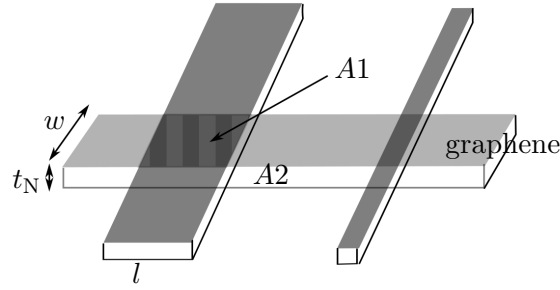


Figure 1.11: Carton shows the geometry of the cross-sectional area $A1$ and $A2$

resistance for MR (Figure 1.12b). When r_b^* is too low, spin relaxation takes place at the electrodes due to the large spin-orbit coupling at the electrodes; when r_b^* is too high, relaxation takes place in the channel, both cases leads to low MR. Figure 1.12b shows that when the spin diffusion length decreases, the window for optimal r_b^* shrinks, therefore restricting the choice of interfacial resistance to an even smaller range.

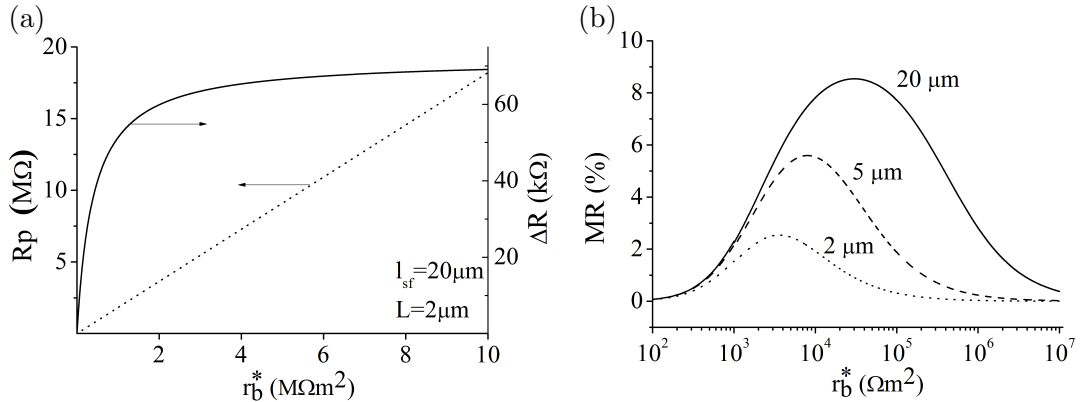


Figure 1.12: (a) ΔR and R_p as a function of r_b^* for Co electrodes and a graphene channel of the length $2 \mu m$ with $l_{sf} = 20 \mu m$. (b) MR vs r_b^* for $l_{sf} = 2, 5$ and $20 \mu m$. The simulation uses $\gamma = 0.5$ and a graphene sheet resistance of $1.5 \times 10^3 \Omega$. Results are similar to those in reference [11]. Details of the simulation are in Appendix A.4.

1.2.4 Non-local MR

The measurement of non-local MR follows the method used by Johnson *et al.* [3]. The advantage of a non-local measurement is that it is able to separate the spin and charge paths to avoid spurious effects, such as anisotropic magnetoresistance (AMR) and tunneling anisotropic magnetoresistance (TAMR). Non-local measurements are now standard. The following paragraph reviews the basic idea.

The calculation of non-local MR for spin valves with semiconducting channels is extended by van Wees *et al.* [12–15] from the metallic spin-valve model derived by Takahashi *et al.* (Equation 1.23) [16].

$$R_{nl} = \pm \frac{\rho_{sq} l_{sf}}{2w} \exp\left(-\frac{L}{l_{sf}}\right) \prod_{i=1}^n \left(\frac{\beta_F \frac{2R_i}{l_{sf}}}{1 - \beta_F^2} \right) \left[\prod_{i=1}^n \left(1 + \frac{\beta_F \frac{2R_i}{l_{sf}}}{1 - \beta_F^2} \right) - \exp\left(-\frac{2L}{l_{sf}}\right) \right]^{-1}, \quad (1.23)$$

where R_{nl} is the nonlocal resistance, ρ_{sq} is the sheet resistance of graphene and R_i is proportional to the ratio between contact resistance and graphene sheet resistance $R_i = \frac{R_c}{\rho_{sq}} w$.

Equation 1.23 is simplified to Equation 1.24 for symmetrical contact or asymmetrical contact with no strong conductivity mismatch, that is, when $R_1 = R_2 = R$.

$$R_{nl} = \pm \frac{2\beta_F^2 \rho_{sq} l_{sf}}{w} \frac{\left(\frac{2R}{l_{sf}}\right)^2 \exp\left(-\frac{L}{l_{sf}}\right)}{\left(1 + \frac{2R}{l_{sf}}\right)^2 - \exp\left(\frac{-2L}{l_{sf}}\right)}. \quad (1.24)$$

According to equation 1.22, the ratio between contact resistance (R_c) and graphene channel resistance (R_{ch}) is $R_c/R_{ch} = \frac{R_c}{\rho_{sq} l_{sf}} w = \frac{R}{l_{sf}}$. Equation 1.24 therefore, shows nonlocal MR exponentially dependent on the channel length L , proportional to β_F^2 and varies with R/l_{sf} . R/l_{sf} describes the ratio of spins that get absorbed into the contact and relax in the channel. Figure 1.13 plots the non-local resistance as a function of contact resistance R_c and spin diffusion length for the graphene spin-valve reported by Tombros *et al.* From this plot, we see that the non-local resistance increases with contact resistance in a similar way as ΔR increases with r_b^* in the local MR expression. The nonlocal resistance R_{nl} then saturates when R_c is much bigger than R_{ch} .

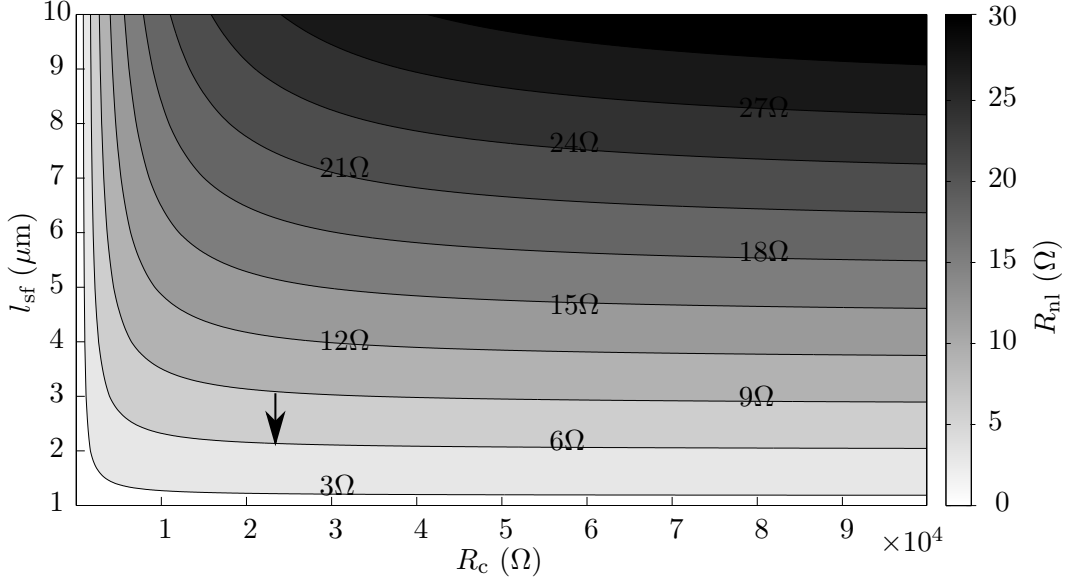


Figure 1.13: Simulated non-local MR, R_{nl} , as a function of contact resistance and spin diffusion length. The parameters used for simulation are the experimental values from Tombros *et al.* [17], that is sheet resistance of graphene $\rho_{sq} = 1.5 \text{ k}\Omega$, width of graphene $w = 2 \mu\text{m}$ and electrode spacing 450 nm. Tombros's device lies at the tip of the arrow.

1.3 Spin relaxation

Spin-orbit coupling plays an important role in spin relaxation. In solids, an electron moving at velocity ν under an electric field feels an effective magnetic field. It is the interaction of electron spin and this effective magnetic field that leads to spin-orbit coupling. During scattering, spin-orbit coupling transfers momentum scattering into spin scattering. In semiconductors, there are four main spin relaxation mechanisms (Figure 1.14) [18–20].

1. The Elliott-Yafet mechanism (EY)

For each momentum scattering event at a local spin-orbit field, such as impurities or phonons, there is a certain probability for the spin to flip. Therefore, in EY relaxation, the spin relaxation time is proportional to the momentum relaxation

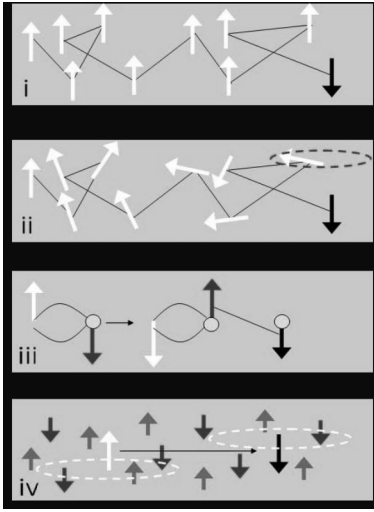


Figure 1.14: Spin relaxation mechanism. (a) The Elliott-Yafet mechanism. (b) The D'yakonov-Perel mechanism. (c) Bir-Aronov-Pikus mechanism. (d) The Hyperfine coupling. Figure taken from reference [19].

time. In the case of graphene, momentum relaxation is mainly due to impurity scattering.

2. The D'yakonov-Perel mechanism (DP)

In the DP mechanism, spin precesses in between two scattering events under its own spin-orbit magnetic field. Therefore, more momentum scattering leads to longer spin relaxation time. In graphene, DP relaxation is mainly due to ripples and graphene curvature.

3. The Bir-Aronov-Pikus mechanism

This mechanism dominates in p-doped semiconductors, where spin-up electrons are exchange coupled with spin-down holes and the total number of spins is conserved. Because spin relaxation of holes by the EY mechanism is faster than that of the electrons, holes act as a sink for spins.

4. Hyperfine coupling

This is the interaction between electron spin and nuclear spin. For an itinerant electron which encounters a large number of nuclei in its path of travel, the effect of spin flip randomises. This mechanism mainly dominates in the case of confined electrons, such as in quantum dot.

1. SPINTRONICS

Spin relaxation in spin-valve devices

Spin relaxation time and spin relaxation length in the non-magnetic channel can be extracted by fitting a Hänle precession curve. Hänle measurements are carried out by applying a magnetic field ($\mu_0 H_\perp$) perpendicular to the magnetisation of electrodes and the plane of the channel, and measuring the non-local voltage as a function of $\mu_0 H_\perp$ (Figure 1.15a) [3]. The non-local spin signal in a perpendicular magnetic field was expressed as [21]:

$$V(B_\perp) = \pm I \frac{P^2}{e^2 N A} \int_0^\infty \left[\frac{1}{4\pi D t} \right] \exp\left[-\frac{L^2}{4D t}\right] \cos(\omega_L t) \exp\left(-\frac{t}{\tau_{sf}}\right) dt \quad (1.25)$$

At zero field, when the magnetisation of the injector and detector are anti-parallel (parallel), the spin accumulation in the channel is large (small), and therefore the device is in the high (low) resistance state (Figure 1.15b). As the field increases, an injected spin precesses in the plane of the channel, and if it precesses 180° by the time it reaches the detector, the device is in the low (high) resistance state. Fitting to the Hänle curve using Equation 1.25 allows one to extract the spin diffusion length, relaxation time and diffusion coefficient. Hänle measurements give reliable estimates of the spin transport properties of the channel when the contact resistance is large, or when the channel length is much longer than the spin diffusion length [12].

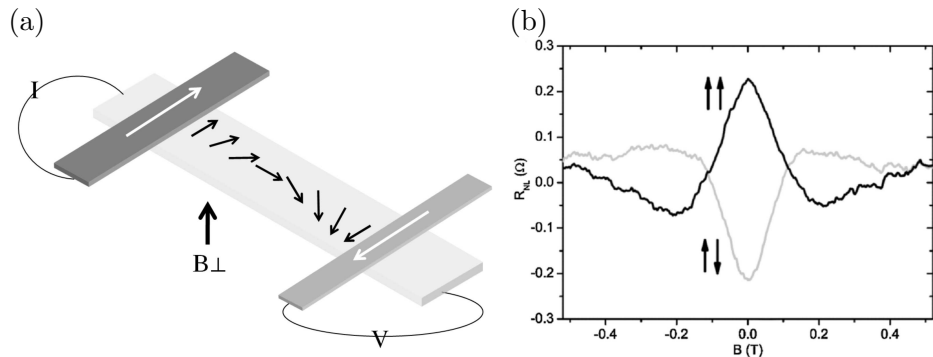


Figure 1.15: (a) Schematic showing the configuration for measurements. The electrodes are either in the parallel or anti-parallel configuration, with the magnetisation along the length of the electrodes in the plane. Magnetic field ($B_\perp = \mu_0 H_\perp$) is applied perpendicular to the electrode magnetisation and $V = V_{nl}$ is measured. (b) Hänle measurements of graphene spin valves with Co electrodes and Al_2O_3 barrier. The gap between the injector and the detector is 5 μm [22].

Chapter 2

Carbon Spintronics

2.1 Introduction

From the discovery of C₆₀ [23], to the identification of the multiwall carbon nanotube (MWCNT) [24], and the isolation of single-layered graphene (SLG) [25], carbon allotropes keep bringing new surprises and excitement to the research community. The importance of carbon material research is not only highlighted by the very large number of publications, but also by being the subject of two Nobel Prizes, first in 1996 for C₆₀ and then in 2010 for graphene. The carbon nanotube (CNT) and graphene have since been extensively studied as a charge (spin) transport channel in electronic (spintronic) devices. CNTs and graphene have large Fermi velocities, weak spin-orbit coupling and weak hyperfine interaction, permitting electron spins to travel a long distance without losing spin polarisation, hence are appealing for use in spin-transistors [5].

2.2 Carbon Spintronics

Before proceeding to review and discuss the literature on CNT and graphene spintronics, it is best to clarify local and non-local measurement geometries. Schematic representations of the different kinds of measurement geometries are shown in Figure 2.1. Local and non-local MR can be calculated using Equation 1.20 and 1.24 in Chapter 1.

CNT spintronics

The early research on CNT spin valves was carried out by Teukagoshi *et al.* in a collaboration between the Hitachi and the Cavendish laboratories in Cambridge [26–28]. Each device consisted of a multiwall carbon nanotube (MWCNT) channel, with Co electrodes

2. CARBON SPINTRONICS

200 nm apart (Figure 2.2a). The transport properties were measured by applying a magnetic field in plane of the contact and perpendicular to the length of the nanotube. A maximum 9% MR was observed at 4.2 K (Figure 2.2b).

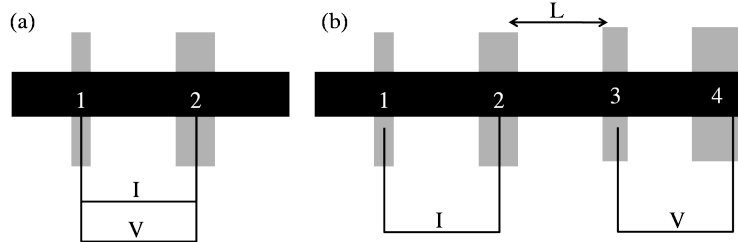


Figure 2.1: (a) Local measurement, where the voltage is applied between two electrodes and the current is measured between the same pair of electrodes. Both electrodes are magnetic metal. (b) Non-local measurement, where current is injected between electrode 1 and 2, and spin accumulation is sensed by electrode 3 at a distance L from electrode 2. In this geometry, electrodes 2 and 3 are ferromagnetic metals, whereas electrodes 1 and 4 are non-magnetic metals. In practice, quite often all four electrodes are made of ferromagnetic metals for simple processing.

Similar experiments were carried out by other researchers and the behaviour of the devices can be summarised as below:

- Random switching [29–31], negative MR [31], positive MR [30, 32, 33] and, more dramatically, sign changes between thermal cycles [32] were reported. The transport properties of the devices are most likely to be controlled by the most transparent local contact point. Inhomogeneity of the CNT/electrode interface adds complications and therefore the reproducibility of the reported results is low.
- Gradual switching. Gradual switching and large resistance at zero magnetic field were due to CNT sampling multiple magnetic domains (Figure 2.2a).
- Asymmetrical switching. Asymmetrical switching was also often reported (Figure 2.2b) [28, 30, 31], and was attributed to exchange bias between the anti-ferromagnetic CoO formed and the Co electrodes.

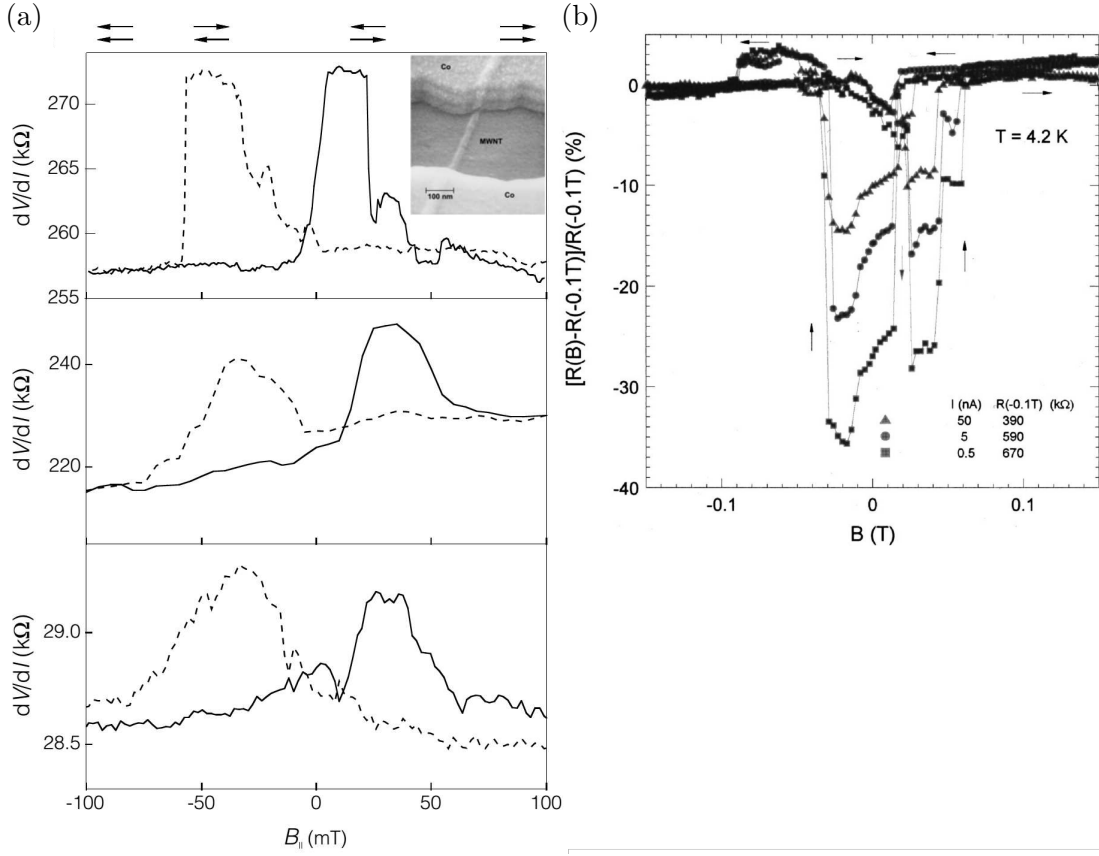


Figure 2.2: (a) Local differential resistance measurement at 4.2 K of MWCNT spin valves consisting of Co electrodes and MWCNT channel. MR varies from 2% to 10% [26]. (b) Local MR measurement of Co/MWCNT/Co spin-valve at 4.2 K. Asymmetrical MR switching was explained by exchange coupling between CoO and Co [31].

Several examples from the literature are presented here to illustrate the points mentioned above.

The study of Jensen *et al.* raised an important point [34]. In their study, hysteretic magnetoresistance was observed in a device containing only one ferromagnetic contact (Ga,Mn)As. The observed MR cannot be explained by spin transport and was attributed to tunnelling anisotropic magnetoresistance (TAMR) [35].

2. CARBON SPINTRONICS

Tombros *et al.* demonstrated spin injection into CNT from Co electrodes at room temperature using the non-local measurement geometry (Figure 2.3a) [32]. In a separate study using Co electrodes and a MWCNT, Chakraborty *et al.* found that before the MR reduced to zero with increasing temperature, it first switched signs from positive to negative and then gradually decreased to zero (Figure 2.3b) [29]. This was explained by the propagation of the non-ferromagnetic cobalt oxide layer at the interface with increasing temperature. L. E. Hueso *et al.* used a different approach, where they placed MWCNT on top of the half metallic $\text{La}_{0.7}\text{Sr}_{0.3}\text{MnO}_3$ electrodes [36]. $\text{MR} = 72\%$ was measured at 5 K, and this gradually disappeared at about 100 K (Figure 2.3c,d). By fitting experimental data into the drift-diffusion model, $\sim 50 \mu\text{m}$ spin diffusion length was estimated. The combination of highly spin polarised $\text{La}_{0.7}\text{Sr}_{0.3}\text{MnO}_3$ electrodes and the natural tunnel barrier formed at the interface were suggested crucial for good spin injection into MWCNT. The small MWCNT and LSMO contact area is important, because it would likely permits sharp switching even if a given electrode contained more than one magnetic domains.

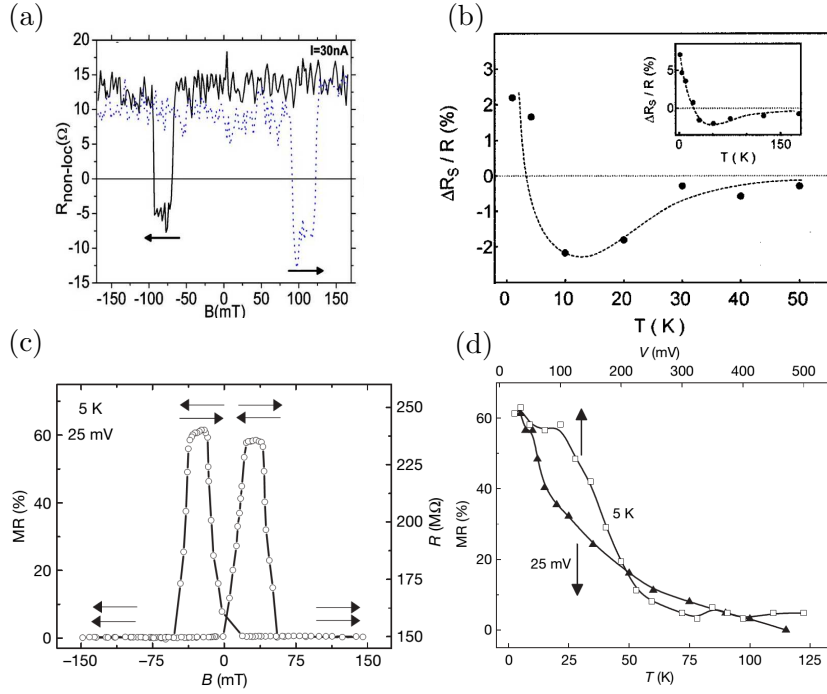


Figure 2.3: (a) Non-local measurement of Co/single-wall CNT/Co spin valve at 4.2 K [32]. (b) Temperature dependence of Co/MWCNT/Co spin-valve signal [29]. (c) Local MR of LSMO/MWCNT/LSMO spin valve at 5K [36]. (d) Temperature dependence of the LSMO/MWCNT/LSMO spin-valve signal [36].

Gate bias was shown to modulate both the magnitude and the sign of the MR [37, 38]. Sahoo *et al.* demonstrated a spin transistor based on a CNT (Figure 2.4) [37]. The oscillation of MR with gate voltage was suggested to be a result of resonance tunnelling. Because a CNT has a long spin diffusion length of 100 μm, when probed with short electrode spacing (250 nm), it behaves like a quantum dot, in which there are spin dependent energy levels, and the MR can be tuned by gating.

Graphene Spintronics

Like CNTs, graphene has weak spin-orbit coupling due to the small atomic number of carbon [39], weak hyperfine interaction due to the absence of nuclear magnetic moment, and was predicted to have a long spin diffusion length and hyperfine interaction, and a long spin diffusion length is expected. Whereas CNT can be metallic and semiconducting, graphene behaves like a good metal, in which both electrons and holes are the

2. CARBON SPINTRONICS

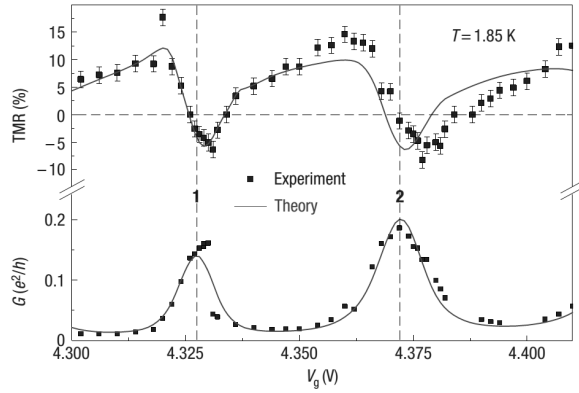


Figure 2.4: Gate dependence of MR and the conductance of PdNi/SWNT/PdNi spin valve measured at 1.85 K [37].

conducting species at Fermi level (Figure 2.5a). One can switch from electron-conduction to hole-conduction easily by tuning the gate voltage. It is worth to note that the plots in Figure 2.5 are the ideal band diagram for isolated graphene/graphite. The actual band diagram will depends on the exact environment that it is in. For example, there have been lots of effort to engineering the band gap of graphene so that its high mobility can be combined with band gap tuning [40].

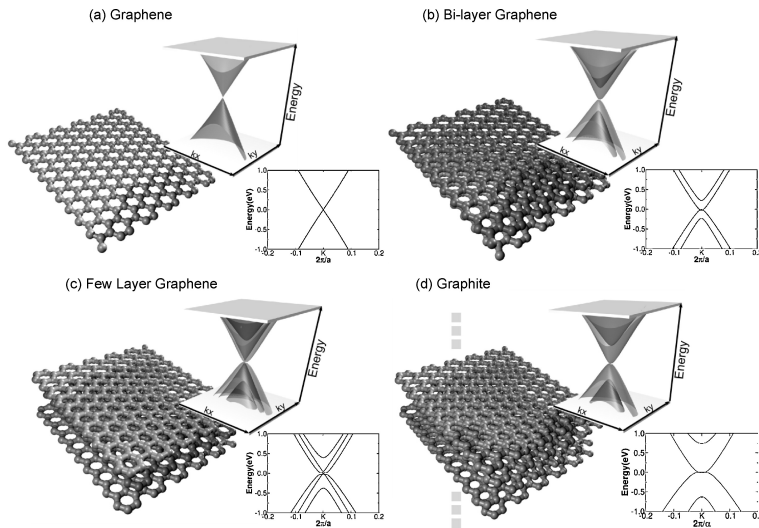


Figure 2.5: Band structure of (a) single-layer graphene, (b) A-B stacked bilayer graphene, (c) A-B-A stacked few-layer graphene, and (d) Graphite. Figure taken from ref. [41].

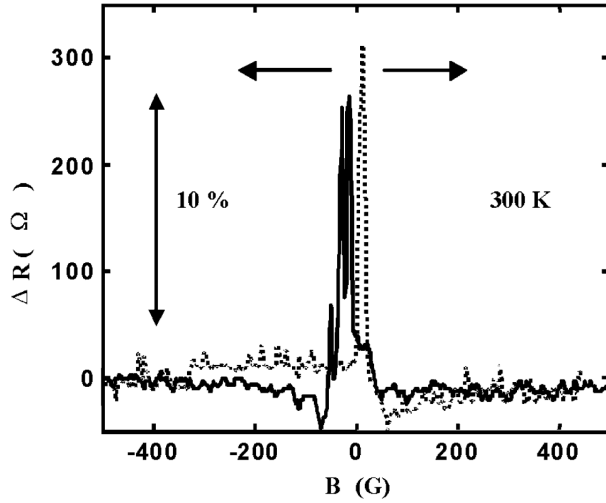


Figure 2.6: MR measured on a Py/single-layer graphene/Py spin valve at 300 K [42].

Since the successful isolation of graphene by mechanical exfoliation [25], it has been used as a spin-transport channel to replace CNTs. The first demonstration of spin transport in graphene was carried out by Hill *et al.* in 2006 (Figure 2.6). The authors assigned the 10% resistance change at 300 K to be a spin-valve signal superimposed on a small AMR background switching. Following this, van Wees, Kawasami and many other research groups tested spin valves with different combinations of electrodes, tunnel barriers, graphene thickness and measurement techniques. The rest of this chapter looks at each of the factors individually, and the table in Figure 2.11 summarises the main results reported in the literature.

Tunnel barriers were introduced to solve the conductivity mismatch problem. The effect of contact resistance on the spin injection was studied and summarised by Han *et al.* (Figure 2.7a) [43, 44]. In the case of a tunnel contact, the spin signal scales with $1/\sigma_G$, whereas spin signal is proportional to σ_G for a transparent contact. Pinholes in the tunnel barrier are detrimental for spin injection, as injected spins can get reabsorbed into the contact through the pinholes, as it is the most transparent part of the contact. Tunnel barriers like Al_2O_3 , TiO_2 and MgO have all been used. Kawakami *et al.* suggested better quality MgO can be achieved by using a Ti seed layer [43] and observed a $1/\sigma_G$ dependence of spin signal on conductivity (Figure 2.7b). In comparison, Jozsa *et al.* observed a σ_G dependence of the spin signal with Al_2O_3 barrier, which is the signature of a transparent or pinhole dominated barrier (Figure 2.7c). But this does not imply

2. CARBON SPINTRONICS

MgO barriers are better than Al₂O₃ barriers, as barrier resistances of tens of MΩ have also been achieved with Al₂O₃ barriers [11]. In fact, the quality of the tunnel barrier was not carefully studied in the literature and its deposition was not very well controlled. The most reliable Al₂O₃ deposition seems to be atomic layer deposition, for which the resistance of the barrier can be tuned by varying the number of cycles [45].

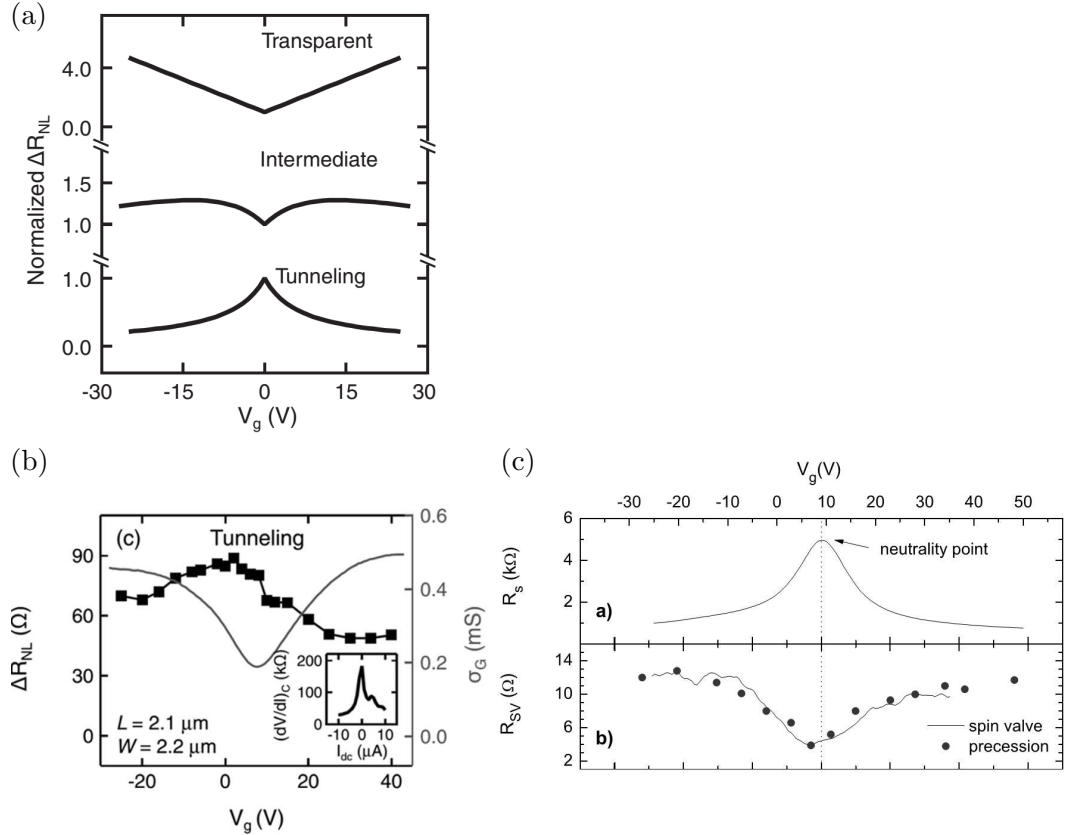


Figure 2.7: (a) Schematics show the gate dependence of non-local spin signal for transparent, intermediate and tunnelling contacts [43]. (b) Nonlocal MR obtained on Co/MgO/SLG/MgO/Co spin valve. Spin-valve signal inversely proportional to the conductivity of graphene, indicates good quality tunnel barrier [43]. (c) Data obtained on Co/Al₂O₃/SLG/Al₂O₃/Co spin-valve, which shows spin signal proportional to graphene conductivity, a signature of transparent or pin-hole dominated interface [46].

Using non-local measurements and Hänle precession, many groups studied the spin relaxation behaviour in graphene as a function of graphene thickness [47–50]. Although there were suggestions that the EY mechanism dominates in SLG, and that DY spin relaxation dominates in BLG [47–49], Yang *et al.* suggested DY dominated relaxation in BLG can deviate at low temperature at the charge neutrality point. Han *et al.* also deduced a combination of the EY and DP mechanism in BLG [47]. The exact relaxation mechanism in graphene is still debatable.

Multilayer graphene (MLG) is thought to be able to screen static charges better from the substrate and from structural defects. Wang *et al.* observed the highest local MR of 9% with a 40 nm-thick graphite flake (Figure 2.8a) [51]. This is much larger than the 1% local MR with single layer graphene reported by Tombros *et al.* (Figure 2.8b) [17]. However, the device resistance in the work of Tombros *et al.* is $\sim 23\text{ k}\Omega$, whereas that of Wang *et al.* is $\sim 145\text{ k}\Omega$. Therefore the smaller MR in the work of Tombros could also be due to pinholes in the Al_2O_3 tunnel barrier. Another study by Maassen *et al.* showed the spin diffusion length and the relaxation time scale linearly with increasing number of layers up to 15 layers (Figure 2.8c) [50].

It is still debatable whether the surface roughness of graphene [46, 52], graphene edges [15] and graphene ripples [49] have significant effects on the spin relaxation. Pi *et al.* studied the spin transport as a function of Au adsorbates on graphene, and found that charged impurities do not have a dominant effect on spin relaxation although they do lead to strong momentum scattering. What is more surprising is that they even found an increasing spin lifetime with increasing Au adsorbates [52]. Two separate studies both demonstrated that graphene edges do not enhance spin relaxation [15]. The group of van Wees studied the effect of graphene edges by fabricating graphene ribbons where the width was varied from 100 nm to 2 μm . They found that graphene edges do not enhance spin relaxation down to 100 nm [15, 49]. Avsar *et al.* arrived at the same conclusion by using CVD graphene, which has more grain boundaries than the exfoliated graphene, and they obtained a similar spin relaxation time ($\sim 200\text{ ps}$) and spin diffusion length ($\sim 1.5\text{ }\mu\text{m}$) [49].

2. CARBON SPINTRONICS

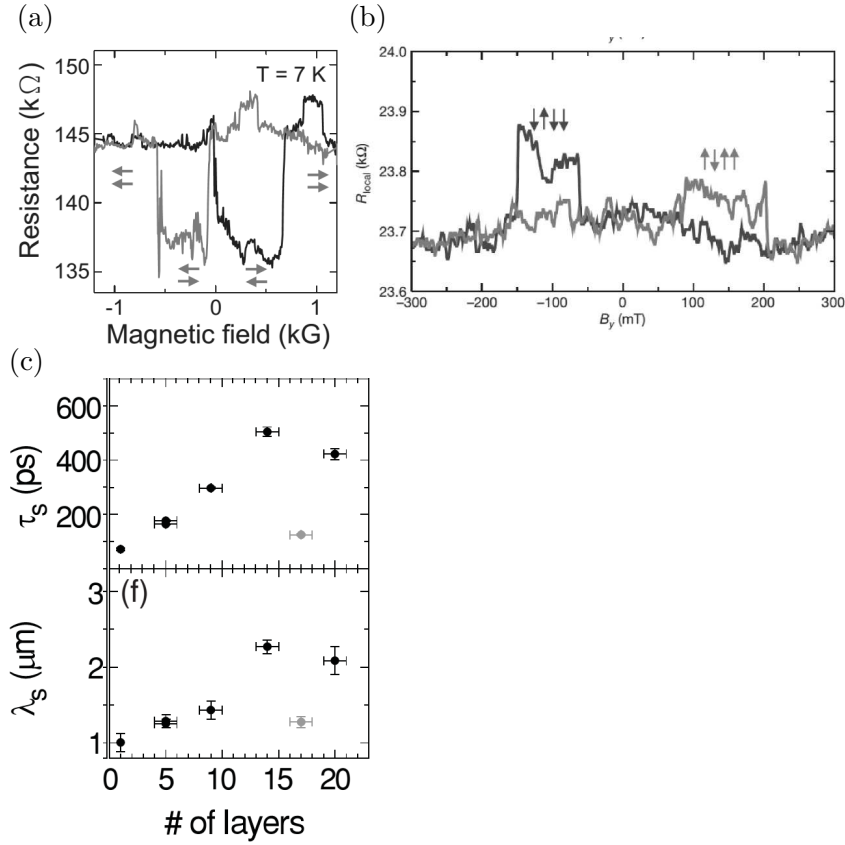


Figure 2.8: (a) Local MR of Co/MgO/graphite/MgO/Co spin valve measured at 7 K. The electrodes spacing is 200 nm [51]. (b) Local MR of Co/Al₂O₃/SLG/Al₂O₃/Co spin valve measured at 4.2 K. The electrodes spacing is 330 nm [17]. (c) Spin relaxation time and spin diffusion length as a function of the number of layers of graphene extracted from Hänle measurements at room temperature [50].

The main driving force for spin relaxation appears to be electrostatic. To provide better electrostatic screening to the spin, and hence to increase the spin relaxation length, the following approaches have been investigated. (1) Using epitaxial graphene ¹ grown on SiC [11, 53]. (2) Using hexagonal BN as a screening layer from the substrate [54]. (3) Suspending graphene from the substrate [55]. Out of the three methods tried, Dlbak *et al.* obtained very promising results using epitaxial graphene. A spin diffusion length of over 100 μm was extrapolated by varying the electrode spacing (Figure 2.9) [11]. A 4.5 μm spin diffusion length was extracted by Zomer *et al.* using BN back support for

¹graphene or graphite that grows epitaxially on Si or C terminated Si substrate.

graphene [54]. However, a similar spin diffusion length ($4.18 \mu\text{m}$) was also obtained with graphene on SiO_2 without BN back support by Yamaguchi *et al.* [45]. The difference between the work of Zomer and Yamaguchi *et al.* is that the former has a much lower contact resistance ($10 \text{ k}\Omega$) as compared to $150 \text{ k}\Omega$ in the work of Yamaguchi *et al.* Therefore, the quality of the tunnel barrier in those works probably had a stronger effect on the spin relaxation than the charge scattering. Suspended graphene has a very high mobility ($200,000 \text{ cm}^2 \text{ V}^{-1}\text{s}^{-1}$) [55], but has not been reported in spin-valves, possibly due to the over-complicated fabrication procedure.

Figure 1.13 in Chapter 1 gives an indication of the limiting factors in achieving a large

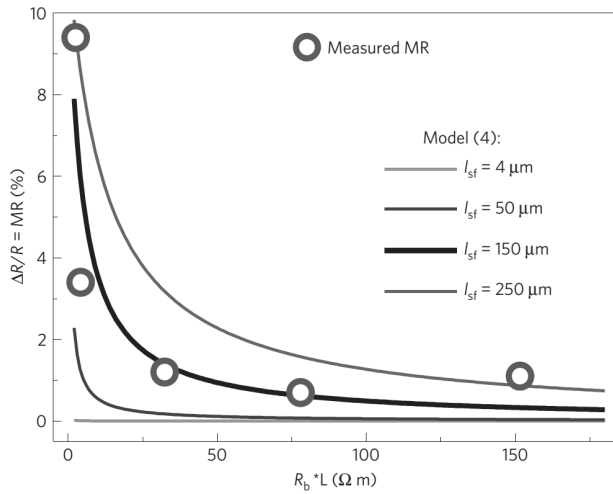


Figure 2.9: Local MR measurement of Co/ Al_2O_3 /epitaxial graphene/ Al_2O_3 spin-valve at 1.4 K. Analysis using the drift-diffusion model gave a spin diffusion length of $150 \mu\text{m}$ [11].

MR in Co/graphene/Co spin valves. The majority of the contact resistances reported in the literature are in the range of 10 to $150 \text{ k}\Omega$, with the exception in the work of Dlubak, but since his work is on local MR, it will not be compared with other non-local MR discussed in this paragraph. In Figure 1.13, R_{nl} reaches saturation when $R_c > 30 \text{ k}\Omega$ for most reported value of l_{sf} . In order to increase R_{nl} , one needs to either increase the spin injection efficiency by improving the quality of the barrier or using electrodes with higher spin polarisation.

The gate dependence of MR varies with the type of barrier as summarised by Han *et*

2. CARBON SPINTRONICS

al. (Figure 2.7a) [43]. For a transparent barrier, MR increases with conductivity/gate bias due to there being more available carriers away from the Dirac point. In the case of tunnelling, MR reduces with gate bias [43, 56]. When the electrode spacing is much shorter than the spin diffusion length of graphene, one can expect quantum interference or Coulomb blockade as seen in nanotube spin valves. Wang *et al.* observed oscillation of MR with gate voltage at 7 K in a spin valve with electrode spacing of 200 nm and a graphite channel (Figure 2.10) [51]. While gate oscillations in CNT spin valve was attributed to quantum interference, similar studies on graphene spin valves are rare and only once reported by Cho *et al.* [57].

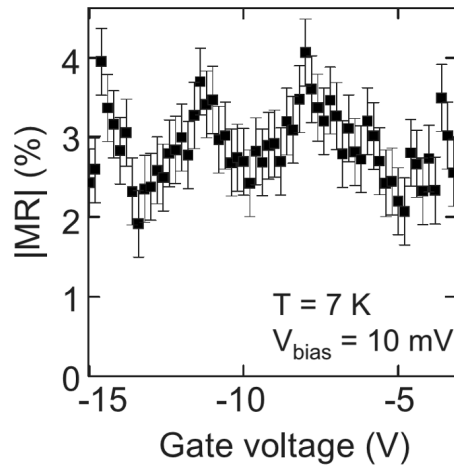


Figure 2.10: Gate dependence of local MR measured at 7 K in graphene spin valve with electrode spacing 200 nm and graphite channel [51].

Spin-valve	L (μm)	R ($\text{k}\Omega$)	Nonlocal MR	Local MR	l_{sf} and τ_{sf}	μ ($\text{cm}^2\text{V}^{-1}\text{s}^{-1}$)	Reference
Py/SLG	0.20			10%			[42]
Co/SLG	1.00		$\sim 100 \text{ m}\Omega$			800-1,700	[58]
	1~3	300	2.1-112 $\text{m}\Omega$		1.5 μm , 84ps		[44]
Py/SLG	0.45		3 Ω (20 K)			2,500	[57]
Co/SLG	3.00	0.3	2 $\text{m}\Omega$		1.2-1.4 μm , 84 ps		[43]
Co/MLG	0.29	1.49	0.6 Ω		8 μm		[59]
	0.25	0.09	5.5 $\text{m}\Omega$	<0.005%			[60]
	1.20	0.20	18 $\text{m}\Omega$	0.02%	1.6 μm , 120 ps		[61]
	0.50	10		0.25% (10 k), 0.4%(2K)			[62]
Co/MgO/SLG	2.10	30-70	130 Ω		2.5-3 μm , 450-500 ps		[43]
	2.10		2 Ω		2.4 μm , 0.5 ns,	1,000-3,000	[47]
Co/MgO (pinhole)/SLG	2.00	6	21 Ω		1.2-1.4 μm , 134 ps		[43]
Co/MgO/BLG			0.1 Ω (20 K)		2 μm , 250-300 ps	400-1,300	[47]
			4 Ω		0.7 μm 0.03-2 ns	700-3,800	[48]
Py/MgO/TLG	1.20	2.2	150 $\text{m}\Omega$		1.5 μm		[63]
Co/MgO/Graphite	0.20	45		12% (7 K)			[51]
Co/ Al_2O_3 /SLG	1~5	23	0.25~2 Ω	0.8%(4.2 K)	1.5-2 μm , 150 ps	2,000	[17]
	0.5~5	1-2	25 $\text{m}\Omega$ -10 Ω		1.5 μm , 60-90 ps		[22]
	3.10	20-40	5-15 Ω		1.1-2.2 μm , 92-185 ps	2,000-5,000	[15]
	3.10	20-40	6-12 Ω		1.2-2 μm ,		[46]
Co/ Al_2O_3 /SLG (ribbon)	1~3	20-40	8 Ω		0.9-1.9 μm , 40-200 ps	2,000-2,500	[15]
Co/ Al_2O_3 /MLG (7 layers)	10.00	2	25 $\text{m}\Omega$		$\sim 3 \mu\text{m}$, 500 ps		[50]
Co/ Al_2O_3 /PTCA/SLG	1.20	150	30 Ω (45 K)		4.18 μm , 175 ps (45 K)	2,500	[45]
Co/ Ti_2O_3 /SLG/BN	20.00	10	0.1 Ω		4.5 μm , 390 ps	40,000	[54]
Py/BN/BLG/BN	0.60	1-2	0.5 Ω		1.14 μm , 56 ps	2,300	[56]
Co/ Al_2O_3 /EPG	2.90	303	20 $\text{m}\Omega$		1 μm , 2.3 ns (4.2 K)	1,900	[53]
	0.8~2	3,800-136,000		0.7-1.14% (1.4 K)	95-285 μm	17,000	[11]
Co/MgO/SLG (CVD)	1.15		4 Ω		1.1 μm , 180 ps	1,400	[49]
Co/MgO/BLG (CVD)	1~2		150 $\text{m}\Omega$		1.35 μm , 285 ps	2,100	[49]

Figure 2.11: Table summarising data for existing spin-valves. The spacing between the electrodes L, MR, spin diffusion length, spin relaxation time and mobility are given. SLG, BLG and MLG stand for single layer, bilayer, and multilayer graphene, respectively. EPG stands for epitaxial graphene. CVD stands for chemical vapour deposition. The measurement temperature is indicated for low temperature measurements, otherwise, values are given for room temperature.

2. CARBON SPINTRONICS

Chapter 3

Manganites

3.1 Introduction

Manganites have the chemical formula $\text{RE}_{1-x}^{3+}\text{AE}_x^{2+}\text{MnO}_3$, where RE^{3+} and AE^{2+} are the rare-earth and alkaline earth ion respectively. Both RE_{1-x}^{3+} and AE_x^{2+} share the A-site while the Mn ion occupies the B site of a perovskite structure (Figure 3.1). Jonker and Van Santen *et al.* first studied a small subset of manganites, $\text{LaAE}_x^{2+}\text{MnO}_3$ in 1950 [64]. They revealed the fundamental physical mechanisms contributing to the magnetic and electrical properties of manganites. By varying the concentration of Mn^{4+} , they found the magnetic properties to be a compromise between the indirect positive exchange and the direct negative exchange. The positive and negative exchange are what we now called double exchange and superexchange respectively.

In the next few years, theoretical models were developed by Zener [66] and Goodenough [67] to explain the experimental observations. The magnetic structure of $\text{La}_{1-x}\text{Ca}_x\text{MnO}_3$ at different concentrations of x were studied by Wollan and Koehler using neutron diffraction, and a phase diagram was constructed [68]. Not much progress was made until the 1990s when Jin *et al.* measured a colossal 12700% resistance change in an epitaxial film of $\text{La}_{0.67}\text{Ca}_{0.33}\text{MnO}_3$ upon applying a magnetic field, which was called CMR for colossal magnetoresistance (Figure 3.2) [69]. It was then found that the double exchange model is insufficient to explain this large resistance change, and electron-lattice coupling was then proposed by Millis and others to account for the CMR effect [70–72].

3. MANGANITES

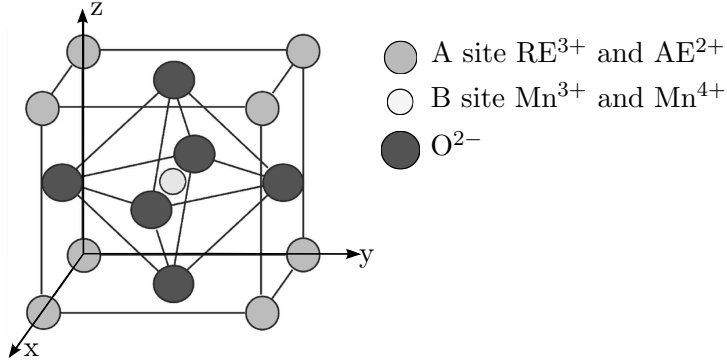


Figure 3.1: Schematic illustrating the structure of the pseudocubic perovskite unit cell. A-cations occupy the corners of the unit cell, and B-cations occupy the octahedral interstitial sites between the O^{2-} -ions [65].

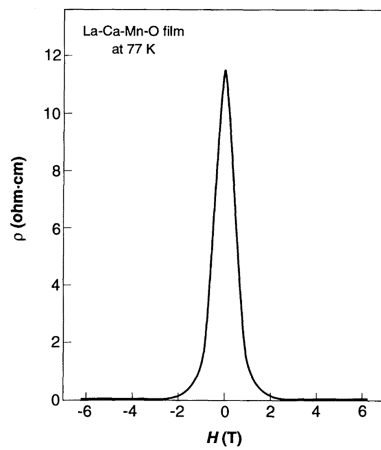


Figure 3.2: Figure shows the colossal magnetoresistance change measured at 77 K [69].

Recent research has been focusing on understanding the CMR effect and the electron–spin–charge correlation with the lattice structure. Many review papers can be found on this topic, for example, in references [65, 73–81]. In addition to the interests in fundamental research, manganites have also been popularly used as magnetic electrodes for spin injection due to the high spin polarisation [82] and high T_C [76, 83, 84]. This dissertation focuses on this latter aspect of manganites, that is, manganites for spintronic applications. The main subject of this chapter is the optimally doped $La_{1-x}Sr_xMnO_3$ around $x = 0.3$, which is a ferromagnetic metal. Other materials, such as $La_{1-x}Ca_xMnO_3$ was occasionally mentioned when necessary. The structure of this chapter is to briefly in-

troduce, by summarising and reviewing the literature, the fundamental mechanisms and models, the magnetic and electronic phases, and the magnetic anisotropy in epitaxial $\text{La}_{1-x}\text{Sr}_x\text{MnO}_3$ ($x \sim 0.3$) thin films.

3.1.1 Crystallographic and electronic structure

In manganites, $\text{RE}_{1-x}^{3+}\text{AE}_x^{2+}\text{MnO}_3$, RE_{1-x}^{3+} can be in the order of increasing ionic radius, Bi^{3+} , Y^{3+} , Gd^{3+} , Sm^{3+} , Nd^{3+} , Pr^{3+} , and La^{3+} . AE^{2+} can be, in the order of increasing ionic radius, Sn^{2+} , Cd^{2+} , Ca^{2+} , Sr^{2+} , Pb^{2+} and Ba^{2+} . By varying the AE^{2+} doping, the Mn ion in principle can adopt two valence states, Mn^{3+} and Mn^{4+} . The $3d$ electrons in Mn^{3+} and Mn^{4+} occupy the $t_{2g}^3e_g^1$ and t_{2g}^3 energy levels respectively, where t_{2g} denotes the localised core electron levels and e_g denotes the higher energy levels occupied by partially itinerant electrons.

The deviation from the cubic perovskite unit cell can be described by the tolerance factor f , which is given by:

$$f = \frac{r_A + r_O}{\sqrt{2}(r_B + r_O)}, \quad (3.1)$$

where r_A , r_B and r_O are the ionic radii of the A-site cation, B-site cation and O^{2-} ion. For a cubic unit cell, we have $f = 1$. The unit cell deviates from cubic to rhombohedral to orthorhombic as f decreases. The tolerance factor f depends on the size and doping level of AE^{2+} , temperature and strain. For example, the parent compound LaMnO_3 (LMO) is orthorhombic, and with increasing Sr doping, the structure transforms to rhombohedral [85]. Increasing the temperature also transforms the more distorted orthorhombic phase to the less distorted rhombohedral or cubic phase.

The tolerance factor directly affects the bandwidth $W = 2Zf$, where Z is the number of manganese nearest neighbours [73]. The bandwidth, Mn-O-Mn bond length and angle, and the doping level, all affect the magnetic and electrical properties of manganites through double exchange, superexchange and electron-lattice coupling, which are reviewed individually next.

3. MANGANITES

3.1.1.1 Double exchange and superexchange

Double exchange

For intermediate doping levels with the AE²⁺ cation, there is in principle a mixed valent state comprising of Mn³⁺ and Mn⁴⁺. The itinerant e_g electron in Mn³⁺ can hop onto O²⁻ and simultaneously from O²⁻ to the empty e_g orbital in Mn⁴⁺, in a process called ‘double exchange’, proposed by Zener *et al.* [66,86]. The two intermediate states, Mn³⁺–O²⁻–Mn⁴⁺ and Mn⁴⁺–O²⁻–Mn³⁺, are energy-degenerate (Figure 3.3a).

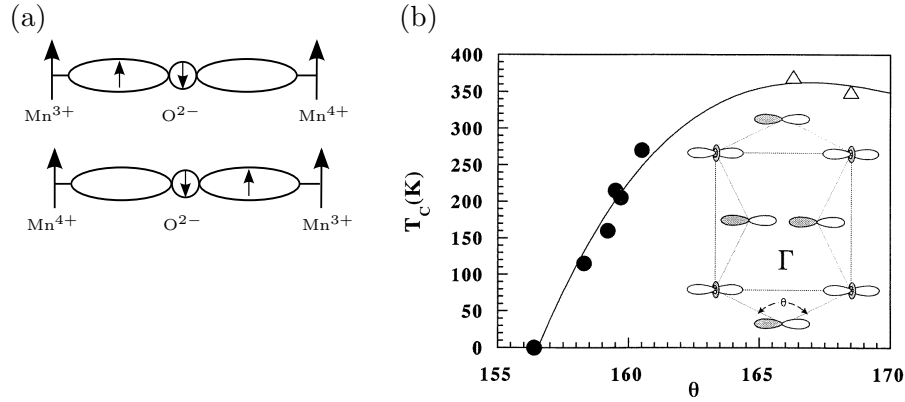


Figure 3.3: (a) Schematic illustration showing the double-exchange mechanism. In double-exchange, simultaneous hopping of an e_g electron from Mn³⁺ to O²⁻, and from O²⁻ to Mn⁴⁺ takes place [73]. (b) Relationship between T_C and average Mn-O-Mn bond angle for ceramic samples of RE_{2/3}³⁺AE_{1/3}²⁺MnO₃, where RE = Nd, Pr, Y and AE = Ca, Sr. The closer the angle to 180°, the higher T_C [87].

The ease of hopping in double exchange is indicated by the hopping parameter t_{ij} (Equation 3.2) [88], where θ is the angle between the localised core spins on atoms i and j , and b_{ij} is a constant. Due to the large on-site Hund coupling, the spins of the itinerant e_g electrons are parallel to the t_{2g} core spins, and hence hopping is easiest when the core spins of two adjacent Mn cations are aligned. In this way, ferromagnetism is coupled to electrical conductivity. Figure 3.3b shows that Curie temperature (T_C) increases with Mn-O-Mn bond angle θ , which influences bandwidth and this b_{ij} .

$$t_{ij} = b_{ij} \cos\left(\frac{\theta_{ij}}{2}\right). \quad (3.2)$$

Double exchange explains very well the similarity between the metal-insulator transition temperature (T_{MI}) and T_C at the intermediate doping levels, for example in $\text{La}_{1-x}\text{Sr}_x\text{MnO}_3$ ($0.175 < x < 0.4$) [85]. Starting below T_C and increasing the temperature, the ferromagnetic order decreases, conduction electron hopping experiences stronger resistance, and hence the resistivity increases with temperature (Figure 3.4a traces for $0.175 < x < 0.4$). As the temperature further increases above T_C in the paramagnetic phase, electron hopping is assisted by thermal energy and hence the resistance decreases with increasing temperature for sufficiently low x . Near T_C , there is a feature in the resistivity, which is suppressed by the application of a magnetic field that aligns core spins (Figure 3.4b).

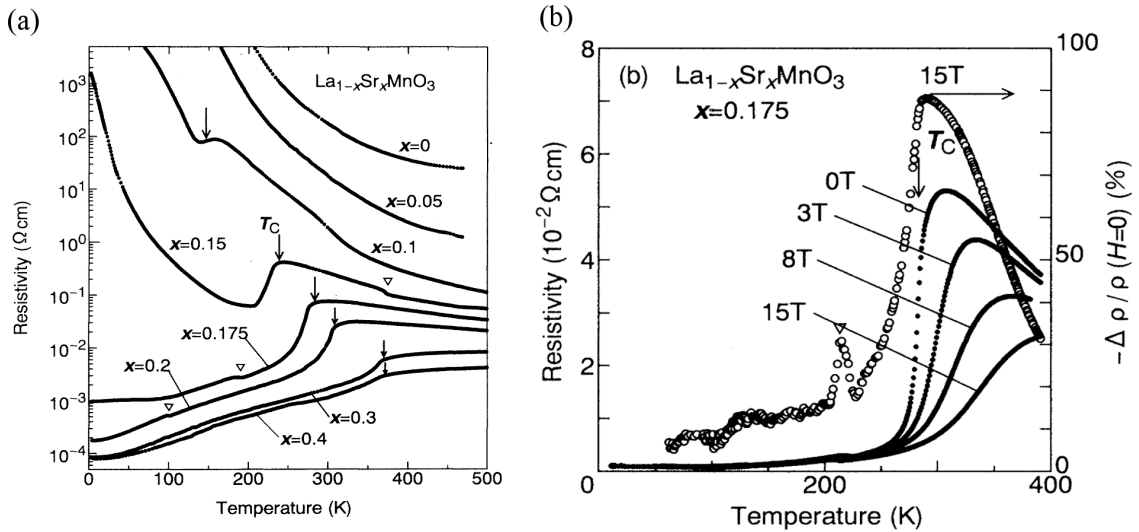


Figure 3.4: (a) Temperature dependence of the $\text{La}_{1-x}\text{Sr}_x\text{MnO}_3$ resistivity for different doping levels. The arrows indicate T_C . (b) Temperature dependence of resistivity for $x = 0.175$ in different magnetic fields [85].

However, the double exchange mechanism cannot explain the presence of the ferromagnetic insulating phase at low temperature in the low doping regime, for example in $\text{La}_{1-x}\text{Sr}_x\text{MnO}_3$ ($0.1 < x < 0.17$) (Figure 3.4a) [85]. It also does not explain the magnitude of the CMR effect and the discrepancies between T_{MI} and T_C [89]. Millis and co-workers proposed that electron-lattice coupling contribution to the large resistance change [70–72]. The electron-lattice coupling can either be static, in which case f controls the hopping, or dynamic, where Jahn-Teller distortions carry a lattice distortion with each mobile electron. Hwang *et al.* demonstrated the effect of f on T_C by replacing

3. MANGANITES

the RE³⁺ and AE²⁺ with different diameter cations, while keeping the AE²⁺ doping level constant [90] (Figure 3.5). They observed an increase in T_C up to $f = 0.93$, after which the T_C decreases. The effects of Jahn-Teller distortions on the magnetic and electrical properties are reviewed next.

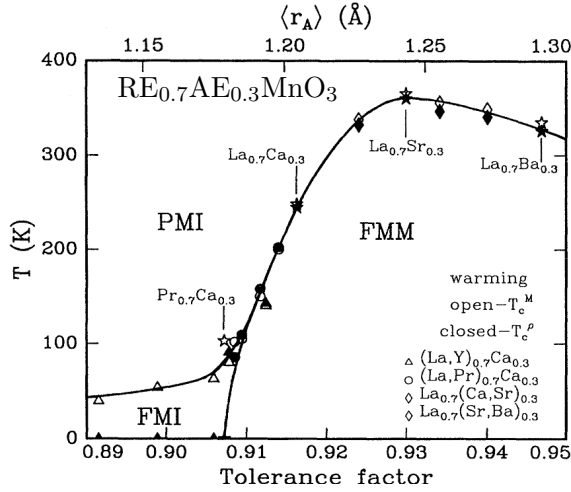


Figure 3.5: T_C as a function of the tolerance factor in $\text{RE}_{0.7}\text{AE}_{0.3}\text{MnO}_3$, where different trivalent and divalent cation are substituted for RE and AE respectively [90].

Superexchange

Superexchange is also an indirect exchange interaction [66]. In this case, the hopping process involves an intermediate virtual state that formed between a fully occupied orbital and an empty orbital. Superexchange can lead to either a ferromagnetic or an antiferromagnetic alignment of spins. In LaMnO_3 where there is only Mn^{3+} , spins align parallel in the plane and antiparallel between planes [91]. In SrMnO_3 where there is only Mn^{4+} , spins align antiparallel.

3.1.1.2 Jahn-Teller distortion

Jahn-Teller distortion is a distortion to the unit cell structure as a result of the preferential orbital occupation. Figure 3.6 shows the mechanism of Jahn-Teller distortion. In an isolated Mn^{3+} ion, the 3d electron energy levels have five-fold degeneracy (Figure 3.6a). In the crystal, the five degenerate levels split into two e_g and three t_{2g} levels in the oxygen octahedral crystal field (Figure 3.6b). In Mn^{3+} , the degenerate orbitals in e_g and t_{2g} levels further split, and resulting in an elongation of the oxygen octahedron along

the z -axis. This is the Jahn-Teller distortion (Figure 3.6c).

Although, this distortion costs elastic energy, the overall energy of Mn^{3+} is lowered as both the e_g and t_{2g} electrons now occupy the lower energy orbitals. However, this distortion is only energetically favourable when the e_g level is singly occupied, for example, in LaMnO_3 . In CaMnO_3 or SrMnO_3 , Mn^{4+} has no e_g electrons [92]. Similarly, Mn^{2+} has two e_g electrons. In both cases, there is no Jahn-Teller distortion.

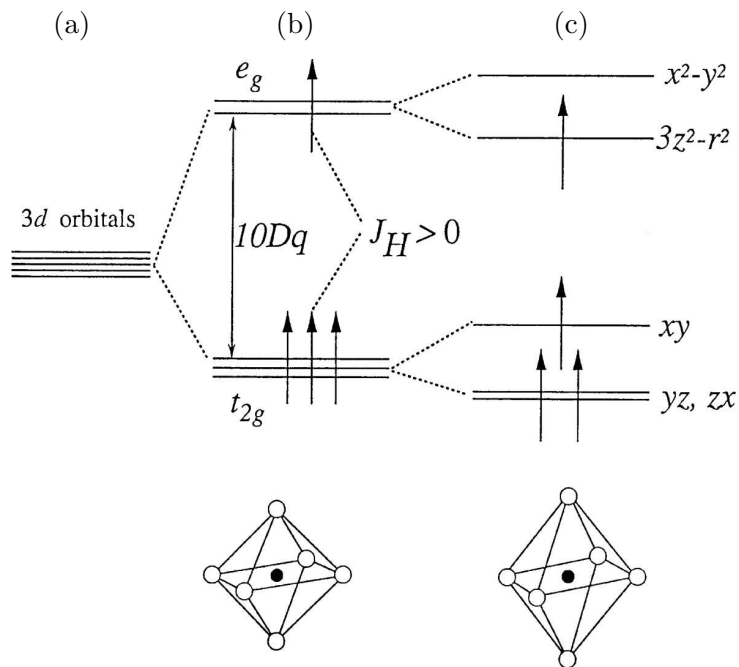


Figure 3.6: (a) In isolated Mn ion, the five $3d$ energy levels are degenerate. (b) The oxygen octahedral crystal field leads to the splitting of the $3d$ levels into lower energy t_{2g} and higher energy e_g levels. (c) For Mn^{3+} in the oxygen octahedron, the t_{2g} and e_g levels further split, and the energy of the system is thus lowered. (d) The occupation of the $d_{3z^2-r^2}$ orbital forces the octahedral to expand along the z -axis. This coupling between orbital occupation and lattice deformation is called the Jahn-Teller distortion [80].

The Jahn-Teller distortion competes with double exchange to determine the magnetic and electronic ground states. Double exchange lowers the kinetic energy by favouring the formation of delocalised electrons, and leads to ferromagnetism and metallicity. The Jahn-Teller distortion lowers the potential energy by raising the e_g and t_{2g} orbital de-

3. MANGANITES

generacy such that the e_g electrons are localised. The balance of the e_g electron hopping and localisation is represented by the factor λ , where $\lambda = E_{\text{lattice}}/t_{\text{eff}}$ ¹ [71]. Here, t_{eff} is very sensitive to the temperature, doping and magnetic field via f and t_{ij} . The effect of temperature and doping on lattice distortion was studied by Booth *et al.* [92]. They measured the variance of the Mn-O bond length as a function of temperature and found that the asymmetry of the Mn-O bond lengths increases dramatically with temperature (Figure 3.7). Both the reduction of t_{eff} and the increase of E_{lattice} lead to a larger λ , and hence a large change of resistance near T_C . Magnetic field increases t_{eff} by aligning core spins, thus favouring metallicity.

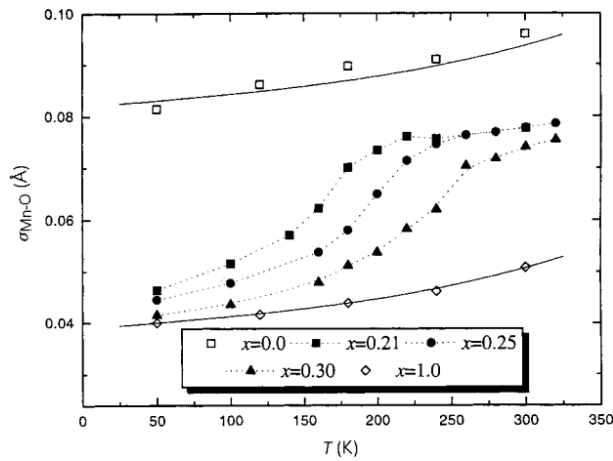


Figure 3.7: The variance of the Mn-O bond length ($\sigma_{\text{Mn-O}}$) as a function of temperature for different doping levels of $\text{La}_{1-x}\text{Ca}_x\text{MnO}_3$. A sharp increase in $\sigma_{\text{Mn-O}}$ is seen near the transition temperature. At low temperature, $\sigma_{\text{Mn-O}}$ approaches that of optimal-doped $\text{La}_{1-x}\text{Ca}_x\text{MnO}_3$ ($x = 0.3$) [92]. The fitted lines are for LaMnO_3 and CaMnO_3 .

3.1.2 Magnetic and electronic phases

The magnetic and electronic ground states in manganites result from a competition between the double exchange interaction and the superexchange interaction. The competition is tailored by the e_g orbital occupation, which itself depends on the doping, the tolerance factor and the Jahn-Teller effect. The phase diagram consists of many phases, each of which has different magnetic, electronic and orbital orders. Varying the doping level x , double exchange competes with the Jahn-Teller distortion and superexchange to

¹ E_{lattice} is the self-trapping energy due to the Jahn-Teller distortion and t_{eff} is the effective hopping matrix for double exchange.

determine the ground state.

The effect of the doping level and electron bandwidth on the magnetic and electronic phases and the orbital structure is summarised by Tobe *et al.* [91] (Figure 3.8).

For large bandwidth material, such as $\text{La}_{1-x}\text{Sr}_x\text{MnO}_3$, the following phases exist [67].

- $x = 0$, there is only Mn^{3+} , the magnetic order is ferromagnetic in the plane and antiferromagnetic between planes. In the xy plane, the $d_{3x^2-r^2}$ and $d_{3y^2-r^2}$ orbitals alternate, and the same order is repeated along the z axis. It is an A type antiferromagnet (AF) insulator. Orbital ordering is schematically shown in Figure 3.8(i).
- $0.2 < x < 0.5$, double exchange dominates, the kinetic energy saving overcomes Jahn-Teller effect, free hopping of the e_g electron decreases the orbital order. The low-temperature ground state is a FM metal. No orbital ordering as schematically shown in Figure 3.8(ii).
- $x = 0.55$, the ground state is an A-type antiferromagnetic metal (AFM). There is $d_{x^2-y^2}$ orbital ordering in the xy plane. Orbital ordering is schematically shown in Figure 3.8(iii).
- $0.55 < x < 0.7$, the ground state is a C-type AFM insulator with $d_{3z^2-r^2}$ orbital ordering along the z -axis. Orbital ordering is schematically shown in Figure 3.8(iv).
- $x > 0.9$, the ground state is a G type AFM insulator with no orbital order, because the e_g orbital in Mn^{4+} is empty.

For smaller bandwidth manganites, in which the ionic radius of the A-site cation is smaller, the hopping parameter is smaller and hence the double exchange interaction is weaker. A charge exchange (CE)-type AFM phase (Figure 3.8 v) develops for doping close to 0.5, and this phase expands to wider doping levels for smaller bandwidth manganites. In the CE phase, charge, spin and orbital ordering coexist. It is in this doping regime that the orbital ordering is most sensitive to magnetic field. Magnetic field reduces the angle between the Mn core spins, hence favoring double exchange, destabilising the orbital ordering, and transforming the charge-ordered insulating state to a spin-aligned metal [93, 94].

3. MANGANITES

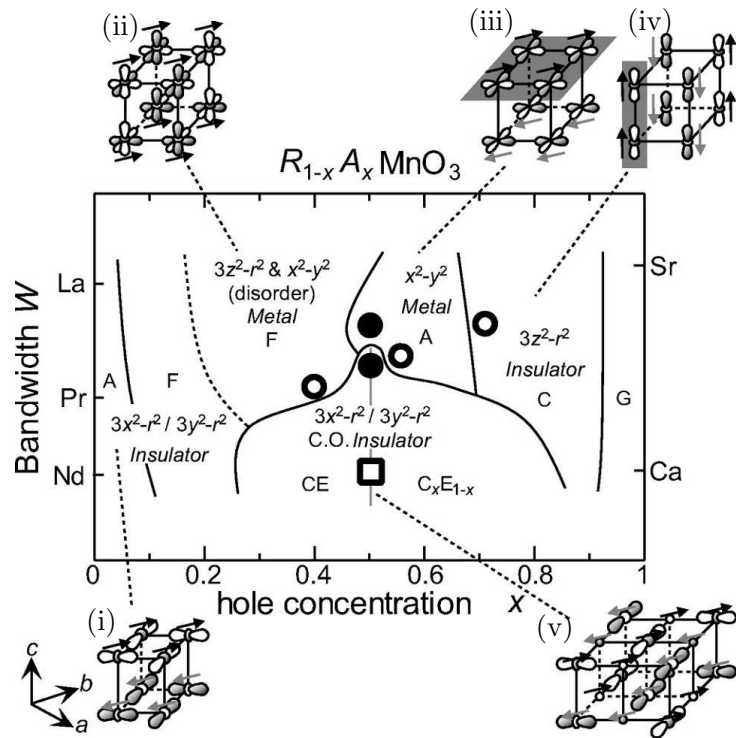


Figure 3.8: Phase diagram showing the electronic and magnetic phases at various bandwidths and hole dopings. C.O. denotes charge order and CE denotes charge exchange. Orbital order is shown in (i-v) [91].

3.2 The magnetic properties of half-metallic $\text{La}_{1-x}\text{Sr}_x\text{MnO}_3$ ($x \sim 0.3$)

Optimally doped $\text{La}_{1-x}\text{Sr}_x\text{MnO}_3$ $x \approx 0.3^1$, is particularly interesting for spintronic applications due to its near 100% spin polarisation [82], i.e. the imbalance between up and down-spin electrons at the Fermi energy. In the early stages of the manganite research, Goodenough predicted that the maximum T_C and conductivity would appear at around 31% Mn⁴⁺ [67]. Experimentally, $T_C \sim 370$ K was measured in $\text{La}_{0.7}\text{Sr}_{0.3}\text{MnO}_3$, both in polycrystalline [64, 90] and single-crystal [85] samples. Figure 3.9 is the phase diagram of single crystalline $\text{La}_{1-x}\text{Sr}_x\text{MnO}_3$, constructed by Urushibara *et al.* from the experimental results, where the maximum T_C was found at $x \sim 0.3$ [85].

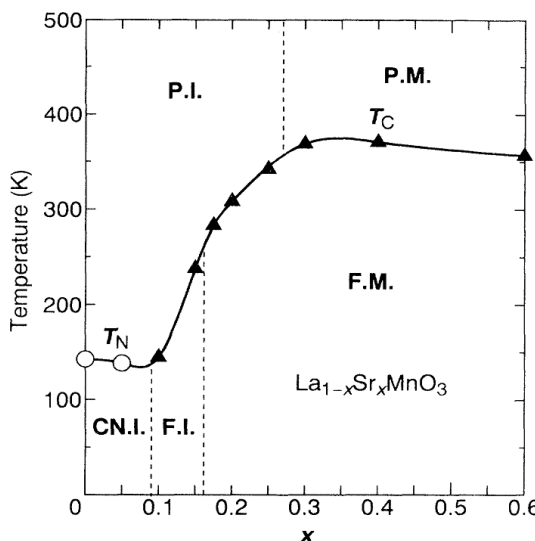


Figure 3.9: LSMO single-crystal phase diagram. The phases are spin-canted insulator (CN.I.), ferromagnetic insulator (F.I.), paramagnetic insulator (P.I.), paramagnetic metal (P.M.), and ferromagnetic metal (F.M) [85].

In order to demonstrate the half metallicity², Park *et al.* employed the photoemission spectrometry and 100% spin polarisation was found in an $\text{La}_{0.7}\text{Sr}_{0.3}\text{MnO}_3$ film at 77 K [82]. Bertacco *et al.* measured an energy gap of about 0.5 eV between the majority and minority spin band using the spin-polarised inverse photoemission spectrometry [95].

¹In this dissertation, $\text{La}_{0.67}\text{Sr}_{0.33}\text{MnO}_3$ at $x = 0.33$ is denoted by LSMO, other doping concentration was specified in their formula.

²In a half metal, electrical conduction is provided by one spin subband only.

3. MANGANITES

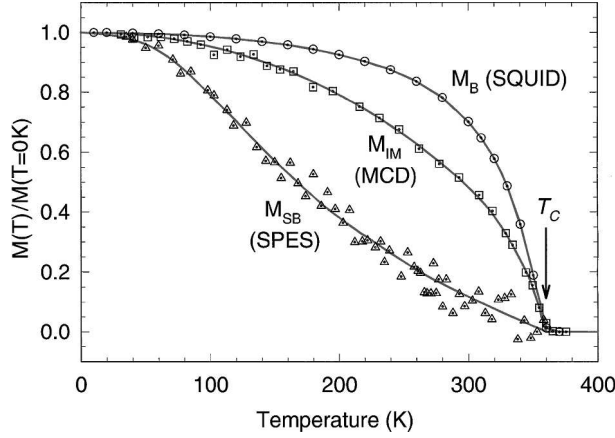


Figure 3.10: Magnetisation versus temperature for an $\text{La}_{0.7}\text{Sr}_{0.3}\text{MnO}_3$ film measured with a SQUID (circles) and with the surface magnetisation of the top 5 nm probed by a magnetic circular dichroism (MCD) (squares) and with the top 0.5 nm probed by the spin-resolved photoemission spectroscopy (SPES) (triangles) [96].

One of the major problems for manganites in spintronic applications is the reduced surface and interfacial magnetisation, and thus the **reduced surface and interfacial spin polarisation**. In the same paper, Park *et al.* reported the surface magnetisation of $\text{La}_{0.7}\text{Sr}_{0.3}\text{MnO}_3$ measured by spin-resolved photoemission spectroscopy (SPES)¹, and found it decreases at a much faster rate than that of the bulk magnetisation measured by a superconducting quantum interference device (SQUID) (Figure 3.10). **The interfacial spin polarisation probed in the spin-tunnelling experiments also decays to zero 60 K–160 K below the bulk T_C** [98–100]. The surface and interfacial spin polarisation is very sensitive to substrate induced strain, orbital reconstruction and chemical inhomogeneities at the surface or interface. The manipulation of the magnetic properties can be realised either through strain or chemical doping, for example by varying the substrates and their orientation [101–111], varying the film thickness [112–114], employing an oxide capping layers [115, 116] or buffer layers [117, 118], etc. **Although, there has been moderate progress tuning the interfacial magnetisation towards the bulk values** [100, 117, 118],

¹IN SPES, spin-polarised electrons are excited by UV light. The electrons are passed through an energy analyser where the electrons with different energy are separated. It was then detected in a Mott-detector. In the detector the electrons are accelerated and scatters on a target, as a result of spin orbit coupling, electrons with opposite spins are scattered by different angle, through which spin-resolution is achieved [97].

3.2 The magnetic properties of half-metallic $\text{La}_{1-x}\text{Sr}_x\text{MnO}_3$ ($x \sim 0.3$)

little improvement has been seen in the surface magnetisation [89, 115, 116].

3.2.1 The effect of strain on epitaxial $\text{La}_{1-x}\text{Sr}_x\text{MnO}_3$ ($x \sim 0.3$)

Epitaxial in-plane strain in thin films tends to reduce the magnetisation and T_C compared to the bulk crystals. Strain alters the Mn-O-Mn bond lengths and angles, which modifies double exchange. Secondly, stain couples with the orbital degree of freedom through the lattice. Lifting the degeneracy of the t_{2g} and e_g levels leads to orbital ordering and hinders the double exchange. In general, a in-plane compressive (tensile) strain favours the out-of-plane (in-plane) orbital filling with respect to the unstained case shown in Figure 3.11a, which contributes to the C-type AFM shown in Figure 3.11b (A-type AFM shown in Figure 3.11c).

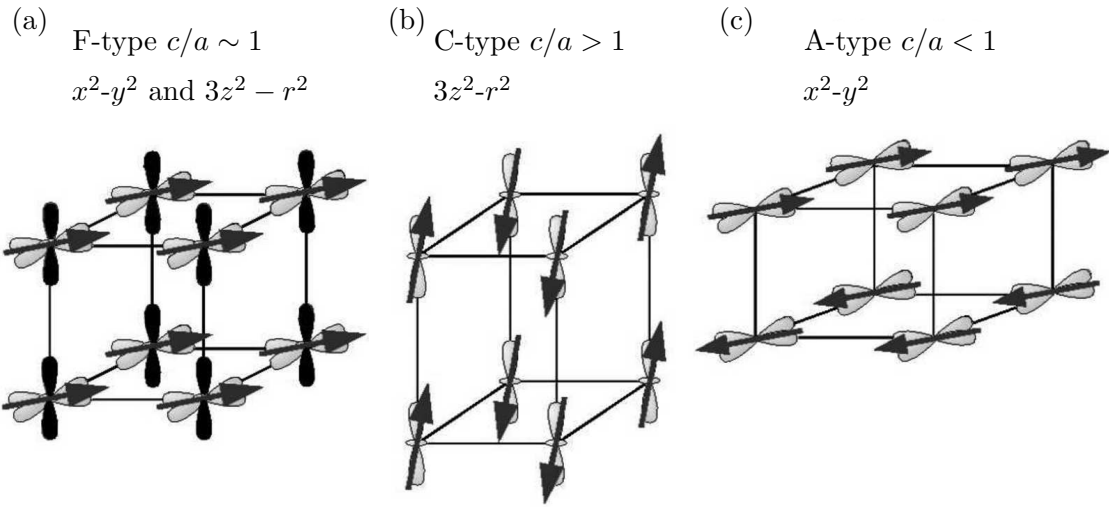


Figure 3.11: Schematic diagrams showing the orbital ordering in the (001)-oriented films under (a) no stress, (b) the compressive stress, and (c) the tensile stress [93]. The in-plane and out-of-plane orbitals in the case of the (001)-oriented film are $d_{x^2-y^2}$ and $d_{3z^2-r^2}$ respectively as shown in figure.

Using low temperature magnetic force microscopy (MFM), Soh *et al.* studied the magnetisation of an epitaxial $\text{La}_{0.77}\text{Sr}_{0.23}\text{MnO}_3$ film grown on a bi-crystal STO (001) substrate, and found the T_C of the film near the grain boundary to be 20 K higher than

3. MANGANITES

elsewhere due to strain relaxation at the grain boundary [119]. Ranno *et al.* found the T_C of a thicker relaxed $\text{La}_{0.7}\text{Sr}_{0.3}\text{MnO}_3$ film (200 nm) on STO (001) to be 30 K higher than that of a thinner strained film (40 nm) [120]. Gao *et al.* found even with a very small lattice mismatch, for example, LSMO on NdGaO_3 , significant shear stress can be induced, which changes the Mn-O-Mn angles and therefore the transport properties [113].

The effect of stain on $\text{La}_{0.7}\text{Sr}_{0.3}\text{MnO}_3$ was studied by growing films on different substrates. Figure 3.12 describes the pseudocubic lattice parameter of the most frequently used substrates. $\text{La}_{1-x}\text{Sr}_x\text{MnO}_3$ films at around $x \sim 0.3$ were grown on a few substrates in the literature, ranging from compressive strain on LaAlO_3 (LAO) [103, 110, 121–123] and NdGaO_3 (NGO) [101, 103, 104, 115, 122, 124], to nearly lattice-matched on LSAT¹ [103, 107, 121, 122], and tensile strain on SrTiO_3 (STO) [102, 103, 105, 108, 121–123, 125–129], and DyScO_3 [125]. When the substrate-induced strain is large, for example, on LaAlO_3 (compressive) [111] and DyScO_3 (tensile) [125], the induced lattice distortion leads to C-type and A-type ordering respectively. This orbital ordering results in a thin layer of material near the film-substrate interface, whose magnetic and electronic properties are suppressed, so it is normally referred as ‘dead layer’. The thickness of the dead layer in $\text{La}_{0.7}\text{Ca}_{0.3}\text{MnO}_3$ was found to increase from 3 nm for films grown on smaller lattice-mismatched substrates, such as NGO and STO, to 15 nm on large lattice-mismatched LaAlO_3 [130–132]. When the substrate-induced stress is small, the ferromagnetic metallic ground state of $\text{La}_{0.7}\text{Sr}_{0.3}\text{MnO}_3$ does not change, although the orbital ordering was found at the free surface [111, 133] and film-substrate interface [109]. Pesquera *et al.* studied the effect of strain on the orbital ordering at the surface of LSMO grown on STO, LaGaO_3 , LAST and NGO using the X-ray linear dichroism [111]. They found the surface of the film to have a preferential out-of-plane $d_{3z^2-r^2}$ occupation irrespective of the substrate used. For a film under a large in-plane tensile strain on an STO substrate, there is a reduced percentage of the out-of-plane occupancy in the film. They proposed this preferential occupation of the $d_{3z^2-r^2}$ is due to the incomplete MnO_6 octahedral on the surface of the film. Separate studies carried out by Aruta and Tebano arrived at a similar conclusion [130, 133].

¹LSAT denotes the substrate $(\text{LaAlO}_3)_{0.3}-(\text{Sr}_2\text{AlTaO}_6)_{0.7}$.

3.2 The magnetic properties of half-metallic $\text{La}_{1-x}\text{Sr}_x\text{MnO}_3$ ($x \sim 0.3$)

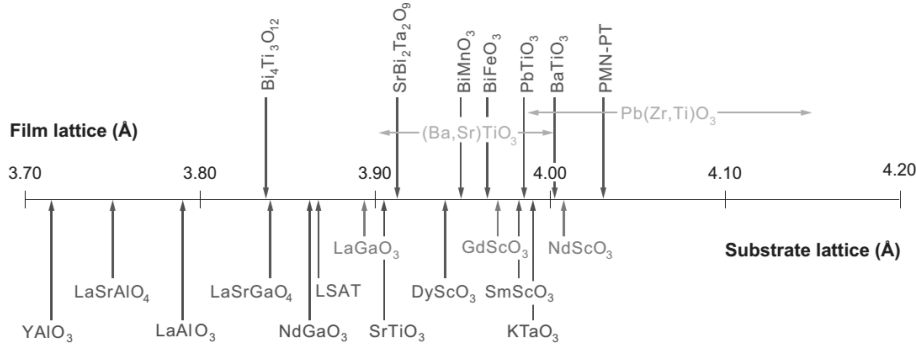


Figure 3.12: Pseudocubic lattice parameters of substrates and films [134].

The orientation of the substrate also plays a role in determining the orbital degree of freedom, in particular, the magnetic properties of the surface [111, 133] and interface [109]. Studies of the (110)_{pc}-oriented $\text{La}_{0.7}\text{Sr}_{0.3}\text{MnO}_3$ [109] and $\text{La}_{0.7}\text{Ca}_{0.3}\text{MnO}_3$ [135] on STO (110) showed a higher T_C and a slower decrease of magnetisation with increasing temperature. Three reasons were proposed for the increased T_C in $\text{La}_{0.7}\text{Sr}_{0.3}\text{MnO}_3$ on SrTiO₃ (110) [135]. Firstly, the surface termination of the STO (110) is more homogenous because the alternating atomic layers are $(2\text{O})^{4-}$ and $(\text{Sr-Ti-O})^{4+}$ (Figure 3.13b), whereas those in STO (001) are $(\text{TiO}_2)^0$ and $(\text{SrO})^0$ (Figure 3.13a). Secondly, in STO (110), the in-plane $d_{3z^2-r^2}$ and out-of-plane $d_{x^2-y^2}$ have a smaller energy splitting, and therefore less tendency for orbital ordering on the surface of the film. Lastly, the atoms on the STO (110) plane are more closely packed and hence the double exchange interaction is stronger [135].

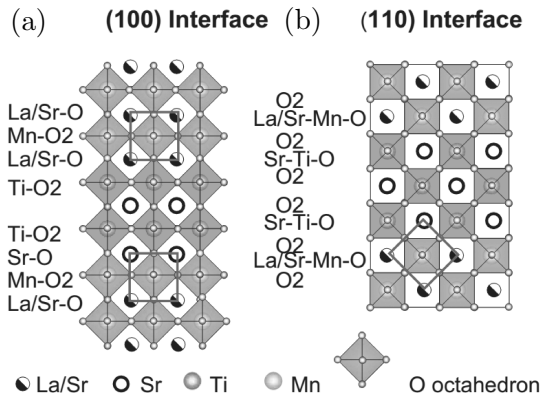


Figure 3.13: Atomic stacking sequence in (a) the (001)-terminated STO substrate, and (b) the (110)-terminated STO substrate [109].

3. MANGANITES

Apart from the strain, there are also chemical modification at the interface and surface. Overdoping of Sr at the $\text{La}_{1-x}\text{Sr}_x\text{MnO}_3/\text{SrTiO}_3$ interface [117, 118, 136] and the film surface [89] were suggested, which leading to the formation of the A-type AFM phases either locally or homogenously over the interface/surface. In order to optimise the magnetic properties, sub-optimum doping [137] or a buffer layer¹ [117, 118] were suggested. Figure 3.14 compares the interfacial magnetisation of an LSMO single crystal, a thin film grown directly on an STO substrate, with and without the LaMnO_3 (LMO) buffer layer [118]. It implies that the insertion of the LMO layer brings the interfacial magnetic properties closer to the single crystal. Phillips *et al.* took a similar approach in order to increase the LSMO surface magnetisation by growing an oxide capping layers of STO and LMO [115]. But both capping layers were found to suppress the surface magnetisation (Figure 3.14b,c). Similar study was also carried out by Valencia *et al.*, and there is no strong evidence that the capping layer increases surface magnetisation [116].

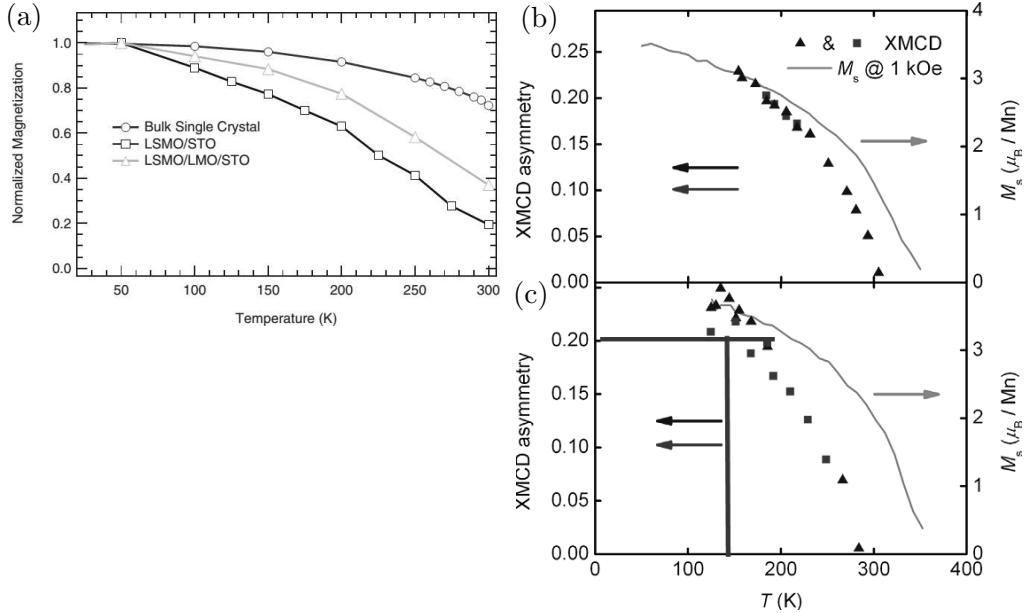


Figure 3.14: (a) Normalised magnetisation verses temperature for LSMO films on STO substrate (squares), on STO substrate with an LMO buffer layer (triangles) and a single crystal LSMO (circles) [118]. (b) XMCD asymmetry and saturation magnetisation of LSMO films on NGO (001) substrates with LMO capping layer, and (c) STO capping layer [115].

¹Layer of material that is under-doped in Sr, which was placed in between the STO and LSMO.

3.2 The magnetic properties of half-metallic $\text{La}_{1-x}\text{Sr}_x\text{MnO}_3$ ($x \sim 0.3$)

3.2.2 Magnetic anisotropy

The switching behaviour of a device strongly depends on the micromagnetic behaviour of the film, which involves the magnetic anisotropy and the domain reversal mechanism. The magnetic anisotropy can be tuned via the crystal structure (magnetocrystalline anisotropy), the stress state (magnetoelastic anisotropy) and the aspect ratio (shape anisotropy). In addition, octahedral rotation, symmetry breaking at the free surface and the film-substrate interface, temperature and the tolerance factor, etc. can all affect the anisotropy of the film.

In untwinned bulk $\text{La}_{0.7}\text{Sr}_{0.3}\text{MnO}_3$, the magnetocrystalline anisotropy dominates, resulting in uniaxial anisotropy with the magnetic easy axis along the diagonal of the unit cell, that is the pseudocubic [111] direction (denoted $[111]_{\text{pc}}$) (Figure 3.15a) [138]. When Konoto *et al.* imaged the $(001)_{\text{pc}}$ surface magnetisation of a cleaved LSMO single crystal using the spin-polarised scanning electron microscopy, they found that the in-plane magnetisation is parallel to a $[110]_{\text{pc}}$ direction [138]. They suggested that the formation of the surface magnetic domain along $[110]_{\text{pc}}$ minimises surface magnetic charge density (Figure 3.15b).

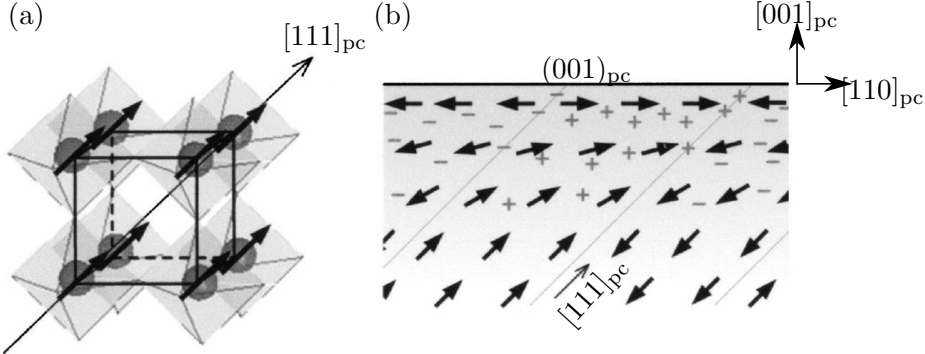


Figure 3.15: (a) Diagram showing the magnetic easy axis in the pseudocubic unit cell of $\text{La}_{0.7}\text{Sr}_{0.3}\text{MnO}_3$. (b) Diagram showing the origin of the surface magnetic domains along $[110]_{\text{pc}}$. Magnetic charges (+, -) form on the surface of the film when the magnetisation within the film impinges on the surface [138].

Epitaxial LSMO films on different substrates with different orientations have different magnetic anisotropy. The table in the end of Chapter 3 summarises the types of mag-

3. MANGANITES

netic anisotropy, specifying the easy and hard axes. To summarise here, two main crystal orientations of LSMO films, $(001)_{pc}$ and $(110)_{pc}$, have been investigated. The $(110)_{pc}$ oriented films were reported to have a higher uniaxial anisotropy, larger magnetisation and higher T_C .

LSMO on STO (001) has biaxial anisotropy due to the small biaxial tensile strain. In this case, the magnetic anisotropy is very sensitive to other factors, for example, the substrate vicinal angle and temperature, etc. In early research, although there was agreement of the biaxial anisotropy of LSMO on STO (001), there was contradiction regarding the orientation of the easy axes. While some researchers found an easy axis along the [100] direction [102, 128], others found it along the [110] axis [103, 108, 110, 129, 139]. This discrepancy could be a result of the different miscut of the substrates, because later research found LSMO grown on STO (001) with large vicinal angle processes uniaxial anisotropy, with easy axis parallel to the step edges [114, 127, 129]. The strength of this surface-step-induced uniaxial anisotropy decreases with increasing temperature, and above 160 K the usual biaxial anisotropy dominates [114]. Other studies relate the temperature dependence of the anisotropy, or the rotation of the easy axis, to the cubic-to-tetragonal structural transition of STO at 103 K [140]. Phillips *et al.* studied the surface magnetic anisotropy of a sub-optimally doped $(001)_{pc}$ -oriented LSMO on NGO (001) using XMCD-PEEM¹, and found a coexistence of biaxial and uniaxial anisotropy at low temperature, with uniaxial anisotropy dominated above 200 K [124].

The magnetic anisotropy has a film-thickness dependence due to (1) strain relaxation, (2) anisotropic strain relaxation, and (3) octahedral rotation or deformation, which is reviewed separately as below.

1. Nishikawa *et al.* studied the anisotropy of LSMO films on NGO (112) for thickness of 20-400 nm. Above 200 nm, as the thickness increases, the proportion of the relaxed film increases, and the biaxial anisotropy present in bulk crystal starts to dominate over the uniaxial anisotropy [104]. They correlated this to the partial relaxation of the film.
2. Vailionis *et al.* reported an anisotropic stress relaxation along the two orthogonal in-plane directions for 40 nm-thick LSMO $(001)_{pc}$ on an NGO (110) substrate.

¹Photoemission electron microscopy (PEEM) with X-ray magnetic circular dichroism (XMCD) contrast. Please see section 6.3.1 for the detail of this technique.

3.2 The magnetic properties of half-metallic $\text{La}_{1-x}\text{Sr}_x\text{MnO}_3$ ($x \sim 0.3$)

Along the $[1\bar{1}0]_{\text{or}}$ direction, there is angular relaxation of γ between the pseudocubic a and b axes, whereas strain relaxation along the $[001]_{\text{or}}$ direction is due to microtwinning [106] (Figure 3.16a).

3. Boschker *et al.* studied the effect of the strain relaxation in relatively thin film of LSMO $(110)_{\text{or}}$ (12 - 40 nm) grown on LSAT (110) , where the in-plane strain along the two in plane axes are the same [107]. Interestingly, they found a biaxial to uniaxial transition while increasing the thickness. They related this uniaxial anisotropy to the increase (decrease) of the d orbital overlap as a result of in-phase (out-of-phase) octahedral rotation along the $[001]_{\text{or}}$ ($[1\bar{1}0]_{\text{or}}$) in-plane axis [107] (Figure 3.16b).

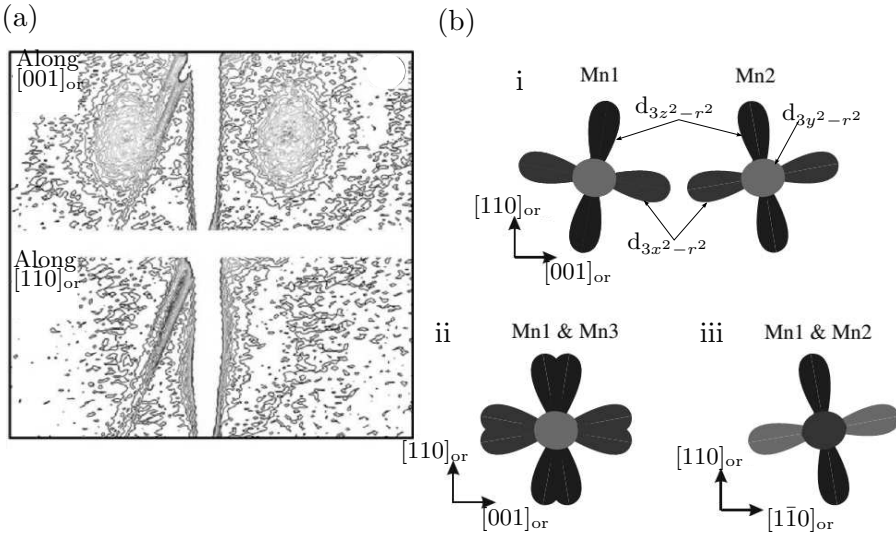


Figure 3.16: (a) XRD reciprocal space maps of LSMO on NGO (110) obtained near the 220_{or} reflection, with the beam direction along [001]_{or} (top) and [1̄10]_{or} (bottom). The satellite peaks are only visible when the beam is along [001]_{or}, indicating an in-plane lattice modulation (microtwinning) along [001]_{or} ref. [106]. (b) Schematics showing the orbital overlap as a result of octahedral rotation. Figure (i) The orbitals of Mn1 and Mn2 viewed along [1̄10]_{or}, (ii) the orbital overlap of Mn1 and Mn3 viewed along [1̄10]_{or} as a result of the out-of-phase octahedral rotation, which gives a magnetic hard axis along [1̄10]_{or}, (iii) orbital overlap of Mn1 and Mn2 viewed along [001]_{or} as a result of the in-phase rotation, which gives a magnetic easy axis along [001]_{or} ref. [107].

3. MANGANITES

In spintronic devices, where the film is typically patterned by lithography, adding a strong shape anisotropy contribution, the micromagnetics is even more complicated. The surface magnetisation of patterned LSMO was studied by XMCD-PEEM in reference [141–143]. The magnetic domain structures of patterned $\text{La}_{0.7}\text{Sr}_{0.3}\text{MnO}_3$ nanostructures on STO (001) and (110) as a function of aspect ratio were studied by Kim *et al.* using XMCD-PEEM [142]. They found that as the aspect ratio increases, more domains align along the long axis of the nanostructure due to the larger shape anisotropy (Figure 3.17). Of particular relevance here, the single-domain state is easier to obtain for the (110)_{pc}-oriented $\text{La}_{0.7}\text{Sr}_{0.3}\text{MnO}_3$ due to the larger uniaxial anisotropy (Figure 3.17b). Interestingly, in the hexagonal nanostructures with all aspect ratio, the magnetic moment is aligned along one direction. This is particularly interesting for the graphene spin valves, because MR is optimised if the electrode are single domain. However, because the magnetic field is applied along the long edge of the nanostructure in [142], and because the size of the pattern is much smaller than the tens-of-microns-sized electrodes described later, it is uncertain if those findings apply here. But the important message is that the tapered ends in rectangles can lead to more homogenous domain structures by reducing the number of nucleation sites.

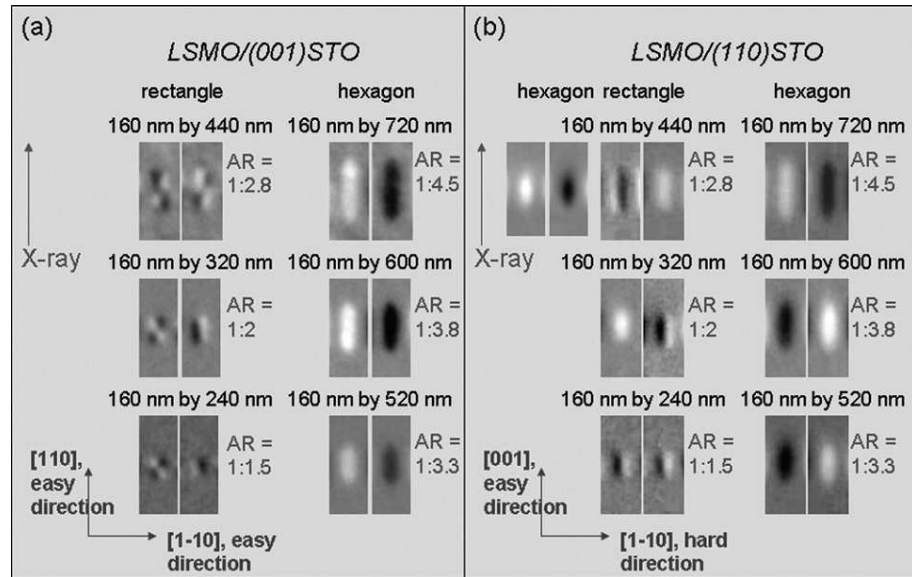


Figure 3.17: XMCD-PEEM images of the $\text{La}_{0.7}\text{Sr}_{0.3}\text{MnO}_3$ nanostructures prepared on an (a) STO (001), and (b) STO (110) substrates. The aspect ratios of the rectangular and hexagonal nanostructures are indicated next to the figures [142].

3.2 The magnetic properties of half-metallic $\text{La}_{1-x}\text{Sr}_x\text{MnO}_3$ ($x \sim 0.3$)

substrate	out-of-plane orientation	in-plane orientation substrate film	Magnetic anisotropy	Magnetic easy axis	Magnetic hard axis	Reference
STO(001)	$[001]_{\text{pc}}$	$[010] \parallel [010]_{\text{pc}}$ $[100] \parallel [100]_{\text{pc}}$	biaxial *	$\langle 110 \rangle$	$\langle 100 \rangle$	[101, 108, 128, 129]
NGO(001) _{or}	$[001]_{\text{pc}}$	$[010]_{\text{or}} \parallel [\bar{1}10]_{\text{pc}}$ $[100]_{\text{or}} \parallel [110]_{\text{pc}}$	uniaxial**	$[010]_{\text{or}}$	$[100]_{\text{or}}$	[101, 124]
NGO(110) _{or}	$[001]_{\text{pc}}$	$[\bar{1}10]_{\text{or}} \parallel [100]_{\text{pc}}$ $[001]_{\text{or}} \parallel [010]_{\text{pc}}$	uniaxial	$[\bar{1}10]_{\text{or}}$	$[001]_{\text{or}}$	[101, 105, 106]
LSAT(110) _c	$[1\bar{1}0]_{\text{or}}$	$[\bar{1}10]_{\text{c}} \parallel [\bar{1}10]_{\text{or}}$ $[001]_{\text{c}} \parallel [001]_{\text{or}}$	biaxial***	$\langle 110 \rangle_{\text{or}}$	$\langle 001 \rangle_{\text{or}}$	[107]
STO(110)	$[110]_{\text{pc}}$	$[1\bar{1}0] \parallel [1\bar{1}0]_{\text{pc}}$ $[001] \parallel [001]_{\text{pc}}$	uniaxial	$[001]$	$[1\bar{1}0]$	[108, 109]
NGO(100) _{or}	$[110]_{\text{pc}}$	$[010]_{\text{or}} \parallel [\bar{1}10]_{\text{pc}}$ $[001]_{\text{or}} \parallel [001]_{\text{pc}}$	uniaxial	$[010]_{\text{or}}$	$[001]_{\text{or}}$	[101, 105]
NGO(112) _{or}	$[011]_{\text{pc}}$	$[\bar{1}10]_{\text{or}} \parallel [100]_{\text{pc}}$ $[\bar{1}\bar{1}1]_{\text{or}} \parallel [01\bar{1}]_{\text{pc}}$	uniaxial	$[\bar{1}10]_{\text{or}}$	$[\bar{1}\bar{1}1]_{\text{or}}$	[104]
NGO(010) _{or}	$[011]_{\text{pc}}$	$[100]_{\text{or}} \parallel [110]_{\text{pc}}$ $[001]_{\text{or}} \parallel [001]_{\text{pc}}$	uniaxial	$[001]_{\text{or}}$	$[100]_{\text{or}}$	[101]

Figure 3.18: Summary for the LSMO films grown on different substrates with different substrate orientations. The subscript ‘c’, ‘pc’, and ‘or’ denote the cubic, pseudocubic and orthorhombic notation. The growth plane is shaded. For non-cubic substrates, the pseudocubic unit cell of the film (black lines) is shown with the orthorhombic unit cell of the substrate (grey lines). * Uniaxial anisotropy was seen with the easy axis along the step terraces direction [114, 129]. ** A biaxial anisotropy contribution was also seen below 200 K [124]. *** A uniaxial anisotropy contribution was seen with the easy axis along $[001]_{\text{or}}$ [107].

3. MANGANITES

Chapter 4

Experimental methods

4.1 Pulsed laser deposition (PLD)

The LSMO films were grown by PLD. Prior to deposition, the substrates (both SrTiO₃ and NdGaO₃) were sonicated in deionised water, ethanol, acetone and isopropanol for about 5 minutes each, and blown dry under an N₂ gas flow. The cleanliness of the substrate surface was checked under an optical microscope before oxygen annealing in a furnace. For oxygen annealing, the substrates were placed in a ceramic boat with the surface facing upwards, and the temperature was ramped to 950°C at a rate of 600°C per minute under continuous oxygen flow. The substrate were annealed for 90 minutes at 950°C, after which the furnace was cooled down to room temperature in O₂ flow. The oxygen annealing condition was found to produce clear atomic step terraces on the surface of the substrate. The exact temperature ramping rate is not critical for this purpose. After annealing, the topography of the substrates was checked using tapping-mode atomic force microscopy (AFM). Examples of the substrates are given in Figure 4.1.

The step height for NGO (001) substrates was ~ 0.4 nm, which is roughly the unit-cell height, and the miscut angle was $\sim 0.08^\circ$. The step height for NGO (100) substrates was ~ 0.3 nm, which was roughly $\frac{\sqrt{2}}{2}a_{pc}$, and the miscut angle was $\sim 0.09^\circ$. For STO (110) substrates, the step height was 0.3 nm and the miscut angle was typically $\sim 0.06^\circ$ measured from AFM after oxygen annealing.

4. EXPERIMENTAL METHODS

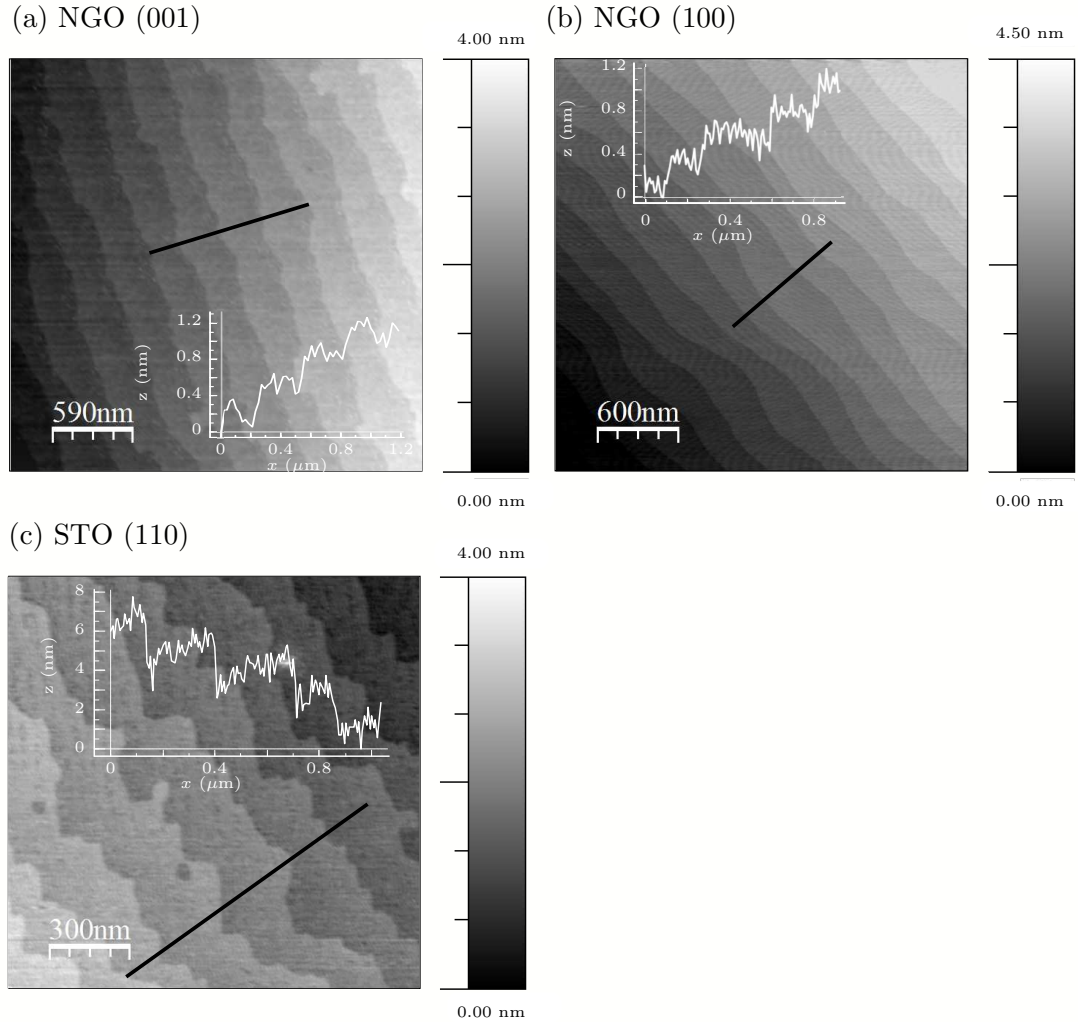


Figure 4.1: AFM topography, obtained using the tapping mode AFM, for oxygen-annealed substrates of (a) NGO (001), (b) NGO (100), and (c) STO (110). The direction of the step terraces varies slightly among different substrates even within the same batch.

4.1 Pulsed laser deposition (PLD)

The LSMO films were deposited by PLD using the ‘Mark X’ system (Figure 4.2).

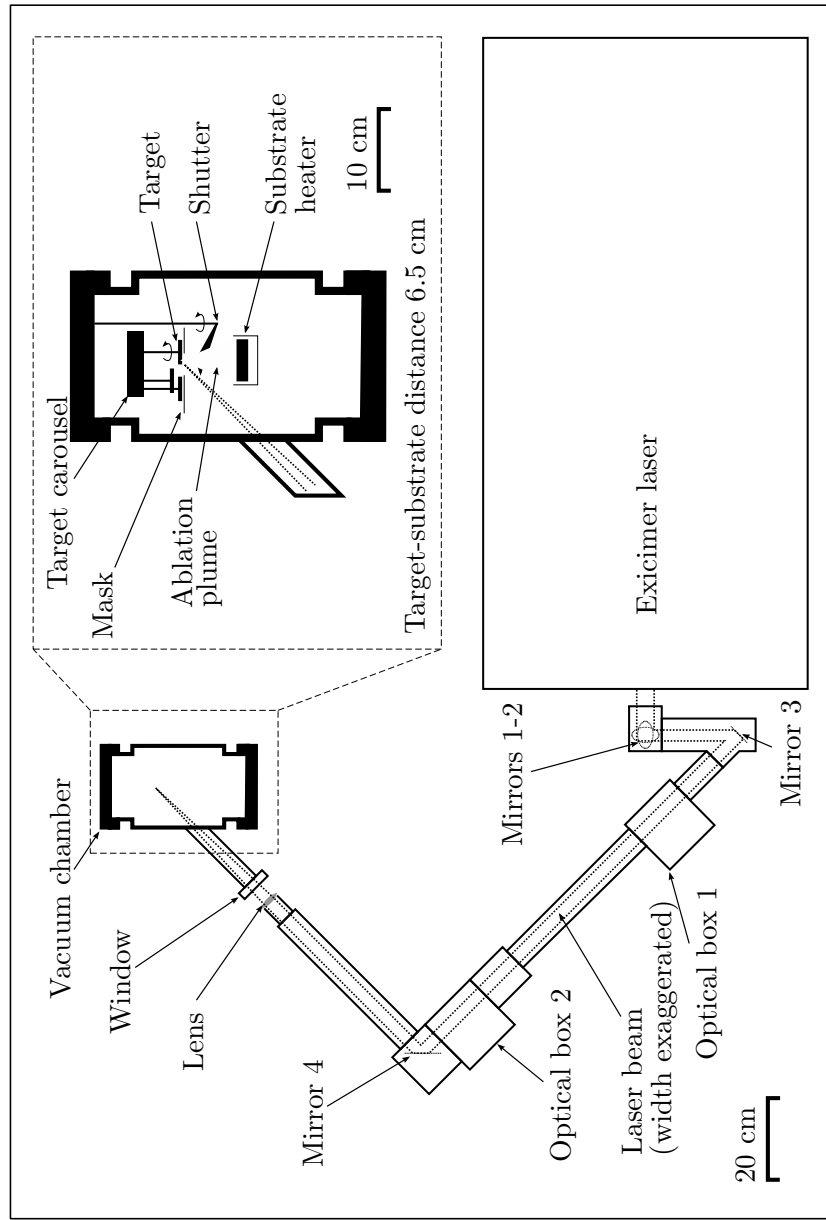


Figure 4.2: Schematic of the pulsed laser deposition system ('Mark X' chamber) taken from the PhD dissertation of Sam Crossley [144].

4. EXPERIMENTAL METHODS

During the deposition, a high energy laser is focused onto the target, which melts the target material locally. The evaporated material gains a kinetic energy of a few tens of eV and travel towards a heated substrate. During its travel towards the target, the evaporated particles collide with the gas molecules, which in this study are oxygen molecules, and dissipate their kinetic energy. The mobility of the species arriving on the substrate surface depends on their kinetic energy and thermal energy. While the former is a function of the laser energy, the target-substrate distance and the oxygen pressure, the later is a function of the substrate temperature. If the arriving species have too low mobility, then island of atoms are more lightly to form and the film surface will be rough. In the case of too high mobility, there wont be enough time for atoms to reach their stable sites in between two laser pulses, and results in large roughness [145]. Therefore to grow high quality epitaxial films, the oxygen pressure, temperature, target-substrate distance and laser energy has to be finely tuned, which can be a very time consuming process. This dissertation focuses on the application of LSMO in spintronics, and therefore has used the deposition condition optimised by previous users of the system directly [146].

1. The target was polished by sandpaper (grade 1200) in order to remove the laser damaged material from the previous deposition. Figure 4.3 shows the SEM image of an ablated LSMO target. The target was coarser where it has been repeatedly hit by the laser beam, probably due to the surface materials melting and refreezing.
2. The chamber was loaded with the target and 1-2 substrates, with the substrates directly underneath the plume (the position of the plume was located by a deposition on to a glass slide). The target-substrate distance was fixed at 6.5 cm. The loaded chamber was pumped over night to a base pressure of 1×10^{-6} mbar.
3. By controlling the O₂ gas inlet needle valve, and the gate valve, the flowing O₂ pressure in the chamber was maintained at 15 ± 0.2 Pa. Once the pressure was relatively stable, the temperature was raised to 750°C at 35°C/min, and slowly increased to 800°C at 10°C/min, at which temperature the substrates were annealed for 30 minutes.
4. The temperature was decreased to the deposition temperature of 775°C at 10°C/min. During the deposition, stoichiometric ablation from the target was achieved using a KrF laser (Lambda Physik Compex 201, 248 nm) operated at 1 Hz. Films grown before run number #23479 ¹ were deposited without a hard mask in Optical box 1

¹The sample number is given by the number of the PLD run, for example #12345 is the deposition

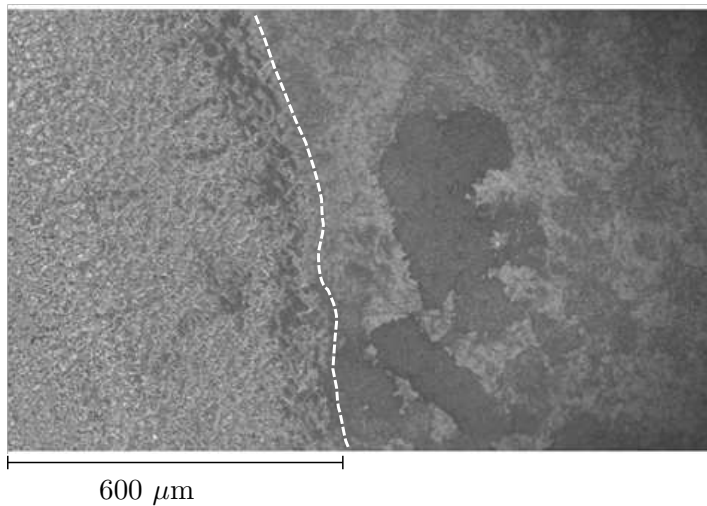


Figure 4.3: SEM image of the LSMO target after ablation using many laser pulses. The area to the left of the white-dotted line is the laser ablated region, where the target appears coarser. Image taken by Zili Zhang from this group.

(Figure 4.2), such that the laser spot at the target was $\sim 8 \text{ mm}^2$, implying fluence of about 2.3 J cm^{-2} . Films deposited later employed a hard mask with an aperture of $15 \text{ mm} \times 4.5 \text{ mm}$. The purpose of the mask was to filter out the lower energy edge of the laser beam. The laser spot on the target becomes more homogeneous and the fluence becomes well defined. The resultant spot size was $\sim 3.8 \text{ mm}^2$ and the fluence was thus 1.7 J cm^{-2} . During the deposition, the target was rotated and a ring of material was ablated.

5. After the deposition, the temperature was reduced to 750°C , and the film was annealed in 55 kPa O_2 for 1 hour.

A list of sample was included in Appendix C, in which the deposition conditions of other films, such as BaTiO_3 , SrTiO_3 and LaAlO_3 etc. were given.

4.2 Atomic force microscopy (AFM)

Tapping Mode AFM (Digital Instruments Nanoscope III) was used as a routine check of the film quality (Chapter 5), the cleanliness of patterned electrodes, and the quality

run number 12345. A letter, a, b, c or d is added to the end if multiple films were prepared during one deposition run, for example #12345b means sample b prepared during deposition run 12345.

4. EXPERIMENTAL METHODS

of graphene/graphite after the transport measurements (Chapter 6).

Figure 4.4 illustrates the working principle of the AFM. In Tapping Mode, the tip on a cantilever is scanned over the surface, oscillating at 5-10% below its resonance frequency. The tip-sample distance, which corresponds to the amplitude setpoint, is kept constant using a feedback circuit that modulates the z -piezo in the cantilever (Figure 4.4a). As the tip approaches feature A (Figure 4.4b), the amplitude of the cantilever oscillation is damped, as measured by the laser beam that reflects from the cantilever and is detected by the photodetector. A voltage is then applied to the z -piezo, and the amplitude height is adjusted to the setpoint. This voltage is then interpreted to give the height of the feature.

Phase contrast imaging was used to check for cleanliness and ripples in the graphene/graphite used in the devices. The phase shift arises due to the dependence of the resonant frequency on the tip-sample interaction force, which is different for a tip tapping on the graphene/graphite and the LSMO.

Conducting tip AFM was performed on a Digital Instruments Dimension 3100. It was used to check the electrical conductivity of graphene in the spin-valve device (Chapter 6). A DC bias was applied in the range of 100 - 600 mV between the tip and one of the four electrodes, and the topography and current were measured at the same time. The electrical current measured is very sensitive to the topography as it affects the tip-sample contact area. A larger contact area gives a higher current. The topographic and electrical measurements were taken during both the trace (tip scanning forward) and the retrace (tip scanning backward). Features that exist both in the trace and retrace represent a genuine electrical signal.

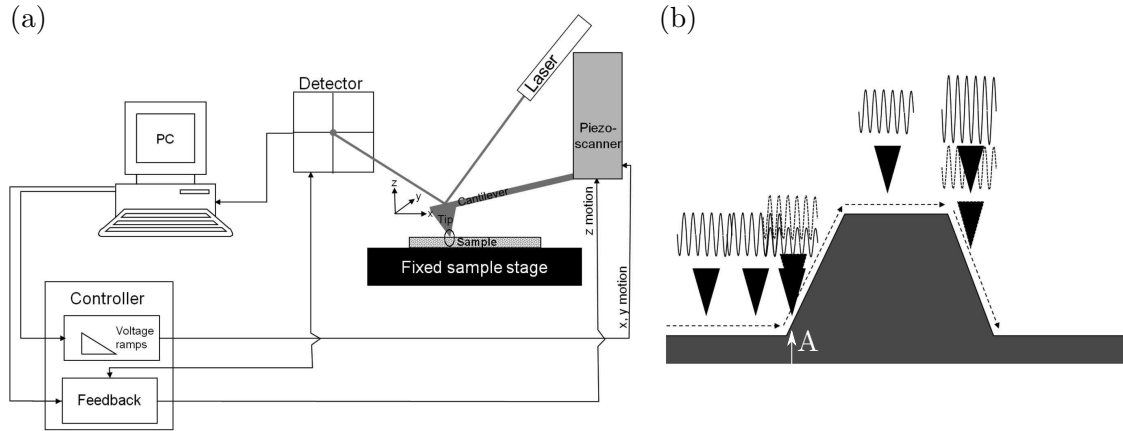


Figure 4.4: (a) Schematic illustration showing the working principle of an AFM. (b) Drawing shows the amplitude modulation that is determined via the feedback circuit. The solid and dashed lines illustrate the oscillation amplitude without and with the amplitude feedback respectively. Illustrations from reference [147].

4.3 X-ray diffraction (XRD)

The majority of X-ray characterisations were carried out using a PANalytical PW3050/65 X’Pert PRO high-resolution diffractometer (instrumental resolution $0.006^\circ 2\theta$). Some data were measured on the PANalytical Empyrean diffractometer (instrumental resolution $0.018^\circ 2\theta$).

A schematic diagram of the optical path is drawn at the top of Figure 4.5. The incident beam of $\text{CuK}\alpha$ ($\lambda = 1.5418\text{\AA}$) radiation passes first through a X-ray mirror to achieve a nearly parallel beam (divergence $< 0.05^\circ$). It then passes through a monochromator to remove $\text{CuK}\alpha_2$. The diffracted beam is detected after either passing through an analyser crystal (monochromator) or a prefix module. The optical combinations mainly used in this work are summarised at the bottom of Figure 4.5.

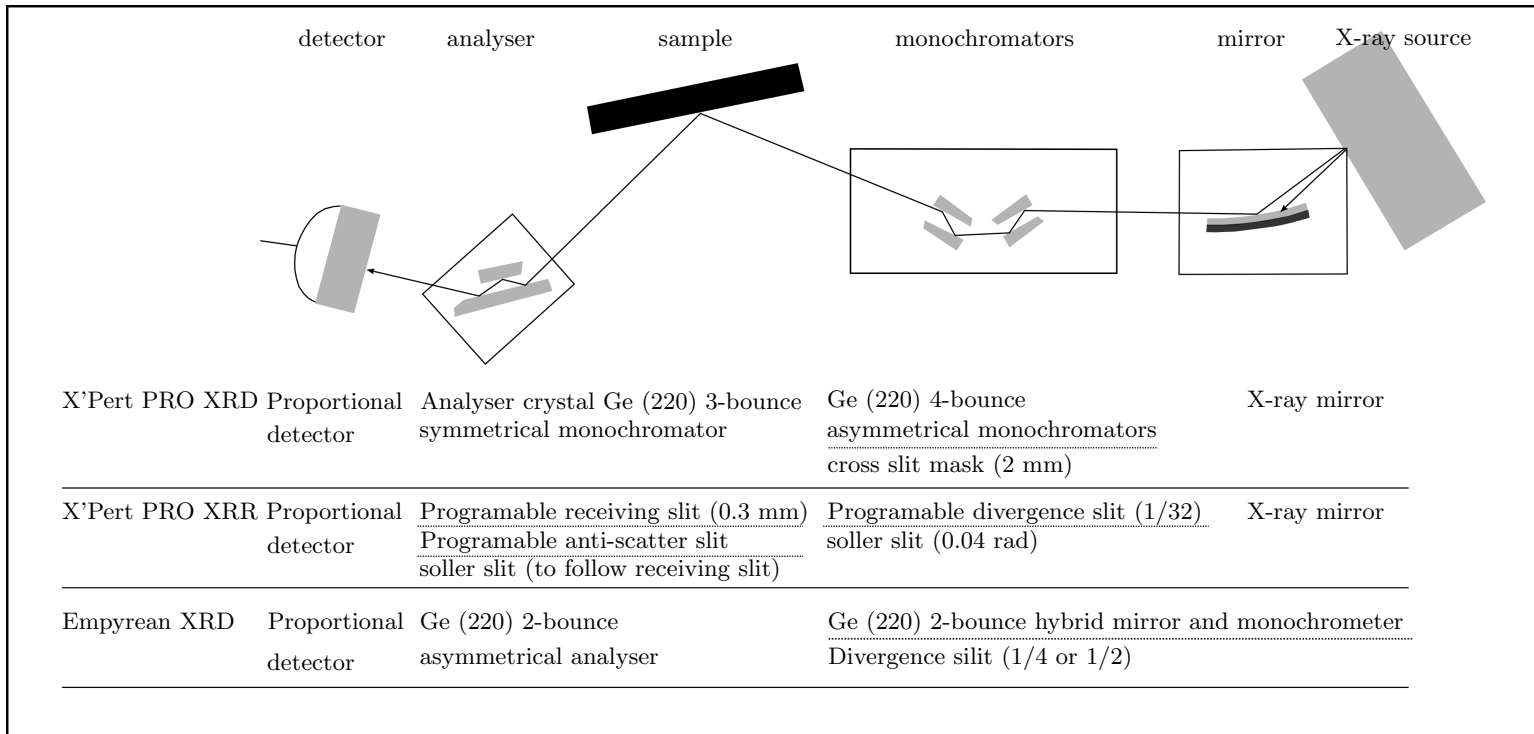


Figure 4.5: (Top) Schematic of the X-ray pathway and the main optical components. (Bottom) Table listing the components and settings used for X-ray diffraction (XRD) and X-ray reflectivity (XRR) measurements with the two diffractometers, X'Pert PRO and Empyrean.

The types of scans used in this dissertation are described below:

1. Rocking curve (ω scan) on a symmetrical peak (Figure 4.6) to check the quality of the film and the substrate. Narrow rocking curves indicate good crystal quality, with less misorientations due to dislocations, in-plane lattice modulations and other structural inhomogeneities.
2. The film quality and out-of-plane lattice parameter were determined from $\omega/2\theta$ scans on the symmetrical peaks (Figure 4.6). The thickness fringes indicate good film quality and homogeneous strain. The out-of-plane lattice parameter was calculated using Bragg's law (Equation 4.3):

$$\lambda = 2d_s \sin \theta_s \quad \text{for the substrate peak,} \quad (4.1)$$

$$\lambda = 2d_f \sin(\theta_s + \Delta\theta) \quad \text{for the film peak.} \quad (4.2)$$

The out-of-plane lattice parameter for the film is therefore

$$d_f = \frac{d_s \sin \theta_s}{\sin(\theta_s + \Delta\theta)}. \quad (4.3)$$

3. The in-plane lattice parameter and the strain state were extracted from a reciprocal space map (RSM) near an asymmetrical hkl peak (Figure 4.6, grey box). The lattice parameters were calculated using the following equation:

$$\frac{1}{d_{hkl}^2} = \frac{h^2}{a^2} + \frac{k^2}{b^2} + \frac{l^2}{c^2}. \quad (4.4)$$

4. X-ray reflectivity (XRR) was performed roughly in the range $\theta = 0 - 8^\circ$, and the measured curves were fitted with the X'Pert Reflectivity software to extract film thickness. For the fitting, three main features were considered, i.e. the critical angle (θ_c), the rate of decay of the intensity, and the intensity oscillations. The critical angle θ_c , is the angle below which total external reflection occurs. When $\theta < \theta_c$, the measured intensity equals the intensity of the incoming beam reflected off the sample surface, and is not constant due to over-illumination of the beam. Mathematically, $\cos \theta = n$, where n is the refractive index of the film (from Snell's law). Increasing the angle, the intensity drops due to transmission into the sample. Topologically rough surfaces or compositional graded interfaces will lead to a

4. EXPERIMENTAL METHODS

faster decay of intensity. The reflected beam from the film surface and the film-substrate interfere and give thickness-dependent fringes. The peak position and film thickness have the following relationship [148]:

$$(\sin \theta_m^2 - \sin \theta_c^2) = \frac{m^2 \lambda^2}{4t^2}, \quad \text{where the } m^{\text{th}} \text{ peak occurs at } \theta_m. \quad (4.5)$$

The amplitude of these fringes is related to the difference in electron density between the film and the substrate.

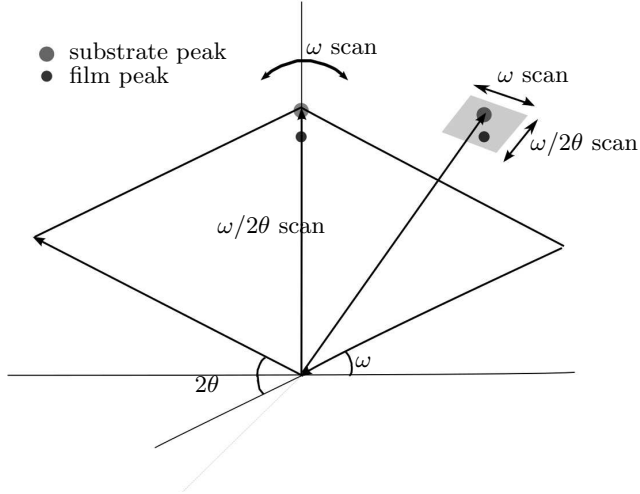


Figure 4.6: Schematic illustration of an ω scan, an $\omega/2\theta$ scan, and a RSM (grey shading) near an asymmetric reflection. The positions of substrate and film peaks are purely schematic, and do not represent the real data.

4.4 Magnetic characterisation

4.4.1 Vibrating sample magnetometry (VSM)

The vibrating sample magnetometry (VSM, Princeton Micromag 3900 vibrating sample magnetometer) was used to study the magnetic properties of the films. Samples were placed in a magnetic field ($\mu_0 H$), and the component of any dipole moment (m) along the field direction was measured (Figure 4.7a). The pick-up coils detect any change in stray field as the sample was vibrating up and down at 90° to the applied magnetic field. This changing stray field induces a voltage in the pick-up coils according to the

Faraday effect. The induced voltage is a measure of the magnetic moment of the sample. Magnetisation measurements can be carried out as a function of the magnetic field, the sample orientation and the temperature.

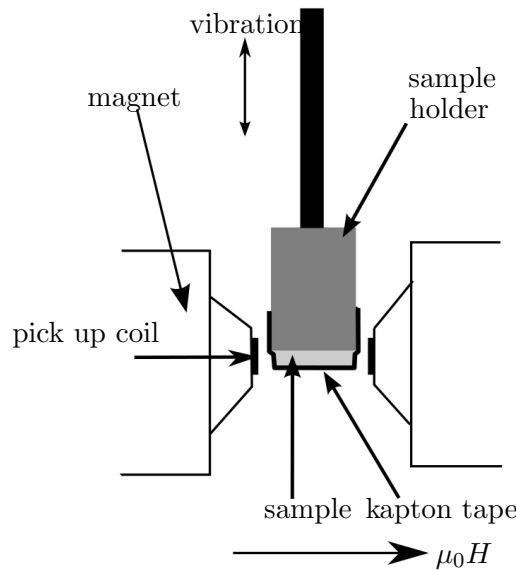


Figure 4.7: Schematic showing the VSM and sample mounting.

For this work, a Princeton MicroMag 390 VSM was used. Before use, the machine was calibrated at room temperature with a Co sample ($m = 22.53 \text{ memu}$) while $\mu_0 H = 1 \text{ T}$ was applied. The LSMO films were attached to the sample holder using Kapton tape, with the surface facing the sample holder. Mounting the sample this way only exposed the back of the sample to the sticky tape, and the surface could be kept relatively clean. Quite often, there was some glue attached to the side of the sample, which could be washed off relatively easily with a cotton bud, isopropanol and acetone.

The paramagnetic/diamagnetic contributions was subtracted from the raw data using the VSM software, assuming that the increases in moment beyond some fraction of the maximum field are paramagnetic in nature. In practice, this fraction was set at 70%.

4. EXPERIMENTAL METHODS

4.4.2 Photoemission electron microscopy with X-ray magnetic circular dichroism contrast (XMCD-PEEM)

Photoemission electron microscopy with the magnetic contrast from X-ray magnetic circular dichroism (XMCD-PEEM) provides a means of imaging the surface magnetisation [149], and so it is used here to study the patterned LSMO electrodes.

The technique is surface sensitive, with a probing depth of ~ 7 nm in the setup used here. The technique is chemically selective with absorption that can be tuned to the L_3 Mn resonance peak. The working principle of PEEM can be summarised as following:

1. The core electrons are excited when the photon energy matches the energy difference between a core electron level and the unoccupied states above the Fermi energy (E_F) (Figure 4.8a).
2. When an excited electron decays to the core-hole state via non-radiative Auger electron emission, a higher energy Auger electron is excited (Figure 4.8b).
3. The Auger electron then suffers multiple inelastic scattering events and causes secondary electron cascade (Figure 4.8c). The cascaded electrons with enough energy to overcome the work function can escape the surface, and they are accelerated towards the detector because the sample is kept at a negative bias voltage 15-20 kV. The number of secondary electrons ejected is proportional to the number of electrons flowing back from the ground to the sample (Figure 4.8d). The emitted electrons are accelerated in the electron-optical column, passing through electromagnetic lenses and form a spatial image on the image plane. The variation of intensity across the sample surface give rises to spatial resolution.

Because the energy gap between the core level and the conduction band is a characteristic of the element involved, PEEM is element specific. The sampling depth of PEEM roughly equals to the escape length of the secondary electrons, which is about 5 nm.

When the irradiating X-rays are circularly polarised, that is, left-handed or right-handed, the magnetic contrast arises due to the preferential excitation of one spin orientation over the other. The contrast is then due to X-ray magnetic circular dichroism (XMCD). The origin of the contrast was explained by Imada *et al.*, using the schematic in Figure 4.9 [150]. Assuming the photon polarisation aligns parallel (antiparallel) with the magnetisation direction in domain I (II) (Figure 4.9a), that is the up-spin minority band (down-spin majority band). At the L_3 absorption peak, with photon spin +1,

more up-spin electrons can be excited from $2p_{3/2}$ in both regions I and II. However, the probability of excitation to the conduction band and therefore the number of secondary electrons generated is higher in region I because there are more empty state above E_F in the up-spin band (Figure 4.9b,c). Region I appears brighter than region II at the L_3 absorption peak (Figure 4.9d). The colour contrast is reversed for L_2 absorption due to the antiparallel coupling between spin and angular momentum in $2p_{1/2}$.

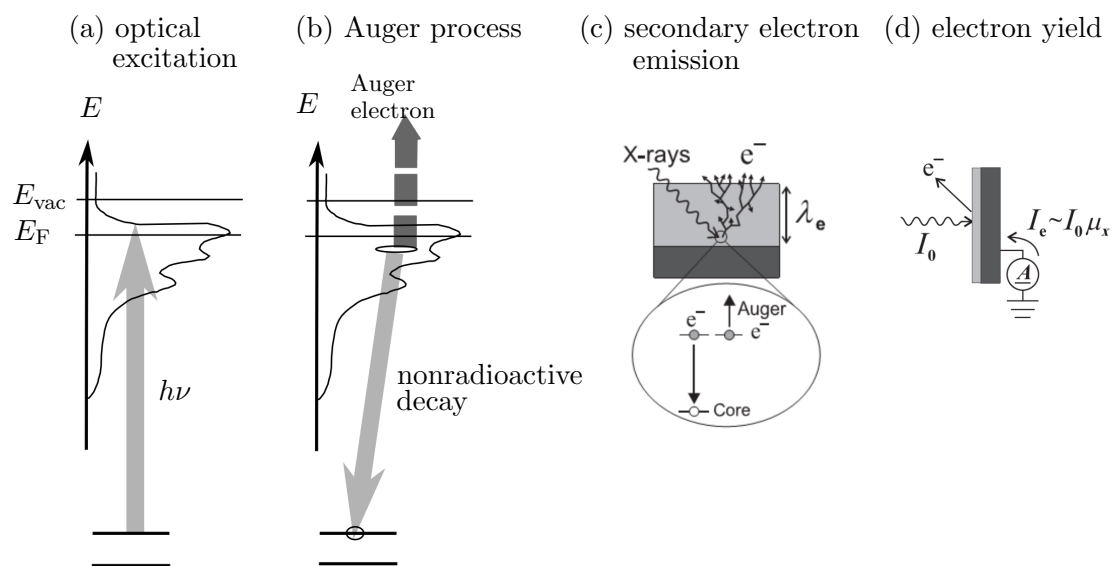


Figure 4.8: Schematic illustration showing (a) core-electron excitation upon absorption of photon, (b) Auger electron emission while the excited electron relaxes back to the core level [149], (c) inelastic scattering of the Auger electron causes a cascade of secondary electrons, and λ_e is the secondary electrons escaping depth, and (d) the number of secondary electrons emitted was measured by current I_e , which is proportional to the incoming photon intensity I_0 and linear absorption coefficient μ_x [151].

4. EXPERIMENTAL METHODS

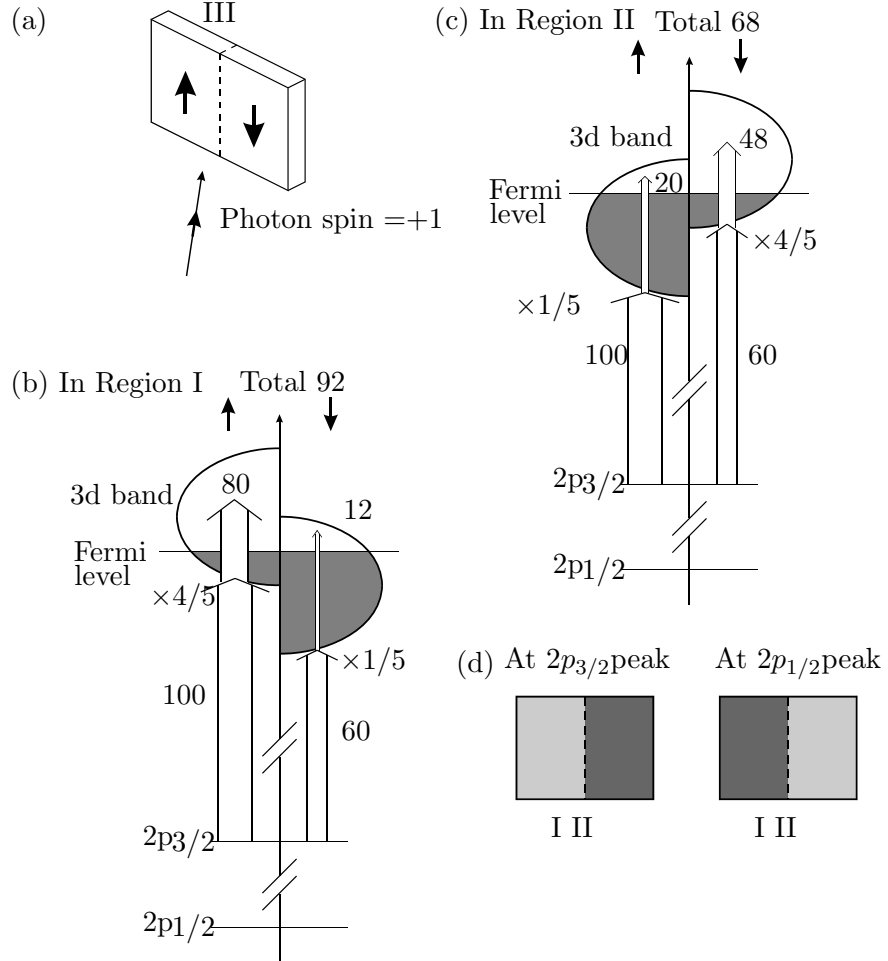


Figure 4.9: Schematic showing (a) Magnetic domains in the sample. Region I has magnetisation \uparrow and region II has magnetisation \downarrow . (b,c) The band diagram of a magnetic material showing the half-filled 3d level and the spin-orbit split 2p level. Arrows indicate the excitation of the core electrons to the empty states in the d orbitals at photon energies corresponding to the L_{2,3} absorption peak. Assuming the occupation of the majority and minority spin bands are 4/5 and 1/5. The transition probabilities of \uparrow and \downarrow spin depends on the relative angle between the photon and spins, and are assumed 100 and 60 in this figure. The percentage excitation of the spin up and down electrons is given. (d) The XMCD contrast at the L₃ and L₂ peaks respectively. Figure from reference [150].

XMCD intensity is affected by:

1. The number of electrons that is available to be excited upon absorption of a photon which is a function of the relative angle between the magnetisation and the incident-beam polarisation vector (Figure 4.10).
2. The number of empty states above E_F , which depends on the strength of the exchange interaction.
3. The degree of circular photon polarisations and the probability of spin relaxation during the excitation process.

Therefore, the XMCD intensity is expressed as [151]:

$$I_{\text{XMCD}} = P_{\text{circ}} \langle \mathbf{m} \rangle \cos \theta \quad (4.6)$$

where P_{circ} is the degree of circular photon polarisation, and $\langle \mathbf{m} \rangle \cos \theta$ is the projection of magnetisation onto the incident-beam polarisation vector (Figure 4.10). It is assumed that the number of emitted secondary electrons (photoelectrons) is proportional to the number of electrons excited from the core level. The measured intensity is then a measure of the magnetisation projected onto the direction of the incoming beam wave-vector. The asymmetry of the intensity, that is the XMCD asymmetry, is then a measure of the proportion of magnetisation along the beam, but does not give an absolute value of magnetisation.

The measurements in this work were carried out at ~ 150 K the base temperature of the system, which was cooled by liquid nitrogen. The procedure for obtaining XMCD-PEEM images was described in [115], which I coauthored, and is quoted in the following paragraph.

“PEEM with XMCD contrast was performed on beamline I06 at the Diamond Light Source, with the x-ray beam at a grazing incidence angle θ of 16° , using an Elmitec SPELEEM-III microscope to image the local zero-field magnetisation to a probe depth of ~ 7 nm and a typical lateral resolution of ~ 50 nm. After imaging with right (+) and left (-) circularly polarised light, the XMCD asymmetry $(I^+ - I^-)/(I^+ + I^-)$ was calculated for each pixel, where $I^\pm = (I_{\text{on}}^\pm - I_{\text{off}}^\pm)/I_{\text{off}}^\pm$ was taken to be the relative intensity of secondary-electron emission arising from x-ray absorption on (I_{on}^\pm at 639.5 eV) and off

4. EXPERIMENTAL METHODS

(I_{off}^{\pm} at 630 eV) the Mn L_3 resonance in order to avoid the influence of inhomogeneous illumination. XMCD asymmetry represents the projection of the local surface magnetisation onto the incident-beam polarisation vector, and therefore measures a component of the local in-plane LSMO magnetisation. Images were acquired with 5 s exposures for each energy and helicity”.

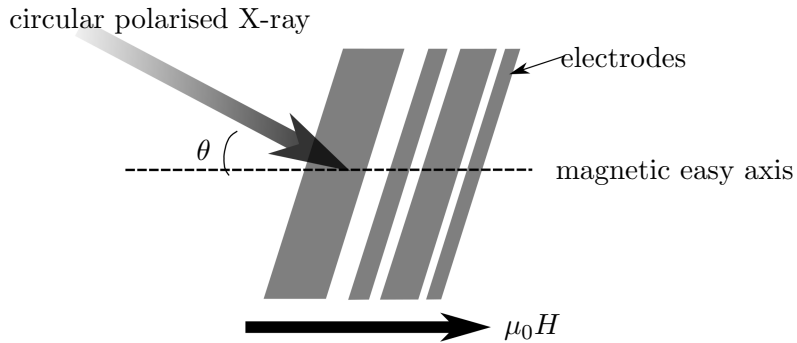


Figure 4.10: Schematic showing the geometry of the experimental set up. The circularly polarised X-ray arrives at incidence angle $\theta = 16^\circ$ with respect to the sample surface. The sample is mounted in such a way that the magnetic field lies along the magnetic easy axis of the electrodes.

4.4.3 Magneto-optic Kerr effect microscopy (MOKE)

The magneto-optic Kerr effect (MOKE) microscopy is based on the rotation of the polarisation of light upon reflection from a magnetic surface [152]. Because the degree of rotation is a function of the magneto-optical interaction between the magnetisation and the electric field component of the incoming light, MOKE spectroscopy and microscopy are used as a tool to locally probe the magnetic properties.

In a magnetic thin film with in-plane magnetisation (\mathbf{M}), there are three configurations of Kerr effect that are classified by the relative alignment of \mathbf{M} and the incident beam. These configurations are longitudinal, transverse and polar [152].

In the longitudinal configuration (Figure 4.11a), \mathbf{M} is in the plane of incidence and has a component parallel to the incident beam. In the transverse configuration, \mathbf{M} is perpendicular to the plane of incidence and incident beam (Figure 4.11b). There is also the polar configuration, where \mathbf{M} is out-of-plane, and is not considered here, because the

LSMO films in this work have in-plane magnetisation.

The linearly polarised light, with a plane-polarised electric field \mathbf{E} , induces electron oscillation along the polarisation direction. A secondary oscillation is induced perpendicular to both \mathbf{M} and \mathbf{E} as a result of the Lorentz force ($v_{\text{Lor}} = -\mathbf{m} \times \mathbf{E}$). The emerging light is composed of two parts, the regular component \mathbf{R}_N , which has the same polarisation plane as the incident light, and the Kerr component \mathbf{R}_K , which is a result of Lorentz force. Because the degree of Kerr rotation is a function of the projection of the magnetisation onto the direction of \mathbf{E} , MOKE is used as a mean of measuring the magnetisation.

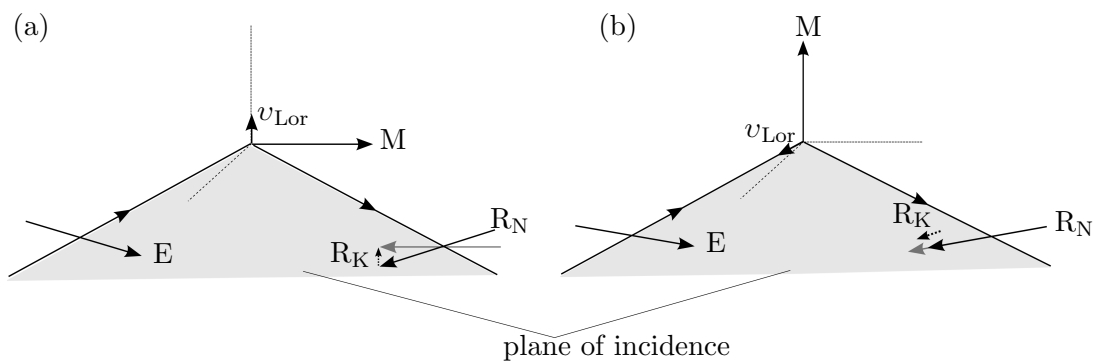


Figure 4.11: Schematic illustration showing the (a) longitudinal and (b) transverse Kerr effect. \mathbf{M} is the magnetisation and lies in the plane of the magnetic film, which in this schematic corresponds to the plane of this paper. The incident plane of light is tilted with respect to the page, as shown by the grey shading. The Lorentz force v_{Lor} is perpendicular to both \mathbf{M} and \mathbf{E} . If $\mathbf{M} = 0$ then the reflected beam has amplitude \mathbf{R}_N . If $\mathbf{M} \neq 0$ then the reflected light polarisation is rotated by \mathbf{R}_K .

MOKE measurement were carried out by Sampo Hämäläinen, under the supervision of Sebastiaan van Dijken, at the Aalto University, Finland. The measurements were carried out in the longitudinal configuration using the set up sketched in Figure 4.12. The polarised light was incident on the sample surface after passing through a polariser, and the reflected light from the sample surface was passed through the analyser, which was set just off the extinction position¹ to give a small intensity on the CCD camera. When $\mathbf{M} = 0$ ($\mathbf{M} = \mathbf{M}_s$), there is no (maximum) rotation of polarisation, and therefore

¹Extinction position arises when the polariser and analyser were set at 90° to each other, so that no light can pass through without polarisation rotation.

4. EXPERIMENTAL METHODS

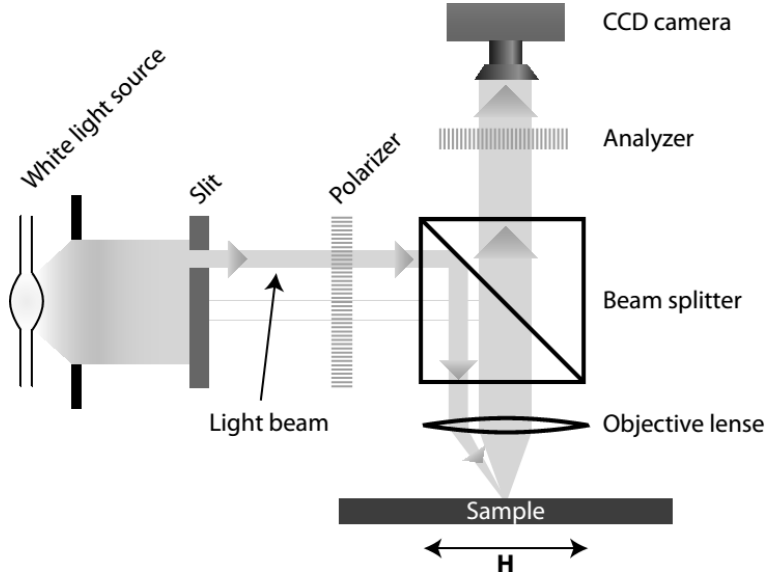


Figure 4.12: Schematic of the MOKE setup, where white light is passed through a polariser and a slit before it is focused on the sample. The reflected light intensity is measured after it has passed through the analyser. Drawing taken from the PhD dissertation of T. Lahtinen [153].

the detected intensity is minimum (maximum).

4.5 Electrical transport measurement

The transport measurements were carried out using the measurement rig and Labview control program set up initially by L.C. Phillips [146]. In this setup, the sample sits on a sample stage with 20-pin connection. Only the last 4 pins were connected with the mini-coax cables and these were used to connect the device. The sample stage was then mounted onto a probe which is lowered into a Janis Research Supertran-VP cryostat. The temperature control is achieved by balancing the heating power, provided by two heaters, one underneath the sample and one slightly above, and cooling power from continuously pumped liquid Helium. The device was grounded with the cryostat, which shares the same ground as the chassis ground in the Keithley 6487 picoammeter. The picoammeter was used as both a voltage source and amp meter. For measuring MR, at each measurement field, resistance $R=dV/dI$ was obtained from measuring current at two bias voltages.

4.5 Electrical transport measurement

Additional practical details that were not presented in reference [146] were given below.

1. Wear anti-static wristband all the time while handling the sample.
2. Once inserted the sample into the cryostat, pumping the sample space with a rough pump for about 15-20 mins before opening the helium inlet valve. This is to pump out as much water as possible before flowing in liquid Helium. However, this does not avoid condensation on the sample completely.
3. Both the transferline and the cryostat vacuum jacket were pumped roughly every two month to achieve stable temperature control and to save helium consumption. After pumping for 5 hours and above, the pressure of both should be in the range of $1-5 \text{ /times } e^{-5} \text{ mbar}$.
4. The measurements were mostly carried out at 10 K with minimum cooling rate. This is to avoid liquid helium splashing on to the surface of the sample, which not only cause random resistive jumps but also cause damage to the sample.
5. During this project, the sample heater lead was removed to reduce the electronic noise. However, this is not ideal as it lead to bad temperature control. A separate ground for the heater will solve this problem.
6. While zero the picoammeter, the device was disconnected to avoid large surge of electrical current passing through the device. During this project, this is done manually. A better approach would be to have a switch box.

4. EXPERIMENTAL METHODS

Chapter 5

Macroscopic magnetic properties of $\text{La}_{0.67}\text{Sr}_{0.33}\text{MnO}_3$ films

A VSM magnetometer was used to study the magnetic properties of $\text{La}_{0.67}\text{Sr}_{0.33}\text{MnO}_3$ (LSMO) films in two different crystal orientations, namely $(001)_{\text{pc}}$ and $(110)_{\text{pc}}$, grown on NGO (001), NGO (100) and STO (110) substrates¹. The films on NGO (001) have BaTiO_3 , SrTiO_3 or LaAlO_3 (LAO) capping layers, as these were employed at an early stage in the project to try to improve spin injection, but this was not successful (see Chapter 6). It is assumed that the capping layers do not affect film magnetisation.

5.1 LSMO (001)_{pc} on NGO (001)

The structural and magnetic properties of LSMO on NGO (001) were studied previously in detail by L. C. Phillips from this laboratory, whose results were reviewed in Chapter 3 and can be found in his PhD thesis [146] and papers [115, 124]. In this section, I show that the LSMO film reported here has the same strain state as reported

¹

- The subscript ‘pc’ stands for pseudocubic. The lattice parameters of rhombohedral LSMO (denoted by subscript ‘r’) are $a_{\text{LSMO}} = [100]_r = 5.465 \text{\AA}$, $c_{\text{LSMO}} = [001]_r = 5.465 \text{\AA}$ [154], which gives a pseudocubic lattice parameter of 3.873\AA .
- The lattice parameters of orthorhombic NGO are $a_{\text{NGO}} = 5.4332 \text{\AA}$, $b_{\text{NGO}} = 5.5034 \text{\AA}$, $c_{\text{NGO}} = 7.7155 \text{\AA}$ [155]. A subscript ‘or’ was used to describe NGO when there might be potential confusion with the crystallographic orientation.
- The Lattice parameter of cubic STO is $a_{\text{STO}} = 3.905 \text{\AA}$ [156].

5. MACROSCOPIC MAGNETIC PROPERTIES OF $\text{La}_{0.67}\text{Sr}_{0.33}\text{MnO}_3$ FILMS

by Phillips *et al.* [124], allowing me to discuss magnetic reversal with reference to the results measured there.

5.1.1 Structural characterisations

Figure 5.1 shows the topography of the LSMO film grown on NGO (001), with the LAO capping layer, that is assumed unimportant here. The surface of the film is atomically flat with visible step terraces. The large particles on the surface are more likely to be contamination due to post-PLD sample handling, and not ablated particles from the target. This is because, if it was ablated cluster of atoms, it would also present in the sample prepared in the same deposition run, i.e. sample 23199b. The orientations of the crystallographic axes were determined from XRD.

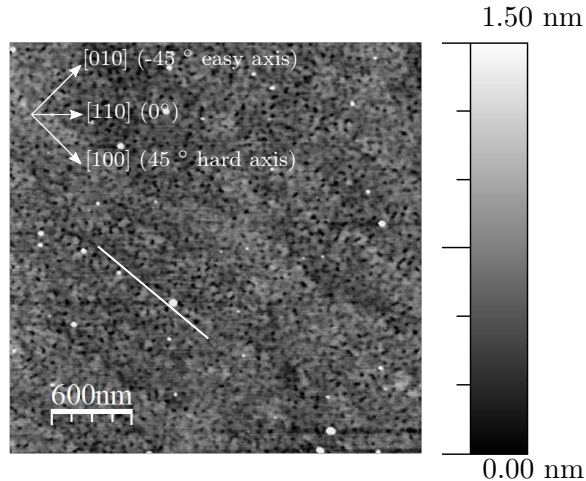


Figure 5.1: AFM topography of the LSMO film grown on NGO (001) (sample #23199a). The in-plane crystallographic directions are marked. The [110] direction lies along the long axis of the 10 mm \times 5 mm substrate. The white line in the lower part of the image marks the atomic terraces direction.

The thicknesses of the LSMO and LAO are 41.3 nm and 0.3 nm, as obtained from the curve fitting to the XRR data of a companion sample (Figure 5.2a). This gives a deposition rate of 0.26 Å per pulse. However, the thickness extracted from XRR curve fitting for the ultra-thin LAO capping layers is not reliable and the estimated 0.3 nm assumes the same deposition rate for LAO and LSMO. In fact, calibration runs for the LSMO and LAO suggest the deposition rate for LAO is 30% slower than LSMO. Even

for the same material, the deposition rate during the early stage of the growth will be different to the overall deposition of the film. Therefore, fitting to the XRR of an ultrathin LAO layer is difficult and not reliable, and in this case, shown as a breakdown of the fitting at $\sim 2.8^\circ$. The thickness can be measured more accurately by using the transmission electron microscopy (TEM), but it is not used because in the PLD system currently used, it is not possible to control the film thickness to that degree of accuracy. For example, the film thickness varies by $\pm 1 - 2 \mu\text{m}$ for a $\sim 30 \mu\text{m}$ thick film. The $\omega/2\theta$ scan gives an out-of-plane lattice parameter of 3.907 \AA , which is similar to that reported by Phillips *et al.* [146], indicating that the film is fully strained (Figure 5.2b).

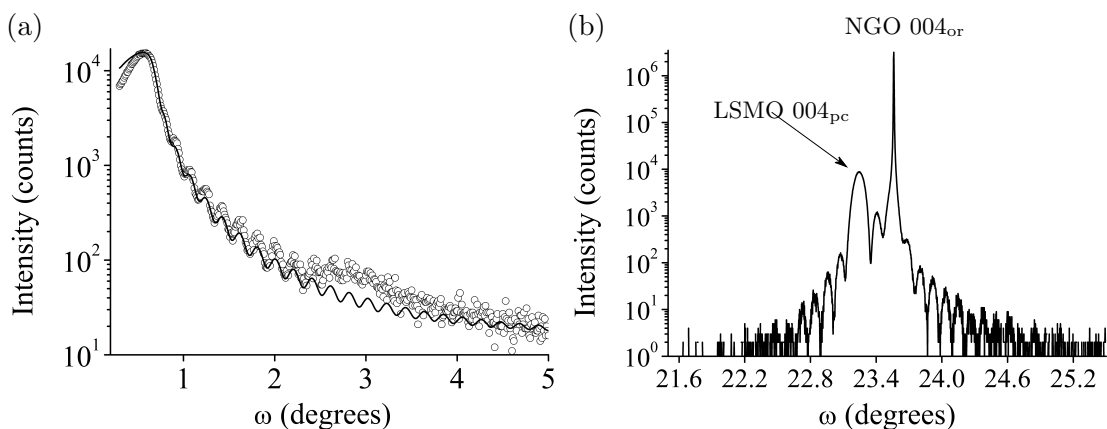


Figure 5.2: (a) The XRR of a companion sample #23199b, where the experimental data (circles) are fitted with the Reflectivity software (solid line). The film thickness extracted from the curve fitting is 41.6 nm. (b) The XRD $\omega/2\theta$ scan at the NGO 004_{or} peak.

5.1.2 Magnetic properties

The magnetic hard axis was at 45° to NGO [110], i.e. along [100] (Figure 5.3). The magnetic easy axis was found to be along [010]. There was no correlation between the easy axis and the atomic step direction.

The magnetic anisotropy of a sub-optimally doped film showed a thermal transition from a biaxial-uniaxial anisotropy coexistent below 200 K to uniaxial anisotropy at room tem-

5. MACROSCOPIC MAGNETIC PROPERTIES OF $\text{La}_{0.67}\text{Sr}_{0.33}\text{MnO}_3$ FILMS

perature (RT) [124]. However, the optimally doped LSMO film studied here may not show the same behaviour. In addition to the magnetic anisotropy, the dynamic switching behaviour of the film is important for spintronic applications. The main magnetisation reversal mechanisms relevant to the LSMO thin films are coherent-rotation and nucleation-propagation [105, 126, 127]. In the literature, magnetisation reversal of LSMO along the easy axis was reported to be nucleation-propagation type at RT [105, 126, 127]. However, a temperature-dependent study is still missing.

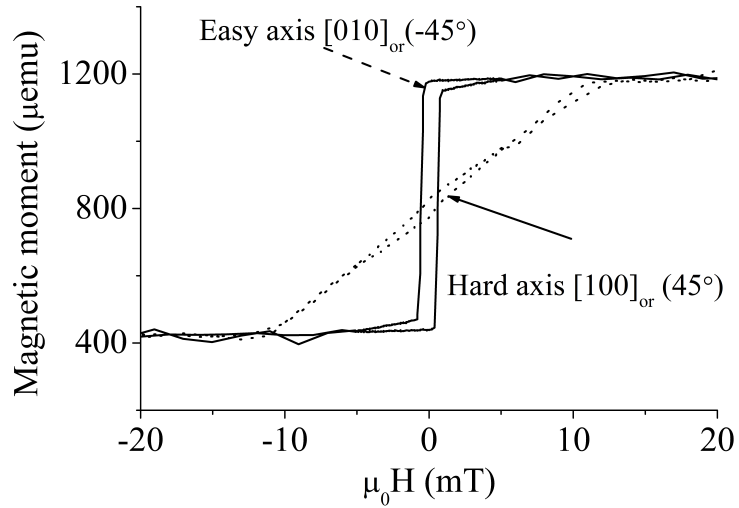


Figure 5.3: The magnetic moment as a function of the magnetic field measured at different angles to the long axis of the substrate ($[110]_{\text{or}}$ axis). The relative direction of the magnetic easy and hard axis to that of the surface terraces is marked in Figure 5.1. Measurements taken on sample #23199b.

To find out if the nucleation-propagation reversal mechanism has a temperature dependence, minor loops¹ [157, 158] and recoil loops² [159] were measured at 150 K and RT.

In the minor loop measurements, the gradient of the first magnetisation loop reveals

¹For the minor loop measurements, the sample was first demagnetised using the demagnetisation program in the software, such that the magnetic field was cycled between positive and negative fields with decreasing magnitude using 1% decrements. A series of hysteresis loops were then measured while gradually increase the magnitude of the field from zero.

²For the recoil loop measurements, the sample was first magnetised using 100 mT, and the magnetisation was measured with incremental increases of field in the negative field range.

whether the reversal is nucleation or propagation limited [157, 158]. A steep curve indicates that propagation is easy, and a shallow curve means domain propagation experiences resistance from pinning centers, such as impurities or domain walls. Room temperature and 150 K were chosen so that the results can be compared with an earlier study [124]. Figure 5.4a,b plot the minor loops measured at 150 K and RT respectively. At both temperatures, due to incomplete demagnetisation, it is not possible to see the first magnetisation trace. At 150 K, propagation of domains experience pinning, shown as the spread in the propagation field and the gradual increase of magnetisation. At RT, the domain wall propagated quickly and there is a steep increase of magnetic moment, indicating lower pinning energy to domain propagation. The film is nearly fully magnetised just beyond the nucleation field (H_n) whereas at 150 K it only reaches about half of the saturation magnetisation.

Recoil loops were measured because to completely demagnetise LSMO is difficult and can take a few hours if one wants to demagnetise it properly. At 150 K, no switching is seen at -4 mT, and only a small portion of the film is switched with every incremental increase from -4 to -8 mT (Figure 5.4c). These recoil loops reveal strong domain-wall pinning in the film at 150 K. At RT, once field reaches the critical field for nucleation $H_n \sim 0.44$ mT, domains are nucleated, and the majority of the film switches, although it does not quite reach the full magnetisation, possibly due to inhomogeneities (Figure 5.4d). Propagation of domain wall is easier at room temperature than 150 K. Therefore, although reversal at both temperatures is the nucleation-propagation type, the reversal is more propagation limited at 150 K.

Strong domain-wall pinning in the electrodes at low temperature is detrimental for device performance, especially in graphene spin-valves, where the contact area spans a few microns and the magnetic domains can be as small as ~ 100 nm (Figure 6.13).

5. MACROSCOPIC MAGNETIC PROPERTIES OF $\text{La}_{0.67}\text{Sr}_{0.33}\text{MnO}_3$ FILMS

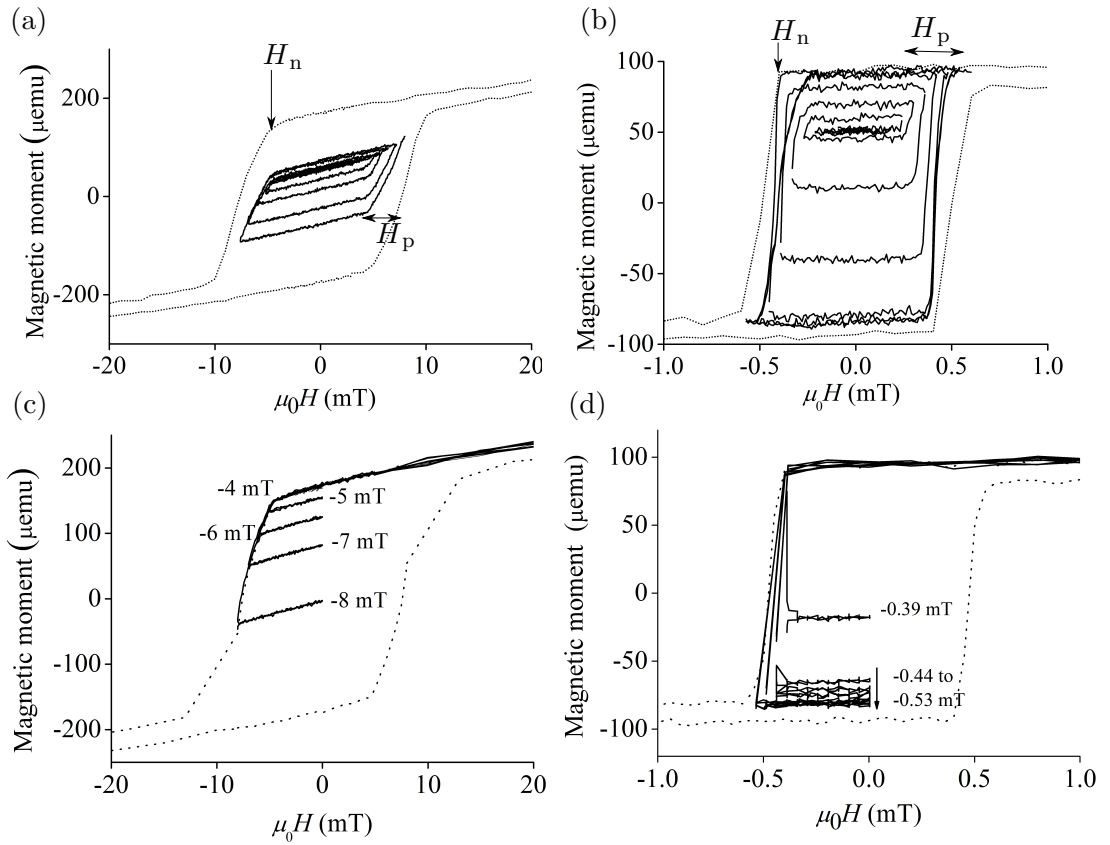


Figure 5.4: The minor loops of LSMO on NGO (001) taken at (a) 150 K, and (b) RT. The major loops are off-set vertically to allow better comparison with the minor loops. The recoil loops measured at (c) 150 K, and (d) RT. The tilt of the hysteresis loops at 150 K might due to inhomogeneities in the film as it has been thermally demagnetised prior to this measurement. Measurements taken on sample 23286s2 from L. C. Phillips.

5.2 LSMO (110)_{pc} on NGO (100)

5.2.1 Structural characterisations

The growth of LSMO on NGO (100), i.e. on a (110)_{pc} surface, is not as easily achieved as growth on NGO (001). The [110]_{pc} direction is more closely packed than the [001]_{pc} direction, and the growth is slower. Using the same deposition condition as that for LSMO (001)_{pc}, the surface of the film does not show sharp atomic terraces (Figure 5.5a).

Better film quality was achieved by placing a hard mask in optical box 1 (Figure 4.2). By doing this, the lower energy edge from the edge of the laser beam was removed and the energy of the laser spot was more homogenous. As a result, the deposition rate was slower, and allowed more time for the atoms to arrange themselves on the surface of the substrate, which is advantageous for growth along the close-packed [110]_{pc} direction. However, due to the slow deposition rate, the deposition for a 30 nm film took \sim 75 minutes instead of \sim 25 minutes. In order to check the effect of laser damage to the target on film quality, sample #23541 and #23539b, were grown. During the deposition of sample #23541, the target was rotating such that the laser ablated a ring of material during a 75 minutes deposition run. For sample #23539b, the target was moved every 25 minutes, so that several rings were ablated by the laser. Therefore there was reduced laser damage on the target during the deposition of sample #23539b.

Sample #23541

Figure 5.5b shows atomic terraces on the film surface.

The deposition rate with the mask is 0.07 Å per pulse, as calculated from the fitting to the XRR curve (Figure 5.6a). The out-of-plane interplanar spacing between the (110)_{pc} planes is 5.526 Å (Figure 5.6b), which is similar to that reported by Mathews *et al.* (5.52 Å) [105], and gives $a_{pc} = b_{pc} = 3.907\text{Å}$. The in-plane lattice parameter can be calculated from an RSM measured near an asymmetrical peak 402_{or}.

5. MACROSCOPIC MAGNETIC PROPERTIES OF $\text{La}_{0.67}\text{Sr}_{0.33}\text{MnO}_3$ FILMS

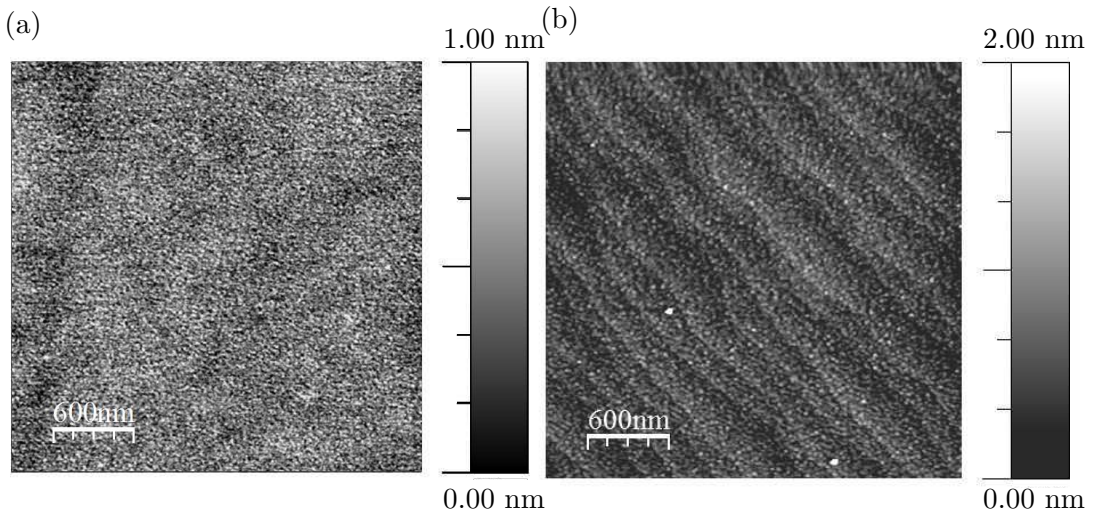


Figure 5.5: The AFM images of LSMO film grown on NGO (100) (a) without a hard mask in optical Box 1 (sample #23338b), and (b) with such a mask (sample #23541c).

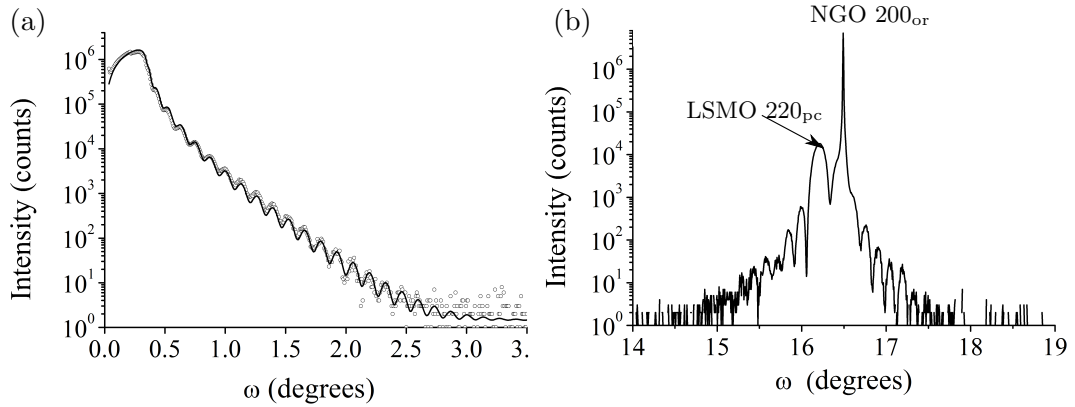


Figure 5.6: (a) The XRR of LSMO on NGO (100). Curve fitting gives a film thickness of 32.6 nm. (b) The XRD $\omega/2\theta$ scan near the NGO 200_{or} peak. Measurements taken on sample #23541a.

The schematics in Figure 5.7 show the film orientation relative to the substrate looking down the [001]_{or} axis, and the positions of asymmetrical 420_{or} and 402_{or} peaks in reciprocal space. Along the in-plane [001]_{or} ([001]_{pc}) direction, the film is fully strained and has the same $Q_{\text{in-plane}}$ ¹ as the substrate (Figure 5.8a). The in-plane c_{pc} lattice parameter of LSMO is therefore $c_{\text{NGO}}/2=3.86 \text{ \AA}$, which gives a compressive strain of -0.3%². Along the in-plane [010]_{or} ([$\bar{1}10$]_{pc}) direction, the majority of the film is fully strained and has the same $Q_{\text{in-plane}}$ value as the substrate. The in-plane tensile strain is $\sim 1\%$ (Figure 5.8b). However, there is some degree of relaxation as marked by the arrow in Figure 5.8b. Along the [010]_{or} direction, strain modifies the angle γ with respect to the unstrained 90° and causing angular relaxation. A similar relaxation of γ was reported for the (110)_{pc}-oriented LSMO on STO (110) [126]. It has also been reported by Infante *et al.* that the (110)_{pc}-oriented La_{0.77}Ca_{0.33}MnO₃ on STO (110) relaxes faster than on STO (001) [135].

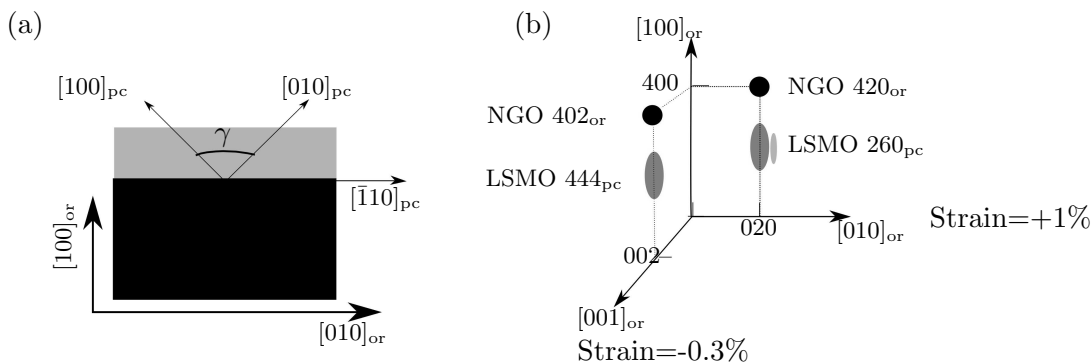


Figure 5.7: Schematic of (a) the crystallographic axes of the film (grey) and substrate (black), looking down [001]_{or} direction, and (b) the 420_{or} and 402_{or} asymmetric peaks in reciprocal space. The small grey ellipse illustrates the diffuse intensity from the relaxed film. The strain along the two in-plane directions is marked in the figure.

¹ $Q_{\text{in-plane}}$ ($Q_{\text{out-of-plane}}$) is the reciprocal of the interplanar spacing projected onto the in-plane (out-of-plane) direction.

²strain = $(a_{\text{film}} - a_{\text{substrate}})/a_{\text{film}}$.

5. MACROSCOPIC MAGNETIC PROPERTIES OF $\text{La}_{0.67}\text{Sr}_{0.33}\text{MnO}_3$ FILMS

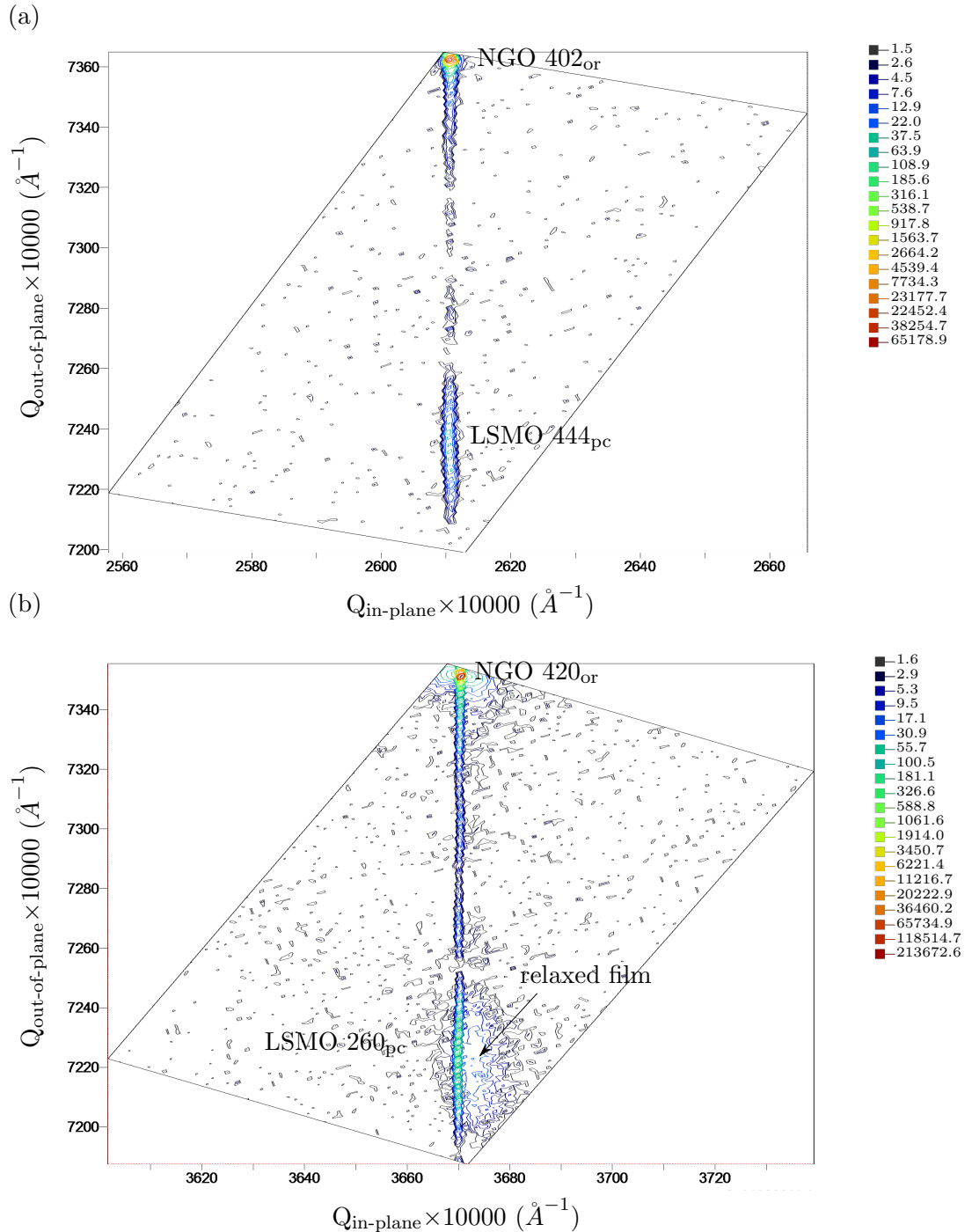


Figure 5.8: Reciprocal space map of LSMO on NGO (100) (sample #23541a) measured near (a) the 402_{or} peak, and (b) the 420_{or} peak. Colour scale indicates the X-ray intensity (counts).

However, it is not possible to exclude the possibility of compositional change in some parts of the film, which can also lead to lattice parameter variations. To check if the relaxed film is related to compositional changes in the target as a result of laser ablation, sample #23539b was grown while the target was moved every 25 minutes.

Sample #23539b

The atomic step terraces were visible on the surface of the LSMO film (Figure 5.9). The thickness of the film was 33.8 nm (Figure 5.10), which is in the same thickness regime as #23541. The out-of-plane interplanar distance between the (110)_{pc} planes is 5.527 Å, which gives $a_{pc}=b_{pc}=3.908$ Å and is similar to sample #23541 (Figure 5.10b).

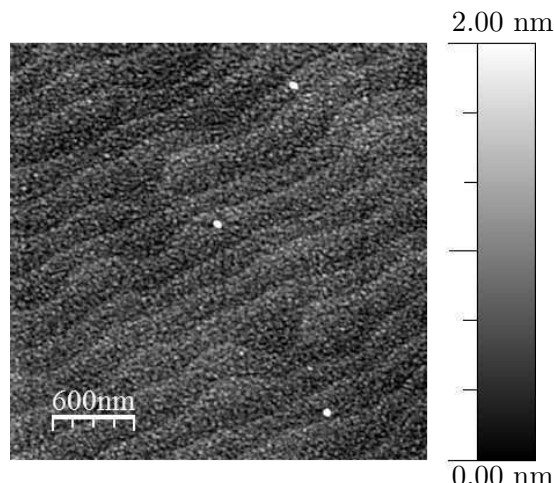


Figure 5.9: AFM image showing the clear surface terraces of the step height. Measurements taken on sample #23539b.

The RSM near the asymmetric 402_{or} peak is similar to sample #23541 (Figure 5.11a). However, the RSM near the 420_{or} peak shows that almost all the film is fully strained, although there is some diffuse intensity on the right-hand side of the film peak. Compared to sample #23541, the amount of relaxed film is very small. As shown by SEM (Figure 4.3), repetitive laser ablation locally damages the target. It is possible that the partially relaxed film in sample #23541 was caused by changes of the target, which could be compositional in nature.

5. MACROSCOPIC MAGNETIC PROPERTIES OF $\text{La}_{0.67}\text{Sr}_{0.33}\text{MnO}_3$ FILMS

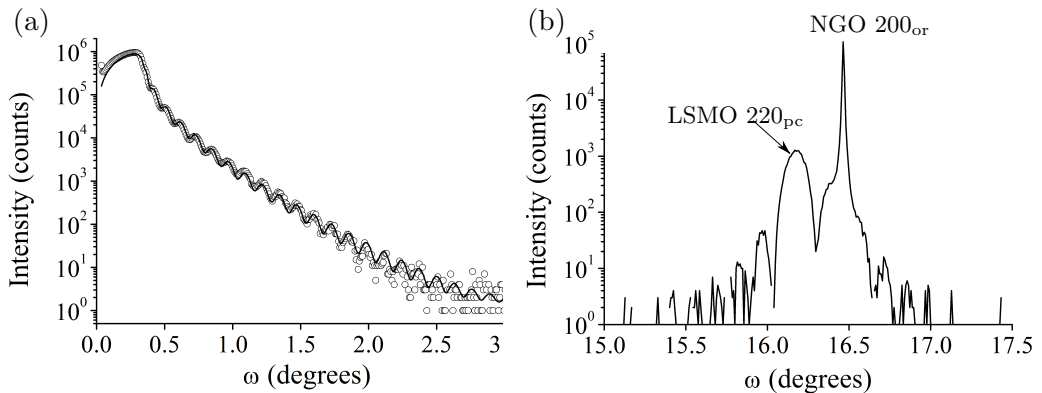


Figure 5.10: (a) XRR of LSMO on NGO (100) (sample #23539b). The curve fitting gives a thickness of 33.8 nm. (b) Out-of-plane $\omega/2\theta$ scan near the NGO 200_{or} peak. Measurements taken on sample #23539.

5.2.2 Magnetic properties

The temperature dependence of the magnetisation was measured in the VSM and the T_C of sample was found to be around 350 K (Figure 5.12).

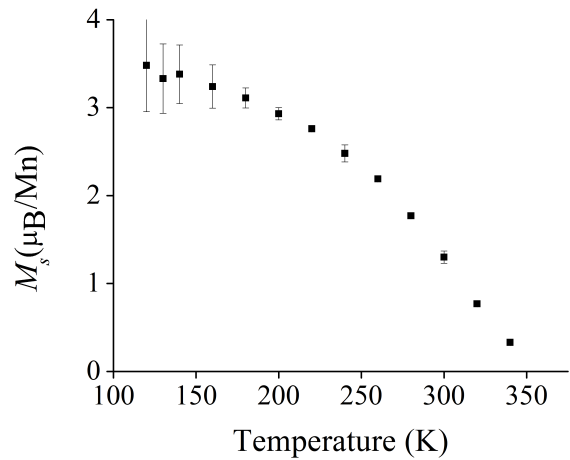


Figure 5.12: Temperature dependence of the magnetisation of LSMO on NGO (100). Measurements taken on sample #23519.

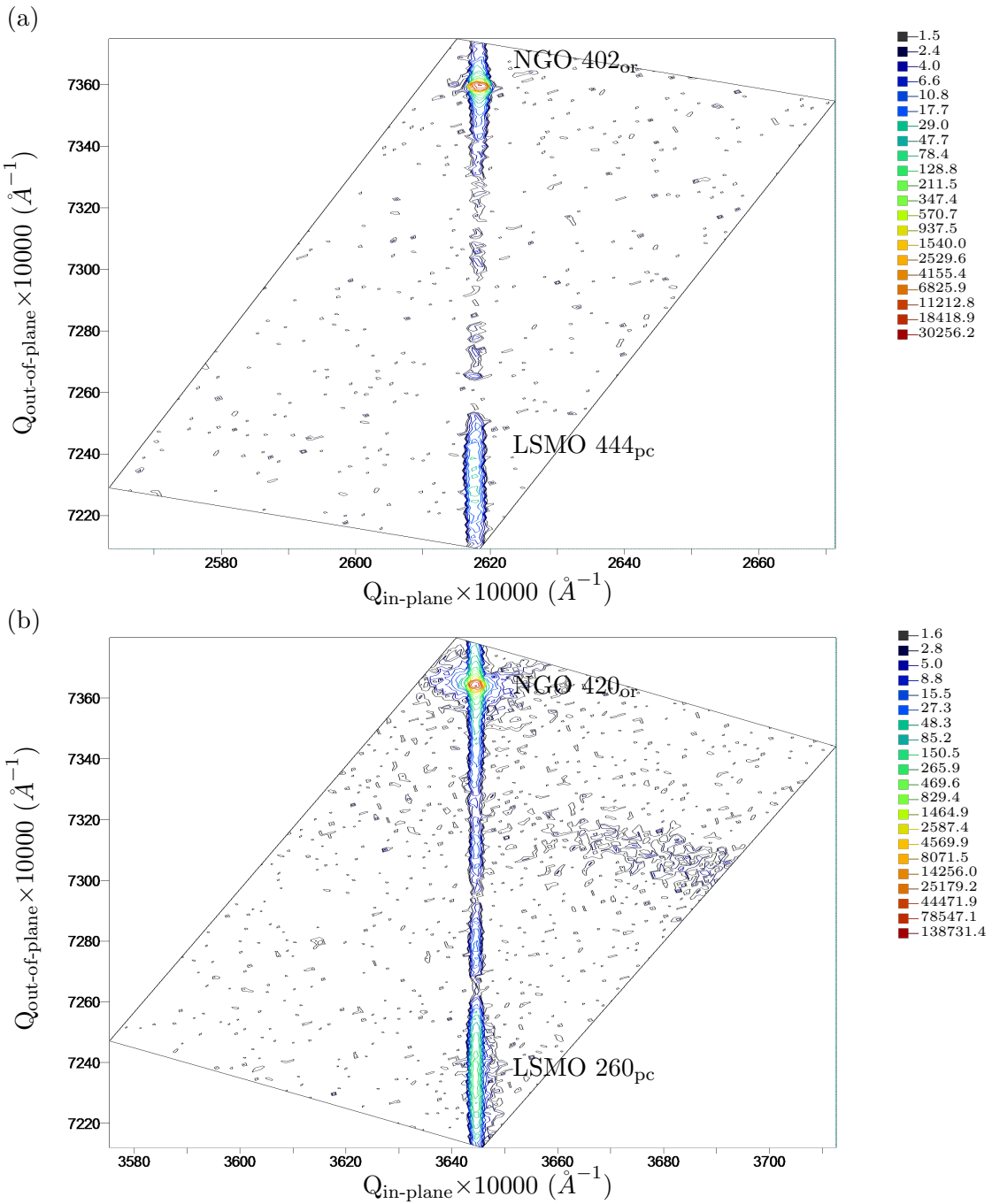


Figure 5.11: RSM of LSMO on NGO (100) (sample #23539b) measured near (a) the 402_{or} peak, and (b) the peak 420_{or}. The difference in $Q_{\text{in-plane}}$ in the maps of sample #23541 and #23539b is due to instrumental offset. Color scale indicates X-ray intensity (counts).

5. MACROSCOPIC MAGNETIC PROPERTIES OF $\text{La}_{0.67}\text{Sr}_{0.33}\text{MnO}_3$ FILMS

Assuming uniaxial anisotropy, $M_r(\varphi)$ should be equal to the projection of M_s onto the field direction, such that $M_r/M_s \propto \cos \varphi$, where φ is the angle between magnetic field and the easy axis. Figure 5.13 shows that LSMO (110)_{pc} has in-plane uniaxial anisotropy at both 150 K and RT.

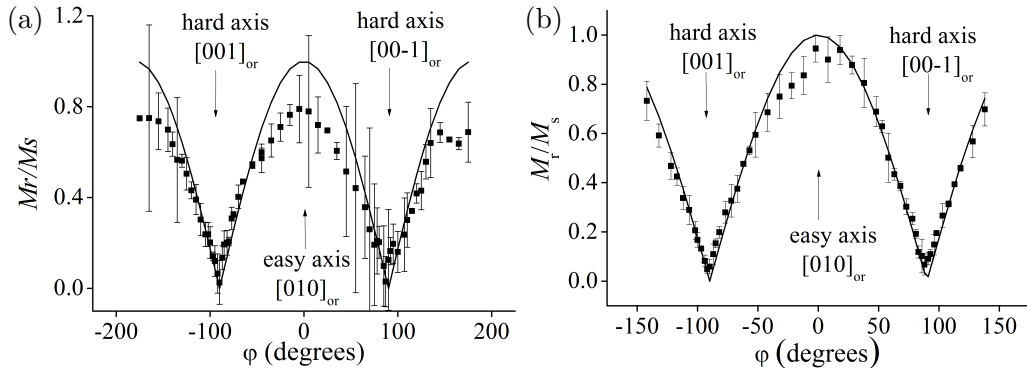


Figure 5.13: M_r/M_s as a function of in-plane orientation φ for LSMO on NGO (100) at (a) 150 K (sample #23126), and (b) RT (sample #23545). The solid line is the $\cos \varphi$ fit to the experimental data (squares).

The angular dependence of M_r is similar to that reported by Mathews *et al.* [105]. However, unlike reference [105], where $M_r = M_s$ along the easy axis, this measurement found M_r being 80% of M_s at 150 K, and approximately 95% at RT. There are several potential reasons for this reduction of M_r/M_s . First of all, temperature fluctuations lead to large uncertainties when extracting the magnetic moment. At RT, where temperature stability is best, the $\cos \varphi$ model fits better to the experimental data. Secondly, the NGO substrate has a large paramagnetic background signal that has to be subtracted to obtain the ferromagnetic (FM) signal. For the low-temperature measurements, because the sample has to be cut small (8.5 mm^2) to fit into the cryostat, which leads to small FM signal. However, the paramagnetic contribution is large due to thick substrate. Thirdly, there is a possibility that the sample plane is slightly tilted such that the applied magnetic field cannot be aligned precisely with the in-plane easy axis. Lastly, there might be a weak out-of-plane magnetisation component because the LSMO film is under in-plane compression. It is difficult to say whether the reduced M_r/M_s is due to experimental errors or an out-of-plane component without further investigations. A temperature-dependent study of the out-of-plane magnetisation using VSM or MFM

would provide useful information for understanding this. It might be difficult to study the out-of-plane magnetisation with VSM provided the large paramagnetic background and the small out-of-plane magnetisation expected.

The in-plane uniaxial anisotropy is also consistent with a linear hard-axis measurement (Figure 5.14) and the squareness of the easy-axis hysteresis loop (Figure 5.15). The hard-axis $M(H)$ data can be fitted with the Stoner-Wohlfarth (SW) coherent-rotation model to extract the uniaxial anisotropy constant K_u and the anisotropy field H_K [157, 160]. The total energy for a uniaxial film under applied field H is:

$$E_{\text{tot}} = K_u \sin^2 \theta - \mu_0 M_s H \cos(\theta - \varphi), \quad (5.1)$$

where θ (φ) is the angle between the magnetisation (applied field) and the magnetic easy axis. The equilibrium magnetisation direction θ for magnetic field applied at any angle φ can be calculated by solving $\partial E / \partial \theta = 0$ and $\partial^2 E / \partial \theta^2 > 0$.

Solving Equation 5.1 for the hard axis by setting $\varphi = 90^\circ$, I get $2K_u \frac{M}{M_s} = \mu_0 H M_s$. Plotting $\frac{M}{M_s}$ against $\mu_0 H$ gives a line whose gradient depends on K_u . Straight-line fitting to the data in Figure 5.14a,b gives $K_u = 35000 \text{ Jm}^{-3}$ and 5400 Jm^{-3} at 150 K and RT, which is $\times 5$ and $\times 3$ the anisotropy of LSMO on NGO (001) respectively. The RT value of K_u is similar to that found by Mathews *et al.* (5700 Jm^{-3}) [105].

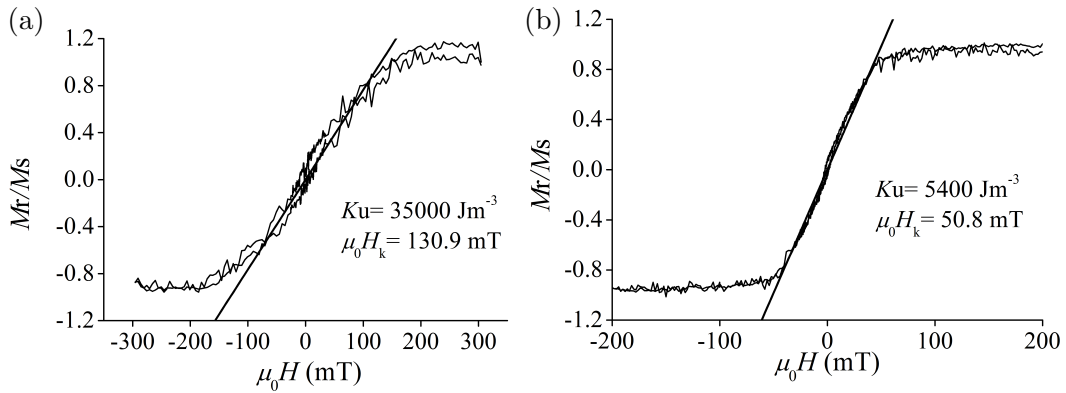


Figure 5.14: $M(H)$ of LSMO on NGO (100) measured along the hard axis at (a) 150 K (sample #23126), and (b) RT (sample #23545). The experimental data were fitted with the Stoner-Wohlfarth coherent-rotation model (straight line) to extract K_u .

5. MACROSCOPIC MAGNETIC PROPERTIES OF $\text{La}_{0.67}\text{Sr}_{0.33}\text{MnO}_3$ FILMS

Along the easy axis, the minor loops and recoil loops were measured to determine the magnetisation reversal mechanism. Figure 5.15a,b plots the minor loops measured at 150 K and RT, revealing nucleation-propagation magnetisation reversal. Due to the large value of K_u , it is much easier to nucleate a domain of opposite magnetic moment and have propagation than it is to slowly rotate the magnetic moment of the whole film by coherent-rotation. Compared to the $(001)_{\text{pc}}$ -oriented LSMO, switching of LSMO $(110)_{\text{pc}}$ is sharper and pinning is weaker. At 150 K, once the domain has nucleated at H_n , the whole film switches sharply. The nucleation events do not always occur at the same magnetic field, because major loops does not always have the same coercivity (not shown here). In addition, propagation is easier shown as the smaller value of H_p than H_n . Therefore, at 150 K, magnetisation reversal of LSMO $(110)_{\text{pc}}$ is nucleation limited rather than propagation limited as for LSMO $(001)_{\text{pc}}$. At RT, probably due to the better temperature stability in the VSM, H_p stays roughly constant. The switching behaviour in the tails of the minor loops ($|\mu_0 H| > 0.5 \text{ mT}$) is interesting. It seems like the majority of the film reverses below 0.5 mT, whereas the rest of the film encounters stronger pinning, suggesting that there are inhomogeneities in the film, probably at the interface or surface.

To summarise, for LSMO $(110)_{\text{pc}}$, the magnetic reversal along the hard axis is mainly coherent-rotation as fitted by the Stoner-wohlforth model, and along the easy axis there is nucleation-propagation.

The nucleation-propagation behaviour can be fitted by the Kondorsky model [105, 161]. In the Kondorsky model, the coercive field $H_c = \frac{H_{c(\varphi=0)}}{\cos \varphi}$. Near the hard axis, the coercive field can be fitted with coherent-rotation model $H_c = \frac{H_K}{2} \sin 2\varphi$ [158]. In Figure 5.16, the circles and triangles are calculated using the Kondorsky model, and the solid line plots the solution of the SW coherent-rotation model. The two types of plots are quite different, and therefore the two types of magnetisation reversal an be easily distinguished. The higher the value of H_K/H_c the more dominant the nucleation-propagation during the magnetic reversal (Figure 5.16 circles and triangles).

Figure 5.17a,b plots the experimental data for H_c as a function of φ , and fits assuming coherent-rotation (dotted line) and the Kondorsky model (solid line). As concluded earlier, the reversal proceeds by coherent-rotation near the hard axis, and by nucleation-propagation near the easy axis. In the intermediate angles of φ , there is contribution from both nucleation-propagation and coherent-rotation (Figure 5.17c,d). From large

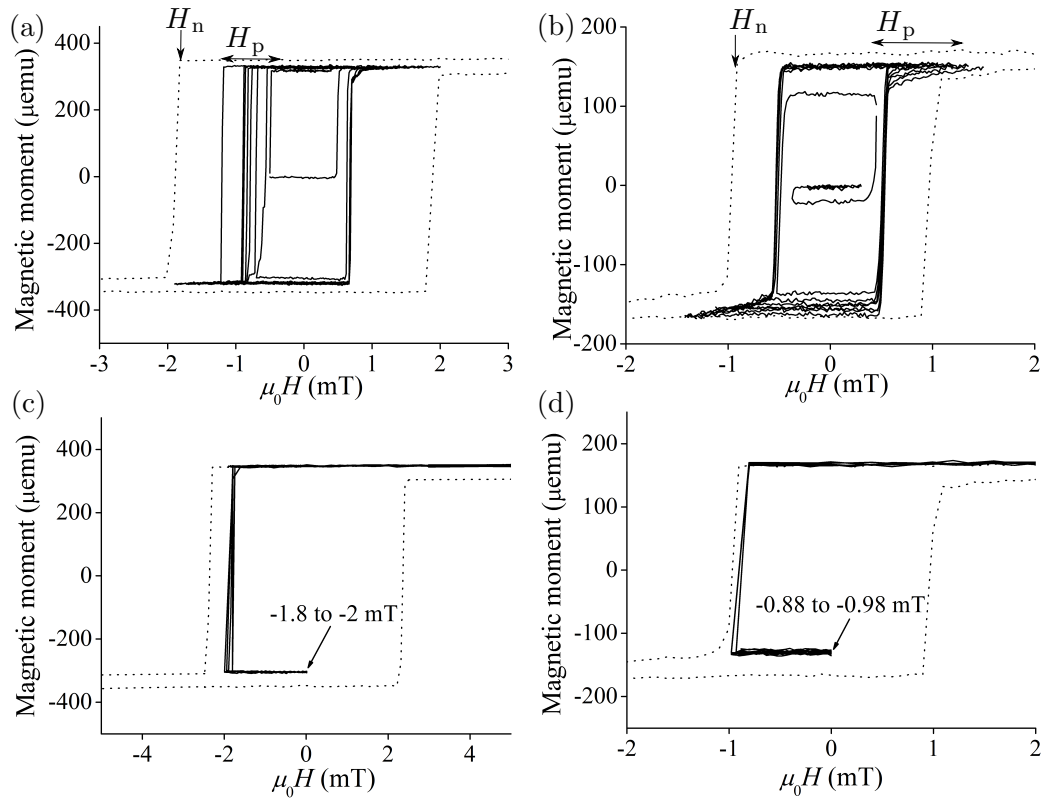


Figure 5.15: Minor loops of LSMO on NGO (100) measured at (a) 150 K, and (b) RT. Recoil loops measured at (c) 150 K, and (d) RT. The dotted lines show major loops. Measurements taken on sample #23519.

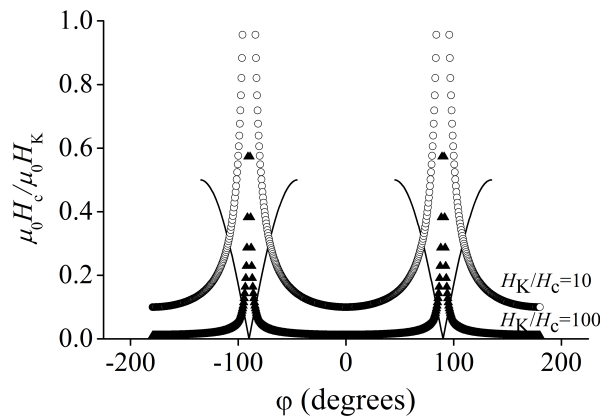


Figure 5.16: The SW coherent-rotation model (solid line) and Kondorsky model (circles and triangles) for the coercivity dependence of φ . For the Kondorsky model, circles were plotted for $H_K/H_c = 10$, and triangles were plotted for $H_K/H_c = 100$.

5. MACROSCOPIC MAGNETIC PROPERTIES OF $\text{La}_{0.67}\text{Sr}_{0.33}\text{MnO}_3$ FILMS

field to the nucleation field H_n , there is gradual change of magnetisation, suggesting the reversal is likely to be coherent-rotation. At H_n , the film switches sharply by nucleation-propagation. The value of H_K/H_c calculated from the hard axis $M(H)$ at RT is 85, and 22 at 150 K, and the fitting in Figure 5.17a,b suggest the reversal is more nucleation-propagation-like at RT. At both temperatures, H_c measured along the hard axis does not exactly equals to zero, which could be due to mis-alignment with the hard axis.

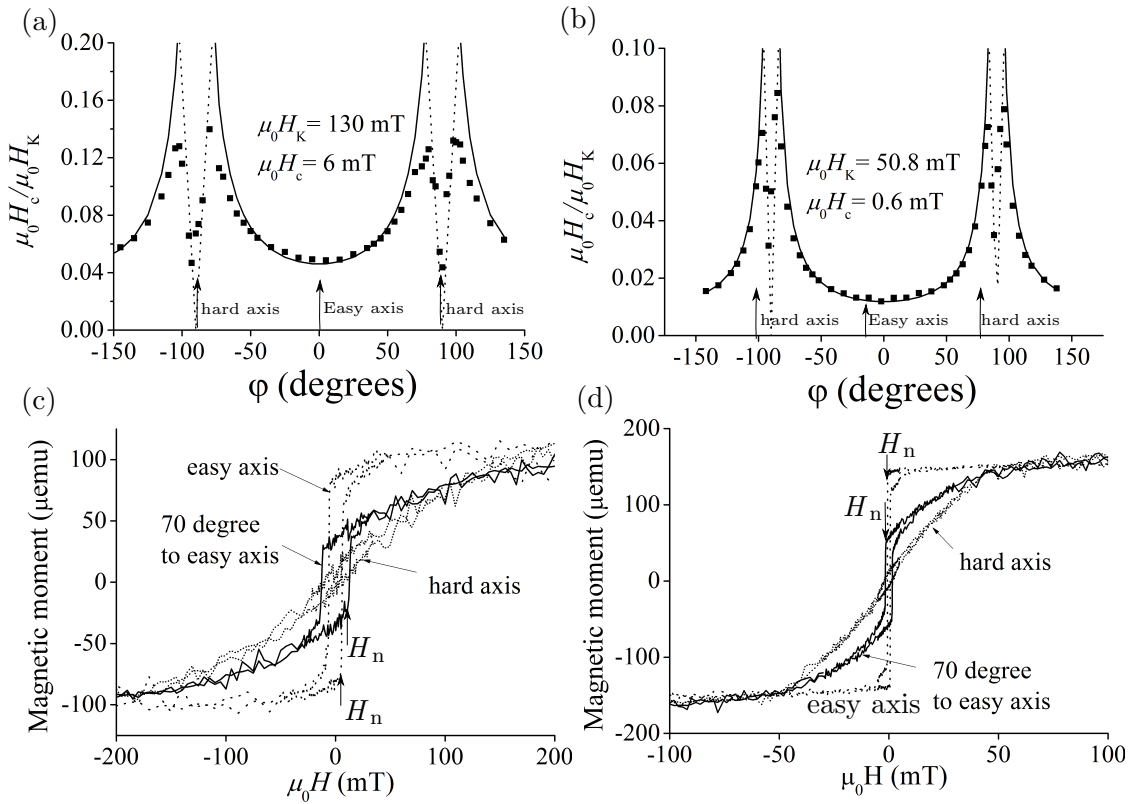


Figure 5.17: Coercivity dependence of φ for LSMO on NGO (100) measured at (a) 150 K (#23126), and (b) RT (sample #23545). Hysteresis loop measured along the easy axis, hard axis and 70° to the easy axis at (c) 150 K, and (b) RT.

5.3 LSMO (110)_{pc} on STO (110)

5.3.1 Structural characterisations

As with LSMO on NGO (100), the growth direction of LSMO on STO (110) is along the close-packed direction and the growth rate is slow. A hard mask in the optical box 1 (Figure 4.2) was used to achieve better film quality. Figure 5.18 compares the topography of films grown with and without the mask. The atomic step terraces are visible on the film grown with mask (Figure 5.18b).

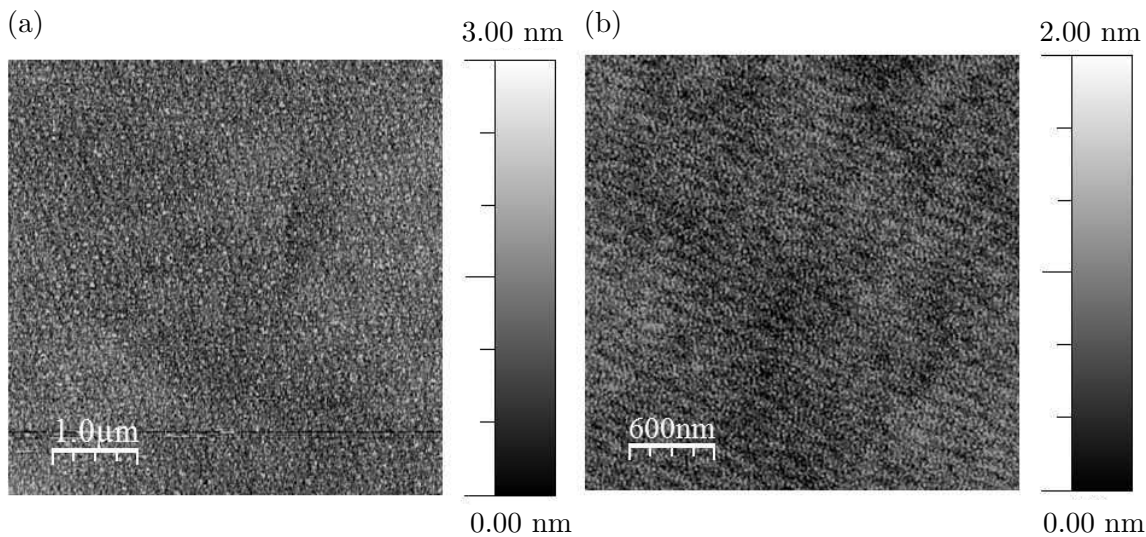


Figure 5.18: AFM imaging of LSMO films grown on STO (110) (a) without the mask (sample #23408a), and (b) with the mask (sample #23482c).

The thickness of LSMO grown without the mask was 68.8 nm (Figure 5.19a). The out-of-plane interplanar spacing between (110)_{pc} planes of LSMO calculated from the $\omega/2\theta$ scan was 5.463 Å (Figure 5.19b), which is similar to that reported by Boschker *et al.* (5.45 Å) [126]. This is smaller than the bulk (110)_{pc} interplanar distance of 5.477 Å due to the in-plane tensile strain from the substrate.

5. MACROSCOPIC MAGNETIC PROPERTIES OF $\text{La}_{0.67}\text{Sr}_{0.33}\text{MnO}_3$ FILMS

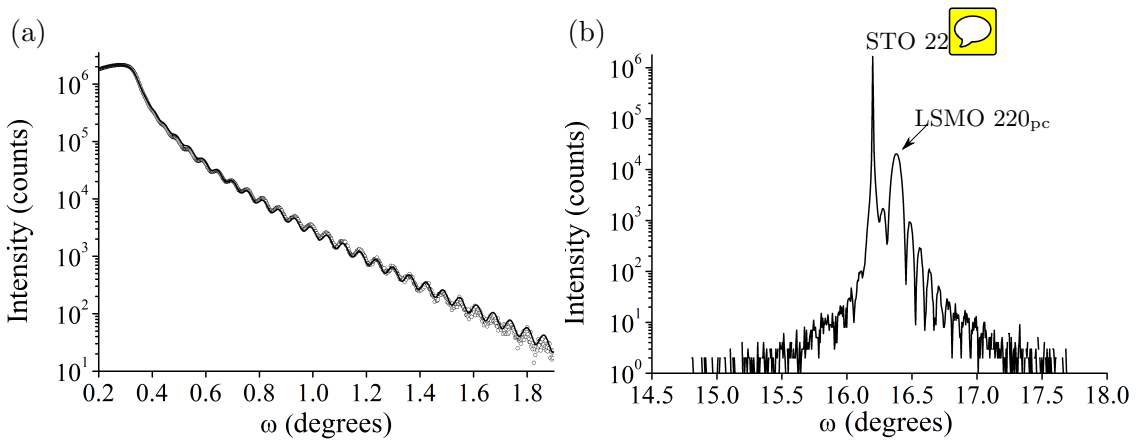


Figure 5.19: (a) XRR of LSMO on STO (110) (sample #23408a), where the experimental data (circles) are fitted using the Reflectivity software (solid line). The fitting gives a thickness of 68.8 nm. (b) Out-of-plane $\omega/2\theta$ scan at the STO 220 peak. Measurements taken on sample #23408b.

Figure 5.20a,b is the schematic illustrations of the film orientation relative to the substrate and the asymmetrical STO 222 and 130 peaks in reciprocal space. Figure 5.21a,b is the RSM maps measured near the 222 and 130 peaks. The 68.8 nm film is fully strained along both of the in-plane axes with 0.8% tensile strain along both directions.

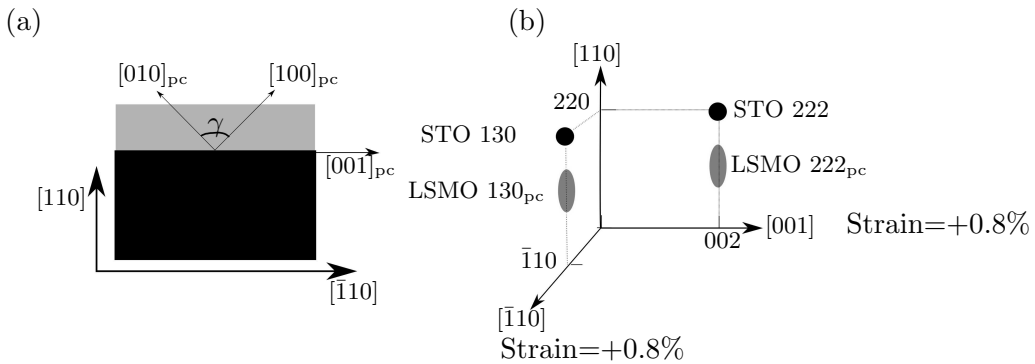


Figure 5.20: Schematic illustration of (a) the crystallographic axes of the film and the substrate, and (b) the STO 222 and 130 asymmetric peaks in the reciprocal space. The strain along the two in-plane directions is indicated in the figure.

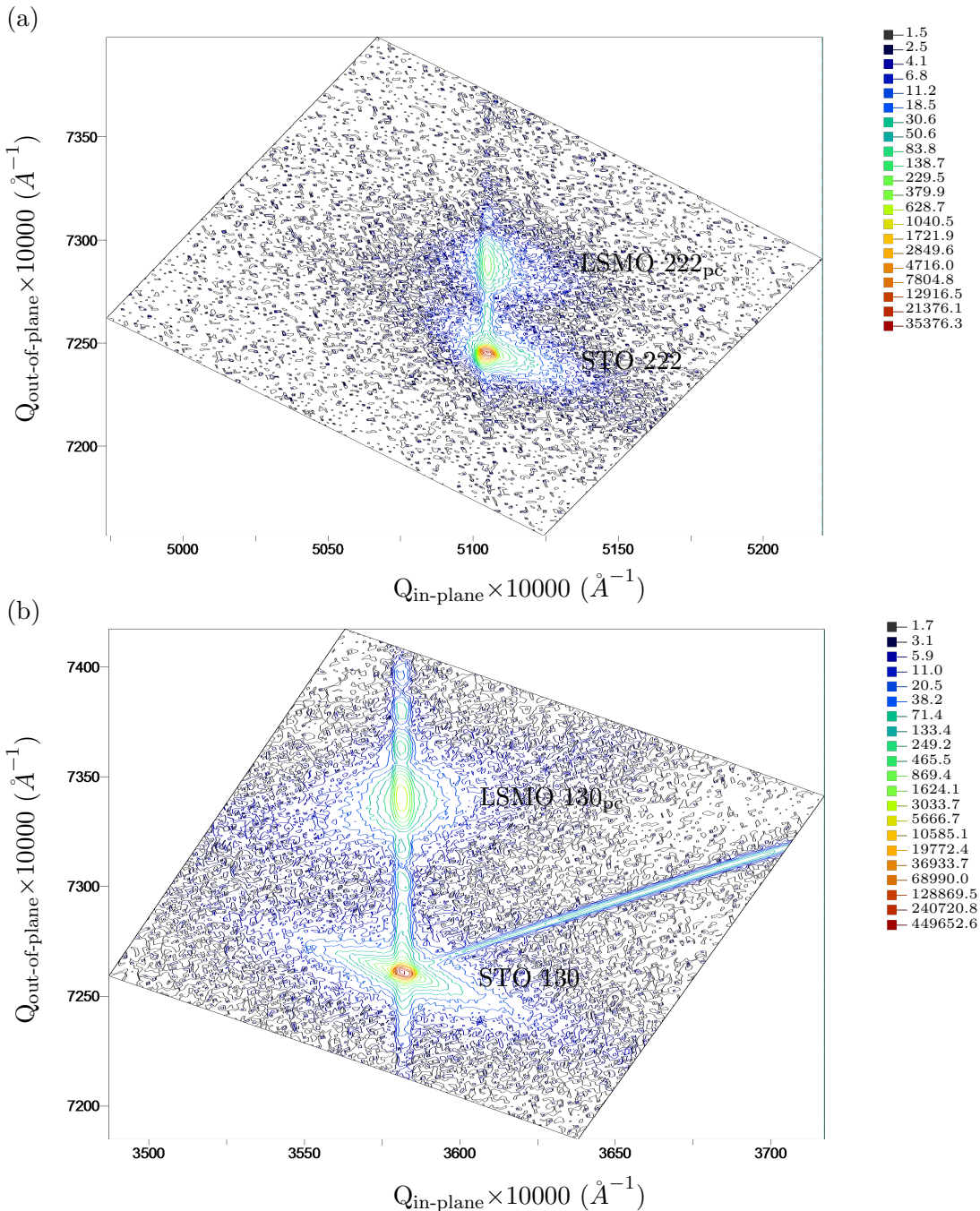


Figure 5.21: RSM measured near (a) the 222 peak, and (b) the 130 peak. Measurements taken on sample #23408b. Color scale indicates X-ray intensity (counts). The streak points towards the substrate peak could due to reduced angular resolution from air scatter in the system [148], or cutting of the X-ray by the primary or secondary analyser crystals.

5.3.2 Magnetic properties

The T_C of the $(110)_{\text{pc}}$ -oriented LSMO on STO (110) is around 350 K (Figure 5.22), similar to LSMO on NGO (100).

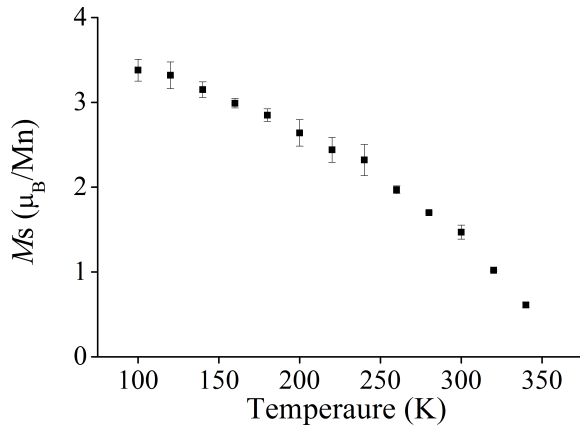


Figure 5.22: Temperature dependence of the magnetisation of LSMO on STO (110). Measurements on sample #23481.

Figure 5.23 shows, for 150 K and RT, that M_r equals the projection of M_s onto the field direction, and that M_r/M_s can be fitted with $\cos \varphi$. This shows that the film has in-plane uniaxial anisotropy, as reported by Boschker *et al.* [126]. As with $M(\varphi)$ for LSMO on NGO (100), M_r along the easy axis is slightly smaller than M_s , and equals to 80% and 90% of M_s at 150 K and RT respectively. A similar result was reported in reference [126], where $M_r \sim 78\% M_s$ at RT, this was attributed to an out-of-plane magnetisation as the result of tilting of the (001) plane with respect to the film-substrate interface.

The uniaxial anisotropy constant was extracted from fitting to the hard axis $M(H)$ data using the coherent-rotation model (Figure 5.24). The values of K_u are 43000 Jm^{-3} and 6500 Jm^{-3} for 150 K and RT respectively.

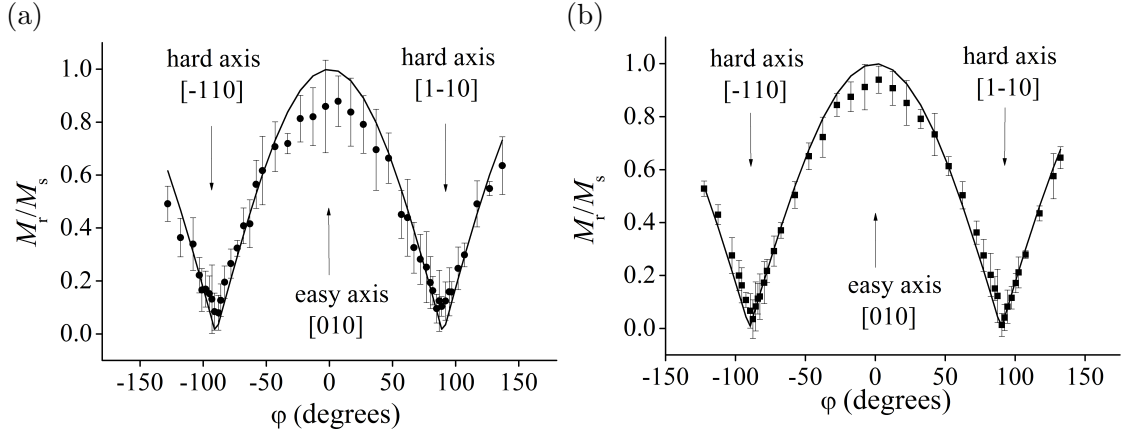


Figure 5.23: M_r/M_s as a function of φ at (a) 150 K , and (b) RT for LSMO on STO (110). The solid line is the $\cos \varphi$ fit to the experimental data. Measurements taken on sample #23539.

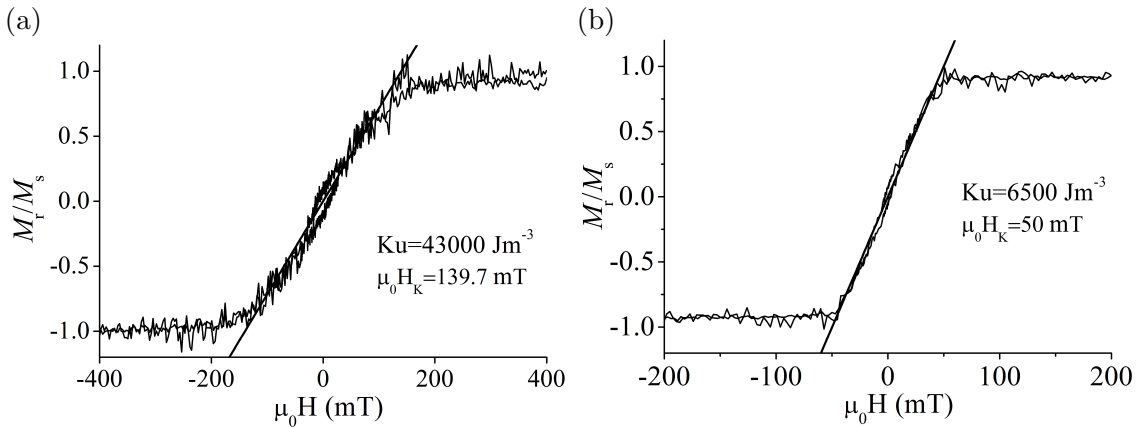


Figure 5.24: $M(H)$ of LSMO on STO (110) (sample #23539) measured along the hard axis at (a) 150 K, and (b) RT. The data were fitted with the SW coherent-rotation model (straight line) in order to extract K_u .

5. MACROSCOPIC MAGNETIC PROPERTIES OF $\text{La}_{0.67}\text{Sr}_{0.33}\text{MnO}_3$ FILMS

The reversal behaviour along the easy axis was studied by measuring the minor loops and recoil loops, as shown in Figure 5.25. As for LSMO on NGO (100), the magnetisation reversal of LSMO on STO (110) is mainly nucleation-propagation. However, the detailed switching behaviour is quite different to LSMO on NGO (100). At 150 K, there is stronger pinning, giving the step-like enlargement of the minor loops as the field increases (Figure 5.25a). In addition to the sharp switching, there is also gradual change of magnetisation for $\mu_0 H > 0.5$ mT. The proportion of gradual switching to sharp switching is larger at RT (Figure 5.25b). The room-temperature minor loops show weak propagation-limited switching. The gradual switching could be a result of inhomogeneity in the film. Prior to this study, the film had been heated to 150°C in air, in order to demagnetise the film. It is possible that this heat treatment damaged the film. A reference sample which was not heat-treated should be measured to give more insight.

The minor loops are asymmetric at 150 K, with sharper switching in the positive field range than the negative field range. However, this asymmetry is not present at RT. Similar asymmetry is also seen in LSMO films on NGO (100) at 150 K (Figure 5.15a) but not at RT (Figure 5.15b). Exactly why this happens is not known.

The recoil loops at both temperatures show nucleation-propagation type reversal (Figure 5.25c,d). At 150 K, the film switches sharply and reaches full magnetisation at the nucleation field (Figure 5.25c). At RT, the majority of the film switches at the nucleation field. A small proportion of the film switches at higher field, shown as the gradual increase of M_s with field that is marked by the arrow in Figure 5.25d. This suggests weak pinning to the domain propagation possibly due to inhomogeneities in the film as a result of the heat treatment.

The magnetisation reversal at different values of φ was examined using the coherent-reversal and the Kondorsky model (Figure 5.26a,b). As for LSMO on NGO (100), the reversal proceeds by nucleation-propagation near the easy axis and there is coherent-rotation near the hard axis. The nucleation-propagation mechanism expands to a larger angular range at RT. At the intermediate angles of φ , the reversal is a combination of coherent-rotation for $\mu_0 H > H_n$ and nucleation propagation at H_n (Figure 5.26 c,d). The proportion of coherent-rotation increases as it gets closer to the hard axis.

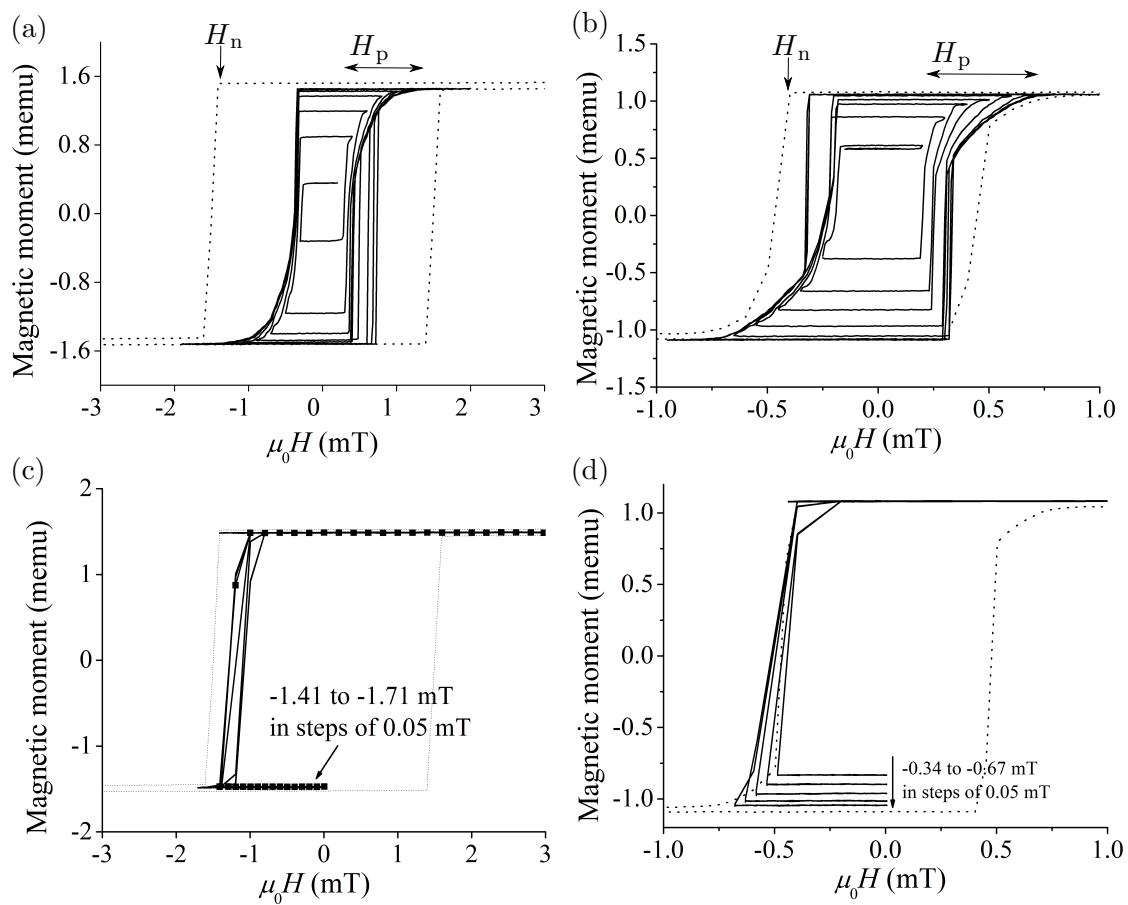


Figure 5.25: Minor loops measured for LSMO on STO (110) at (a) 150 K, and (b) RT. Recoil loops measured at (c) 150 K, and (d) RT. The dotted lines plot the major loops. Measurements on sample #23293s2, by L. C. Phillips.

5. MACROSCOPIC MAGNETIC PROPERTIES OF $\text{La}_{0.67}\text{Sr}_{0.33}\text{MnO}_3$ FILMS

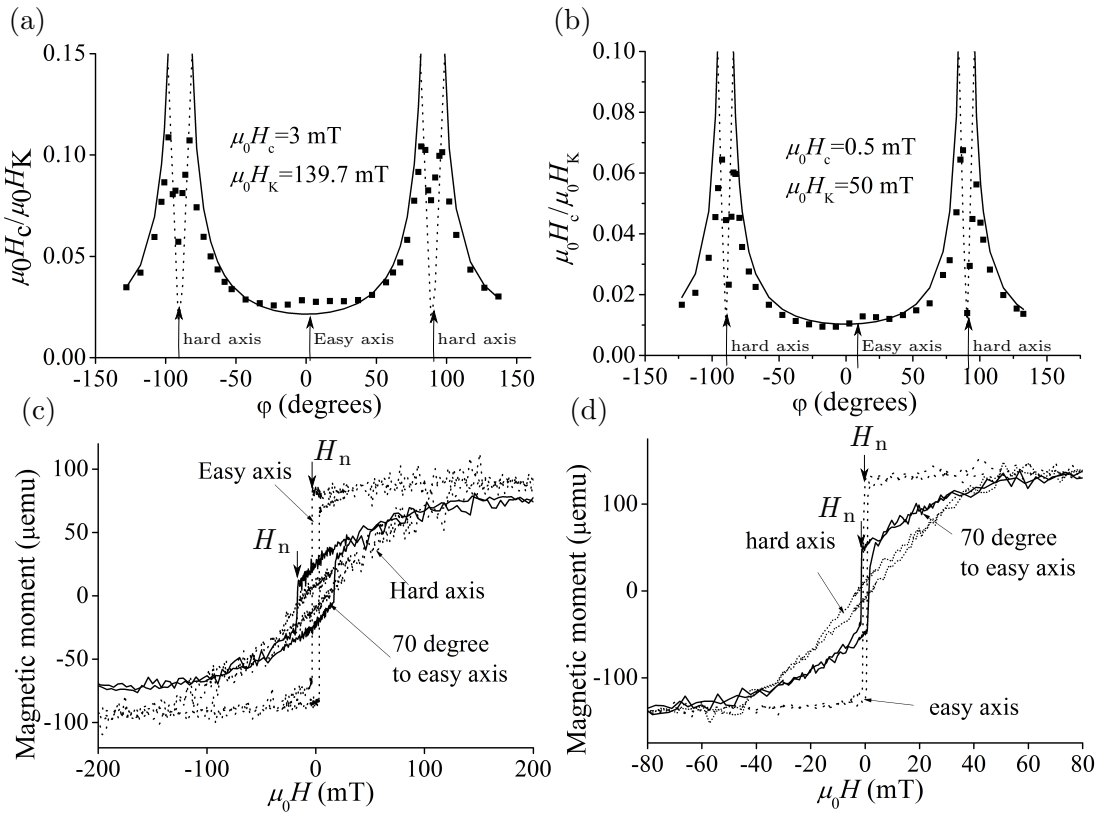


Figure 5.26: Coercivity of LSMO on STO (110) (sample #23539), measured as a function of φ at (a) 150 K, and (b) RT. The experimental data were fitted assuming Kondorsky model (solid line) and the Stoner-Wohlfarth coherent-rotation model (dashed line). Hysteresis loops measured along the easy axis, hard axis and 70° to the easy axis at (c) 150 K, and (d) RT.

5.4 The effect of Au capping layer on the magnetic property of epitaxial LSMO film

In this project, the Au capping layers were used as a sacrificial layer to protect the surface of the LSMO film from photoresist contamination during the lithography. It has been reported that a Au capping layer leads to a degradation of the surface magnetisation of LSMO [116, 162]. However, there is no direct comparison regarding the degree of degradation in terms of the different methods of Au deposition. The possible methods of depositing Au layer in this laboratory are PLD, where the Au can be grown in-situ at room temperature after the LSMO deposition, or by ex-situ resistive evaporation in the clean room. If surface magnetisation degradation due to the Au capping cannot be avoided, then it is important to find out which method causes the least damage. This section compares the temperature dependence of the magnetisation for LSMO capped with Au according to the two methods.

Two samples of 5 nm-thick LSMO on STO (001), were prepared in the same deposition run. The thickness was chosen to be as small as possible for accurate measurement in the VSM. STO (001) substrates were chosen because they do not have a paramagnetic background. LSMO on STO (110), which was used in the actual device of interest (Chapter 6), would have been a better choice, but it was not available when this experiment was carried out.

Figure 5.27 shows the temperature dependence of the magnetisation when the Au capping layer was deposited by PLD (PLD-Au) and evaporation (E-Au). The low-temperature magnetisation decreased by $\sim 50\%$, and the T_C by ~ 100 K in the PLD-Au sample (Figure 5.27a). Because the deposition was carried out at low pressure, the high-energy plume arrived the sample surface with a kinetic energy and damaged the LSMO surface [145]. Growing under an O₂ ambient would reduce the kinetic energy of the arriving particles, but Au would not stick to the LSMO surface well. In contrast, the E-Au sample does not show large decrease in T_C (Figure 5.27b). The discrepancy in the low-temperature magnetisation might due to temperature instability during the measurement or insufficient time for the sample to reach thermal equilibrium with the environment. Compared to PLD, evaporated Au arrives on the surface of the LSMO film much more gently, and is therefore less likely to damage the LSMO surface, but de-oxygenation of the LSMO surface is very likely during evaporation because the sample sits in a vacuum chamber that heats as evaporation proceeds. A study by Dörr *et al.*

5. MACROSCOPIC MAGNETIC PROPERTIES OF $\text{La}_{0.67}\text{Sr}_{0.33}\text{MnO}_3$ FILMS

reported that oxygen diffusion can take place at a relatively moderate temperature of $\sim 80^\circ$ in $\text{La}_{0.7}\text{Ca}_{0.3}\text{MnO}_3$ prepared by sputtering [163]. Although the reported 80° is for a different manganite that is grown by different method, the surface magnetisation is in any case delicate. In order to avoid this problem, the patterned electrodes were annealed at 750°C in 55 kPa O_2 for one hour, after etching away the Au and before they were used for the devices.

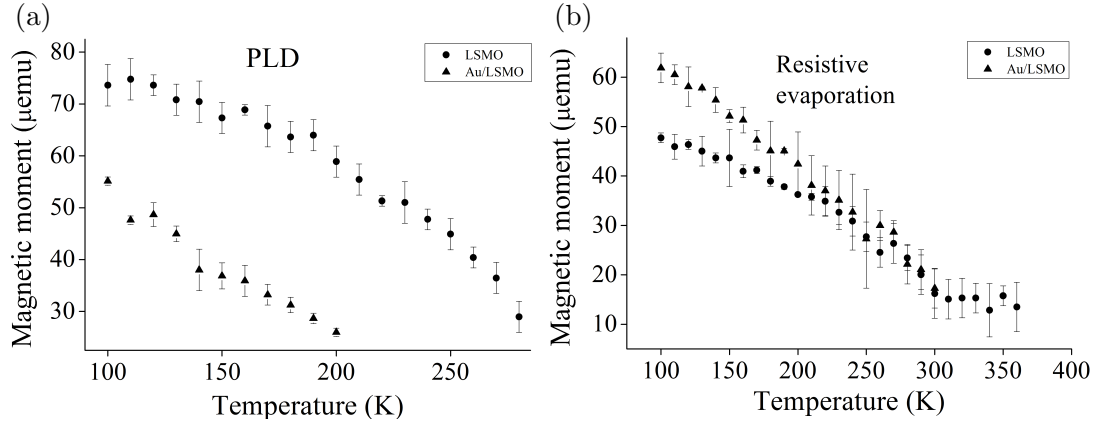


Figure 5.27: $M(T)$ for 5 nm of LSMO grown on STO (001) measured before (dots) and after (triangles) depositing a Au capping layer (10 nm) using (a) PLD at room temperature at a base pressure of 1.95×10^{-6} mbar (sample #23275a), and (b) resistive evaporation (sample #23275b). The error bars were added individually to the measurements at each temperature, because the magnitude of the noise depends on temperature stability. The error bars were calculated considering the deviation of magnetic moment from the average magnetisation at each field.

5.5 Conclusions

The magnetic anisotropy and the reversal mechanisms are summarised in Table 5.1.

The $(110)_{\text{pc}}$ -oriented LSMO films have stronger uniaxial anisotropy than the $(001)_{\text{pc}}$ -oriented LSMO, as shown by the larger K_u at both 150 K and RT.

The magnetisation-reversal mechanism in all LSMO films is nucleation-propagation near the easy axis, which can be modelled with the Kondorsky model. Coherent-rotation is seen near the hard axis, and can be modelled by the Stoner-Wohlfarth model. The range of angles within which nucleation-propagation dominates is larger at RT than 150 K and this can be explained by the larger H_K/H_c ratio at RT.

For LSMO $(001)_{\text{pc}}$ on NGO (001) , domain propagation experiences pinning from domain walls. Therefore, magnetisation reversal is propagation limited. The degree of pinning reduces at RT, shown as the sharper switching in both minor and recoil loops.

For LSMO $(110)_{\text{pc}}$ on NGO (100) , the reversal is nucleation limited, that is, once the domain nucleates, the propagation is quick and full magnetisation is reached through sharp switching. At low temperature, the nucleation events are very sensitive to temperature, which also explains the instability of the electrode switching in the devices (Chapter 6).

For LSMO $(110)_{\text{pc}}$ on STO (110) , the magnetisation reversal is mainly nucleation limited and the majority of the film switches sharply. However, domain propagation experiences resistance near the end of the switching event, seen as a gradual change of magnetisation at higher magnetic fields. This gradual change of magnetisation is thought to be a result of inhomogeneities introduced to the film from the thermal demagnetisation process in air. At RT, the film shows weak propagation-limited reversal.

Evaporation of the Au on the LSMO surface was found to cause less damage to the magnetisation than in situ-PLD, and so it was used for device fabrication.

5. MACROSCOPIC MAGNETIC PROPERTIES OF $\text{La}_{0.67}\text{Sr}_{0.33}\text{MnO}_3$ FILMS

	K_u (J/m ³)		K_b (J/m ³)		H_K (mT)		Easy axis		Hard axis		Reversal mechanism	
	150 K	RT	150 K	RT	150 K	RT	150 K	RT	150 K	RT	150 K	RT
(001) _{pc} LSMO on NGO (001) _{or} [124]	6500	1800	570				[010] and [100]	[010]	[100]	[100]	propagation limited	propagation limited (weak)
(110) _{pc} LSMO on NGO (100) _{or}	35000	5400			130.9 (=22 H_c)	50.8 (=150 H_c)	[010]	[010]	[001]	[001]	nucleation limited	nucleation limited
(110) _{pc} LSMO on STO (110)	43000	6500			139.7 (= 47 H_c)	50 (=100 H_c)	[010]	[010]	[001]	[001]	nucleation limited	propagation limited (weak)

Table 5.1: Table summarizing K_u , K_b , H_K , the direction of the easy and hard axes, and the reversal mechanism at 150 K and RT.

Chapter 6

Characterisation and Magneto-transport measurements of Graphene Spin-Valve Devices

This chapter describes the fabrication, characterisation and electrical measurements of the graphene spin-valves. The LSMO electrodes were prepared on three types of substrates, NGO (001), NGO (100) and STO (110), using ultraviolet (UV) photolithography. The patterning used masks designed by Lee C. Phillips. The fabrication process was modified as the project proceeded. Very clean electrodes with surface atomic terraces have been fabricated, by using a protective layer of Au, by replacing the milled LSMO between electrodes with amorphous material deposited from the NGO target by PLD in a vacuum and at room temperature (PLD back-filling), and by post-annealing the patterned electrodes in oxygen. The graphene transfer was carried out mainly by Matteo Barbone and some by Antonio Lombardo under the supervision of Andrea C. Ferrari in the Nanomaterials and Spectroscopy Group at the Department of Engineering in Cambridge. Matteo Barbone modified the transfer process (section 6.1.2), which resulted in significantly lower device resistance. This is crucial for achieving successful spin injection. In a collaborative work with Sarnjeet S. Dhesi at Diamond Light Source, working together as a team with Lee C. Phillips, Massimo Ghidini, Xavier Moya and Francesco Maccherozzi, we imaged the surface magnetisation of the electrodes using PEEM with XMCD contrast. This work shows that the electrodes prepared on NGO (100) and STO (110) substrates are much better than electrodes on NGO (001), and they switch sharply and have very well defined parallel and anti-parallel states at remanence. Magneto-optic Kerr effect magnetometry (MOKE) measurements on the electrodes were

6. CHARACTERISATION AND MAGNETO-TRANSPORT MEASUREMENTS OF GRAPHENE SPIN-VALVE DEVICES

carried out by Sampo Hämäläinen under the supervision of Sebastiaan van Dijken at Aalto University, Finland. The patterned electrodes have the easy axis across the length of the electrodes, as expected, due to the large uniaxial anisotropy of LSMO on NGO (100) and STO (110) (see Chapter 5 and references [105, 126]). The electrical transport measurement were carried out by me alone using the measurement set-up established by Lee C. Phillips. $MR = 5.5\% (\Delta R = 1.5 \text{ M}\Omega)$ was measured on a device with approximately 10-layer graphene, and LSMO electrodes on STO (110), which leads to an estimated spin diffusion length of about $70 \mu\text{m}$.

6.1 Device fabrication

6.1.1 Photolithography

Before photolithography, a 10 nm-thick Au was evaporated on to the surface of the LSMO film in a resistance evaporator (BOC Edwards Auto 306) in order to protect the film surface from photoresist contamination. The chamber was cryo-pumped for 1 hour with liquid nitrogen to a base pressure of 10^{-6} mbar . The growth rate was 0.5 \AA/s at 3.6 A. During the evaporation, the temperature in the chamber increased gradually and reaches about 60°C at the end of a 10 nm deposition. Evaporation was used in preference to in-situ Au deposition by the PLD, because high-energy species arriving at the sample surface can damage the surface magnetic properties of the film. Photoresist (AZ5214) was spin coated onto the film at 6000 rpm over 30 s, and baked at 115°C for 60 s as optimised from the previous users. The electrodes were patterned using the UV photolithography, with masks designed by Lee Phillips shown in Figure 6.1 [146].

Two masks were used, mask ‘b’ with a straight lead from each electrode to its contact pad (Figure 6.1a) and mask ‘b+’ with a ‘U’ turn along the lead (Figure 6.1b). The purpose of the ‘U’ turn was to filter out less favorable domains that may propagate from the contact pads. Operating the mask aligner (Karl Suss MJB3) in contact mode, the film was brought into contact with the mask. The first exposure to UV light was to remove the thicker photoresist along the edges of the film (edge beads) and define an area with uniform resist thickness for the device patterning. The first exposure time was typically 70 s, but varied slightly depending on the sample. For example, a slightly longer exposure time was used when working with a sample that has residual photoresist from previous lithography attempts. Once exposed, the pattern was developed using the

solution AZ351B (an aqueous solution of $\text{Na(OH)}_{\text{aq}}$). The typical developing time for the edge beads was 60 s. After developing, the sample was washed in de-ionised water and dried. The second exposure defined the electrodes, with 5 s of UV and 40 s in the developer. While developing, the photoresist gets thinner, and the interference pattern changes and completely disappears when completely developed. This interference effect was used as a reference for fine adjustment of the developing time.

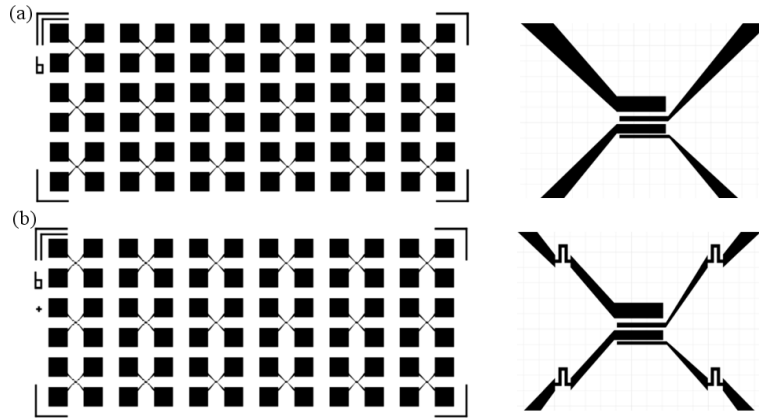


Figure 6.1: The lithography mask designs used for patterning the electrodes. In each device, detailed in the right, the width of the four electrodes from bottom to top is 2, 6, 3 and 10 μm , and the gaps are 1, 2 and 3 μm . (a) Mask ‘b’. (b) Mask ‘b+’, where a ‘U’ turn is introduced between the electrodes and the square contact pads.

The patterned sample was then placed in the Ar ion-miller, which was rotated for homogeneous milling rate and water-cooled to avoid over-heating of the sample. Either one of two millers (SIMS miller and Whizzy miller) was used, depending on the availability. The base pressure before milling was 2×10^{-6} mbar and the milling pressure was $\sim 3 \times 10^{-4}$ mbar with Ar 2 % O₂ gas mixture. The milling parameter used were beam voltage 500 V, beam current 15 mA, and acceleration voltage 100 V. 500 V beam voltage was found to produce much cleaner electrodes than 1000 V, possibly due to sample heating or photoresist hardening when using the higher beam voltage. During the milling process, the Ar ions were accelerated towards the sample. The area of the film that is not covered by the photoresist was milled away, although the thick photoresist was partially milled away as well. Because the LSMO mills slowly, milling time was controlled to be as short as possible so that there was enough photoresist left to protect the LSMO film surface. The idea was to stop milling just reaching the substrate, but in

6. CHARACTERISATION AND MAGNETO-TRANSPORT MEASUREMENTS OF GRAPHENE SPIN-VALVE DEVICES

practice, this is hardly achieved despite performing calibration run just before sample patterning. Therefore, to check the milling depth, a reference sample was placed next to the sample. The sample is slightly over-milled to ensure there is no thin photoresist bridge the electrodes.

After patterning, the sample was either annealed at the same condition as that was used in the post annealing step during the film deposition, which was 55 kPa of oxygen at 750°C for one hour, or back-filled with amorphous NGO from the target in the PLD chamber and then annealed.

Back filling in the PLD from the NGO target was carried out at room temperature in a roughly pumped chamber with $P \approx 0$ Pa. The deposition uses fluence $\sim 2.3 \text{ Jcm}^{-2}$ at 1Hz, which gives a deposition rate of 5 nm per minute. It has advantages over the commonly used silica back-filling by sputtering. PLD is more directional and the deposition rate is more consistent than sputtering. However, it is still very difficult to perfectly fill up the gaps to the same level as the electrodes. Figure 6.2a shows the AFM scan of the electrodes back-filled using the PLD. The edges of the electrodes are flat, and hence the curvature for graphene on top is smaller.

Oxygen annealing not only improved the surface cleanliness of the sample, in terms of the recovered atomic terraces on the surface of the electrodes (Figure 6.2b), it also re-oxygenated the sample in case of deoxygenation during the lithography. A sign of deoxygenation was that the transparent STO substrate appeared black after Ar-ion milling, and becoming transparent again after high temperature oxygen annealing.

Oxygen annealing of the electrodes on STO (110) is very important because the argon ion milled STO substrate is conducting. After oxygen annealing, the STO becomes insulating. A reference sample on the STO (110) substrate consisting just the patterned electrodes and no graphene was measured to show there is no conduction path through the STO substrate (Figure 6.3).

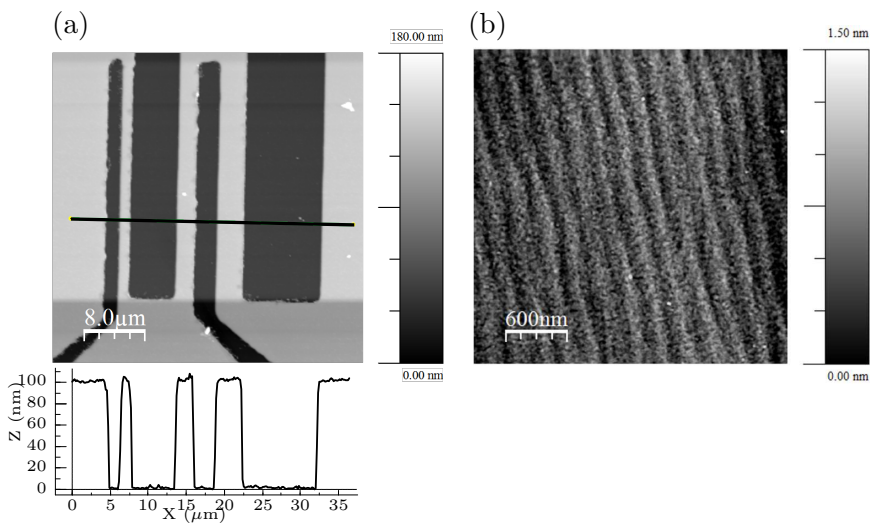


Figure 6.2: AFM images showing the topography of the device after back-filling from the NGO target and oxygen annealing. (a) AFM topography of the electrodes of device #23419 2b. (b) AFM image taken on an electrode of device #23545 1b, which shows the recovered step terraces on the surface of the electrode.

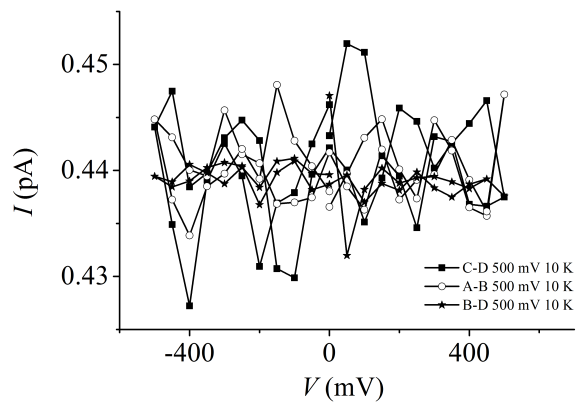


Figure 6.3: I-V curve measured on the reference electrodes on STO (110), which shows the substrate is insulating after oxygen annealing. Measurement taken on sample #23408b.

6. CHARACTERISATION AND MAGNETO-TRANSPORT MEASUREMENTS OF GRAPHENE SPIN-VALVE DEVICES

6.1.2 Graphene transfer

Once the electrodes were defined, the graphene was exfoliated and transferred onto them by Matteo Barbone and Antonio Lombardo. A mixture of graphene, multilayer graphene and graphite were obtained from micromechanical cleavage of highly oriented pyrolytic graphite (HOPG) (Graphenium) using silicon dicing tape (Ultron LMT). These flakes were then transferred on to a 300 nm-thick coating of SiO₂ on Si. Graphene on SiO₂ can be identified in optical microscopy because its existence modulated the interference of light on the SiO₂ layer and hence it appeared different in colour to the substrate. The number of layers of graphene was identified through a combination of optical contrast analysis, profile fitting to its Raman spectrum [164] and AFM. Once identified, the graphene was transferred on to the electrodes by wet transfer in isopropanol (IPA), wet transfer in an ethanol-water mixture, or dry transfer.

The wet transfer mainly followed the recipe of Reina *et al.* with some modifications (Figure 6.4) [165].

- A sacrificial Poly(methyl methacrylate) (PMMA) layer was spin coated onto the graphene/SiO₂/Si stack. It was then baked in air at 120°.
- In reference [165], PMMA/graphene was then detached from the substrate either by etching away the SiO₂ layer in NaOH at 90° or simply soaking in water. In this dissertation, isopropanol (IPA) was used for the transfer instead of water and there is no heating involved in this process. IPA has lower surface tension and hence there is less strain on the graphene while the solvent is drying off. This process was later modified by using an ethanol-water mixture. Ethanol is a smaller molecule than the IPA molecule and therefore has lower boiling point, so trapped ethanol at the interface is more easily removed than IPA or water. Water was added to ethanol to reduce the volatility to the point the flake can be handled during alignment.
- To place graphene deterministically on top of the electrodes, the electrodes were brought up against the PMMA/graphene, which was still floating on the liquid surface, and careful alignment was achieved under the optical microscope.
- PMMA was then washed away by carefully releasing acetone onto the top of the device. As shown in section 6.2.2, there was always some residual PMMA on the graphene in the finished device.

6.1 Device fabrication

The chip with the finished device was then pumped in high vacuum (10^{-7} mbar) in order to remove any trapped solvent.

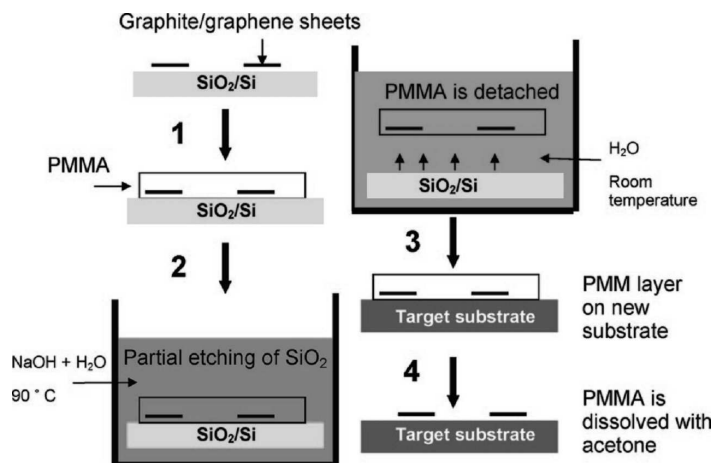


Figure 6.4: Figure showing the method for graphene transfer in solution adopted from Reina *et al.* [165]

The dry transfer process followed the procedure established by Hunt *et al.* [166,167]. Instead of exfoliating graphene onto a glass slide, it was exfoliated on to a ‘glass/tape/polymer release layer’ stack. The tape was a transparent scotch tape (by Sellotape), which was used to decrease the adhesion of the polymer release layer to the glass and allowing low temperature release. The polymer release layer is either low-molecular-weight Poly(methyl methacrylate) (lwPMMA) or methyl/n-butyl methacrylate copolymer (Elvacite) (Figure 6.5a). The structure was flipped so that the graphene faced the electrodes. It was then carefully aligned with the electrodes on a heated stage using a micromanipulator (Figure 6.5b). Once aligned, the substrate was heated to 130°C, in order to melt the lwPMMA (70°C for Elvacite) and release the graphene. Residual polymer was then dissolved away using acetone, and the sample was left at high vacuum prior to the measurement.

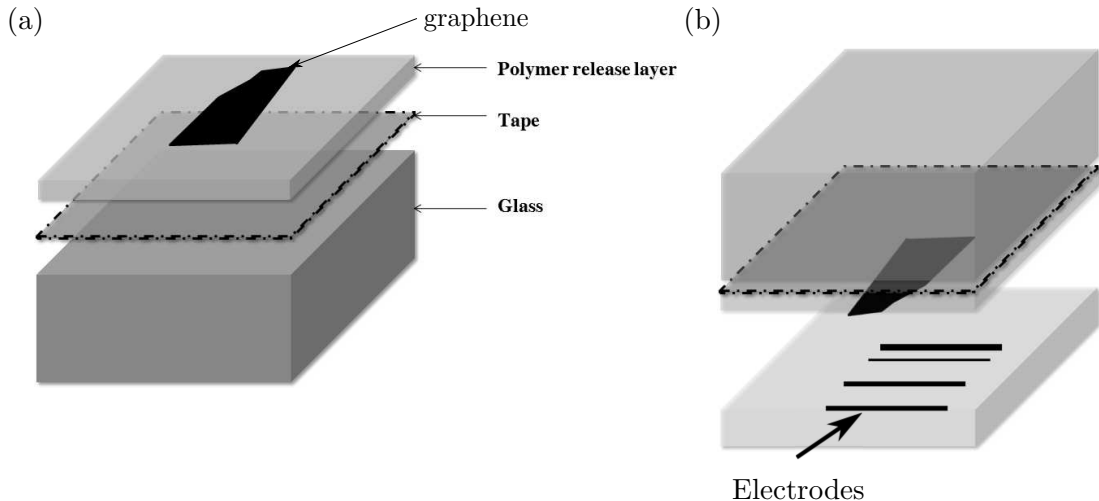


Figure 6.5: Schematic shows the dry transfer method adopted from Hunt *et al.*. See the text for description [166, 167].

6.2 Device characterisations

6.2.1 Raman spectrometry

Raman spectrometry measurements on (multilayer) graphene were carried out primarily by Matteo Barbone, and also by Antonio Lombardo, using pristine flakes before the transfer, and over the electrodes after transfer. The measurements were taken using a Renishaw spectrometer at 514 nm, and beam power below 1 mW at room temperature. Details of the measurement is as reported in reference [164]. The spectra of the \sim 10-layer (determined from AFM) graphene flake are shown in Figure 6.6. The G peak at \sim 1584 cm $^{-1}$ is associated with the stretching of bonds between the sp 2 atoms in the rings and along the chain, and the shape of the peak does not evolve with the number of layers. After transfer, the G peak is not visible in the large background of SrTiO₃ (dotted line). The 2D peak at 2702 cm $^{-1}$ is related to the breathing mode of the hexagonal rings of sp 2 carbon atoms. It is absent in pristine graphene, where there is structural symmetry, and it is activated by the structural defects. Profile fitting to the 2D peak suggests that there is 5 layers of graphene in the flake.

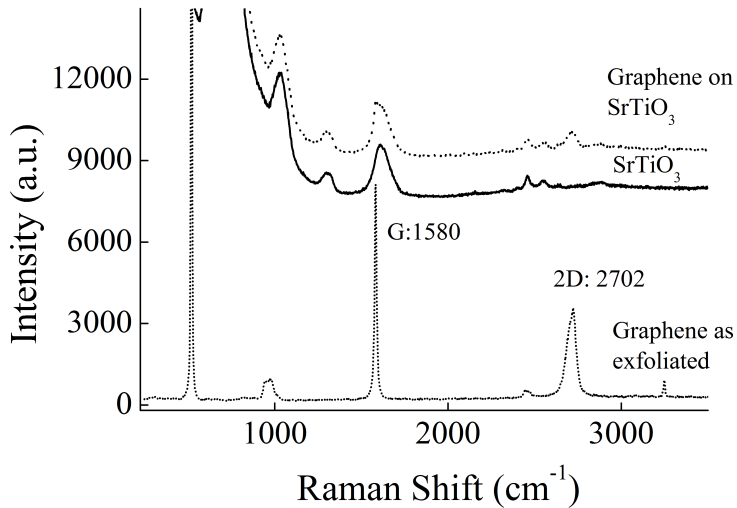


Figure 6.6: Raman spectra of the multilayer graphene as prepared on SiO₂ coated Si substrate (short-dotted line), on the electrodes (dotted line). The spectrum of STO is represented by the solid line. Measurements taken on the flake and device used to show 5.5% MR, i.e. sample #23481.

6.2.2 Atomic force microscopy

Here the topography of the devices prepared using the different methods is compared.

Wet transfer in IPA

AFM images of the devices were taken after the transport measurements using Tapping Mode. Tapping Mode AFM in general will not damage graphene, but the device is delicate mechanically and very sensitive to static charge. To avoid any likely damage to the device, AFM, conducting tip AFM and MOKE measurements on the device were only carried out after transport measurement. Figures 6.7 and 6.8 show two devices both transferred in IPA, while the graphene in device #22988a1 (Figures 6.7) is a single-layer while that in #23199b (Figure 6.8) is a bilayer. The visibility of the SLG in Figure 6.7a is very low and there are no visible wrinkles. The identification of its position is easier when combined with the optical image shown in Figure 6.7b. There are clearly some polymer residuals left from the transfer (Figure 6.7a, inside the rectangle). The ringed feature in Figure 6.7a could either be aggregated polymer residual or trapped solvent underneath the residual polymers.

6. CHARACTERISATION AND MAGNETO-TRANSPORT MEASUREMENTS OF GRAPHENE SPIN-VALVE DEVICES

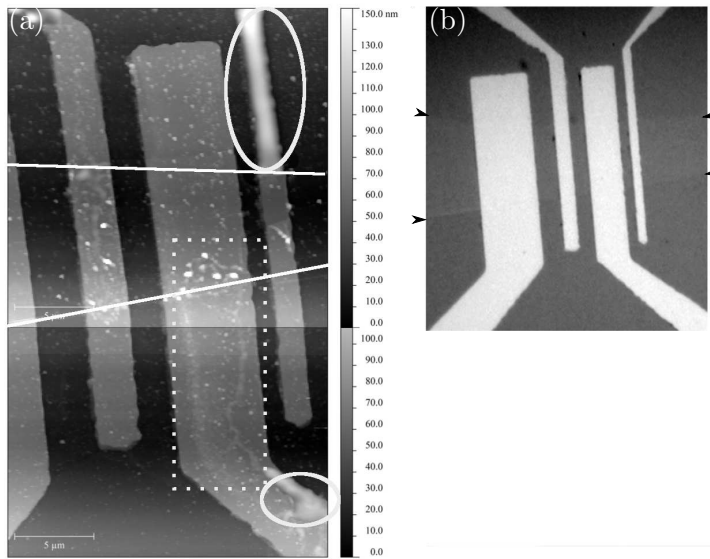


Figure 6.7: (a) AFM image of device #22988a1, with graphene positioned by wet transfer in IPA, taken after transport measurements. (b) Optical image where graphene shows contrast on the substrate.

The bilayer graphene, which is decorated with lots of wrinkles and possibly has more polymer residual than the device #22988a1, can be seen more easily (Figure 6.8). Figure 6.8b-e show the phase-contrast images in smaller area scans on each electrode. The topography or phase contrast images are similar for all four electrodes A-D, suggesting similar interfacial properties, but A, B and C are electrically connected and D is electrically disconnected.

6.2 Device characterisations

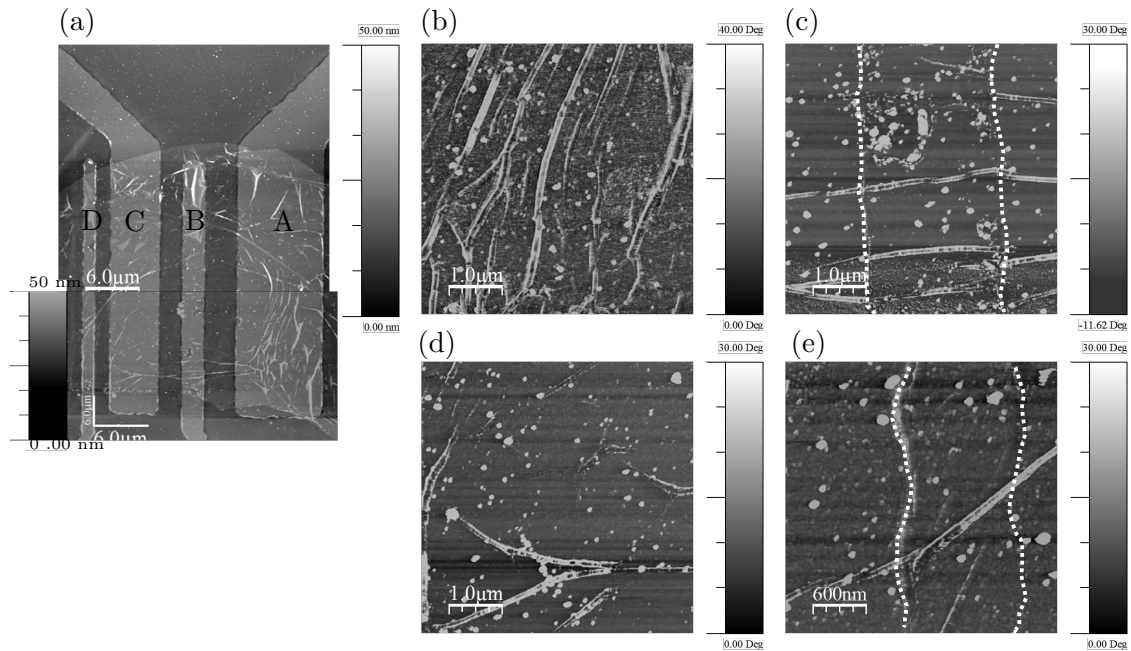


Figure 6.8: (a) AFM topography of device #23199 transferred in IPA. (b,c,d,e) Phase contrast images sampling electrodes A, B, C and D respectively. Dashed lines in (c) and (e) are the traces of the edge of the electrodes.

Conducting-tip AFM measurements (CTAFM) were also performed on the widest electrode, electrode A of device #23199b. Figure 6.9a shows the topography, and panels b,c show the trace and retrace of the measured current. Contact homogeneity may not be as good as the CTAFM data suggest, as injected current can spread very fast in graphene. Therefore even if the conduction is through a point contact, CTAFM cannot necessarily resolve it. The fact that there is no sharp change in electrical conductivity shows that the electrical conduction is not affected by the graphene curvature at the edges of the electrodes. Wrinkles do not seem to have much effect on conductivity either, because where there is wrinkles in Figure 6.9a, the measured current is larger in Figure 6.9b,c. This is an artefact in CTAFM. When the tip scans the graphene wrinkle, the contact area between the tip and the graphene increases and gives higher current. There are patches with high resistance (ringed in the images), which could either be due to contamination on the surface, at the interface or damage to the graphene.

6. CHARACTERISATION AND MAGNETO-TRANSPORT MEASUREMENTS OF GRAPHENE SPIN-VALVE DEVICES

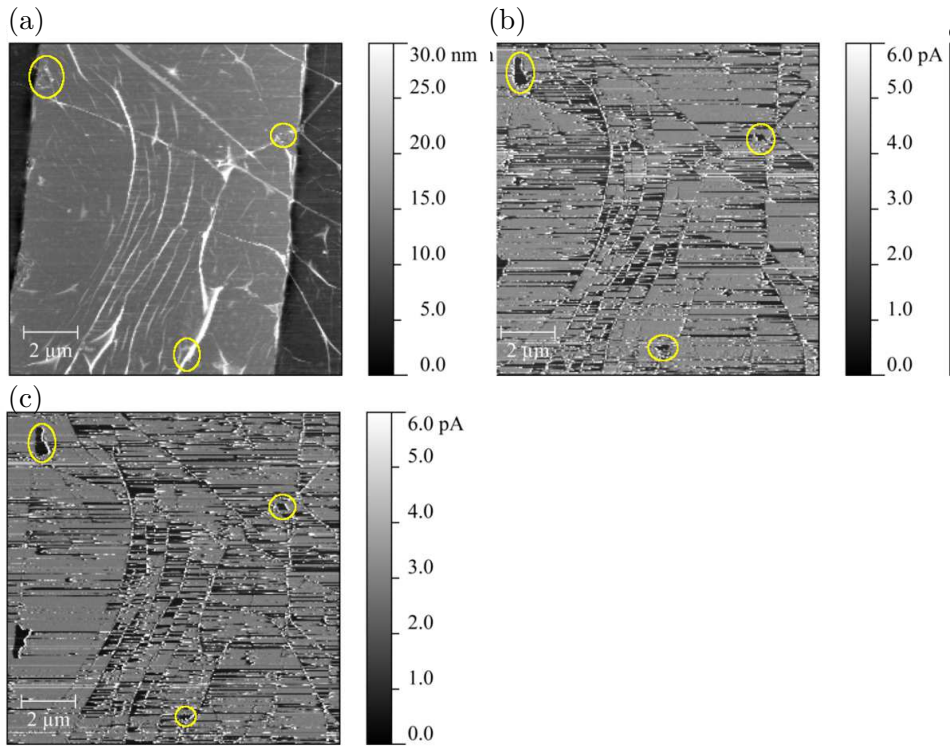


Figure 6.9: (a) Topography obtained from CTAFM measurement of electrode A in device #23199b comprising bilayer graphene. (b,c) Current contrast in the trace and retrace scans, respectively at 600 mV bias. Ringed areas are highly resistive.

Wet transfer in an ethanol-water mixture

Devices transferred in ethanol-water mixture appear to produce cleaner samples. Out of the two devices transferred in ethanol, one showed 5.5% MR in the transport measurement (Device #23481 2a, Figure 6.28), which is the highest MR seen among all the transfer methods. Figure 6.10 shows topographical and the phase contrast image for device #23481 2a. When comparing #23481 2a with other devices, it is clear that both the electrodes and the graphite flake are much cleaner. The thickness of the flake is ~ 3.5 nm (insert to Figure 6.10). Theoretically, the thickness of single layer graphene is 0.345 nm. However, ranges of thickness have been measured (0.35-1 nm) by AFM due to contamination [168]. Therefore, AFM on its own does not give reliable result for the number of layers of graphene. Profile fitting to the Raman 2D peak suggests there are five layers of graphene. Figure 6.11 shows AFM images of the other two devices transferred in the ethanol-water mixture. Both have thinner graphene than #23481 2a.

6.2 Device characterisations

Sample #23482c has a trilayer graphene and #23482d has a bilayer graphene, but neither showed MR.

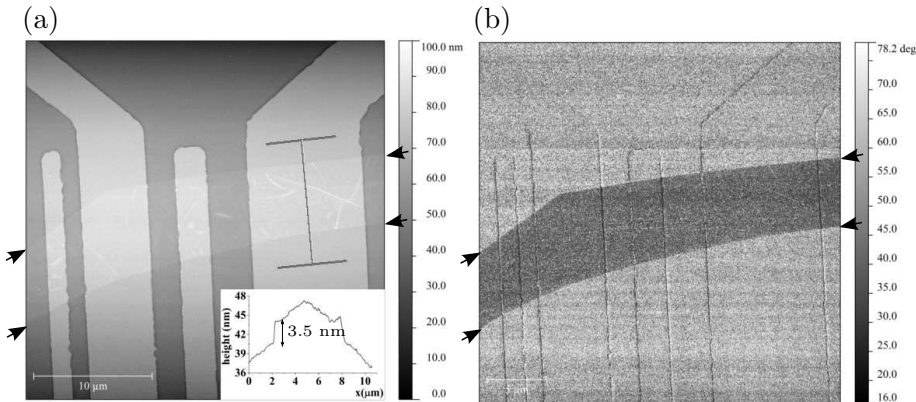


Figure 6.10: (a) AFM topography of device #23481 2a transferred in the ethanol-water mixture. Inset shows cross-sectional profile taken along the bar in the main image. (b) Phase contrast image. The arrows in the images are guides for identification of the flake.

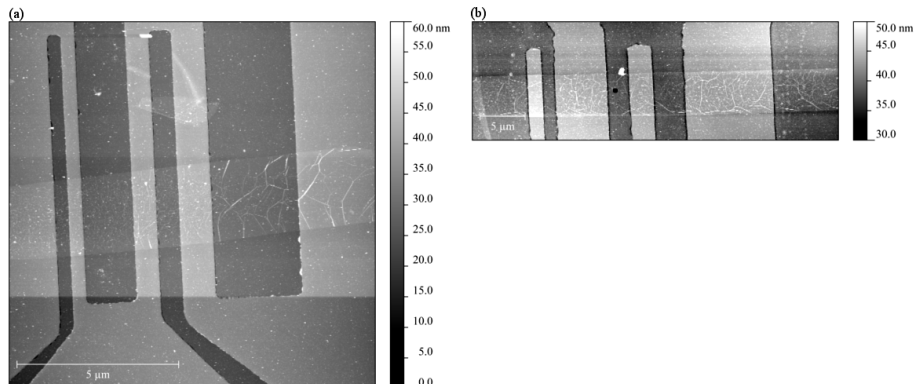


Figure 6.11: AFM topography of (a) device #23482c, which has trilayer graphene, and (b) device #23482d, which has bilayer graphene. Both devices were transferred in the ethanol-water mixture.

Dry transfer

Compared to the wet transfer, dry transfer is less established and still in the process of modification. Initially, low-temperature PMMA was used as the polymer release layer. It was heated to 130°C to release the graphene. Because of the high-temperature treatment, a large quantity of residuals were left after melting and dissolving. These can be seen as fine

6. CHARACTERISATION AND MAGNETO-TRANSPORT MEASUREMENTS OF GRAPHENE SPIN-VALVE DEVICES

lines in Figure 6.12b. In device #23488d (Figure 6.12c), there are trapped gas bubbles, presumably due to heating. Heating should be avoided, or minimised to preserve the surface magnetic properties of the LSMO electrodes. In later experiments, IwPMMA is replaced with Elvacite, which has a lower glass transition temperature (T_g), and therefore allows the transfer to be performed at lower temperatures (65~70°C).

The above topography studies using AFM suggests graphene transfer in the ethanol-water mixture gives the cleanest device, which is critical for successful spin injection into the channel.

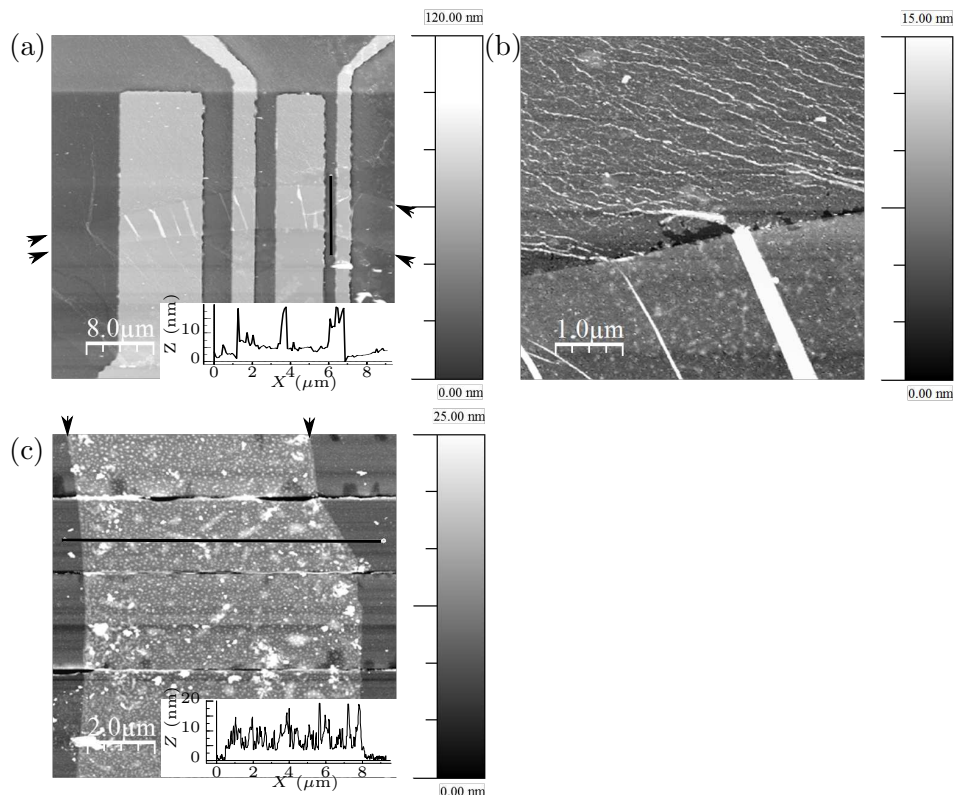


Figure 6.12: AFM topography of (a) device #23488b made by dry transfer using IwPMMA scaffolding. Inset to (a) is a cross-sectional profile taken along the bar in the main image. The flake is ~ 7 nm thick. (b) small-area scan of electrode A, where polymer residuals show up as fine lines. (c) device #23488d. Inset to (c) is a cross-sectional profile taken along the bar in the main image. The flake is 5 nm thick. Bubbles trapped at the interface are visible in the image and the height profile.

6.3 Magnetic properties of the LSMO electrodes

6.3.1 XMCD-PEEM images

Using PEEM with XMCD contrast (see Chapter 4), the surface magnetisation of the LSMO electrodes on NGO (001), NGO (100) and STO (110), was imaged at remanence after magnetic field pulses, at the \sim 150 K base temperature of the system, which was cooled with liquid nitrogen. For electrodes on NGO (001), before exposure to a magnetic field¹, there are alternating arrays of domains with opposite magnetisations along the length of each electrode (Figure 6.13a). The magnetisation in each domain lies along the easy axis of the film. The domain sizes are smaller in thinner electrodes due to the larger demagnetisation field. On applying a large magnetic field along the easy axis, all four electrodes are uniformly magnetised, and the subsequent remanent state comprises a single domain, with magnetisation parallel (white) or antiparallel (black) to the beam direction (Figure 6.13b,f). The XMCD asymmetry of the electrode after fully magnetised is \simeq 10%. However, one cannot tell if the remanent magnetisation M_r equals the saturation magnetisation M_s , because it is not possible to image with the magnetic field on. When cycling the applied magnetic field, the electrodes switched by nucleation-propagation. During magnetisation reversal, there is strong pinning to prevent domain propagation, which results in alternating domains of opposite magnetisation along the length of each electrode. The size of the domains varies from sub-micron to hundreds of microns (Figure 6.13c-e,g-i).

¹The so-called ‘virgin state’ may not be a true virgin state, because the sample may experience stray magnetic fields during fabrication.

6. CHARACTERISATION AND MAGNETO-TRANSPORT MEASUREMENTS OF GRAPHENE SPIN-VALVE DEVICES

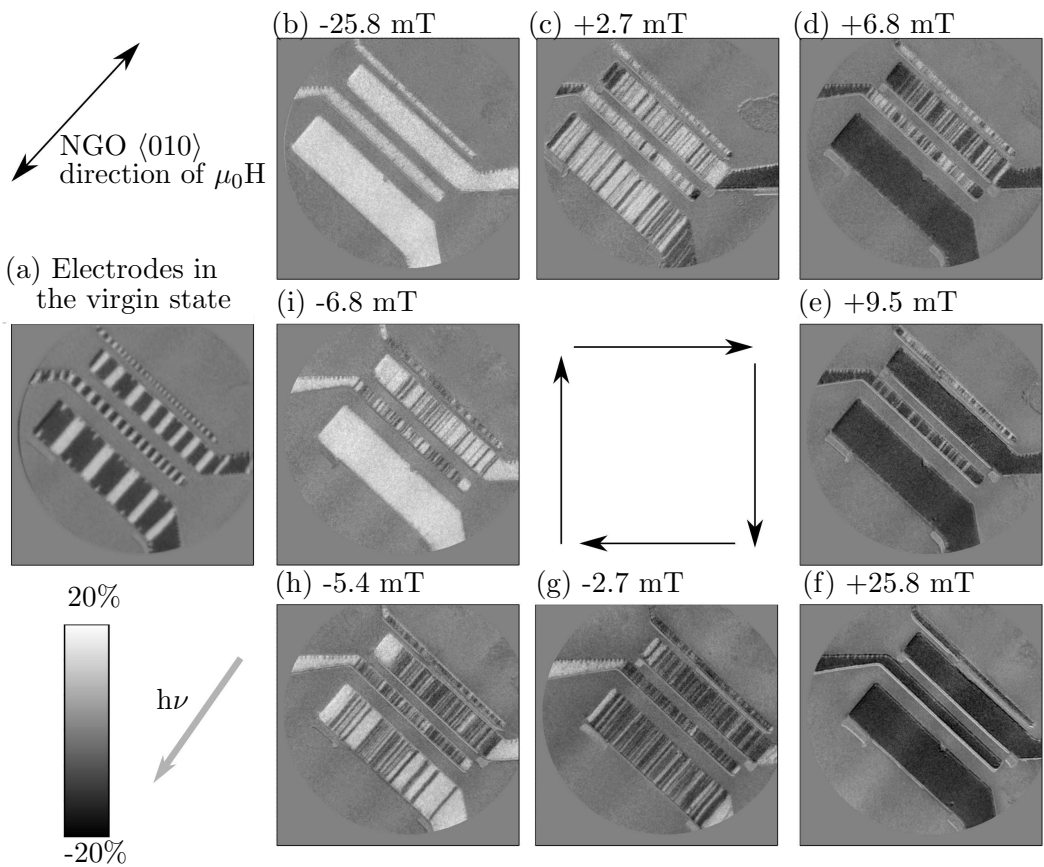


Figure 6.13: PEEM-XMCD images of the patterned LSMO electrodes on a NGO (001) substrate (sample #23284s2). The magnetic field $\mu_0 H$ was applied along the $\langle 010 \rangle$ axis of the substrate. The in-plane projection of the X-ray beam aligns roughly along the magnetic easy axis. Images were taken after removing the field. Field of view (FOV) is 50 μm . (a) The domain structure of the electrodes in the virgin state. (b-i) Remanent magnetisation of the electrodes measured in a repeatable magnetic-field cycle after applying various magnetic field.

6.3 Magnetic properties of the LSMO electrodes

Electrodes on NGO (100) switch sharply. The switching of electrodes A and B seems to be coupled. This might due to incomplete milling of LSMO films in some area between the two electrodes. The XMCD asymmetry of the electrode after fully magnetised is $\simeq 20\%$.

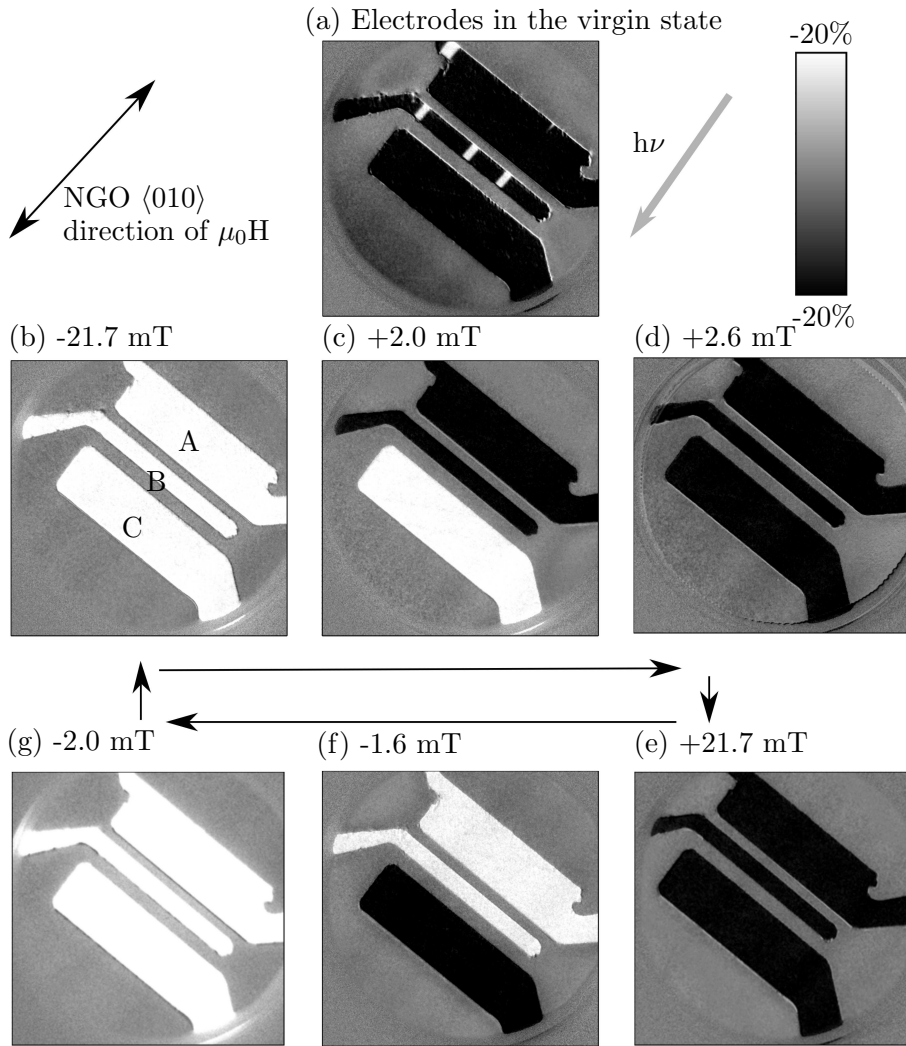


Figure 6.14: PEEM-XMCD images of the patterned LSMO electrodes on a NGO (100) substrate (sample #23288s1). (a) The domain structure of the electrodes in its virgin state. (b-f) Remanence magnetisation state of the electrodes measured in a magnetic field cycle. The direction of magnetic field and X-ray beam are shown in inset. FOV is 50 μm .

6. CHARACTERISATION AND MAGNETO-TRANSPORT MEASUREMENTS OF GRAPHENE SPIN-VALVE DEVICES

The virgin state in electrodes on STO (110) appears different to that on the NGO (001) substrate (Figure 6.15a), possibly due to the magnetic field effect in the environment. The electrodes switch sharply and independently of each other (Figure 6.15). The switching mechanism is nucleation-probation as it is on the NGO (001) substrate. However the effect of pinning on domain propagation is weaker and the remanent states composes of single domains. The XMCD asymmetry is $\simeq 20\%$.

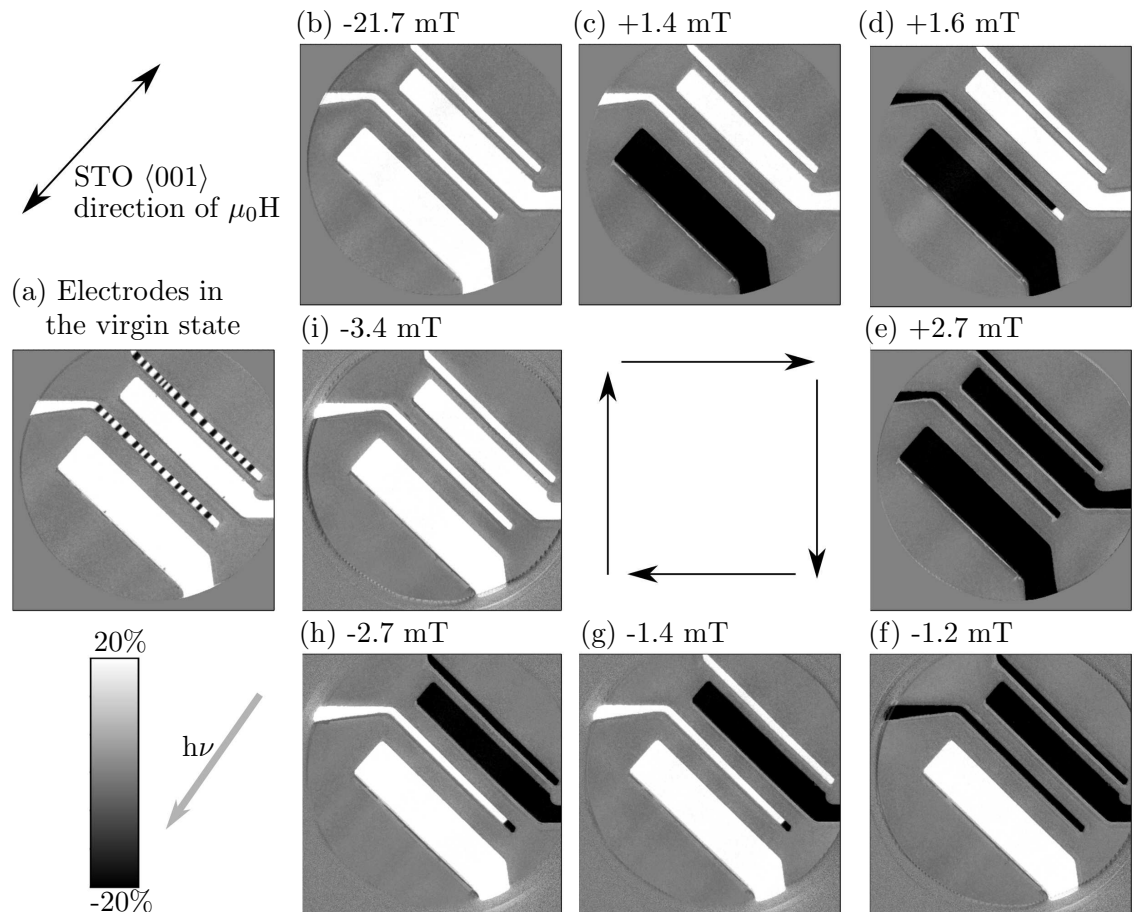


Figure 6.15: PEEM-XMCD images of patterned LSMO electrodes on a STO (110) substrate (sample #23293s1). (a) The domain structure of the electrodes in its virgin state. (b-i) Remanent magnetisation state of the electrodes measured in a magnetic field cycle. The direction of magnetic field and X-ray beam is shown in inset. FOV is 50 μm .

6.3 Magnetic properties of the LSMO electrodes

6.3.2 MOKE measurements

For electrodes that switch cleanly, LSMO on STO (110) substrate (Figure 6.15) and NGO (100) (Figure 6.14), MOKE was used to investigate the switching while sweeping the magnetic field. The magnetic field was applied perpendicular to the length of the electrodes, that is along the easy axis. The $M(H)$ of the electrodes from the working device (#23481) was measured at 5 K, which is inaccessible with PEEM at Diamond Light Source. At room temperature, electrodes could be sampled individually. At low temperature, sometimes, it was only possible to measure all four electrodes together as the resolution was reduced.

For electrodes on STO (110), the switching shows clear easy-axis square hysteresis loops at all measurement temperatures, which are room temperature (Figure 6.16), \sim 100 K (Figure 6.17) and 10 K (Figure 6.18). The measurements on electrode B and D are noiser due to the thin width of the electrodes (Figure 6.16b,d). The switching at \sim 90 K has similar clear square easy axis hysteresis loop but with larger coercivity than at room temperature (Figure 6.17).

6. CHARACTERISATION AND MAGNETO-TRANSPORT MEASUREMENTS OF GRAPHENE SPIN-VALVE DEVICES

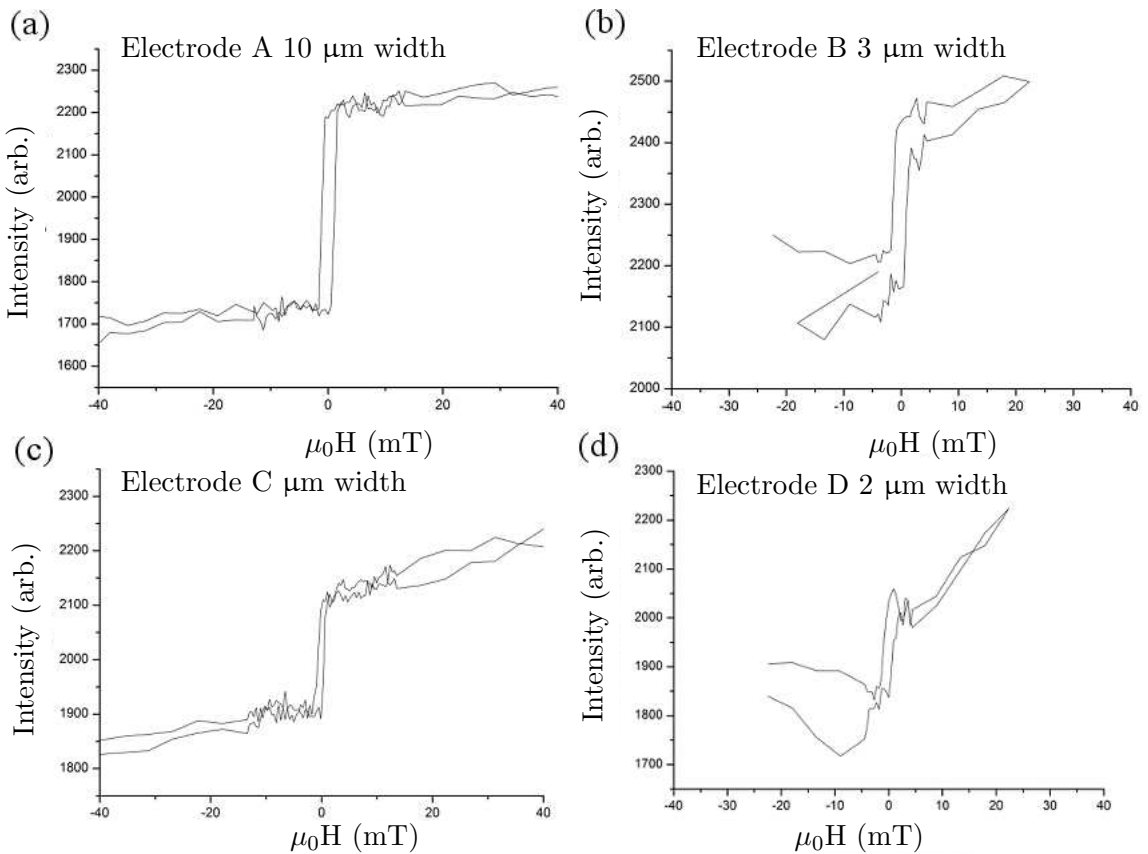


Figure 6.16: MOKE measurement along the easy axis of device #23293s1 at room temperature. (a), (b), (c) and (d) are the hysteresis loops measured on electrodes A (10 μm width), B (3 μm width), C (6 μm width) and D (2 μm width) respectively at room temperature.

6.3 Magnetic properties of the LSMO electrodes

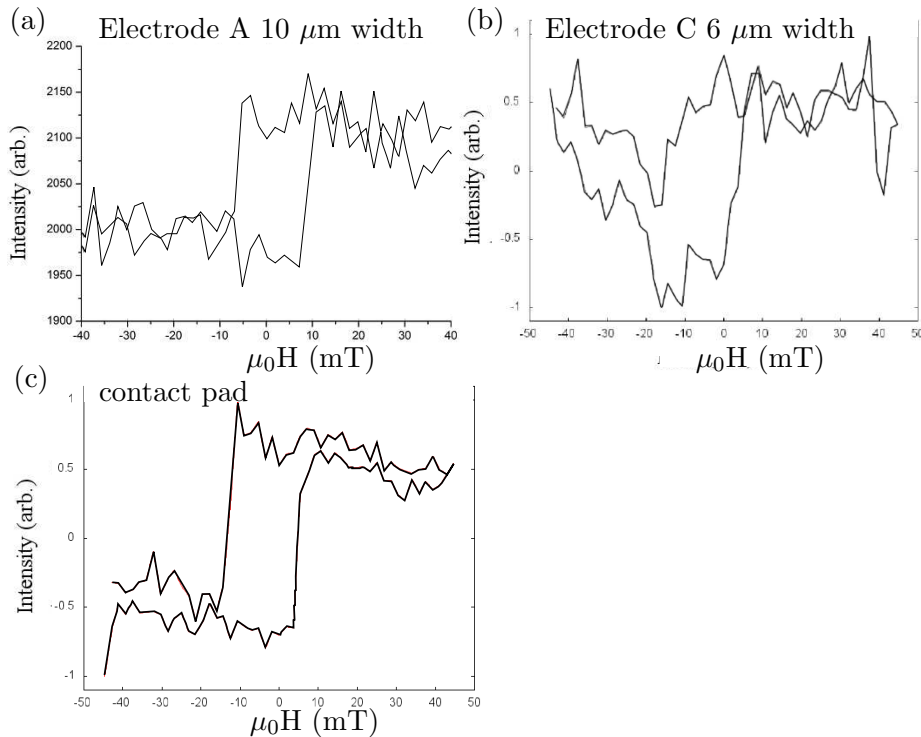


Figure 6.17: MOKE measurements along the easy axis of device #23293s1 on STO (110) at low temperature. (a) and (c) are hysteresis loops measured on electrodes A and C respectively at 90 K. The field of view is $\sim 420 \times 300 \mu\text{m}$. (c) Hysteresis loop measured on a contact pad at 86 K.

The hysteresis loops of the electrodes were also measured at the transport measurement temperature, that is 10 K. Both the contact pad and the electrodes has strong uniaxial anisotropy, which is proven by the clear square hysteresis loops along the easy axis and no signal along the hard axis (Figure 6.18). A single sweep is presented in Figure 6.18a, because the electrode switches by nucleation-propagation, which is sensitive to temperature fluctuations. Therefore, averaging of few sweeps would not represent the true switching process in the pad. However, averaging of many sweeps has to be taken for measurements on the single electrode, due to the high level of noise and hence results in slightly gradual switching around -10 mT in Figure 6.18b. Measurement along the hard axis showed similar linear slope that of the cryoglass, therefore the signal is close to noise level after background subtraction.

6. CHARACTERISATION AND MAGNETO-TRANSPORT MEASUREMENTS OF GRAPHENE SPIN-VALVE DEVICES

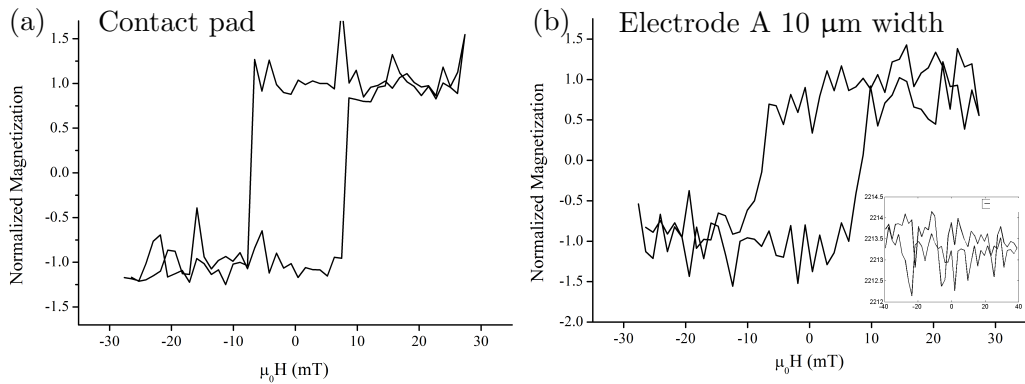


Figure 6.18: MOKE measurements along the easy axis of device #23481 on STO (110) at 10 K on (a) the contact pad (single sweep), and (b) electrode A (average of five sweeps). The inset to (b) is the measurement along the hard axis.

The switching of LSMO on NGO (100) along the easy axis shows clear square hysteresis loop at room temperature (Figure 6.19) and low temperature (Figure 6.20).

6.3 Magnetic properties of the LSMO electrodes

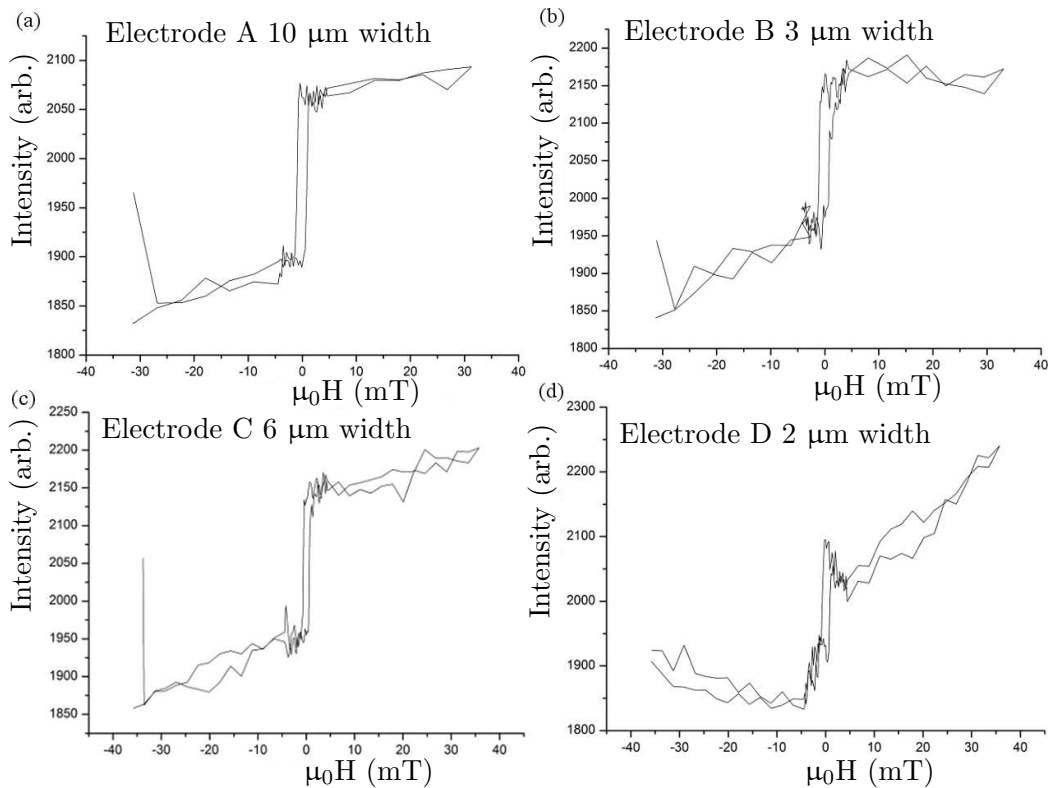


Figure 6.19: MOKE measurements of device #23288s1 on NGO (100) at room temperature. (a), (b), (c) and (d) corresponding to measurements on electrodes A, B, C and D respectively.

6. CHARACTERISATION AND MAGNETO-TRANSPORT MEASUREMENTS OF GRAPHENE SPIN-VALVE DEVICES

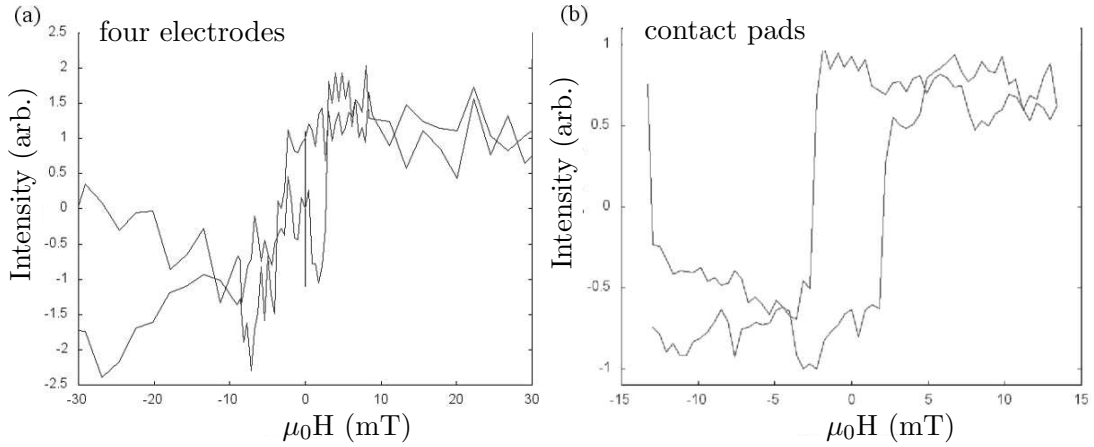


Figure 6.20: MOKE measurements of device #23288s1 on NGO (100) at low temperature. (a) Measurement for all four electrodes at 144 K. (b) Measurement for the pad at 150K.

For the two devices with clean switching, the switching field of the electrodes and contact pad is summarised in Figure 6.21 for room temperature and low temperature. The electrode switching fields do not have a strong correlation with electrode width, which further confirms the nucleation-propagation type switching seen in the XMCD-PEEM measurement (Figure 6.15 and 6.14).

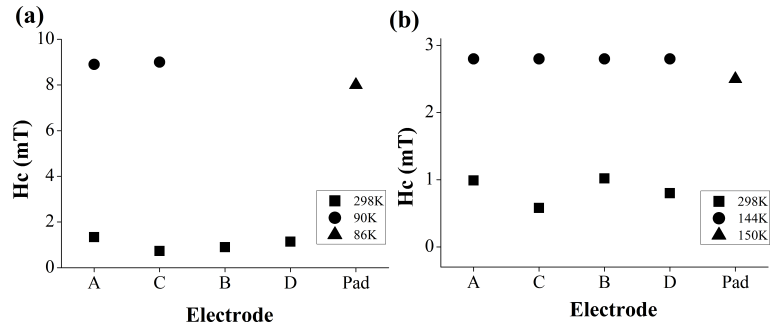


Figure 6.21: Plots showing the switching field for the individual electrode and one contact pad at room temperature, and near 100 K. X-axis labels identify the region sampled. (a) Device #23293s1 on STO (110). (b) Device #23288s1 on NGO (100). For low-temperature measurements of the electrodes, an average switching field for the four electrodes was measured.

6.4 Magneto-transport measurements

This section summarises the transport measurements results. A table describing all the devices tested is given at the end of the chapter.

Back-filling is important for increasing the device stability, because it not only provides a mechanical support to the graphene, but it also tends to reduce the amount of solvent trapped underneath the graphene. Figure 6.22 shows the optical image of device #23338a on NGO (100), which does not have the amorphous NGO back-filling, and so the depth of the trench is ~ 200 nm. The optical contrast in Figure 6.22 is probably due to the solvent trapping between the electrodes underneath the graphene. The device is not conducting as a result of this.

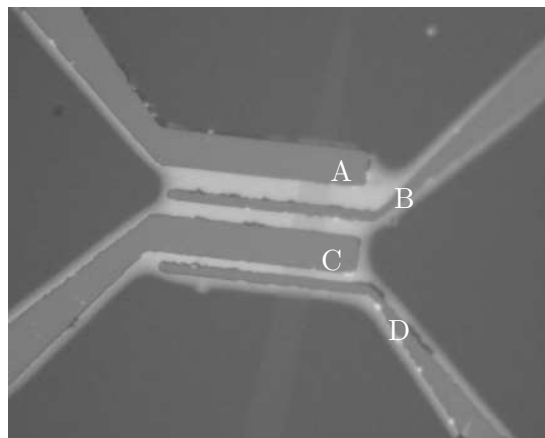


Figure 6.22: Optical image of device # 23338a on a NGO (100) substrate taken after the transfer and before electrical measurement.

6.4.1 Devices with tunnel barriers

Devices with insulating barriers, BaTiO_3 (BTO), SrTiO_3 (STO) or LaAlO_3 (LAO), have very high resistance, in the range of few hundreds of $\text{M}\Omega$ to $100 \text{ G}\Omega$. Figure 6.23 plots the $I - V$ curve and the conductance as a function of bias voltage between electrode C and D in device #22988a on NGO (001) which has BTO barrier. The device is insulating between electrode pairs A-B and B-D. Although C-D shows conducting behaviour at temperatures above 100 K, the resistance is large (4-10 $\text{G}\Omega$). The device is insulating

6. CHARACTERISATION AND MAGNETO-TRANSPORT MEASUREMENTS OF GRAPHENE SPIN-VALVE DEVICES

below 50 K where MR is expected. Above 100 K, and below 150 K, the device shows tunnelling-like conduction which turns ohmic at 180 K (Figure 6.23). Other devices that show similar weak tunnelling, and linear $I - V$ characteristics, with no MR are #22988, #23488b and #23488d (see Appendix B).

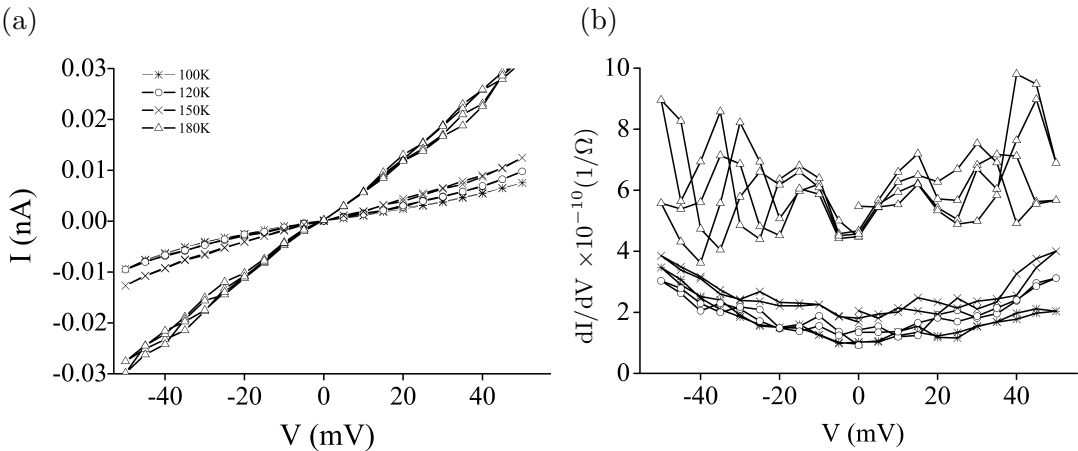


Figure 6.23: (a) $I - V$ measurement between electrode C and D in device #22988a on NGO (001) with a 2.5 Å-thick BTO barrier. (b) dI/dV versus V of the data in (a), which shows weak tunneling-like conduction below 150 K.

Figure 6.24 shows the $I - V$ characteristic of device #23063b on NGO (001), which has a 1 nm-thick STO barrier. The resistance of this device is about $500 \text{ M}\Omega$. As the bias was increased from 200 mV to 400 mV, the shape of the $I - V$ curves changed from almost linear at 200 mV to a diode-like asymmetrical $I - V$ at 400 mV (Figure 6.24a). The sharp increase in conductivity at high bias and the asymmetry seen in Figure 6.24a might be related to burning or the aggregation of interfacial residuals as a result of Joule heating. Although this is beneficial for having a cleaner graphene, it should be avoided in order to protect the surface electrical and magnetic properties of LSMO, especially in an oxygen-deficient atmosphere. The sharp jumps are indicative of unstable contacts. Device resistance does not vary much with temperature, as shown in Figure 6.24b. Conduction between electrode B and C shows similar behaviour (Figure 6.24c,d). Other devices, #23338b and #23482d, with similar asymmetrical $I - V$ curves are reported in Appendix B.

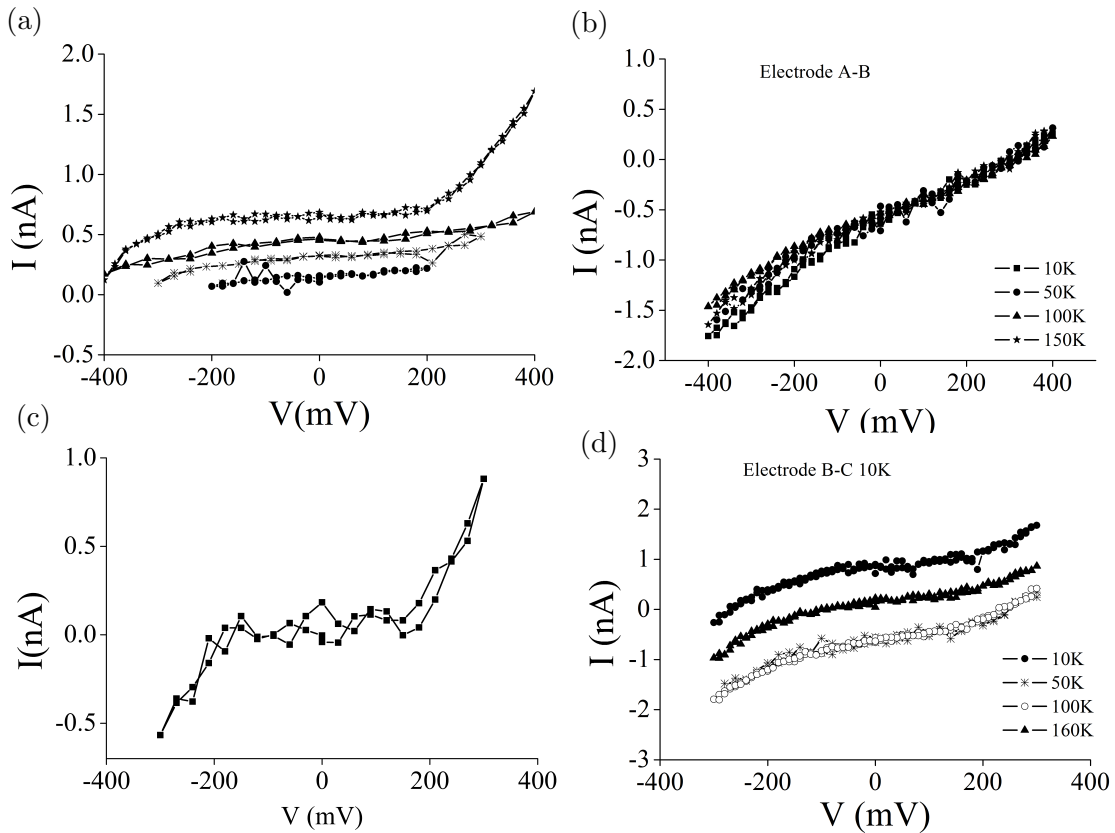


Figure 6.24: $I - V$ characteristic of device # 23063b NGO (001)_{or}, which has 1 nm-thick STO tunnel barrier, and graphene transferred in IPA. (a) $I - V$ measured between electrodes A and B at 10 K. The plots were measured with gradually increasing bias, which shows the change of conduction during the measurement. (b) $I - V$ between electrodes A and B measured at 10 K, 50 K, 100 K and 150 K. (c) $I - V$ curve measured between electrode B and C at 10 K. (d) $I - V$ curves measured between B and C at 10 K, 50 K, 100 K and 160 K. The shift along the vertical axis is due to the current offset.

6.4.2 Devices with no tunnel barriers

For the devices with no tunnel barrier, the resistance between the electrodes lies in the range of $20\text{ M}\Omega$ to $50\text{ G}\Omega$. The ability to achieve $20\text{ M}\Omega$ of resistance is the key for successful spin transport. Figure 6.25 shows two devices prepared on STO (110) substrates, with the graphene transferred in IPA. Both #23408 and #23419 are insulating, and the current measured is about the limit the Keithley picoammeter can detect. The non zero current measured at zero voltage is due to the current offset in the Keithley meter. Because the current offset is larger than the actual current measured, these $I-V$ curves are not a measure of the electrical property of the device and similar feature is often seen in very resistive device, which does not show MR.

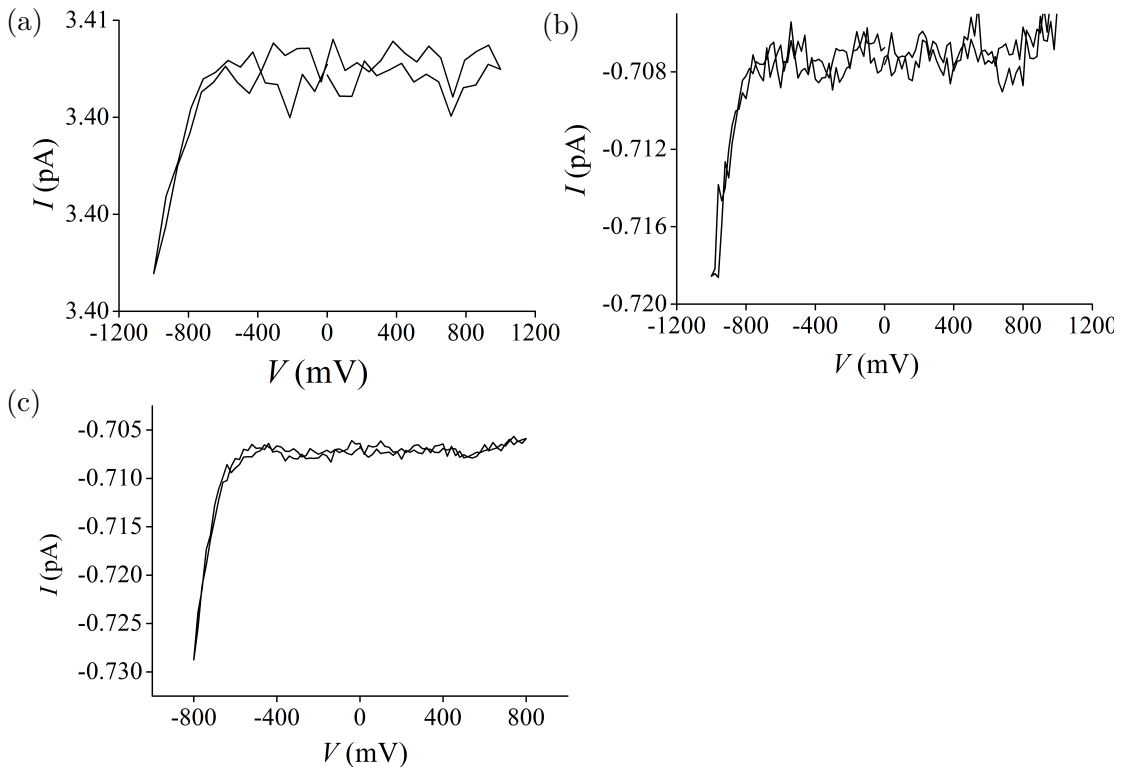


Figure 6.25: (a) I-V characteristics of device #23408 on a STO (110) substrate. The Trilayer graphene in this device was transferred in IPA. (b,c) I-V curve of device #23419 on a STO (110) substrate, measured between electrodes B-C and C-D, respectively. The bilayer graphene was transferred in IPA.

6.4 Magneto-transport measurements

After replacing IPA with the ethanol-water mixture, the resistance was reduced to 10-50 M Ω in devices #23481 and #23482c (on STO (110)), respectively, which is the lowest resistance measured and suitable for successful spin injection. Figure 6.26a shows symmetrical tunnelling transport between the A and B electrodes in device #23482c. The electrical conduction behaviour in the C-D electrode pair is gradually changing as the voltage is swept, probably due to unstable contact. This kind of inhomogeneity is often seen in the graphene devices.

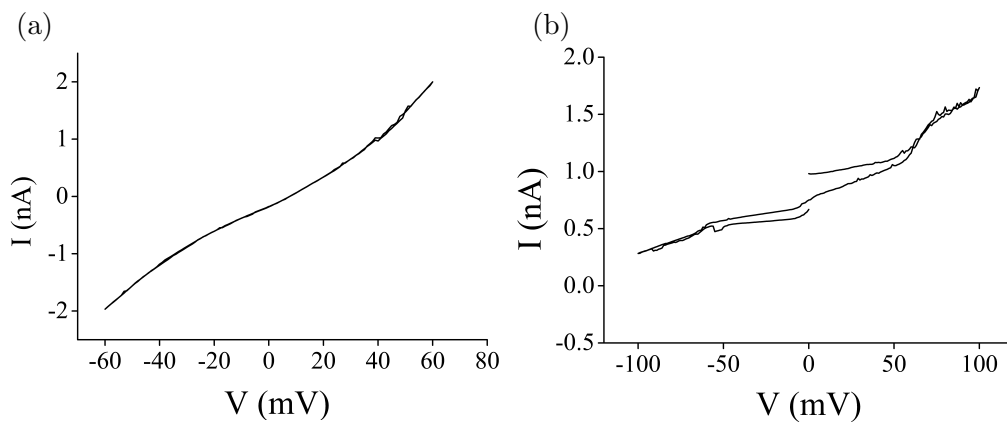


Figure 6.26: I-V curves measured between (a) electrodes A and B, (b) C and D of device #23482c on STO (100) substrate at 10 K. The trilayer graphene was transferred in the ethanol-water mixture.

Device #23481 is the only device that showed MR among the 15 devices measured, demonstrating the challenging nature of this project. The $I - V$ and dI/dV curves between electrode pairs A-B and B-C (Figure 6.27) show tunnelling characteristics.

6. CHARACTERISATION AND MAGNETO-TRANSPORT MEASUREMENTS OF GRAPHENE SPIN-VALVE DEVICES

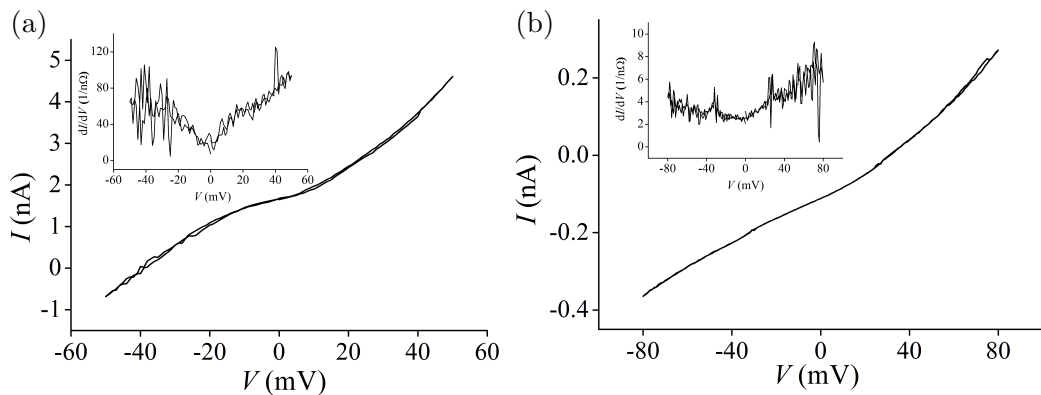


Figure 6.27: $I - V$ curves measured between (a) the electrodes A and B, and (b) the electrodes B and C, for device #23481 on STO (110) at 10 K. Insets plot dI/dV versus V .

Figure 6.28a shows the average of three MR sweeps, each of which is plotted in Figure 6.28b,c,d. In Figure 6.28a, the parallel and antiparallel resistances are well defined and the resistance change is reproducible over the three sweeps plotted in (b), (c) and (d), during a measurement time of 21 minutes, particularly in the downward sweep direction (dotted lines). Subsequent sweeps on the same device have became very noisy and showed large resistance jumps. During the measurement, the heater underneath the sample was disconnected in order to reduce the electronic noise. However, this caused temperature instabilities due to the increasing cooling power from the continuous flow of liquid helium. The difficulty associated with both temperature control and the instability nature of the device made the transport measurement difficult. The switching fields are 14 mT and 33 mT. The 14 mT switching field is roughly the same as that measured by MOKE at 10 K (Figure 6.18).

TAMR can be excluded because the electrodes switch sharply, by 180° and one by one, as imaged at ~ 150 K in XMCD-PEEM (Figure 6.15), with the easy axis across the length of each electrode. MOKE measurements on the electrodes separately confirmed easy axis behaviour across the length of the electrodes at 10 K, eliminating the possibility of transverse domains (Figure 6.18). The MR is about 5.5%, although it is arguable that there is a 1% uncertainty depending on where one takes the R_P level. However, for large values of γ , as is the case for LSMO, the uncertainty in MR does not lead to as large an error in l_{sf} as it does for Co or permalloy as discussed later.

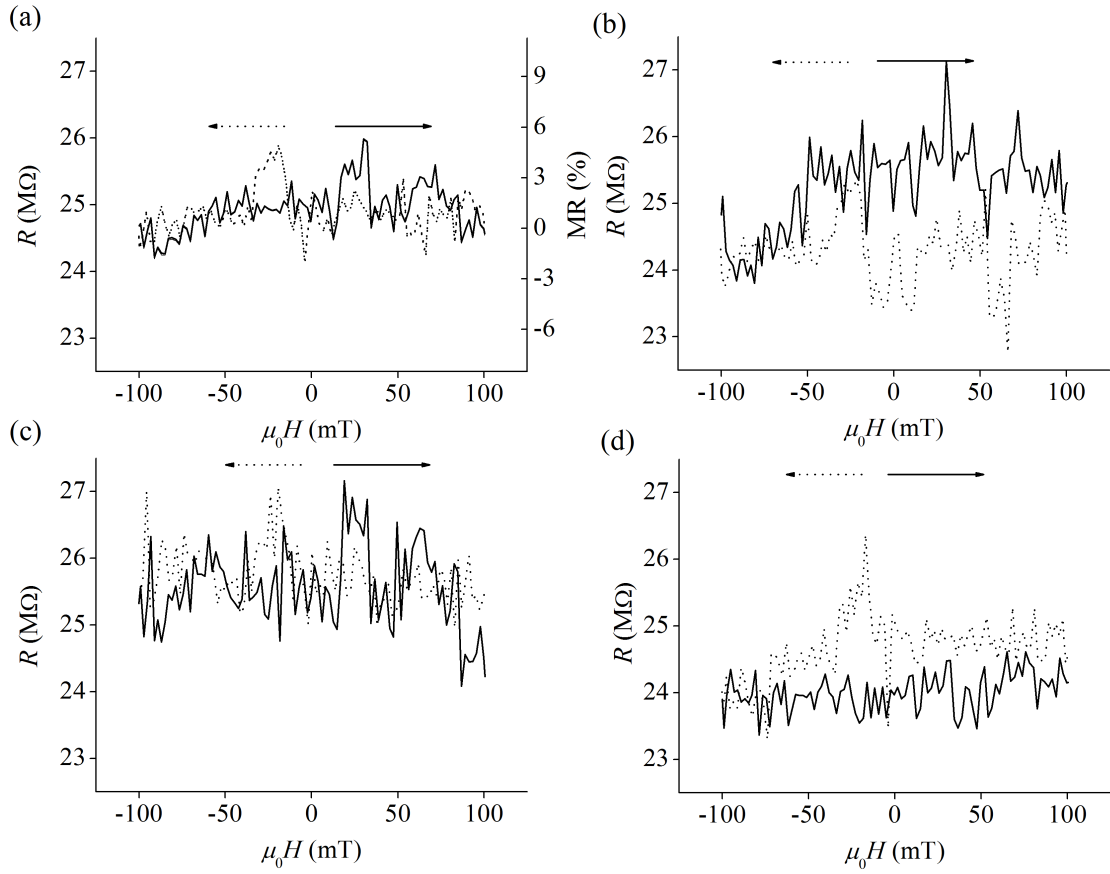


Figure 6.28: Magnetotransport measurement of device #23481 2a on an STO (110) substrate, between electrodes B and C with spacing 2 μm at 10 K. At each measurement field, when sweeping up (solid line) and down (dotted line), resistance $R=\text{d}V/\text{d}I$, was obtained from measuring current at two bias voltages (50 mV and 80 mV). (a) Shows the average of the three sweeps plotted in b, c and d.

In the following paragraphs, the low-field MR is analysed using the drift-diffusion model, and the main limiting factors for achieving large MR are discussed. The significance of this work will then be discussed in the context of the literature.

Using the drift-diffusion model, I calculated the expected MR as a function of spin diffusion length l_{sf} , interfacial spin polarisation γ and interfacial resistance¹ r_b^* for the measured device with $R_P = 24.8 \text{ M}\Omega$ (Figure 6.29). It was assumed that $0.6 < \gamma < 0.9$, which is a reasonable assumption based on the interfacial spin polarisation $0.54 < \gamma < 0.95$

¹Note that r_b^* is related to γ through $r_b^* = \frac{R_P}{2(1-\gamma^2)}$ (see section 1.2.3).

6. CHARACTERISATION AND MAGNETO-TRANSPORT MEASUREMENTS OF GRAPHENE SPIN-VALVE DEVICES

extracted from spin-polarised tunnelling experiments [98, 169–171] (spectroscopy measurements give $\gamma = 1$ [82, 95, 172]). The corresponding r_b^* then falls in the range $19 \text{ M}\Omega < r_b^* < 65 \text{ M}\Omega$. For the measured MR = 5.5 %, reading from Figure 6.29, the spin diffusion length falls in the range $60 \mu\text{m} < l_{sf} < 95 \mu\text{m}$. Note that smaller values of γ give longer spin diffusion lengths.

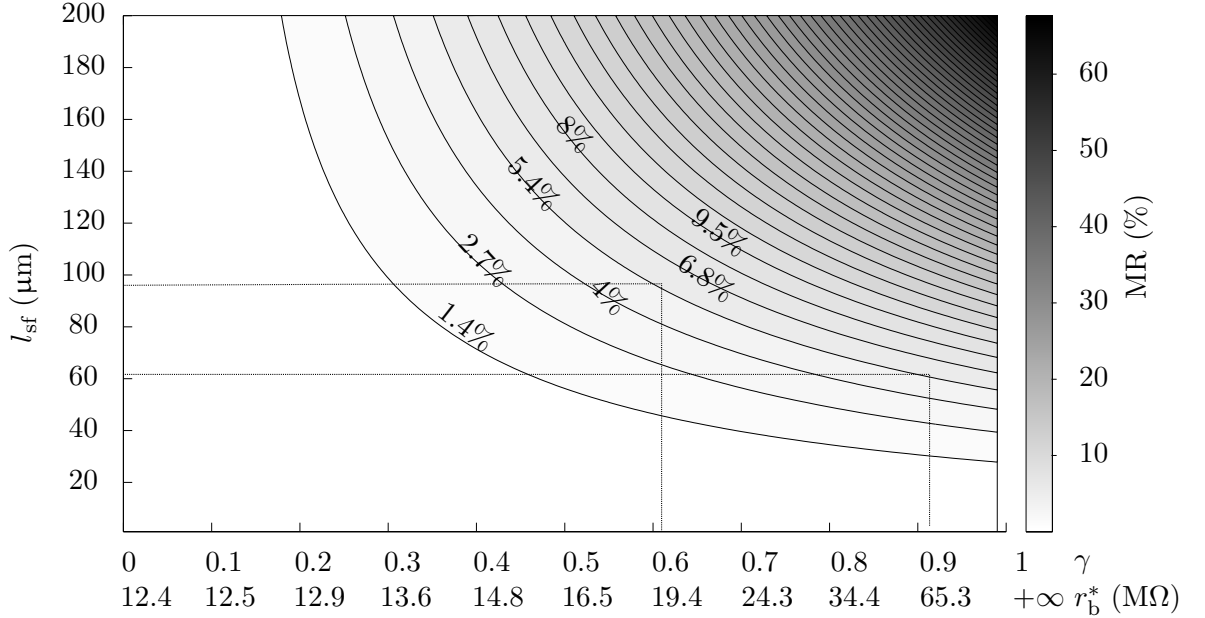


Figure 6.29: Simulated MR as a function of interfacial spin polarisation γ and spin diffusion length l_{sf} using the drift-diffusion model. I used the experimental values $R_P = 24 \text{ M}\Omega$, graphite flake width $7 \mu\text{m}$, electrode spacing $2 \mu\text{m}$ and electrode width $6 \mu\text{m}$. Material constants used are: graphene sheet resistance $R_s = 1.5 \text{ k}\Omega$, $\rho_{\text{LSMO}} = 10^{-6} \Omega\text{m}$ and $\beta_{\text{LSMO}} = 0.95$. The Matlab simulation script can be found in Appendix A.4.

Three main factors that affect device MR are:

The interfacial properties (γ or r_b^)*

As shown in Figure 6.29, unless γ is in the lower regime of spin polarisation, which is believed to not be, due to the high spin polarisation already demonstrated in tunnel junctions [98, 169, 170, 172] and the giant MR observed in multiwall carbon nanotube (MWCNT) spin-valves [36], the value of l_{sf} does not vary strongly with γ , as shown by

the relatively flat contours for $\gamma > 0.6$. Therefore, a moderate value of $\gamma = 0.8$ can be used for analysis, as used for LSMO-MWCNT-LSMO devices [36]. Even if this is over-optimistic, using $\gamma = 0.8$ still will not produce a very wrong value of l_{sf} .

The device resistance R_P

For $\gamma = 0.8$, which corresponds to $l_{sf} \sim 70 \mu\text{m}$, MR was plotted as a function of r_b^* , but this time with γ at 0.8 and with varying device resistance R_P , i.e. varying $r_b^* = \frac{R_P}{2(1-\gamma^2)}$ (Figure 6.30). The interfacial resistance of the measured device is marked by the arrow in the figure. Because the device resistance is close to the upper limit of the optimum window in r_b^* , to further increase MR, one need to reduce R_P . The minimum device resistance measured in this project was $10 \text{ M}\Omega$. The minimum device resistance measured in the CNT spin-valve by Hueso *et al.* was about $50 \text{ M}\Omega$ [36]. With the more complicated graphene transfer process, reducing R_P could be a very challenging task. However, larger interfacial area is available in principle.

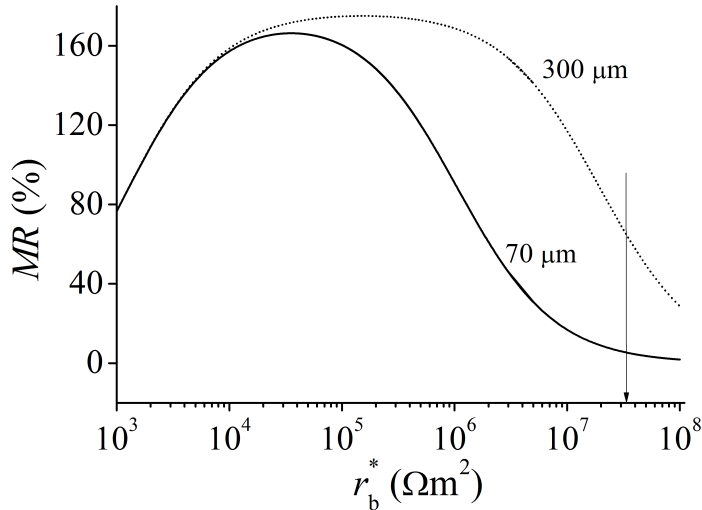


Figure 6.30: Simulated MR as a function of r_b^* for spin diffusion lengths of 70 and 300 μm . The solid curve represents the measured device #23481 on STO (110) that shows MR. The arrow corresponds to the interfacial resistance of the device for $\gamma = 0.8$, as used in the simulation.

The spin diffusion length l_{sf}

Increasing l_{sf} will expand the window for achieving large MR. It would require $l_{sf} \sim 300 \mu\text{m}$ to achieve similar MR as reported for the MWCNT spin-valve. This may require a break

6. CHARACTERISATION AND MAGNETO-TRANSPORT MEASUREMENTS OF GRAPHENE SPIN-VALVE DEVICES

through in graphene fabrication. Varying the number of graphene layers could be relevant here.

Here the main results are summarised for easy comparison with the literature. To remind, this study found $\text{MR} = 5.5\%$ and $l_{\text{sf}} = 70 \mu\text{m}$ on a 3.5 nm-thick flake with a 2 μm electrode spacing.

In the literature, the commonly reported spin diffusion length for multilayer graphene ($l_{\text{sf}} = 3 - 8 \mu\text{m}$) [50, 51, 59] was found to be longer than the corresponding value for single-layer graphene ($l_{\text{sf}} = 0.7 - 3 \mu\text{m}$) (see Table in Figure 2.11), apart from the three cases in references [11, 45, 54] that are discussed separately in the three paragraph below. Although many papers have been published on graphene spinvalves, there are very few studies reporting significant local MR. The study by Wang *et al.* reported local MR $\sim 10\%$ at 7 K, which decreased to $\sim 2.5\%$ as the graphite thickness was reduced from 40 nm to 10 nm [51]. It is still the highest local MR reported, but long distance spin transport was not demonstrated as the electrode spacing was 200 nm, and no value of l_{sf} was reported.

Zomer *et al.* reported spin transport over an impressive 20 μm spacing on a single layer graphene supported by boron nitride (BN), and deduced $l_{\text{sf}} = 4.5 \mu\text{m}$ at room temperature [54]. They did not report low-temperature measurements, so their results is not directly comparable to this study, but it is possible that $l_{\text{sf}} = \sqrt{(D\tau_s)}$ does not vary strongly with temperature, given that a separate study by Han *et al.* on SLG did not find significant temperature dependence for the spin relaxation time (τ_s) and the diffusion coefficient (D) at the neutrality point [47]. The longer l_{sf} reported in this work has benefitted from the much larger device resistance, 24.8 M Ω as suppose to 10 k Ω , which eliminates spin relaxation at the contact. Moreover, the multilayer graphene is transferred onto the electrodes as the very last step of the fabrication process, reducing physical damage to the flake, as would otherwise occur in a typical fabrication process where the tunnel barriers and electrodes are sputtered onto the graphene.

When a tunnel barrier in a graphene spin-valve was fabricated by the atomic layer deposition (ALD), which is a much gentler process than sputtering. Film made from ALD may be more compact and less prone to pinholes. Yamaguchi *et al.* achieved better tunnel barrier quality and found a similar $l_{\text{sf}} = 4.18 \mu\text{m}$ to Zomer *et al.* in a bilayer graphene, but without the complication of adding BN support [45].

Long l_{sf} over a wide range (95–285 μm) was reported by Dlbak *et al.* on epitaxial graphene, with values below 160 μm attributed to the graphene sampling more than one magnetic domains [11]. Despite the long spin diffusion length, the switching is gradual and asymmetric about zero magnetic field. The resistance value at zero field is larger than R_P , indicating that the electrodes do not adopt a truly parallel state at remanence. In comparison, the current study investigated the micromagnetics of the electrodes at both room temperature and low temperature, employing multiple characterisations including macroscopic VSM study of the unpatterned film, microscopic imaging of the electrodes with XMCD-PEEM at remanence and a local study with MOKE while sweeping magnetic field on the same set of electrodes and at the same measurement temperature as used for transport. All of these studies arrive at the conclusion that the electrodes under investigation are single domain and that they switch independently and sharply by nucleation-propagation. Therefore, it was possible to eliminate the possibility of TAMR [35, 173] and AMR, which could be easily misinterpreted as spin transport through graphene.

Using the same LSMO electrodes on NGO (001) as used for MWCNT spin-valves [36], spin injection into graphene was not observed, partly due the large device resistance ($> 500 \text{ M}\Omega$). But importantly, the graphene, was a few microns wide, and is therefore likely to sample multiple domains. The use of large uniaxial anisotropy (110)_{pc}-oriented LSMO electrodes is the key for successful spin injection into graphene.

Sample Number	substrate	film	thickness (nm)	barrier (Å)	Number of layers of	Transfer method	Device resistance	I-V	MR
22988a	NGO (001)	LSMO	40	BTO 2.5	single	IPA	4-10 GΩ	linear-weakly tunnelling	
22988a2	NGO (001)	LSMO	40	BTO 2.5	thick flake	IPA	100 GΩ	linear	
22988b	NGO (001)	LSMO	39	BTO 2.5	single	IPA	No conduction		
23063a	NGO (001)	LSMO	39	STO 10	bilayer with PMMA scaffolding	IPA	No conduction		
23063b	NGO (001)	LSMO	39	STO 10		IPA	500 MΩ	asymmetrical	
23199b	NGO (001)	LSMO	45	LAO 2.9	bilayer	IPA	5-10 GΩ	linear	
23338a	NGO (100)	LSMO	45	No	bilayer	IPA	No conduction		
23338b	NGO (100)	LSMO	45	No	bilayer	IPA	1 GΩ	asymmetrical	
23408b	STO (110)	LSMO	69	No	trilayer	IPA	100 GΩ	asymmetrical	
23419	STO (110)	LSMO	42	No	bilayer	IPA	100 GΩ	asymmetrical	
23481	STO (110)	LSMO	30	No	3.5 nm	Ethanol-water	20-30 MΩ	tunnelling	5.5% at 10 K
23482c	STO (110)	LSMO	30	No	trilayer	Ethanol-water	10-50 MΩ	tunnelling	
23482d	STO (110)	LSMO	30	No	bilayer	Ethanol-water	20 GΩ	asymmetrical	
23488b	STO (110)	LSMO	30	No	7.5 nm	Dry transfer	3 GΩ	linear-weakly tunnelling	
23488d	STO (110)	LSMO	30	No	5 nm	Dry transfer	10-50 GΩ	linear	

Table 6.1: Table summarizing all devices tested.

Chapter 7

Conclusions

The present work identifies and emphasises the importance of understanding the micro-magnetic properties of LSMO electrodes in order to achieve successful spin injection into graphene. The spin-transport properties of graphene are studied by measuring the local MR and deducing $l_{sf} = 70 \mu\text{m}$. In the literature, a wide range of spin diffusion lengths, from 0.3 nm to 285 μm , have been reported (as summarised in the table in Figure 2.11). This disagreement is often explained by the differences in graphene quality, interfacial cleanliness and roughness, and the tunnel barrier quality. This dissertation identifies that it is important to consider the magnetic switching of the electrodes.

I have studied magnetic anisotropy and magnetisation reversal in unpatterned LSMO films on NGO (001), NGO (100) and STO (110). I found that the (110)_{pc}-oriented LSMO film, on NGO (100) and STO (110), have a stronger uniaxial anisotropy than the (001)_{pc}-oriented LSMO on NGO (001). In all three cases, magnetisation reversal proceeds via nucleation-propagation, and the easy-axis coercivity is similar to the nucleation field. For LSMO on NGO (001), magnetisation reversal is propagation limited. The angular dependence of the coercivity near the easy axis can be fitted using the Kondorsky model. As the applied magnetic field direction approaches the hard axis, there is an increasing contribution from coherent rotation. Hard-axis magnetisation shows the expected linear dependence on magnetic field, and can be fitted with the Stoner-Wohlfarth coherent-rotation model. By contrast, the (110)_{pc}-oriented LSMO films, on either NGO (100) or STO (110), show large uniaxial anisotropy with nucleation limited magnetisation reversal, and were patterned for graphene spin valves.

The patterning procedure used to achieve clean LSMO electrodes involves the temporary

7. CONCLUSIONS

incorporation of a protective Au layer on the LSMO surface during the lithographic patterning, and a subsequent oxygen anneal after this Au has been etched away. Different graphene transfer methods were attempted by my collaborators Antonio Lombardo and Matteo Barbone, under the supervision of Andrea C. Ferrari. The use of an ethanol-water mixture gave the cleanest graphene and the lowest contact resistance.

The switching behaviour of the patterned LSMO electrodes on NGO (100) and STO (110) was obtained using MOKE by Sampo Hämäläinen under the supervision of Sebastiaan van Dijken. Contact pads and electrodes each showed easy-axis hysteresis loop when the measurement direction lay across the length of the electrodes, and hard-axis behaviour along the length of the electrodes. XMCD-PEEM measurements showed the electrodes on NGO (001) switched gradually such that the switching fields of the individual electrodes cannot be distinguished. No MR could have been measured for devices on NGO (001) because, as subsequently discovered, the electrodes do not adopt wholly parallel and antiparallel states. The XMCD-PEEM images of electrodes on NGO (100) and STO (110) showed that the electrodes switched sharply and individually, by nucleation-propagation, with each electrode comprising a single magnetic domain.

Transport measurements for devices prepared using an STO (110) substrate demonstrated spin injection into multilayer graphene with a local MR of 5.5% at 10 K. Both TAMR and AMR can be excluded because they require the presence of transverse domains, which are not present, as confirmed by XMCD-PEEM images at \sim 150 K, and as confirmed by MOKE measurements at the MR measurement temperature of 10 K. I therefore conclude that the measured MR is genuinely due to spin transport through graphene, and I am able to extract $l_{sf} = 70 \mu\text{m}$ using the drift-diffusion model. This is longer than all reported values of l_{sf} , apart from the values of 95–285 μm reported by Dlbak *et al.* for epitaxial graphene [11]. However, the long l_{sf} obtained by Dlbak *et al.* is compromised by the lack of micromagnetic data, such that TAMR cannot be excluded.

This work is also distinguished with respect to existing practice in three ways:

- The present study utilised epitaxial magnetic electrodes, in which the magnetic anisotropy is dominated by the magnetocrystalline and magnetoelastic anisotropy. This is distinct from polycrystalline magnetic thin films, such as Co and permalloy, which are widely used, and for which the magnetic anisotropy is dominated by shape anisotropy. One advantage of LSMO is that it is an oxide, and so it is

relatively stable in air.

- The graphene was placed on the top of the LSMO electrodes instead of underneath, so that the LSMO could be grown epitaxially at high temperature.
- Spin injection occurs through a naturally formed tunnel barrier instead of an artificially fabricated tunnel barrier. The latter might damage the underlaying graphene.

Further improvements to the present work are possible, with the aim to reduced device resistance, or increased spin diffusion lengths. Both critically depend on the cleanliness of the graphene transfer. Reproducibility is the main challenge in this project and will probably remains so until one has more control over the graphene transfer. Until now, it is still not known what path the spin follows once it is in the channel, therefore, few layer graphene or thick flake are still very interesting to explore. Only with high degree of reproducibility of the devices, the real physics of graphene and few layer graphene can be truly understood and compared, the realisation of the spin-FET idea can then be implemented. In order to achieve the above, some intermediate experiments could be done to understand the effect of back-filled material, such as amorphous NdGaO₃ used in this thesis, on the electron mobility and spin relaxation. High dielectric material, such as HfO₂ might be a much better material to use than NdGaO₃.

7. CONCLUSIONS

Appendix A

The drift-diffusion model

The analysis of the magnetoresistance (MR) in this dissertation follows the drift-diffusion model, which was initially proposed for spin transport through multilayers of ferromagnetic metals by Valet and Fert [6]. The derivation of the solution for two layers of materials, layer A and layer B, were reproduced in this section following references [6, 7].

In Section A.1, a general solution was derived, where the layers A and B can be any combinations of ferromagnetic metal and non-magnetic metal. Solution for a specific configuration, such as the ferromagnetic/ferromagnetic metal interface (FMM/FMM), and ferromagnetic/non-magnetic metal interface (FMM/NMM), were given in Section A.2 and A.3. Section A.4 presents the Matlab simulation scripts used for graphene spin-valve analysis in this dissertation.

A.1 General Expression

The core equations used in the drift-diffusion model are A.1, which states the diffusion of spins as that for the diffusion of particles, and A.2 which is the Ohms law and describes the electrical properties of the diffusing particles.

$$\frac{e}{\sigma_{\pm}} \frac{\partial J_{\pm}}{\partial z} = \frac{\mu_{+} - \mu_{-}}{l_{\pm}^2}, \quad (\text{A.1})$$

$$J_{\pm} = \frac{\sigma_{\pm}}{e} \frac{\partial \mu_{\pm}}{\partial z}. \quad (\text{A.2})$$

Note here the spin diffusion length l_{sf} is a result of both spin orientations and is expressed as $(1/l_{\text{sf}})^2 = (1/l_{+})^2 + (1/l_{-})^2$. The chemical potential of the spin is $\mu_{\pm} = \bar{\mu} \pm \Delta\mu$, where $\bar{\mu}$ is spin independent.

A. THE DRIFT-DIFFUSION MODEL

Substituting μ_{\pm} into A.2 and solving A.1, the following is obtained:

$$\frac{\partial^2(\bar{\mu} \pm \Delta\mu)}{\partial z^2} = \frac{\mu_+ - \mu_-}{l_{\pm}^2} = \pm \frac{2\Delta\mu}{l_{\pm}^2} \quad (\text{A.3})$$

Because $\bar{\mu}$ is spin independent and it has a linear dependence on z , $\frac{\partial^2\bar{\mu}}{\partial z^2} = 0$. Subsituting l_{sf} for l_{\pm} and assuming the spin relaxation length for spin-up and down electrons are equal, i.e. $l_+ = l_-$, equation A.3 can be reduced to:

$$\frac{\partial^2\Delta\mu}{\partial z^2} = \frac{\Delta\mu}{l_{\text{sf}}^2}; \quad (\text{A.4})$$

Solving the differential equation A.4 results in a general solution for $\Delta\mu$ (equation A.5). Equation A.5 describes spin accumulation as a function of the distance away from the interface with the FMM electrode due to spin relaxation.

$$\Delta\mu = a \exp(z/l_{\text{sf}}) + b \exp(-z/l_{\text{sf}}), \quad (\text{A.5})$$

where a and b are constants.

From A.2

$$J_+ = \frac{\sigma_+}{e} \frac{\partial\mu_+}{\partial z}, \quad (\text{A.6})$$

$$J_- = \frac{\sigma_-}{e} \frac{\partial\mu_-}{\partial z}. \quad (\text{A.7})$$

Because $J = J_+ + J_-$ and is constant, $\frac{\partial(J_+ + J_-)}{\partial z} = 0$. Subsituting A.6 and A.7 into this equation, resulting in:

$$\frac{\partial^2(\sigma_+\mu_+ + \sigma_-\mu_-)}{\partial z^2} = 0, \quad (\text{A.8})$$

and hence

$$\sigma_+\mu_+ + \sigma_-\mu_- = 0 \quad (\text{A.9})$$

Combining Equation A.5 and A.9, a general solution can be obtained by considering appropriate boundary conditions:

$$J_{\pm}(z = z_0^+) = J_{\pm}(z = z_0^-), \quad (\text{A.10})$$

$$\mu_{\pm}(z = z_0^+) - \mu_{\pm}(z = z_0^-) = r_{\pm}eJ_{\pm}(z = z_0), \quad (\text{A.11})$$

A.1 General Expression

where r_{\pm} is the spin-dependent interfacial resistance and is $r_{\pm} = 2r_b^*[1 \pm \gamma]$. It has the value zero when interfacial relaxation is neglected.

The general expression for μ_{\pm} , $\Delta\mu$, $F(z)$ ¹, and J_{\pm} are the following:

$$\mu_+(z) = (1 - \beta_n^2)e\rho_n^*Jz + K_1^n + (1 + \beta_n)[K_2^n \exp(\frac{z}{l_{sf}^n}) + K_3^n \exp(-\frac{z}{l_{sf}^n})], \quad (\text{A.12})$$

$$\mu_-(z) = (1 - \beta_n^2)e\rho_n^*Jz + K_1^n - (1 - \beta_n)[K_2^n \exp(\frac{z}{l_{sf}^n}) + K_3^n \exp(-\frac{z}{l_{sf}^n})], \quad (\text{A.13})$$

$$\Delta\mu(z) = K_2^n \exp(\frac{z}{l_{sf}^n}) + K_3^n \exp(-\frac{z}{l_{sf}^n}), \quad (\text{A.14})$$

$$F(z) = (1 - \beta_n^2)\rho_n^*J + \frac{\beta_n}{el_{sf}^n}[K_2^n \exp(\frac{z}{l_{sf}^n}) - K_3^n \exp(-\frac{z}{l_{sf}^n})], \quad (\text{A.15})$$

$$J_+(z) = (1 - \beta_n)\frac{J}{2} + \frac{1}{2er_n}[K_2^n \exp(\frac{z}{l_{sf}^n}) - K_3^n \exp(-\frac{z}{l_{sf}^n})], \quad (\text{A.16})$$

$$J_-(z) = (1 + \beta_n)\frac{J}{2} - \frac{1}{2er_n}[K_2^n \exp(\frac{z}{l_{sf}^n}) - K_3^n \exp(-\frac{z}{l_{sf}^n})]. \quad (\text{A.17})$$

In the above equations, when the superscript n is substituted for A (B), the corresponding material parameter or constant refers to material A (B). The values of K_1^A , K_2^A , K_3^A , K_1^B , K_2^B and K_3^B can be obtained by using the boundary conditions in A.11.

For zero interfacial resistance, at $z = 0$:

$$\mu_{\pm}^A = \pm(1 \pm \beta_A)K_2^A, \quad \mu_{\pm}^B = K_1^B \pm (1 \pm \beta_B)K_2^A, \quad (\text{A.18})$$

$$\Delta\mu_A = K_2^A, \quad \Delta\mu_B = K_3^B, \quad (\text{A.19})$$

$$F_A = (1 - \beta_A^2)\rho_A J + K_2^A \frac{\beta_A}{el_{sf}^A}, \quad F_B = (1 - \beta_B^2)\rho_B J - K_3^B \frac{\beta_B}{el_{sf}^B}, \quad (\text{A.20})$$

$$J_{\pm}^A = (1 \mp \beta_A)\frac{J}{2} \pm K_2^A \frac{1}{2er_A}, \quad J_{\pm}^B = (1 \mp \beta_B)\frac{J}{2} \mp K_3^B \frac{1}{2er_B}. \quad (\text{A.21})$$

For the first boundary condition A.10, substituting for J_{\pm}^A and J_{\pm}^B

$$K_1^B + (1 + \beta_B)K_3^B - (1 + \beta_A)K_2^A = 2r_b^*(1 + \gamma)e[(1 - \beta_A)\frac{J}{2} + K_2^A \frac{1}{2er_A}] \quad (\text{A.22})$$

$$K_1^B - (1 - \beta_B)K_3^B + (1 - \beta_A)K_2^A = 2r_b^*(1 - \gamma)e[(1 + \beta_A)\frac{J}{2} - K_2^A \frac{1}{2er_A}] \quad (\text{A.23})$$

¹ $F(z) = \frac{1}{e} \frac{\partial\mu}{\partial z}$

A. THE DRIFT-DIFFUSION MODEL

For the second boundary condition A.11, substituting for μ_{\pm}^B , μ_{\pm}^A , and J_{\pm} , and solving the two equations simultaneously leads to:

$$K_3^B - K_2^A = r_b^* e J (\gamma - \beta_A) + \frac{K_2^A \gamma_b^*}{r_N} \quad (\text{A.24})$$

Solving A.23 and A.24 together gives the following results.

$$r_n = \rho_n^* l_{sf}^F, \quad (\text{A.25})$$

$$K_1^A = 0, \quad (\text{A.26})$$

$$K_2^A = J[(\beta_A - \beta_B) + (\beta_A - \gamma) \frac{r_b^*}{\rho_B l_{sf}^B}] \frac{e \rho_A l_{sf}^A \rho_B l_{sf}^B}{\rho_B l_{sf}^B + \rho_A l_{sf}^A + r_b^*}, \quad (\text{A.27})$$

$$K_3^A = 0, \quad (\text{A.28})$$

$$K_1^B = (1 + \beta_A) K_2^A - (1 + \beta_B) K_3^B + r_b^*(1 + \gamma) e [J(1 - \beta_A) + \frac{K_2^A}{e \rho_A l_{sf}^A}], \quad (\text{A.29})$$

$$K_2^B = 0, \quad (\text{A.30})$$

$$K_3^B = [(\beta_A - \beta_B) \rho_A l_{sf}^A + r_b^*(\gamma - \beta_B)] \frac{e J \rho_B l_{sf}^B}{\rho_B l_{sf}^B + \rho_A l_{sf}^A + r_b^*}. \quad (\text{A.31})$$

A.2 FMM/FMM Interface

When the magnetisations of the identical ferromagnets A and B are parallel, $\beta_A = \beta_B = \beta$ and for transparent interface $r_b^* = 0$,

$$K_1^A = K_2^A = K_3^A = K_1^B = K_2^B = K_3^B = 0 \quad (\text{A.32})$$

For A:

$$\mu_{\pm}^A(z) = (1 - \beta^2) e \rho_A^* J z, \quad (\text{A.33})$$

$$\Delta \mu^A(z) = 0, \quad (\text{A.34})$$

$$F^A(z) = (1 - \beta^2) \rho_A^* J, \quad (\text{A.35})$$

$$J_{\pm}^A(z) = (1 \mp \beta) \frac{J}{2}. \quad (\text{A.36})$$

$$(\text{A.37})$$

For B:

$$\mu_{\pm}^B(z) = (1 - \beta^2) e \rho_B^* J z, \quad (\text{A.38})$$

$$\Delta \mu^B(z) = 0, \quad (\text{A.39})$$

$$F^B(z) = (1 - \beta^2) \rho_B^* J, \quad (\text{A.40})$$

$$J_{\pm}^B(z) = (1 \mp \beta) \frac{J}{2}. \quad (\text{A.41})$$

$$(\text{A.42})$$

When the magnetisation of A and B are antiparallel,

$$K_1^A = K_3^A = K_1^B = K_2^B = 0, \quad (\text{A.43})$$

$$K_2^A = 2eJ\beta \frac{r_A r_A}{r_A + r_B} \quad (r_{A(B)} = \rho_{A(B)} l_{sf}^{A(B)}), \quad (\text{A.44})$$

$$K_3^B = 2eJ\beta \frac{r_A r_B}{r_A + r_B}. \quad (\text{A.45})$$

For A:

$$\mu_{\pm}^A(z) = (1 - \beta^2)e\rho_A^* J z \pm (1 \mp \beta)K_2^A \exp\left(\frac{z}{l_{sf}^A}\right), \quad (\text{A.46})$$

$$\Delta\mu^A(z) = K_2^A \exp\left(\frac{z}{l_{sf}^A}\right), \quad (\text{A.47})$$

$$F^A(z) = (1 - \beta^2)\rho_A^* J + \frac{\beta}{el_{sf}^A} K_2^A \exp\left(\frac{z}{l_{sf}^A}\right), \quad (\text{A.48})$$

$$J_{\pm}^A(z) = (1 \mp \beta)\frac{J}{2} \pm \frac{1}{2er_A} K_2^A \exp\left(\frac{z}{l_{sf}^A}\right). \quad (\text{A.49})$$

$$(\text{A.50})$$

For B:

$$\mu_{\pm}^B(z) = (1 - \beta^2)e\rho_B^* J z \pm (1 \mp \beta)K_3^B \exp\left(-\frac{z}{l_{sf}^B}\right), \quad (\text{A.51})$$

$$\Delta\mu^B(z) = K_3^B \exp\left(-\frac{z}{l_{sf}^B}\right), \quad (\text{A.52})$$

$$F^B(z) = (1 - \beta^2)\rho_B^* J - \frac{\beta}{el_{sf}^B} K_2^B \exp\left(-\frac{z}{l_{sf}^B}\right), \quad (\text{A.53})$$

$$J_{\pm}^B(z) = (1 \pm \beta)\frac{J}{2} \pm \frac{1}{2er_B} K_2^B \exp\left(-\frac{z}{l_{sf}^B}\right). \quad (\text{A.54})$$

$$(\text{A.55})$$

A. THE DRIFT-DIFFUSION MODEL

A.3 FMM/NMM Interface

Assuming a transparent interface with $r_b^* = 0$, ferromagnetic A with $\beta_A = \beta$, and non-magnetic metal B with $\beta_B = 0$, the following constants are obtained:

$$K_1^A = 0, \quad (\text{A.56})$$

$$K_2^A = eJ\beta \frac{r_A r_B}{r_A + r_B} \quad (r_{A(B)} = \rho_{A(B)} l_{sf}^{A(B)}), \quad (\text{A.57})$$

$$K_3^A = 0, \quad (\text{A.58})$$

$$K_1^B = \beta [eJ\beta \frac{r_A r_B}{r_A + r_B}], \quad (\text{A.59})$$

$$K_2^B = 0, \quad (\text{A.60})$$

$$K_3^B = eJ\beta \frac{r_A r_B}{r_A + r_B}. \quad (\text{A.61})$$

For A:

$$\mu_{\pm}^A(z) = (1 - \beta^2)e\rho_A^* J z \pm (1 \pm \beta)K_2^A \exp\left(\frac{z}{l_{sf}^A}\right), \quad (\text{A.62})$$

$$\Delta\mu^A(z) = K_2^A \exp\left(\frac{z}{l_{sf}^A}\right), \quad (\text{A.63})$$

$$F^A(z) = (1 - \beta^2)\rho_A^* J + \frac{\beta}{el_{sf}^A} K_2^A \exp\left(\frac{z}{l_{sf}^A}\right), \quad (\text{A.64})$$

$$J_{\pm}^A(z) = (1 \mp \beta) \frac{J}{2} \pm \frac{1}{2er_A} K_2^A \exp\left(\frac{z}{l_{sf}^A}\right). \quad (\text{A.65})$$

$$(A.66)$$

For B:

$$\mu_{\pm}^B(z) = e\rho_B^* J z + K_1^B \pm K_3^B \exp\left(-\frac{z}{l_{sf}^B}\right), \quad (\text{A.67})$$

$$\Delta\mu^B(z) = K_3^B \exp\left(-\frac{z}{l_{sf}^B}\right), \quad (\text{A.68})$$

$$F^B(z) = \rho_B^* J, \quad (\text{A.69})$$

$$J_{\pm}^B(z) = \frac{J}{2} \mp \frac{1}{2er_B} K_3^B \exp\left(-\frac{z}{l_{sf}^B}\right). \quad (\text{A.70})$$

$$(A.71)$$

A.4 Analysis of graphene spin-valves using the drift-diffusion model

The Matlab simulation scripts appear in the next two pages.

```

% Script used for Co/Graphene/Co spin valve simulation.
pack
clc
rbstar=1e2:1e1:1e3
rbstar2=1e3:1e1:1e5
rbstar3=1e5:1e3:1e7
%for graphene
w=1.5e-6 % width of the graphene strip
tN=2e-6 %length of the channel
rhoNsq=1.5e3 %sheet resistance for exfoliated graphene = 1-2 KOhm square
lsfN=2e-6 %5um
RN=(rhoNsq/w)*lsfN % here rN is same as Rch in Dlbak's paper~2e3
%for Co electrodes
beta=0.46
rF=4.5e-15 % for Co
lsff=60e-9
l=6e-9 % width of the electrode 6um
gamma=0.3
RF=rF/(w*l)
%calculation
%for the lower range
DeltaR1=2*(beta*RF+gamma*rbstar).^2./((rbstar+RF)*cosh(tN/lsfN)+(RN/2)*(1+(rb
star/RN).^2)*sinh(tN/lsfN))
r01=2*(1-beta.^2)*RF+RN*(tN/lsfN)+2*(1-gamma.^2)*rbstar
rSI1=2*((beta-
gamma).^2*RF*rbstar+RN*(beta.^2*RF+gamma.^2*rbstar)*tanh(tN/(2*lsfN)))/((RF+rbst
ar)+RN*tanh(tN/(2*lsfN)))
Rp1=r01+rSI1
MR1=(DeltaR1./Rp1)
x1=rbstar
% for the middle range
DeltaR2=2*(beta*RF+gamma*rbstar2).^2./((rbstar2+RF)*cosh(tN/lsfN)+(RN/2)*(1+
rbstar2/RN).^2)*sinh(tN/lsfN))
r02=2*(1-beta.^2)*RF+RN*(tN/lsfN)+2*(1-gamma.^2)*rbstar2
rSI2=2*((beta-
gamma).^2*RF*rbstar2+RN*(beta.^2*RF+gamma.^2*rbstar2)*tanh(tN/(2*lsfN)))/((RF+rb
star2)+RN*tanh(tN/(2*lsfN)))
Rp2=r02+rSI2
MR2=(DeltaR2./Rp2)
x2=rbstar2
%for the high range
DeltaR3=2*(beta*RF+gamma*rbstar3).^2./((rbstar3+RF)*cosh(tN/lsfN)+(RN/2)*(1+
rbstar3/RN).^2)*sinh(tN/lsfN))
r03=2*(1-beta.^2)*RF+RN*(tN/lsfN)+2*(1-gamma.^2)*rbstar3
rSI3=2*((beta-
gamma).^2*RF*rbstar3+RN*(beta.^2*RF+gamma.^2*rbstar3)*tanh(tN/(2*lsfN)))/((RF+rb
star3)+RN*tanh(tN/(2*lsfN)))
Rp3=r03+rSI3
MR3=(DeltaR3./Rp3)
x3=rbstar3

%plot
figure
semilogx(x1,MR1,'+',x2,MR2,'+',x3,MR3,'+')
xlabel ('rbstar')
ylabel ('MR')

```

```

% Script used for simulating LSMO/Graphene/LSMO spin-valve analysis
clc
pack
gamma=[0:0.01:1]
lsfN=[1e-6:1e-6:200e-6]
[gamma,lsfN]=meshgrid(gamma,lsfN)

Rp=24e6 %parallel resistance =24 Mohm
rbstar=Rp./(2.* (1-gamma.^2)) % Fert (25) when tF>>lsff and tN<<lsfN

%for graphene
w=7e-6 % width of the graphene strip in um between B-C electrodes in device
23481
L=2e-6 %length of the graphene channel in um
rhoNsq=1.5e3 %sheet resistance for exfoliated graphene = 1-2 KOhm
Rch=rhoNsq*lsfN/w %convert rN from Fert notation to Rch used in Dlubak

%for the LSMO
l=6e-6 %width of the electrode
beta=0.95
rhoF=1e-6 %resistivity of LSMO in Ohm m
rhoFs=rhoF/(1-beta^2)
lsff=60e-9
RF=(rhoFs/(l*w))*lsff %convert rF from the Fert notation to RF notation used
in Dlubak

%calculation
DeltaR=2.* (beta*RF+gamma.*rbstar).^2./((rbstar+RF).*cosh(L./lsfN)+(Rch/2).* (1
+(rbstar./Rch).^2).*sinh(L./lsfN))
MR=100.* (DeltaR./Rp)

%plot figure
contourf(gamma,lsfN,MR,50) %z axis plotted in 50 steps
colormap(gray)
xlabel ('gamma')
ylabel ('lsfN')
colorbar

```

Appendix B

Other graphene spin-valves results

B.1 Negligible or no tunnelling $I - V$ characteristic

This section reported the $I - V$ curves for all the devices that showed linear and weakly tunnelling $I - V$ characteristics. Device #22988a2 on a NGO (001) substrate, transferred in IPA showed a linear $I - V$ curve above 100 K, with a resistance of about $100 \text{ G}\Omega$.

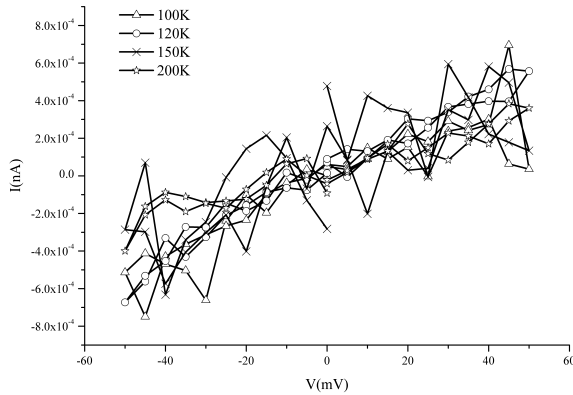


Figure B.1: $I - V$ curve of Device #22988 2a on NGO (001), measured between electrodes B and C at 100-200 K. Other electrode combinations do not show conduction.

Device #23488b on STO (110), with graphene fabricated by dry transfer has a resistance of about $3 \text{ G}\Omega$.

B. OTHER GRAPHENE SPIN-VALVES RESULTS

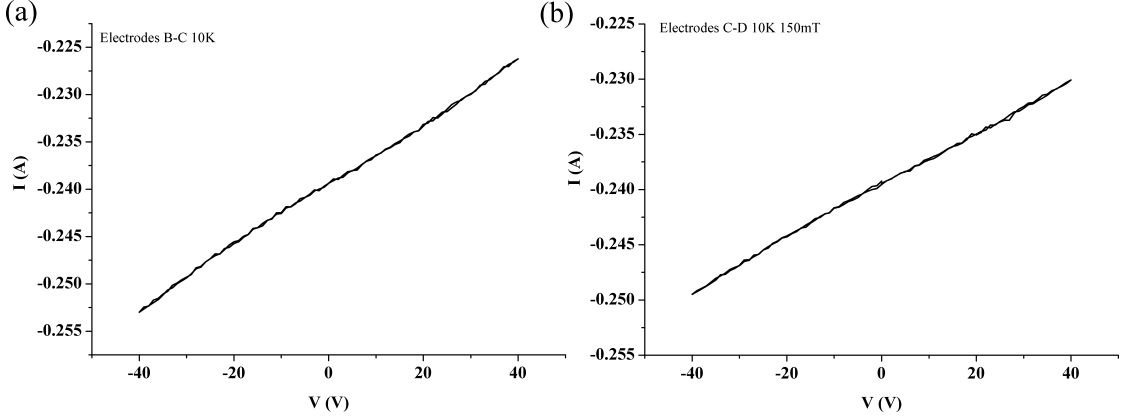


Figure B.2: $I - V$ curves of device #23488b on STO (110), between electrode pairs (a) B-C measured at 10 K, and (b) C-D measured at 10 K.

Device #23488d fabricated by graphene dry transfer, which had resistance values 10-50 G Ω .

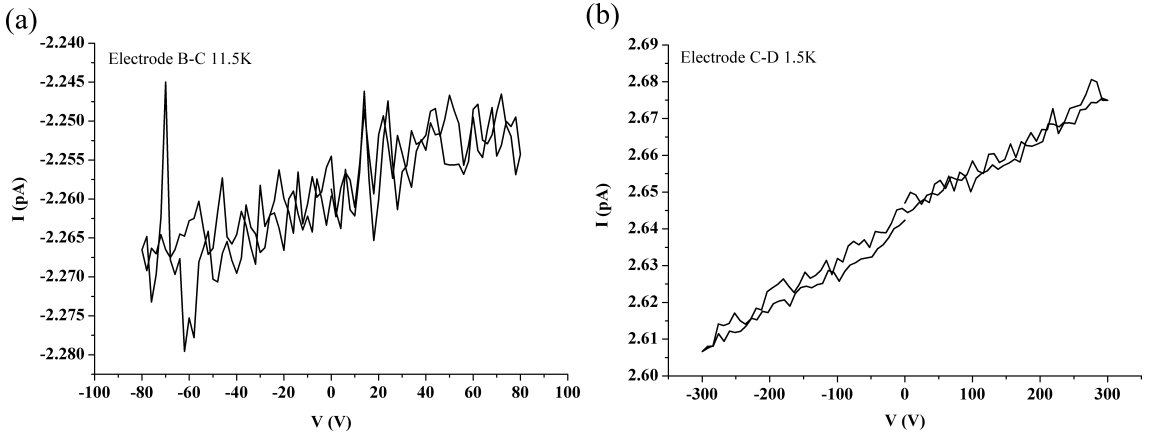


Figure B.3: $I - V$ curves of device #23488d measured between electrode pairs (a) B-C with 10 G Ω resistance, and (b) C-D with 50 G Ω resistance.

B.2 Asymmetrical $I - V$ characteristic

This section reports all the devices that had asymmetrical $I - V$ curves. Device #23338b on a NGO (100), fabricated by graphene transfer in IPA shows conduction between electrode pairs A-B and B-D. The resistance between A and B increased from 1 G Ω to 50 G Ω when retested 6 days later, and that between B-D increased from 1 G Ω to 10 G Ω .

B.2 Asymmetrical $I - V$ characteristic

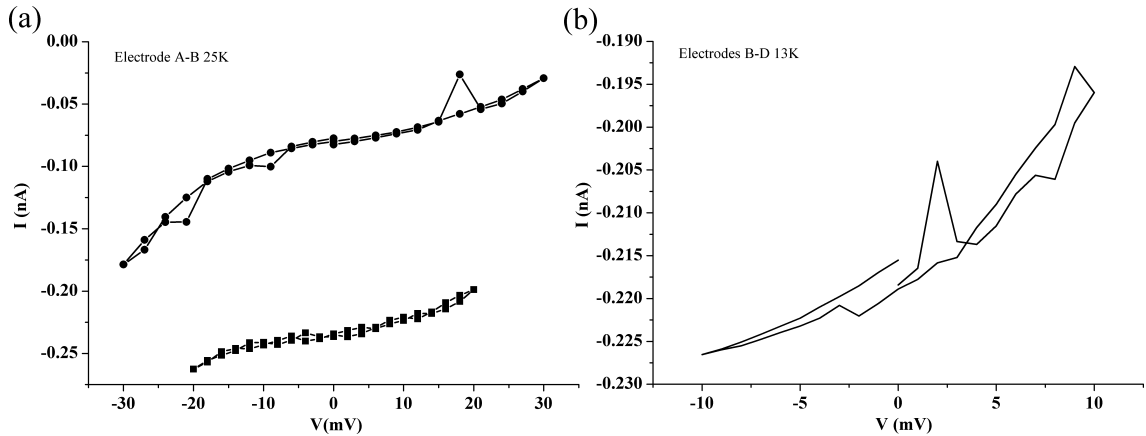


Figure B.4: $I - V$ curves of device #23338b on NGO (100), measured between electrode pairs (a) A-B at 25 K, and (b) B-D at 13 K.

Device #23482d on a STO (110), fabricated by graphene transfer in the ethanol-water mixture has a resistance of about $20 \text{ G}\Omega$.

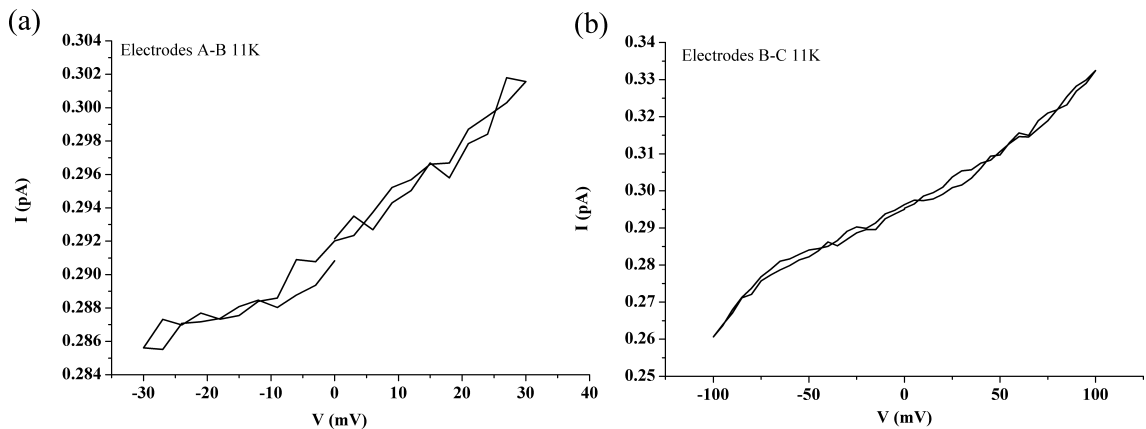


Figure B.5: $I - V$ curves of device #23482d on STO (110), measured between electrode pairs (a) A-B at 11 K, and (b) B-C at 11 K.

B. OTHER GRAPHENE SPIN-VALVES RESULTS

Appendix C

List of samples

C. LIST OF SAMPLES

Sample number	Deposition date	Substrate	Layer 1 and condition	Layer 2 and condition	Layer 3 and condition
#22908	06/12/2010	NGO (001)	<u>LSMO 0.33;</u> 5x5 mm 2	A (800°C, 5 Pa, 1 h); D (775°C, 162 mJ, 15 Pa, 261 pulses); PA (750°C, 55 kPa).	
#22920	13/01/2011	NGO (001)	<u>LSMO 0.33;</u> 5x5 mm 2	A (800°C, 5 Pa, 1 h); D (775°C, 162 mJ, 15 Pa, 1240 pulses); PA (750°C, 55 kPa).	
#22931	24/01/2011	NGO (001)	<u>LCMO 0.3;</u> A (800°C, 5 Pa, 1 h); D (775°C, 162 mJ, 15 Pa, 833 pulses);	<u>LCMO 0.42;</u> D (775°C, 162 mJ, 15 Pa, 125 pulses);	<u>LCMO 0.3;</u> D (775°C, 162 mJ, 15 Pa, 417 pulses); PA (750°C, 55 kPa).
#22961	07/03/2011	NGO (001)	<u>LSMO 0.33;</u> A (800°C, 5 Pa, 1 h); D (775°C, 162 mJ, 15 Pa, 833 pulses);	<u>BTO;</u> D (775°C, 162 mJ, 15 Pa, 15 pulses);	<u>LSMO 0.33;</u> D (775°C, 162 mJ, 15 Pa, 417 pulses); PA (750°C, 55 kPa).
#22963	13/03/2011	NGO (001)	<u>LSMO 0.33;</u> A (800°C, 5 Pa, 1 h); D (775°C, 162 mJ, 15 Pa, 2066 pulses);	<u>BTO;</u> D (775°C, 162 mJ, 15 Pa, 15 pulses);	<u>LCMO 0.3;</u> D (775°C, 162 mJ, 15 Pa, 417 pulses); PA (750°C, 55 kPa).
#22983	18/04/2011	NGO (001)	<u>LSMO 0.33;</u> A (800°C, 5 Pa, 1 h); D (775°C, 162 mJ, 15 Pa, 1653 pulses);	<u>BTO;</u> D (775°C, 162 mJ, 15 Pa, 15 pulses);	<u>LCMO 0.3;</u> D (775°C, 162 mJ, 15 Pa, 417 pulses); PA (750°C, 55 kPa).
#22988	29/04/2011	NGO (001)	<u>LSMO 0.33;</u> A (800°C, 5 Pa, 1 h); D (775°C, 162 mJ, 15 Pa, 1567 pulses);	<u>BTO;</u> D (775°C, 162 mJ, 15 Pa, 10 pulses); PA (750°C, 56 kPa).	

#23005	25/05/2011	NGO (001)	<u>LSMO 0.33:</u> A (800°C, 5 Pa, 1 h); D (775°C, 180 mJ, 15 Pa, 207 pulses); PA (750°C, 57 kPa).
#23030	15/07/2011	NGO (001)	<u>SRO:</u> A (800°C, 15 Pa, 1 h); D (600°C, 150 mJ, 10 Pa, 360 pulses); PA (500°C, 53 kPa).
#23039	25/07/2011	NGO (001)	<u>SRO:</u> A (800°C, 15 Pa, 1 h); D (775°C, 150 mJ, 10 Pa, 360 pulses); PA (500°C, 53 kPa).
#23043	11/08/2011	NGO (001)	<u>SRO:</u> A (800°C, 15 Pa, 1 h); D (700°C, 150 mJ, 10 Pa, 600 pulses); PA (500°C, 55 kPa).
#23056	05/09/2011	NGO (001)	<u>SRO:</u> A (800°C, 15 Pa, 1 h); D (600°C, 150 mJ, 15 Pa, 600 pulses); PA (500°C, 56 kPa).
#23062	13/09/2011	NGO (001)	<u>SRO:</u> A (800°C, 15 Pa, 1 h); D (600°C, 150 mJ, 10 Pa, 600 pulses); PA (500°C, 55 kPa).
#23063	16/09/2011	NGO (001)	<u>LSMO 0.33:</u> <u>STO:</u> A (800°C, 15 Pa, 1 h); D (775°C, 165 mJ, 15 Pa, 1567 pulses); D (775°C, 162 mJ, 15 Pa, 40 pulses); PA (750°C, 55 kPa).
#23077	26/10/2011	NGO (001)	<u>LAO:</u> A (800°C, 15 Pa, 1 h); D (775°C, 162 mJ, 15 Pa, 600 pulses); PA (750°C, 57 kPa).

C. LIST OF SAMPLES

#23088	11/11/2011	STO (001)	<u>SRO:</u> HF etched A (800°C, 15 Pa, 1 h); D (600°C, 150 mJ, 10 Pa, 360 pulses); PA (500°C, 55 kPa).
#23094	23/11/2011	NGO (001)	Annealed at 800°C, 15 Pa for 1 hr to check the substrate topography
#23097	25/11/2011	STO (001)	<u>SRO:</u> Annealed at 1000°C A (800°C, 15 Pa, 1 h); D (600°C, 180 mJ, 10 Pa, 360 pulses); PA (500°C, 48 kPa).
#23102	02/12/2011	NGO (001)	<u>LAO:</u> A (950°C, 15 Pa, 1 h); D (775°C, 162 mJ, 15 Pa, 360 pulses); PA (750°C, 54 kPa).
#23104	08/12/2011	NGO (001)	<u>LAO:</u> A (800°C, 15 Pa, 1 h); D (775°C, 162 mJ, 15 Pa, 360 pulses); PA (750°C, 54 kPa).
#23106	12/12/2011	NGO (001)	<u>STO:</u> A (800°C, 15 Pa, 1 h); D (775°C, 180 mJ, 15 Pa, 300 pulses); PA (750°C, 55 kPa).
#23111	18/12/2011	STO (001)	<u>SRO:</u> A (800°C, 15 Pa, 1 h); D (600°C, 180 mJ, 10 Pa, 360 pulses); PA (500°C, 48 kPa).
#23126	06/02/2012	NGO (001)	<u>LSMO 0.33:</u> 5x5 mm 2 A (800°C, 15 Pa, 1 h); D (775°C, 162 mJ, 15 Pa, 1000 pulses); PA (750°C, 53 kPa).

#23128	08/02/2012	NGO (001)	<u>LSMO 0.33:</u> 5x5 mm A (800°C, 15 Pa, 1 h); 2 D (775°C, 162 mJ, 15 Pa, 1000 pulses); PA (750°C, 53 kPa).
#23167	24/05/2012	NGO (001)	<u>LSMO 0.33:</u> Calibration run with the new heater A (800°C, 15 Pa, 1 h); D (775°C, 162 mJ, 15 Pa, 1567 pulses); PA (750°C, 56 kPa).
#23172	28/05/2012	NGO (001)	<u>LSMO 0.33:</u> Calibration run with the new heater A (800°C, 15 Pa, 1 h); D (800°C, 180 mJ, 15 Pa, 1567 pulses); PA (750°C, 56 kPa).
#23181	07/07/2012	NGO (001)	<u>LSMO 0.33:</u> Calibration run with the new heater A (800°C, 15 Pa, 1 h); D (775°C, 180 mJ, 15 Pa, 1567 pulses); PA (750°C, 53 kPa).
#23189	18/06/2012	NGO (001)	<u>LSMO 0.33:</u> Calibration run with the new heater A (800°C, 15 Pa, 1 h); D (775°C, 180 mJ, 15 Pa, 1567 pulses); PA (750°C, 54.6 kPa).
#23193	22/06/2012	NGO (001)	<u>LSMO 0.33:</u> <u>LAO:</u> A (800°C, 15 Pa, 1 h); D (775°C, 180 mJ, 15 Pa, 1567 pulses); D (775°C, 180 mJ, 15 Pa, 10 pulses); PA (750°C, 54.6 kPa).
#23199	28/06/2012	NGO (001)	<u>LSMO 0.33:</u> <u>LAO:</u> A (800°C, 15 Pa, 1 h); D (775°C, 180 mJ, 15 Pa, 1567 pulses); D (775°C, 180 mJ, 15 Pa, 10 pulses); PA (750°C, 54.6 kPa).
#23224	16/07/2012	NGO (001)	<u>LSMO 0.33:</u> <u>BTO:</u> <u>SRO:</u> A (800°C, 15 Pa, 1 h); D (775°C, 180 mJ, 15 Pa, 1045 pulses); D (775°C, 180 mJ, 15 Pa, 35 pulses); D (600°C, 150 mJ, 10 Pa, 1045 pulses); PA (500°C, 55 kPa).

C. LIST OF SAMPLES

#23229	17/17/2012	NGO (001)	<u>SRO:</u> A (800°C, 15 Pa, 1 h); D (600°C, 150 mJ, 10 Pa, 1045 pulses);	<u>BTO:</u> D (775°C, 180 mJ, 15 Pa, 35 pulses);	<u>LSMO 0.33:</u> D (775°C, 180 mJ, 15 Pa, 1045 pulses); PA (500°C, 54.6 kPa).
#23238	21/07/2012	NGO (001)	<u>LSMO 0.33:</u> A (800°C, 15 Pa, 1 h); D (775°C, 180 mJ, 15 Pa, 174 pulses); PA (750°C, 54.6 kPa).		
#23260	08/08/2012	Si	<u>Au:</u> D (RT, 180 mJ, 1.95e-6 mbar, 600 pulses);		
#23267	17/08/2012	NGO (001)	<u>LSMO 0.33:</u> A (800°C, 15 Pa, 1 h); D (775°C, 180 mJ, 15 Pa, 174 pulses); PA (750°C, 55 kPa).		
#23275	28/08/2012	STO (001)	<u>LSMO 0.33:</u> A (800°C, 15 Pa, 1 h); D (775°C, 180 mJ, 15 Pa, 174 pulses); PA (750°C, 55 kPa, 1 hr).		
#23296	27/09/2012	STO (001)	<u>LSMO 0.33:</u> A (800°C, 15 Pa, 1 h); D (775°C, 180 mJ, 15 Pa, 1567 pulses); PA (750°C, 55 kPa, 1 hr).		
#23300	01/10/2012	#23275a	<u>Au:</u> D (RT, 160 mJ, 1.95e-6 mbar, 600 pulses).		
#23325	22/10/2012	#23267	<u>NGO:</u> D (RT, 160 mJ, 15 Pa, 5 Hz, 2500 pulses). PA (750°C, 55 kPa, 1 hr).		
#23338	27/10/2012	NGO (100)	<u>LSMO 0.33:</u> A (800°C, 15 Pa, 1 h); D (775°C, 180 mJ, 15 Pa, 1567 pulses); PA (750°C, 52,7 kPa, 1 hr).		

#23341	29/10/2012	#23338	<u>NGO:</u> D (RT, 180 mJ, vacuum, 2 Hz, 1560 pulses).
#23371	30/11/2012	NGO (100)	<u>LSMO 0.33:</u> A (800°C, 15 Pa, 1 h); D (775°C, 180 mJ, 15 Pa, 1567 pulses); PA (750°C, 53 kPa, 1 hr).
#23408	11/02/2013	STO (110)	<u>LSMO 0.33:</u> A (800°C, 15 Pa, 1 h); D (775°C, 180 mJ, 15 Pa, 1567 pulses); PA (750°C, 53 kPa, 1 hr).
#23419	20/02/2013	STO (110)	<u>LSMO 0.33:</u> A (800°C, 15 Pa, 1 h); D (775°C, 180 mJ, 15 Pa, 1000 pulses); PA (750°C, 55 kPa, 1 hr).
#23439	08/03/2013	#23419	<u>NGO:</u>
		#23408	D (RT, 160 mJ, 2 Hz, 1-2 Pa, 2136 pulses for #23419). D (RT, 160 mJ, 2 Hz, 1-2 Pa, 1356 pulses for #23408).
#23443	10/03/2013	#23419	post annealing of patterned electrodes
		#23408	PA (750°C, 55 kPa, 1 hr).
#23450	14/03/2013	NGO (001)	<u>BTO:</u> A (800°C, 5 Pa, 1 h); D (775°C, 180 mJ, 10 Pa, 250 pulses); PA (750°C, 55 kPa, 1 hr).
#23454	17/03/2013	NGO (001)	<u>LSMO 0.33:</u> <u>BTO:</u> A (800°C, 5Pa, 1 h); D (775°C, 180 mJ, 15 Pa, 714 pulses); D (775°C, 180 mJ, 10 Pa, 29 pulses); PA (750°C, 55 kPa, 1 hr).
#23455	17/03/2013	NGO (001)	<u>LSMO 0.33:</u> <u>BTO:</u> A (800°C, 5Pa, 1 h); D (775°C, 180 mJ, 15 Pa, 680 pulses); D (775°C, 180 mJ, 10 Pa, 18 pulses); PA (750°C, 55 kPa, 1 hr).

C. LIST OF SAMPLES

#23457	18/03/2013	NGO (001)	<u>LSMO 0.33:</u> A (800°C, 5Pa, 1 h); D (775°C, 180 mJ, 15 Pa, 680 pulses);	<u>BTO:</u> D (775°C, 180 mJ, 10 Pa, 18 pulses); PA (750°C, 55 kPa, 1 hr).
#23460	19/03/2013	NGO (001)	<u>LSMO 0.33:</u> A (800°C, 5Pa, 1 h); D (775°C, 180 mJ, 15 Pa, 680 pulses);	<u>BTO:</u> D (775°C, 180 mJ, 10 Pa, 18 pulses); PA (750°C, 55 kPa, 1 hr).
#23479	31/03/2013	NGO (001)	<u>LSMO 0.33:</u> annealed at 950°C in O ₂ , 1 hr	A (800°C, 15 Pa, 0.5 h); D (775°C, 180 mJ, 15 Pa, 4320 pulses with mask); PA (750°C, 55 kPa, 1 hr).
#23480	01/04/2013	STO (110)	<u>LSMO 0.33:</u> annealed at 950°C in O ₂ , 1 hr	A (800°C, 15 Pa, 0.5 h); D (775°C, 180 mJ, 15 Pa, 4440 pulses with mask); PA (750°C, 55 kPa, 1 hr).
#23481	03/04/2013	STO (110)	<u>LSMO 0.33:</u> annealed at 950°C in O ₂ , 1 hr	A (800°C, 15 Pa, 0.5 h); D (775°C, 180 mJ, 15 Pa, 4440 pulses with mask); PA (750°C, 55 kPa, 1 hr).
#23482	05/04/2013	STO (110)	<u>LSMO 0.33:</u> annealed at 950°C in O ₂ , 1 hr	A (800°C, 15 Pa, 0.5 h); D (775°C, 180 mJ, 15 Pa, 4440 pulses with mask); PA (750°C, 55 kPa, 1 hr).
#23488	09/04/2013	STO (110)	<u>LSMO 0.33:</u> annealed at 950°C in O ₂ , 1 hr	A (800°C, 15 Pa, 0.5 h); D (775°C, 180 mJ, 15 Pa, 4440 pulses with mask); PA (750°C, 55 kPa, 1 hr).
#23498	15/04/2013	#23480 #23488	NGO: D (RT, 160 mJ, 1 Hz, 0 Pa, 240 pulses).	

#23500	16/04/2013	#23480	<u>NGO:</u> #23481 D (RT, 160 mJ, 1 Hz, 0 Pa, 360 pulses). #23482b #23482c
#23503	18/04/2013	#23482d	<u>NGO:</u> #23488b D (RT, 160 mJ, 1 Hz, 0 Pa, 690 pulses). #23488d #23488c #23488a #23482a
#23519	04/05/2013	NGO (100)	<u>LSMO 0.33;</u> annealed at A (800°C, 15 Pa, 0.5 h); 950°C in O ₂ , D (775°C, 180 mJ, 15 Pa, 4440 pulses with mask); 1 hr PA (750°C, 55 kPa, 1 hr).
#23539	21/05/2013	NGO (100)	<u>LSMO 0.33;</u> annealed at A (800°C, 15 Pa, 0.5 h); 950°C in O ₂ , D (775°C, 180 mJ, 15 Pa, 4440 pulses with mask); 1 hr PA (750°C, 55 kPa, 1 hr).
#23541	23/05/2013	NGO (100)	<u>LSMO 0.33;</u> annealed at A (800°C, 15 Pa, 0.5 h); 950°C in O ₂ , D (775°C, 180 mJ, 15 Pa, 4440 pulses with mask); 1 hr PA (750°C, 55 kPa, 1 hr).
#23545	27/05/2013	NGO (100)	<u>LSMO 0.33;</u> annealed at A (800°C, 15 Pa, 0.5 h); 950°C in O ₂ , D (775°C, 180 mJ, 15 Pa, 4440 pulses with mask); 1 hr PA (750°C, 55 kPa, 1 hr).
#23548	31/05/2013	#23519	<u>NGO:</u>
		#23541b	D (RT, 160 mJ, 1 Hz, 0 Pa, 480 pulses).
#23549	03/06/2013	#23541c	<u>NGO:</u>
		#23539c	D (RT, 160 mJ, 1 Hz, 0 Pa, 600 pulses).
		#23539d	

C. LIST OF SAMPLES

#23562	16/06/2013	NGO (100)	<u>LSMO 0.33:</u> annealed at 950°C in O ₂ , 1 hr	A (800°C, 15 Pa, 0.5 h); D (775°C, 180 mJ, 15 Pa, 4440 pulses with mask); PA (750°C, 55 kPa, 1 hr).
#23574	25/06/2013	STO (110)	<u>LSMO 0.33:</u> annealed at 950°C in O ₂ , 1 hr	A (800°C, 15 Pa, 0.5 h); D (775°C, 180 mJ, 15 Pa, 4440 pulses with mask); PA (750°C, 55 kPa, 1 hr).
#23595	15/07/2013	#23541a #23545 #23574b #23562	NGO: D (RT, 160 mJ, 1 Hz, 0 Pa, 720 pulses).	

References

- [1] A. Fert and I. Campbell, “Two-Current Conduction in Nickel,” *Physical Review Letters*, vol. 21, no. 16, pp. 1190–1192, 1968. [5](#)
- [2] A. Fert, “The origin, development and future of spintronics,” *Uspekhi Fizicheskikh Nauk*, vol. 178, no. 12, p. 1336, 2008. [5, 6](#)
- [3] M. Johnson and R. Silsbee, “Interfacial charge-spin coupling: Injection and detection of spin magnetization in metals,” *Physical Review Letters*, vol. 55, no. 17, pp. 1790–1793, 1985. [5, 7, 19, 22](#)
- [4] P. van Son, H. van Kempen, and P. Wyder, “Boundary Resistance of the Ferromagnetic-Nonferromagnetic Metal Interface,” *Physical Review Letters*, vol. 58, no. 21, pp. 2271–2273, 1987. [6, 7](#)
- [5] S. Datta and B. Das, “Electronic analog of the electro-optic modulator,” *Applied Physics Letters*, vol. 56, no. 7, pp. 665–667, 1990. [6, 7, 23](#)
- [6] T. Valet and A. Fert, “Theory of the perpendicular magnetoresistance in magnetic multilayers,” *Physical Review B*, vol. 48, no. 10, pp. 7099–7113, 1993. [8, 10, 13, 16, 17, 149](#)
- [7] A. Fert and H. Jaffrè, “Conditions for efficient spin injection from a ferromagnetic metal into a semiconductor,” *Physical Review B*, vol. 64, p. 184420, 2001. [8, 10, 14, 15, 16, 149](#)
- [8] A. Fert, J. George, H. Jaffrè, and R. Mattana, “Semiconductors between spin-polarized sources and drains,” *IEEE Transactions on Electron Devices*, vol. 54, pp. 921–932, 2007. [8](#)
- [9] G. Schmidt, D. Ferrand, L. W. Molenkamp, A. T. Filip, and B. J. van Wees, “Fundamental obstacle for electrical spin injection from ferromagnetic metal into a diffusive semiconductor,” *Physical Review B*, vol. 62, no. 8, p. R4790, 2000. [15](#)

REFERENCES

- [10] E. Rashba, “Theory of electrical spin injection: Tunnel contacts as a solution of the conductivity mismatch problem,” *Physical Review B*, vol. 62, no. 24, pp. R16267–R16270, 2000. [15](#)
- [11] B. Dlubak, M.-B. Martin, C. Deranlot, B. Servet, S. Xavier, R. Mattana, M. Sprinkle, C. Berger, W. A. De Heer, F. Petroff, *et al.*, “Highly efficient spin transport in epitaxial graphene on SiC,” *Nature Physics*, vol. 8, no. 7, pp. 557–561, 2012. [18](#), [30](#), [32](#), [33](#), [35](#), [142](#), [143](#), [146](#)
- [12] T. Maassen, I. Vera-Marun, M. Guimarães, and B. van Wees, “Contact-induced spin relaxation in hanle spin precession measurements,” *Physical Review B*, vol. 86, no. 23, p. 235408, 2012. [19](#), [22](#)
- [13] F. Jedema, M. Nijboer, A. Filip, and B. Van Wees, “Spin injection and spin accumulation in all-metal mesoscopic spin valves,” *Physical Review B*, vol. 67, no. 8, p. 085319, 2003. [19](#)
- [14] F. Jedema, M. Costache, H. Heersche, J. Baselmans, and B. van Wees, “Electrical detection of spin accumulation and spin precession at room temperature in metallic spin valves,” *Applied physics letters*, vol. 81, no. 27, pp. 5162–5164, 2002. [19](#)
- [15] M. Popinciuc, C. Józsa, P. J. Zomer, N. Tombros, a. Veligura, H. T. Jonkman, and B. J. van Wees, “Electronic spin transport in graphene field-effect transistors,” *Physical Review B*, vol. 80, no. 21, pp. 1–13, 2009. [19](#), [31](#), [35](#)
- [16] S. Takahashi and S. Maekawa, “Spin injection and detection in magnetic nanostructures,” *Physical Review B*, vol. 67, no. 5, p. 052409, 2003. [19](#)
- [17] N. Tombros, C. Jozsa, M. Popinciuc, H. T. Jonkman, and B. J. van Wees, “Electronic spin transport and spin precession in single graphene layers at room temperature.,” *Nature*, vol. 448, pp. 571–4, 2007. [20](#), [31](#), [32](#), [35](#)
- [18] E. E. Y. Tsymbal and I. Žutić, *Handbook of spin transport and magnetism*. CRC Press, 2012. [20](#)
- [19] J. Fabian, A. Matos-Abiague, C. Ertler, P. Stano, and I. Zutic, “Semiconductor spintronics,” *Acta Physica Slovaca*, vol. 57, no. 4, pp. 565 – 907, 2007. [20](#), [21](#)
- [20] I. Žutić, J. Fabian, and S. D. Sarma, “Spintronics: Fundamentals and applications,” *Reviews of modern physics*, vol. 76, no. 2, p. 323, 2004. [20](#)

- [21] F. Jedema, H. Heersche, A. Filip, J. Baselmans, and B. Van Wees, “Electrical detection of spin precession in a metallic mesoscopic spin valve,” *Nature*, vol. 416, no. 6882, pp. 713–716, 2002. [22](#)
- [22] N. Tombros, S. Tanabe, A. Veligura, C. Jozsa, M. Popinciuc, H. Jonkman, and B. van Wees, “Anisotropic Spin Relaxation in Graphene,” *Physical Review Letters*, vol. 101, no. 4, pp. 2–5, 2008. [22](#), [35](#)
- [23] H. Kroto, A. Allaf, and S. Balm, “C₆₀: Buckminsterfullerene,” *Chemical Reviews*, vol. 91, no. 6, pp. 1213–1235, 1991. [23](#)
- [24] S. Iijima *et al.*, “Helical microtubules of graphitic carbon,” *nature*, vol. 354, no. 6348, pp. 56–58, 1991. [23](#)
- [25] K. S. Novoselov, A. K. Geim, S. V. Morozov, D. Jiang, Y. Zhang, S. V. Dubonos, I. V. Grigorieva, and A. A. Firsov, “Electric field effect in atomically thin carbon films,” *Science*, vol. 306, pp. 666–9, 2004. [23](#), [29](#)
- [26] K. Tsukagoshi, B. W. Alphenaar, and H. Ago, “Coherent transport of electron spin in a ferromagnetically contacted carbon nanotube,” *Nature*, vol. 401, no. 6753, pp. 572–574, 1999. [23](#), [25](#)
- [27] K. Tsukagoshi and B. Alphenaar, “Spin-polarized transport in carbon nanotubes,” *Superlattices and Microstructures*, vol. 27, no. 5, pp. 565–570, 2000. [23](#)
- [28] B. Alphenaar, K. Tsukagoshi, and H. Ago, “Spin electronics using carbon nanotubes,” *Physica E: Low-dimensional Systems and Nanostructures*, vol. 6, no. 1, pp. 848–851, 2000. [23](#), [24](#)
- [29] S. Chakraborty, K. M. Walsh, B. W. Alphenaar, L. Liu, and K. Tsukagoshi, “Temperature-mediated switching of magnetoresistance in Co-contacted multiwall carbon nanotubes,” *Applied Physics Letters*, vol. 83, no. 5, pp. 1008–1010, 2003. [24](#), [26](#), [27](#)
- [30] B. Zhao, I. Monch, H. Vinzelberg, T. Muhl, and C. M. Schneider, “Spin-coherent transport in ferromagnetically contacted carbon nanotubes,” *Applied Physics Letters*, vol. 80, no. 17, pp. 3144–3146, 2002. [24](#)
- [31] B. Zhao, I. Monch, T. Muhl, H. Vinzelberg, and C. M. Schneider, “Spin-dependent transport in multiwalled carbon nanotubes,” *Journal of Applied Physics*, vol. 91, no. 10, pp. 7026–7028, 2002. [24](#), [25](#)

REFERENCES

- [32] N. Tombros, S. Van Der Molen, and B. Van Wees, “Separating spin and charge transport in single-wall carbon nanotubes,” *Physical Review B*, vol. 73, no. 23, p. 233403, 2006. [24](#), [26](#), [27](#)
- [33] D. Orgassa, G. J. Mankey, and H. Fujiwara, “Spin injection into carbon nanotubes and a possible application in spin-resolved scanning tunnelling microscopy,” *Nanotechnology*, vol. 12, pp. 281–4, 2001. [24](#)
- [34] A. Jensen, J. R. Hauptmann, J. Nygård, and P. E. Lindelof, “Magnetoresistance in ferromagnetically contacted single-wall carbon nanotubes,” *Physical Review B*, vol. 72, no. 3, p. 035419, 2005. [25](#)
- [35] C. Gould, C. Rüster, T. Jungwirth, E. Grgis, G. Schott, R. Giraud, K. Brunner, G. Schmidt, and L. Molenkamp, “Tunneling anisotropic magnetoresistance: a spin-valve-like tunnel magnetoresistance using a single magnetic layer,” *Physical review letters*, vol. 93, no. 11, p. 117203, 2004. [25](#), [143](#)
- [36] L. E. Hueso, J. M. Pruneda, V. Ferrari, G. Burnell, J. P. Valdés-Herrera, B. D. Simons, P. B. Littlewood, E. Artacho, A. Fert, and N. D. Mathur, “Transformation of spin information into large electrical signals using carbon nanotubes,” *Nature*, vol. 445, no. 7126, pp. 410–413, 2007. [26](#), [27](#), [140](#), [141](#), [143](#)
- [37] S. Sahoo, T. Kontos, J. Furer, C. Hoffmann, M. Gräber, A. Cottet, and C. Schönenberger, “Electric field control of spin transport,” *Nature Physics*, vol. 1, no. 2, pp. 99–102, 2005. [27](#), [28](#)
- [38] H. T. Man, I. J. W. Wever, and A. F. Morpurgo, “Spin-dependent quantum interference in single-wall carbon nanotubes with ferromagnetic contacts,” *Physical Review B*, vol. 73, pp. 1–4, June 2006. [27](#)
- [39] D. Huertas-Hernando, F. Guinea, and A. Brataas, “Spin-orbit coupling in curved graphene, fullerenes, nanotubes, and nanotube caps,” *Physical Review B*, vol. 74, no. 15, 2006. [27](#)
- [40] Y. Zhang, T.-T. Tang, C. Girit, Z. Hao, M. C. Martin, A. Zettl, M. F. Crommie, Y. R. Shen, and F. Wang, “Direct observation of a widely tunable bandgap in bilayer graphene,” *Nature*, vol. 459, no. 7248, pp. 820–823, 2009. [28](#)
- [41] M. Terrones, A. R. Botello-Méndez, J. Campos-Delgado, F. López-Urías, Y. I. Vega-Cantú, F. J. Rodríguez-Macías, A. L. Elías, E. Muñoz-Sandoval, A. G. Cano-Márquez, J.-C. Charlier, *et al.*, “Graphene and graphite nanoribbons: Morphology,

- properties, synthesis, defects and applications," *Nano Today*, vol. 5, no. 4, pp. 351–372, 2010. [28](#)
- [42] E. W. Hill, A. K. Geim, K. Novoselov, F. Schedin, and P. Blake, "Graphene spin valve devices," *Magnetics, IEEE Transactions on*, vol. 42, no. 10, pp. 2694–2696, 2006. [29](#), [35](#)
- [43] W. Han, K. Pi, K. McCreary, Y. Li, J. J. Wong, A. Swartz, and R. Kawakami, "Tunneling spin injection into single layer graphene," *Physical review letters*, vol. 105, no. 16, p. 167202, 2010. [29](#), [30](#), [34](#), [35](#)
- [44] W. Han, K. Pi, W. Bao, K. M. McCreary, Y. Li, W. H. Wang, C. N. Lau, and R. K. Kawakami, "Electrical detection of spin precession in single layer graphene spin valves with transparent contacts," *Applied Physics Letters*, vol. 94, no. 22, p. 222109, 2009. [29](#), [35](#)
- [45] T. Yamaguchi, S. Masubuchi, K. Iguchi, R. Moriya, T. Machida, and O. Al, "Tunnel spin injection into graphene using Al_2O_3 barrier grown by atomic layer deposition on functionalized graphene surface," *Journal of Magnetism and Magnetic Materials*, vol. 324, no. 5, pp. 849–852, 2012. [30](#), [33](#), [35](#), [142](#)
- [46] C. Józsa, T. Maassen, M. Popinciuc, P. J. Zomer, A. Veligura, H. T. Jonkman, and B. J. van Wees, "Linear scaling between momentum and spin scattering in graphene," *Physical Review B*, vol. 80, p. 241403, Dec. 2009. [30](#), [31](#), [35](#)
- [47] W. Han and R. K. Kawakami, "Spin Relaxation in Single-Layer and Bilayer Graphene," *Physical Review Letters*, vol. 107, p. 047207, 2011. [31](#), [35](#), [142](#)
- [48] T.-Y. Yang, J. Balakrishnan, F. Volmer, A. Avsar, M. Jaiswal, J. Samm, S. Ali, A. Pachoud, M. Zeng, M. Popinciuc, *et al.*, "Observation of long spin-relaxation times in bilayer graphene at room temperature," *Physical review letters*, vol. 107, no. 4, p. 047206, 2011. [31](#), [35](#)
- [49] A. Avsar, T.-Y. Yang, S. Bae, J. Balakrishnan, F. Volmer, M. Jaiswal, Z. Yi, S. R. Ali, G. Guntherodt, B. H. Hong, *et al.*, "Toward wafer scale fabrication of graphene based spin valve devices," *Nano letters*, vol. 11, no. 6, pp. 2363–2368, 2011. [31](#), [35](#)
- [50] T. Maassen, F. Dejene, M. Guimaraes, C. Józsa, and B. Van Wees, "Comparison between charge and spin transport in few-layer graphene," *Physical Review B*, vol. 83, no. 11, p. 115410, 2011. [31](#), [32](#), [35](#), [142](#)

REFERENCES

- [51] W. Wang, K. Pi, Y. Li, Y. Chiang, P. Wei, J. Shi, and R. Kawakami, “Magnetotransport properties of mesoscopic graphite spin valves,” *Physical Review B*, vol. 77, no. 2, pp. 1–4, 2008. [31](#), [32](#), [34](#), [35](#), [142](#)
- [52] K. Pi, W. Han, K. M. McCreary, A. G. Swartz, Y. Li, and R. K. Kawakami, “Manipulation of Spin Transport in Graphene by Surface Chemical Doping,” *Physical Review Letters*, vol. 104, p. 187201, May 2010. [31](#)
- [53] T. Maassen, J. J. van den Berg, N. IJbema, F. Fromm, T. Seyller, R. Yakimova, and B. J. van Wees, “Long spin relaxation times in wafer scale epitaxial graphene on SiC (0001),” *Nano letters*, vol. 12, no. 3, pp. 1498–1502, 2012. [32](#), [35](#)
- [54] P. Zomer, M. Guimarães, N. Tombros, and B. van Wees, “Long-distance spin transport in high-mobility graphene on hexagonal boron nitride,” *Physical Review B*, vol. 86, no. 16, p. 161416, 2012. [32](#), [33](#), [35](#), [142](#)
- [55] K. Bolotin, K. Sikes, Z. Jiang, M. Klima, G. Fudenberg, J. Hone, P. Kim, and H. Stormer, “Ultrahigh electron mobility in suspended graphene,” *Solid State Communications*, vol. 146, no. 9, pp. 351–355, 2008. [32](#), [33](#)
- [56] T. Yamaguchi, Y. Inoue, S. Masubuchi, S. Morikawa, M. Onuki, K. Watanabe, T. Taniguchi, R. Moriya, and T. Machida, “Electrical spin injection into graphene through monolayer hexagonal boron nitride,” *Applied Physics Express*, vol. 6, no. 7, p. 073001, 2013. [34](#), [35](#)
- [57] S. Cho, Y.-F. Chen, and M. S. Fuhrer, “Gate-tunable graphene spin valve,” *Applied Physics Letters*, vol. 91, no. 12, p. 123105, 2007. [34](#), [35](#)
- [58] W. Han, W. Wang, K. Pi, K. McCreary, W. Bao, Y. Li, F. Miao, C. Lau, and R. Kawakami, “Electron-Hole Asymmetry of Spin Injection and Transport in Single-Layer Graphene,” *Physical Review Letters*, vol. 102, pp. 1–4, Apr. 2009. [35](#)
- [59] H. Goto, A. Kanda, T. Sato, S. Tanaka, Y. Ootuka, S. Odaka, H. Miyazaki, K. Tsukagoshi, and Y. Aoyagi, “Gate control of spin transport in multilayer graphene,” *Applied Physics Letters*, vol. 92, no. 21, p. 212110, 2008. [35](#), [142](#)
- [60] M. Ohishi, M. Shiraishi, R. Nouchi, T. Nozaki, T. Shinjo, and Y. Suzuki, “Spin Injection into a Graphene Thin Film at Room Temperature,” *Japanese Journal of Applied Physics*, vol. 46, no. 25, pp. L605–L607, 2007. [35](#)

- [61] M. Shiraishi, M. Ohishi, R. Nouchi, N. Mitoma, T. Nozaki, T. Shinjo, and Y. Suzuki, “Robustness of Spin Polarization in Graphene-Based Spin Valves,” *Advanced Functional Materials*, vol. 19, pp. 3711–3716, Dec. 2009. [35](#)
- [62] M. Nishioka and a. M. Goldman, “Spin transport through multilayer graphene,” *Applied Physics Letters*, vol. 90, no. 25, p. 252505, 2007. [35](#)
- [63] Y. Liu, H. Idzuchi, Y. Fukuma, O. Rousseau, Y. Otani, and W. Lew, “Spin injection properties in trilayer graphene lateral spin valves,” *Applied Physics Letters*, vol. 102, no. 3, pp. 033105–033105, 2013. [35](#)
- [64] G. Jonker and J. Van Santen, “Ferromagnetic compounds of manganese with perovskite structure,” *physica*, vol. 16, no. 3, pp. 337–349, 1950. [37](#), [47](#)
- [65] N. Mathur and P. Littlewood, “Mesoscopic texture in manganites,” *Physics Today*, vol. 56, p. 25, 2003. [38](#)
- [66] C. Zener, “Interaction between the d-Shells in the Transition Metals. II. Ferromagnetic Compounds of Manganese with Perovskite Structure,” *Physical Review*, vol. 82, no. 3, pp. 403–405, 1951. [37](#), [40](#), [42](#)
- [67] J. Goodenough, “Theory of the Role of Covalence in the Perovskite-Type Manganites $[\text{La}, \text{M(II)}]\text{MnO}_3$,” *Physical Review*, vol. 100, no. 2, pp. 564–573, 1955. [37](#), [45](#), [47](#)
- [68] E. Wollan and W. Koehler, “Neutron Diffraction Study of the Magnetic Properties of the Series of Perovskite-Type Compounds $[(1 - x)\text{La}, x\text{Ca}]\text{MnO}_3$,” *Physical Review*, vol. 100, no. 2, p. 545, 1955. [37](#)
- [69] S. Jin, T. H. Tiefel, M. McCormack, R. A. Fastnacht, R. Ramesh, and L. H. Chen, “Thousandfold Change in Resistivity in Magnetoresistive La-Ca-Mn-O Films.,” *Science (New York, N.Y.)*, vol. 264, no. 5157, pp. 413–415, 1994. [37](#), [38](#)
- [70] A. J. Millis, P. B. Littlewood, and B. I. Shraiman, “Double Exchange Alone Does Not Explain the Resistivity of $\text{La}_{1-x}\text{Sr}_x\text{MnO}_3$,” *Physical Review Letters*, vol. 74, no. 25, p. 5144, 1995. [37](#), [41](#)
- [71] A. Millis, B. I. Shraiman, and R. Mueller, “Dynamic Jahn-Teller effect and colossal magnetoresistance in $\text{La}_{1-x}\text{Sr}_x\text{MnO}_3$,” *Physical review letters*, vol. 77, pp. 175–178, 1996. [37](#), [41](#), [44](#)

REFERENCES

- [72] A. Millis, “Lattice effects in magnetoresistive manganese perovskites,” *Nature*, vol. 392, no. 6672, pp. 147–150, 1998. [37](#), [41](#)
- [73] J. M. D. Coey, “Mixed-valence manganites,” *Advances in Physics*, vol. 48, no. 2, pp. 167–293, 1999. [38](#), [39](#), [40](#)
- [74] J. M. D. Coey and C. L. Chien, “Half-Metallic Ferromagnetic Oxides,” *MRS Bulletin*, vol. 28, pp. 720–724, Jan. 2011. [38](#)
- [75] M. B. Salamon and M. Jaime, “The physics of manganites: Structure and transport,” *Reviews of Modern Physics*, vol. 73, no. 3, p. 583, 2001. [38](#)
- [76] A. Haghiri-Gosnet and J. Renard, “CMR manganites: physics, thin films and devices,” *Journal of Physics D: Applied Physics*, vol. 36, no. 8, p. R127, 2003. [38](#)
- [77] A. Ramirez, “Colossal magnetoresistance,” *Journal of Physics: Condensed Matter*, vol. 9, no. 39, p. 8171, 1997. [38](#)
- [78] E. Dagotto, T. Hotta, and A. Moreo, “Colossal magnetoresistant materials: the key role of phase separation,” *Physics Reports*, vol. 344, no. 1, pp. 1–153, 2001. [38](#)
- [79] D. G. Schlom, L.-Q. Chen, X. Pan, A. Schmehl, and M. A. Zurbuchen, “A thin film approach to engineering functionality into oxides,” *Journal of the American Ceramic Society*, vol. 91, no. 8, pp. 2429–2454, 2008. [38](#)
- [80] Y. Tokura and Y. Tomioka, “Colossal magnetoresistive manganites,” *Journal of Magnetism and Magnetic Materials*, vol. 200, pp. 1–23, 1999. [38](#), [43](#)
- [81] Y. Tokura, “Critical features of colossal magnetoresistive manganites,” *Reports on Progress in Physics*, vol. 69, no. 3, p. 797, 2006. [38](#)
- [82] J.-H. Park, E. Vescovo, H.-J. Kim, C. Kwon, R. Ramesh, and T. Venkatesan, “Direct evidence for a half-metallic ferromagnet,” *Nature*, vol. 392, no. 6678, pp. 794–796, 1998. [38](#), [47](#), [140](#)
- [83] M. Bowen, J.-L. Maurice, A. Barthélémy, M. Bibes, D. Imhoff, V. Bellini, R. Bertacco, D. Wortmann, P. Seneor, E. Jacquet, *et al.*, “Using half-metallic manganite interfaces to reveal insights into spintronics,” *Journal of Physics: Condensed Matter*, vol. 19, no. 31, p. 315208, 2007. [38](#)
- [84] M. Bibes and A. Barthelemy, “Oxide spintronics,” *Electron Devices, IEEE Transactions on*, vol. 54, no. 5, pp. 1003–1023, 2007. [38](#)

REFERENCES

- [85] A. Urushibara, Y. Moritomo, T. Arima, A. Asamitsu, G. Kido, and Y. Tokura, “Insulator-metal transition and giant magnetoresistance in $\text{La}_{1-x}\text{Sr}_x\text{MnO}_3$,” *Physical Review B*, vol. 51, no. 20, p. 14103, 1995. [39](#), [41](#), [47](#)
- [86] C. Zener, “Interaction Between the d Shells in the Transition Metals,” *Physical Review*, vol. 81, no. 3, pp. 440–444, 1951. [40](#)
- [87] J. García-Muñoz, J. Fontcuberta, M. Suaaidi, and X. Obradors, “Bandwidth narrowing in bulk magnetoresistive oxides,” *Journal of Physics: Condensed Matter*, vol. 8, no. 50, p. L787, 1996. [40](#)
- [88] P. de Gennes, “Effects of Double Exchange in Magnetic Crystals,” *Physical Review*, vol. 118, no. 1, pp. 141–154, 1960. [40](#)
- [89] R. Bertacco, A. Tagliaferri, M. Riva, L. Signorini, M. Cantoni, A. Cattoni, F. Ciccacci, B. Davidson, F. Maccherozzi, I. Vobornik, *et al.*, “Surface electronic and magnetic properties of $\text{La}_{2/3}\text{Sr}_{1/3}\text{MnO}_3$ thin films with extended metallicity above the Curie temperature,” *Physical Review B*, vol. 78, no. 3, p. 035448, 2008. [41](#), [49](#), [52](#)
- [90] H. Hwang, S. Cheong, P. Radaelli, M. Marezio, and B. Batlogg, “Lattice effects on the magnetoresistance in doped lamno₃,” *Physical Review Letters*, vol. 75, no. 5, p. 914, 1995. [42](#), [47](#)
- [91] K. Tobe, T. Kimura, and Y. Tokura, “Anisotropic optical spectra of doped manganites with pseudocubic perovskite structure,” *Physical Review B*, vol. 69, no. 1, p. 014407, 2004. [42](#), [45](#), [46](#)
- [92] C. Booth, F. Bridges, G. Kwei, J. Lawrence, A. Cornelius, and J. Neumeier, “Direct Relationship between Magnetism and MnO₆ Distortions in $\text{La}_{1-x}\text{Ca}_x\text{MnO}_3$,” *Physical review letters*, vol. 80, no. 4, p. 853, 1998. [43](#), [44](#)
- [93] Y. Tokura, “Orbital Physics in Transition-Metal Oxides,” *Science*, vol. 288, pp. 462–468, Apr. 2000. [45](#), [49](#)
- [94] M. Tokunaga, N. Miura, Y. Tomioka, and Y. Tokura, “High-magnetic-field study of the phase transitions of $\text{R}_{1-x}\text{Ca}_x\text{MnO}_3$ ($\text{R} = \text{Pr}, \text{Nd}$),” *Physical Review B*, vol. 57, no. 9, p. 5259, 1998. [45](#)

REFERENCES

- [95] R. Bertacco, M. Portalupi, M. Marcon, L. Duo, F. Ciccacci, M. Bowen, J. Contour, and A. Barthelemy, “Unoccupied electron states of $\text{La}_{0.7}\text{Sr}_{0.3}\text{MnO}_3$,” *Journal of magnetism and magnetic materials*, vol. 242, pp. 710–712, 2002. [47](#), [140](#)
- [96] J.-H. Park, E. Vescovo, H.-J. Kim, C. Kwon, R. Ramesh, and T. Venkatesan, “Magnetic Properties at Surface Boundary of a Half-Metallic Ferromagnet $\text{La}_{0.7}\text{Sr}_{0.3}\text{MnO}_3$,” *Phys. Rev. Lett.*, vol. 81, pp. 1953–1956, Aug 1998. [48](#)
- [97] F. Reinert and S. Hfner, “Photoemission spectroscopy from early days to recent applications,” *New Journal of Physics*, vol. 7, no. 1, p. 97, 2005. [48](#)
- [98] Y. Lu, X. W. Li, G. Q. Gong, G. Xiao, A. Gupta, P. Lecoer, J. Z. Sun, Y. Y. Wang, and V. P. Dravid, “Large magnetotunneling effect at low magnetic fields in micrometer-scale epitaxial $\text{La}_{0.67}\text{Sr}_{0.33}\text{MnO}_3$ tunnel junctions,” *Physical Review B*, vol. 54, no. 12, pp. 8357–8360, 1996. [48](#), [140](#)
- [99] J. Sun, D. Abraham, K. Roche, and S. Parkin, “Temperature and bias dependence of magnetoresistance in doped manganite thin film trilayer junctions,” *Applied physics letters*, vol. 73, no. 7, pp. 1008–1010, 1998. [48](#)
- [100] V. Garcia, M. Bibes, A. Barthélémy, M. Bowen, E. Jacquet, J.-P. Contour, and A. Fert, “Temperature dependence of the interfacial spin polarization of $\text{La}_{2/3}\text{Sr}_{1/3}\text{MnO}_3$,” *Physical Review B*, vol. 69, p. 052403, 2004. [48](#)
- [101] H. Boschker, M. Mathews, E. Houwman, H. Nishikawa, A. Vailionis, G. Koster, G. Rijnders, and D. Blank, “Strong uniaxial in-plane magnetic anisotropy of (001)- and (011)-oriented $\text{La}_{0.67}\text{Sr}_{0.33}\text{MnO}_3$ thin films on NdGaO_3 substrates,” *Physical Review B*, vol. 79, no. 21, pp. 1–6, 2009. [48](#), [50](#), [57](#)
- [102] Y. Suzuki, H. Y. Hwang, and R. B. V. Dover, “The role of strain in magnetic anisotropy of manganite thin films,” *Science*, vol. 71, no. July, pp. 140–142, 1997. [48](#), [50](#), [54](#)
- [103] F. Tsui, M. C. Smoak, T. K. Nath, and C. B. Eom, “Strain-dependent magnetic phase diagram of epitaxial $\text{La}_{0.67}\text{Sr}_{0.33}\text{MnO}_3$ thin films,” *Applied Physics Letters*, vol. 76, no. 17, pp. 2421–2423, 2000. [48](#), [50](#), [54](#)
- [104] H. Nishikawa, E. Houwman, H. Boschker, M. Mathews, D. H. A. Blank, and G. Rijnders, “Rotation of the magnetic easy axis in $\text{La}_{0.67}\text{Sr}_{0.33}\text{MnO}_3$ thin film on NdGaO_3 (112),” *Applied Physics Letters*, vol. 94, no. 4, p. 042502, 2009. [48](#), [50](#), [54](#), [57](#)

REFERENCES

- [105] M. Mathews, E. P. Houwman, H. Boschker, G. Rijnders, and D. H. a. Blank, “Magnetization reversal mechanism in $\text{La}_{0.67}\text{Sr}_{0.33}\text{MnO}_3$ thin films on NdGaO_3 substrates,” *Journal of Applied Physics*, vol. 107, no. 1, p. 013904, 2010. [48](#), [50](#), [57](#), [82](#), [85](#), [92](#), [93](#), [94](#), [110](#)
- [106] A. Vailionis, H. Boschker, E. Houwman, G. Koster, G. Rijnders, and D. H. Blank, “Anisotropic stress relief mechanism in epitaxial $\text{La}_{0.67}\text{Sr}_{0.33}\text{MnO}_3$ films,” *Applied Physics Letters*, vol. 95, no. 15, pp. 152508–152508, 2009. [48](#), [55](#), [57](#)
- [107] H. Boschker, M. Mathews, P. Brinks, E. Houwman, A. Vailionis, G. Koster, D. H. A. Blank, and G. Rijnders, “Uniaxial contribution to the magnetic anisotropy of $\text{La}_{0.67}\text{Sr}_{0.33}\text{MnO}_3$ thin films induced by orthorhombic crystal structure,” *Journal of Magnetism and Magnetic Materials*, vol. 323, pp. 2632–2638, Nov. 2011. [48](#), [50](#), [55](#), [57](#)
- [108] L. M. Berndt, V. Balbarin, and Y. Suzuki, “Magnetic anisotropy and strain states of (001) and (110) colossal magnetoresistance thin films,” *Applied Physics Letters*, vol. 77, no. 18, p. 2903, 2000. [48](#), [50](#), [54](#), [57](#)
- [109] J. X. Ma, X. F. Liu, T. Lin, G. Y. Gao, J. P. Zhang, W. B. Wu, X. G. Li, and J. Shi, “Interface ferromagnetism in (110)-oriented $\text{La}_{0.67}\text{Sr}_{0.33}\text{MnO}_3/\text{SrTiO}_3$ ultrathin superlattices,” *Physical Review B*, vol. 79, p. 174424, 2009. [48](#), [50](#), [51](#), [57](#)
- [110] K. Steenbeck and R. Hiergeist, “Magnetic anisotropy of ferromagnetic $\text{La}_{0.67}(\text{Sr,Ca})_{0.33}\text{MnO}_3$ epitaxial films,” *Applied Physics Letters*, vol. 75, no. 12, p. 1778, 1999. [48](#), [50](#), [54](#)
- [111] D. Pesquera, G. Herranz, A. Barla, E. Pellegrin, F. Bondino, E. Magnano, F. Sánchez, and J. Fontcuberta, “Surface symmetry-breaking and strain effects on orbital occupancy in transition metal perovskite epitaxial films,” *Nature communications*, vol. 3, p. 1189, 2012. [48](#), [50](#), [51](#)
- [112] J.-L. Maurice, F. Pailloux, A. Barthélémy, O. Durand, D. Imhoff, R. Lyonnet, A. Rocher, and J.-P. Contour, “Strain relaxation in the epitaxy of $\text{La}_{2/3}\text{Sr}_{1/3}\text{MnO}_3$ grown by pulsed-laser deposition on SrTiO_3 (001),” *Philosophical Magazine*, vol. 83, no. 28, pp. 3201–3224, 2003. [48](#)
- [113] G. Gao, Z. Yin, Z. Huang, S. Jin, and W. Wu, “The thickness evolution of orthorhombic lattice distortions in heteroepitaxial $\text{La}_{0.67}\text{Ca}_{0.33}\text{MnO}_3/\text{NdGaO}_3$

REFERENCES

- (110)_{Or} observed by x-ray reciprocal space mapping,” *Journal of Physics D: Applied Physics*, vol. 41, no. 15, p. 152001, 2008. [48](#), [50](#)
- [114] M. Mathews, F. M. Postma, J. Cock Lodder, R. Jansen, G. Rijnders, and D. H. A. Blank, “Step-induced uniaxial magnetic anisotropy of La_{0.67}Sr_{0.33}MnO₃ thin films,” *Applied Physics Letters*, vol. 87, no. 24, p. 242507, 2005. [48](#), [54](#), [57](#)
- [115] L. Phillips, F. Maccherozzi, X. Moya, M. Ghidini, W. Yan, J. Soussi, S. Dhesi, and N. Mathur, “Tuning La_{0.67}Sr_{0.33}MnO₃ surface magnetism using LaMnO₃ and SrTiO₃ caps,” *Journal of Magnetism and Magnetic Materials*, vol. 355, no. 0, pp. 331 – 333, 2014. [48](#), [49](#), [50](#), [52](#), [73](#), [79](#)
- [116] S. Valencia, Z. Konstantinovic, D. Schmitz, A. Gaupp, L. Balcells, and B. Martínez, “Interfacial effects in manganite thin films with different capping layers of interest for spintronic applications,” *Physical Review B*, vol. 84, p. 024413, 2011. [48](#), [49](#), [52](#), [105](#)
- [117] H. Yamada, Y. Ogawa, Y. Ishii, H. Sato, M. Kawasaki, H. Akoh, and Y. Tokura, “Engineered interface of magnetic oxides,” *Science*, vol. 305, no. 5684, pp. 646–648, 2004. [48](#), [52](#)
- [118] J. J. Kavich, M. P. Warusawithana, J. W. Freeland, P. Ryan, X. Zhai, R. H. Kodama, and J. N. Eckstein, “Nanoscale suppression of magnetization at atomically assembled manganite interfaces: XMCD and XRMS measurements,” *Physical Review B*, vol. 76, p. 014410, 2007. [48](#), [52](#)
- [119] Y.-A. Soh, G. Aeppli, N. D. Mathur, and M. G. Blamire, “Mesoscale magnetism at the grain boundaries in colossal magnetoresistive films,” *Phys. Rev. B*, vol. 63, p. 020402, Dec 2000. [50](#)
- [120] L. Ranno, “Strain-induced magnetic anisotropy in epitaxial manganite films,” *Applied Surface Science*, vol. 188, pp. 170–175, Mar. 2002. [50](#)
- [121] Y. Konishi, Z. Fang, M. Izumi, T. Manako, M. Kasai, H. Kuwahara, M. Kawasaki, K. Terakura, and Y. Tokura, “Orbital-state-mediated phase-control of manganites,” *Journal of the Physical Society of Japan*, vol. 68, no. 12, pp. 3790–3793, 1999. [50](#)
- [122] a. Tebano, a. Orsini, P. G. Medaglia, and G. Balestrino, “Disentangling strain effects in manganite heterostructures,” *Applied Physics Letters*, vol. 94, no. 24, p. 242503, 2009. [50](#)

REFERENCES

- [123] Y. Konishi, “Epitaxial growth and strain of manganite thin films,” *Materials Science and Engineering B*, vol. 56, pp. 158–163, Nov. 1998. [50](#)
- [124] L. Phillips, M. Ghidini, X. Moya, F. Maccherozzi, S. Dhesi, and N. Mathur, “Low-temperature transverse magnetic domains in nominally uniaxial $\text{La}_{0.67}\text{Sr}_{0.33}\text{MnO}_3$ films on NdGaO_3 (001),” *Journal of Physics D: Applied Physics*, vol. 46, no. 3, p. 032002, 2013. [50](#), [54](#), [57](#), [79](#), [80](#), [82](#), [83](#), [108](#)
- [125] B. Wang, L. You, P. Ren, X. Yin, Y. Peng, B. Xia, L. Wang, X. Yu, S. M. Poh, P. Yang, *et al.*, “Oxygen-driven anisotropic transport in ultra-thin manganite films,” *Nature communications*, vol. 4, 2013. [50](#)
- [126] H. Boschker, J. Kautz, E. P. Houwman, G. Koster, D. H. Blank, and G. Rijnders, “Magnetic anisotropy and magnetization reversal of $\text{La}_{0.67}\text{Sr}_{0.33}\text{MnO}_3$ thin films on SrTiO_3 (110),” *Journal of Applied Physics*, vol. 108, p. 103906, 2010. [50](#), [82](#), [87](#), [97](#), [100](#), [110](#)
- [127] P. Perna, C. Rodrigo, E. Jimnez, F. J. Teran, N. Mikuszeit, L. Mchin, J. Camarero, and R. Miranda, “Tailoring magnetic anisotropy in epitaxial half metallic $\text{La}_{0.7}\text{Sr}_{0.3}\text{MnO}_3$ thin films,” *Journal of Applied Physics*, vol. 110, no. 1, p. 013919, 2011. [50](#), [54](#), [82](#)
- [128] Y. Suzuki, H. Y. Hwang, S.-W. Cheong, T. Siegrist, R. B. van Dover, a. Asamitsu, and Y. Tokura, “Magnetic anisotropy of doped manganite thin films and crystals,” *Journal of Applied Physics*, vol. 83, no. 11, p. 7064, 1998. [50](#), [54](#), [57](#)
- [129] Z.-H. Wang, G. Cristiani, and H.-U. Habermeier, “Uniaxial magnetic anisotropy and magnetic switching in $\text{La}_{0.67}\text{Sr}_{0.33}\text{MnO}_3$ thin films grown on vicinal SrTiO_3 (100),” *Applied physics letters*, vol. 82, p. 3731, 2003. [50](#), [54](#), [57](#)
- [130] A. Tebano, C. Aruta, S. Sanna, P. G. Medaglia, G. Balestrino, A. A. Sidorenko, R. De Renzi, G. Ghiringhelli, L. Braicovich, V. Bisogni, and N. B. Brookes, “Evidence of Orbital Reconstruction at Interfaces in Ultrathin $\text{La}_{0.67}\text{Sr}_{0.33}\text{MnO}_3$ Films,” *Physical Review Letters*, vol. 100, p. 137401, 2008. [50](#)
- [131] M. Bibes, M.-J. Casanove, L. Balcells, S. Valencia, B. Martnez, J.-C. Ousset, and J. Fontcuberta, “Magnetotransport properties of fully strained epitaxial thin films of $\text{La}_{2/3}\text{Ca}_{1/3}\text{MnO}_3$ grown on SrTiO_3 ,” *Applied Surface Science*, vol. 188, no. 1-2, pp. 202–208, 2002. [50](#)

REFERENCES

- [132] J. Z. Sun, D. W. Abraham, R. A. Rao, and C. B. Eom, “Thickness-dependent magnetotransport in ultrathin manganite films,” *Applied Physics Letters*, vol. 74, no. 20, pp. 3017–3019, 1999. [50](#)
- [133] C. Aruta, G. Ghiringhelli, V. Bisogni, L. Braicovich, N. Brookes, a. Tebano, and G. Balestrino, “Orbital occupation, atomic moments, and magnetic ordering at interfaces of manganite thin films,” *Physical Review B*, vol. 80, no. 1, pp. 1–8, 2009. [50, 51](#)
- [134] D. G. Schlom, L.-Q. Chen, C.-B. Eom, K. M. Rabe, S. K. Streiffer, and J.-M. Triscone, “Strain tuning of ferroelectric thin films,” *Annu. Rev. Mater. Res.*, vol. 37, pp. 589–626, 2007. [51](#)
- [135] I. C. Infante, F. Sánchez, J. Fontcuberta, M. Wojcik, E. Jedryka, S. Estradé, F. Peiró, J. Arbiol, V. Laukhin, and J. P. Espinós, “Elastic and orbital effects on thickness-dependent properties of manganite thin films,” *Physical Review B*, vol. 76, p. 224415, 2007. [51, 87](#)
- [136] M. Izumi, Y. Ogimoto, T. Manako, M. Kawasaki, and Y. Tokura, “Interface Effect and Its Doping Dependence in $\text{La}_{1-x}\text{Sr}_x\text{MnO}_3/\text{SrTiO}_3$ Superlattices,” *Journal of the Physics Society Japan*, vol. 71, no. 11, pp. 2621–2624, 2002. [52](#)
- [137] M. Izumi, Y. Ogimoto, Y. Konishi, T. Manako, M. Kawasaki, and Y. Tokura, “Perovskite superlattices as tailored materials of correlated electrons,” *Materials Science and Engineering B*, vol. 84, no. 1-2, pp. 53–57, 2001. [52](#)
- [138] M. Konoto, T. Kohashi, K. Koike, T. Arima, Y. Kaneko, Y. Tomioka, and Y. Tokura, “Magnetic domain structure of a $\text{La}_{0.7}\text{Sr}_{0.3}\text{MnO}_3$ (001) surface observed by a spin-polarized scanning electron microscope,” *Applied Physics Letters*, vol. 84, no. 13, p. 2361, 2004. [53](#)
- [139] P. Lecoئur, P. L. Trouilloud, G. Xiao, A. Gupta, G. Q. Gong, and X. W. Li, “Magnetic domain structures of $\text{La}_{0.67}\text{Sr}_{0.33}\text{MnO}_3$ thin films with different morphologies,” *Journal of Applied Physics*, vol. 82, no. 8, p. 3934, 1997. [54](#)
- [140] A. M. Haghiri-Gosnet, J. Wolfman, B. Mercey, C. Simon, P. Lecoئur, M. Korzenski, M. Hervieu, R. Desfeux, and G. Baldinozzi, “Microstructure and magnetic properties of strained $\text{La}_{0.7}\text{Sr}_{0.3}\text{MnO}_3$ thin films,” *Journal of Applied Physics*, vol. 88, no. 7, pp. 4257–4264, 2000. [54](#)

- [141] Y. Takamura, R. V. Chopdekar, A. Scholl, A. Doran, J. A. Liddle, B. Harteneck, and Y. Suzuki, “Tuning magnetic domain structure in nanoscale $\text{La}_{0.7}\text{Sr}_{0.3}\text{MnO}_3$ islands.,” *Nano letters*, vol. 6, pp. 1287–91, June 2006. [56](#)
- [142] E. J. Kim, J. L. R. Watts, B. Harteneck, A. Scholl, A. Young, A. Doran, and Y. Suzuki, “Magnetic domain structure of $\text{La}_{0.7}\text{Sr}_{0.3}\text{MnO}_3$ nanoislands: Experiment and simulation,” *Journal of Applied Physics*, vol. 109, no. 7, p. 07D712, 2011. [56](#)
- [143] J. Rhensius, C. A. F. Vaz, A. Bisig, S. Schweitzer, J. Heidler, H. S. Krner, A. Locatelli, M. A. Nio, M. Weigand, L. Mchin, F. Gaucher, E. Goering, L. J. Heyderman, and M. Klui, “Control of spin configuration in half-metallic $\text{La}_{0.7}\text{Sr}_{0.3}\text{MnO}_3$ nano-structures,” *Applied Physics Letters*, vol. 99, no. 6, p. 062508, 2011. [56](#)
- [144] S. Crossley, *Electrocaloric materials and devices*. PhD thesis, Department of Materials Science and Metallurgy, 2013. [61](#)
- [145] P. Willmott and J. Huber, “Pulsed laser vaporization and deposition,” *Reviews of Modern Physics*, vol. 72, no. 1, p. 315, 2000. [62](#), [105](#)
- [146] L. C. Phillips, *Spintronic devices with highly spin-polarised manganite electrodes and graphene channels*. PhD thesis, University of Cambridge, January 2012. [62](#), [76](#), [77](#), [79](#), [81](#), [110](#)
- [147] R. Oliver, “Characterisation techniques 1:scanning probe microscopy,” 2010. [65](#)
- [148] D. K. Bowen and B. K. Tanner, *X-ray metrology in semiconductor manufacturing*. CRC Press, 2006. [68](#), [99](#)
- [149] C. M. Schneider and G. Schönhense, “Investigating surface magnetism by means of photoexcitation electron emission microscopy,” *Reports on Progress in Physics*, vol. 65, no. 12, pp. 1785–1839, 2002. [70](#), [71](#)
- [150] S. Imada, A. Sekiyama, and S. Suga, “Soft x-ray spectroscopy and microspectroscopy of correlated materials: photoemission and magnetic circular dichroism,” *Journal of Physics: Condensed Matter*, vol. 19, p. 125204, 2007. [70](#), [72](#)
- [151] J. Stöhr and H. C. Siegmann, *Magnetism: Magnetism From Fundamentals to Nanoscale Dynamics*, vol. 152. Springer, 2006. [71](#), [73](#)
- [152] A. Hubert and R. Schaefer, *Magnetic Domains: The analysis of magnetic microstructures*. Springer, 3rd ed., 2009. [74](#)

REFERENCES

- [153] T. Lahtinen *et al.*, “Ferromagnetic-ferroelectric domain coupling in multiferroic heterostructures,” 2013. [76](#)
- [154] A. Hammouche, E. Siebert, and A. Hammou, “Crystallographic, thermal and electrochemical properties of the system $\text{La}_{1-x}\text{Sr}_x\text{MnO}_3$ for high temperature solid electrolyte fuel cells,” *Materials Research Bulletin*, vol. 24, no. 3, pp. 367 – 380, 1989. [79](#)
- [155] W. Marti, P. Fischer, J. Schefer, and F. Kubel, “Structure characterization with neutron powder data of LaGaO_3 and NdGaO_3 based on X-ray single-crystal data: evidence for an inversion center,” *Zeitschrift für Kristallographie*, vol. 211, no. 12, pp. 891–894, 1996. [79](#)
- [156] J. Hutton and R. J. Nelmes, “High-resolution studies of cubic perovskites by elastic neutron diffraction. II. SrTiO_3 , KMnF_3 , RbCaF_3 and CsPbCl_3 ,” *Journal of Physics C: Solid State Physics*, vol. 14, no. 12, p. 1713, 1981. [79](#)
- [157] B. D. Cullity and C. D. Graham, *Introduction to magnetic materials*. Wiley. com, 2011. [82](#), [83](#), [93](#)
- [158] O. Fruchart, “An overview of magnetisation reversal. i. some basics: Single-domain concept and their use in materials.” European school of magnetism presentation, 2007. [82](#), [83](#), [94](#)
- [159] M. Ghidini, G. Zangari, I. Prejbeanu, G. Pattanaik, L. Buda-Prejbeanu, G. Asti, C. Pernechele, and M. Solzi, “Magnetization processes in hard Co-rich Co–Pt films with perpendicular anisotropy,” *Journal of applied physics*, vol. 100, no. 10, pp. 103911–103911, 2006. [82](#)
- [160] R. Skomski, *Simple models of magnetism*. Oxford University Press Oxford, 2008. [93](#)
- [161] S. Reich, S. Shtrikman, and D. Treves, “Angular variation of coercivity in orthoferrite single crystals,” *Journal of Applied Physics*, vol. 36, no. 1, p. 140, 1965. [94](#)
- [162] S. Brivio, M. Cantoni, D. Petti, a. Cattoni, R. Bertacco, M. Finazzi, F. Ciccacci, a. Sidorenko, G. Allodi, and M. Ghidini, “Decrease of the Curie temperature in $\text{La}_{0.67}\text{Sr}_{0.33}\text{MnO}_3$ thin films induced by Au capping,” *Materials Science and Engineering: B*, vol. 144, no. 1-3, pp. 93–96, 2007. [105](#)

- [163] K. Dörr, J. De Teresa, K. Müller, D. Eckert, T. Walter, E. Vlakhov, K. Nenkov, and L. Schultz, “Preparation and properties of epitaxial $\text{La}_{0.7}\text{Ca}_{0.3}\text{MnO}_{3-\delta}$ films with reduced carrier density,” *Journal of Physics: Condensed Matter*, vol. 12, no. 31, p. 7099, 2000. [106](#)
- [164] A. C. Ferrari, J. C. Meyer, V. Scardaci, C. Casiraghi, M. Lazzeri, F. Mauri, S. Piscanec, D. Jiang, K. S. Novoselov, S. Roth, and A. K. Geim, “Raman Spectrum of Graphene and Graphene Layers,” *Phys. Rev. Lett.*, vol. 97, p. 187401, Oct 2006. [114](#), [116](#)
- [165] A. Reina, H. Son, L. Jiao, B. Fan, M. S. Dresselhaus, Z. Liu, and J. Kong, “Transferring and Identification of Single- and Few-Layer Graphene on Arbitrary Substrates,” *Journal of Physical Chemistry C*, vol. 112, pp. 17741–17744, Nov. 2008. [114](#), [115](#)
- [166] B. Hunt, J. Sanchez-Yamagishi, A. Young, M. Yankowitz, B. LeRoy, K. Watanabe, T. Taniguchi, P. Moon, M. Koshino, P. Jarillo-Herrero, *et al.*, “Massive dirac fermions and hofstadter butterfly in a van der waals heterostructure,” *Science*, vol. 340, no. 6139, pp. 1427–1430, 2013. [115](#), [116](#)
- [167] P. Zomer, S. Dash, N. Tombros, and B. van Wees, “A transfer technique for high mobility graphene devices on commercially available hexagonal boron nitride,” *Applied Physics Letters*, vol. 99, no. 23, pp. 232104–232104, 2011. [115](#), [116](#)
- [168] P. Nemes-Incze, Z. Osváth, K. Kamarás, and L. Biró, “Anomalies in thickness measurements of graphene and few layer graphite crystals by tapping mode atomic force microscopy,” *Carbon*, vol. 46, no. 11, pp. 1435–1442, 2008. [120](#)
- [169] M. Viret, M. Drouet, J. Nassar, J. Contour, C. Fermon, and A. Fert, “Low-field colossal magnetoresistance in manganite tunnel spin valves,” *EPL (Europhysics Letters)*, vol. 39, no. 5, p. 545, 1997. [140](#)
- [170] J. Sun, L. Krusin-Elbaum, P. Duncombe, A. Gupta, and R. Laibowitz, “Temperature dependent, non-ohmic magnetoresistance in doped perovskite manganate trilayer junctions,” *Applied physics letters*, vol. 70, no. 13, pp. 1769–1771, 1997. [140](#)
- [171] M. Bowen, M. Bibes, A. Barthélémy, J.-P. Contour, A. Anane, Y. Lematre, and A. Fert, “Nearly total spin polarization in $\text{La}_{2/3}\text{Sr}_{1/3}\text{MnO}_3$ from tunneling experiments,” *Applied Physics Letters*, vol. 82, no. 2, p. 233, 2003. [140](#)

REFERENCES

- [172] M. Bowen, A. Barthélémy, M. Bibes, E. Jacquet, J.-P. Contour, A. Fert, F. Cicacci, L. Duò, and R. Bertacco, “Spin-polarized tunneling spectroscopy in tunnel junctions with half-metallic electrodes,” *Physical review letters*, vol. 95, no. 13, p. 137203, 2005. [140](#)
- [173] C. Rüster, C. Gould, T. Jungwirth, J. Sinova, G. Schott, R. Giraud, K. Brunner, G. Schmidt, and L. Molenkamp, “Very large tunneling anisotropic magnetoresistance of a (Ga,Mn)As/GaAs/(Ga,Mn)As stack,” *Physical review letters*, vol. 94, no. 2, p. 027203, 2005. [143](#)